Dissecting Molecular Events of Phase Separation of Fused in Sarcoma Using Single-Molecule FRET, HomoFRET, and Vibrational Raman Spectroscopy

Ashish Joshi

A thesis submitted for the partial fulfillment of the degree of

Doctor of Philosophy

Department of Biological Sciences

Indian Institute of Science Education and Research Mohali

Knowledge City, Sector 81, SAS Nagar, Manauli PO, Mohali 140306, Punjab, India.

May 2024

Dedicated to my co-workers

"Success is not final; failure is not fatal:
it is the courage to continue that counts."

- Winston Churchill

Declaration

The work presented in this thesis has been carried out by me under the guidance of Prof. Samrat Mukhopadhyay at the Indian Institute of Science Education and Research Mohali. This work has not been submitted in part or in full for a degree, a diploma, or a fellowship to any other university or institute. Whenever contributions of others are involved, every effort is made to indicate this clearly, with due acknowledgment of collaborative research and discussions. This thesis is a bona fide record of my original work, and all sources listed within have been detailed in the bibliography.

Ashish Joshi

Date:

Place:

In my capacity as the supervisor of the candidate's thesis work, I certify that the above statements by the candidate are true to the best of my knowledge.

Prof. Samrat Mukhopadhyay

Date:

Place:

Acknowledgments

The completion of this Ph.D. thesis has been a collective effort supported by numerous individuals. I want to express my gratitude to those who have accompanied me on this journey and provided invaluable assistance. My heartfelt thanks go to all the colleagues with whom I've collaborated. Your collective contributions, no matter the scale, have played a vital role in shaping the outcome, and I appreciate how things have unfolded.

Above all, my gratitude extends to Prof. Samrat Mukhopadhyay, my Ph.D. supervisor, for welcoming me into an incredible research group and involving me in stimulating projects. His boundless curiosity, thirst for knowledge, and unwavering dedication continually inspired me to push my limits. Witnessing his relentless dedication and passion, I now fully comprehend his favorite saying, “Success is no accident.” His sincerity and commitment, both as a researcher and an educator, are truly commendable. Beyond scientific knowledge, he imparted invaluable lessons on critical thinking and being a well-rounded individual. His mentorship not only shaped my scientific acumen but also influenced my personal growth, from posture to communication. His mentorship not only shaped my scientific thinking but also influenced my personal growth.

I'm grateful to Prof. Anand K. Bachhawat and Dr. Mahak Sharma, my thesis committee members, for their invaluable insights, yearly evaluations, and enriching discussions that have significantly contributed to my progress.

I want to thank all my teachers throughout my life. I would like to give a special thanks to Prof. Nimisha Sharma for showing belief in me and giving me my first-ever research lab exposure during my undergrad. I want to thank Dr. Vaibhav Bhardwaj for mentoring me and teaching me basic molecular biology during my undergrad. I would also like to thank Prof. Ranjith for being my lifelong teacher and a very good friend.

I want to thank all my colleagues for their great collaborations. I owe special thanks to Dr. Anamika Avni, Anuja Walimbe, Lisha Arora, Snehasis Sarkar, Swastik, Prince, Dhruba Chatterjee, and Dr. Sandeep K. Rai for their contributions to my thesis work. I thank Prof. Dorothee Dormann (Johannes Gutenberg University of Mainz, Germany) for her kind gift of FUS full-length, FUS-eGFP, and PRMT1 plasmids. Prof. Elizabeth Rhoades (University of Pennsylvania, USA) and Prof. Nicolas L. Fawzi (Brown University, USA) for their kind gifts

of tau and FUS-LC DNA plasmids. I acknowledge IISER Mohali for providing financial support.

Special thanks go to Dr. Mily Bhattacharya for her continuous support and contagious enthusiasm. I was fortunate enough to discuss several projects with her, which eventually yielded a beautiful collaboration. Her cheerful demeanor, kindness, and unwavering positivity are traits I deeply admire. I'm immensely grateful for her contributions to our manuscripts and valuable suggestions that significantly enhanced my research. Her presence has been a constant source of inspiration, always keeping me motivated and smiling.

I'm thankful for the research facilities at IISER Mohali that greatly supported my work. Vidya bhaiya's dedication to lab cleanliness ensured smooth experiments. Taseen, the technician, was instrumental in capturing fluorescent images. I also extend gratitude to the hostel, academic, administrative, and library staff for their contributions. Special thanks to the canteen, mess staff, and everyone who ensured a steady supply of energy for my prolonged experiments.

I extend my sincere gratitude to Dr. Priyanka Dogra, my mentor and guiding light in the early stages of my Ph.D. Her unwavering support, encouragement, and guidance were invaluable throughout my journey. From mastering laboratory techniques to cultivating a scientific mindset, she played a pivotal role in shaping my development. Joining Priyanka's subgroup on that first day at Samrat’s lab felt like destiny's guiding hand, shaping the course of my journey in the most impactful way possible

I owe a heartfelt acknowledgment to one of the purest souls I have ever met throughout my life, Dr. Anamika Avni, for her unwavering support. Beyond aiding in experiments and manuscripts, she made exploring Chandigarh's diverse cuisines an unforgettable experience. The memories we made together are etched in my heart. If there is one friend I have to take from IISER for my entire life, it is Anamika for sure. She taught me the power of hard work and consistency to achieve anything you want. One of her favorite quotes, *“You belong,”* makes complete sense to me now. Seeing her performance in the toughest situations gave me confidence in myself throughout this journey.

I consider myself incredibly fortunate to have been part of a lab filled with extraordinary individuals. The wealth of knowledge and experience from both past and present lab members was an invaluable source of learning for me. Dr. Priyanka Madhu introduced the importance of handmade tea in the lab; Dr. Aishwarya Aggarwal is like my good-to-go senior. She has always extended her help in all possible ways and is always full of both life and scientific

suggestions. She also helped me with my ordering duties during my initial days. I want to express my gratitude to Dr. Debapriya Das and Dr. Sayanta Mahapatra for always giving me good scientific suggestions. Their company made them so easily approachable that sometimes I even forget that they are my seniors. Deep 10 P.M. discussions with Dr. Das and a short standup from Dr. Mahapatra will always have a special corner in my heart.

I feel incredibly fortunate to be a part of a group that feels more like a family. I want to thank all the current members of SM lab Shalini, Sneha, Snehasis, Dhruba, Roopali, Anuja, Anusha, Lisha, Dr. Sandeep, and Dr. Dipankar for bearing me till the end. I would like to give a special thanks to our post-doctoral fellow, Dr. Dipankar Bhowmik, for always providing optimism and support during the toughest end phase of my Ph.D. He is truly a great scientist and a wonderful soul to be around. I will always cherish all the laughter from Anusha, and I would like to take her calmness and very strong mindset for general life problems. Their presence made this journey uniquely special. Many of life's problems were solved over cups of tea, creating moments I'll always treasure. From engaging in scientific discussions over coffee to being there as friends, they've been an invaluable part of my journey at IISER Mohali. I would like to express my gratitude to Roopali Khanna for taking away all the ordering responsibilities from me and bearing my short temperance while ordering lab consumables. I would like to acknowledge Dhruba Chatterjee for taking all my UPS and Eppendorf instruments responsibility, making my belief stronger in humanity, and teaching me the benefits of selflessness.

I want to thank my batchmates, Lisha Arora and Dr. Sandeep K. Rai, for always supporting me. They held me intact during the darkest of my time. My “Bro” Lisha has served me a lot of good food throughout this journey, and I must say I enjoy our Tom and Jerry fight a lot and hope to keep it continuing forever. Lisha, being a good listener, was always my go-to friend for discussing all my personal and professional issues. I can't thank God enough for giving me Sandeep, a younger brother and an incredible friend who has been a constant pillar of support. His assistance in managing lab duties made everything seamless. We both share a lot in common in our life, and I wish to keep him as my brother forever. I'm incredibly blessed to have them both in my life.

I want to convey my sincere gratitude to all my current and past mentees. I have always been fortunate to mentor very talented and exceptionally hardworking students. All of my students, including Swastik, Anuja, Snehasis, and Sneha, have been exceptional teammates. I would like

to thank Anuja Walimbe and Snehasis Sarkar for all their support and help throughout my PhD. I want to express my special thanks to Snehasis. Despite being the youngest member, he swiftly mastered all the necessary skills and provided exceptional assistance to complete my ongoing projects. I feel blessed to have Snehasis and Anuja as my (favorite) mentees, who I think have all the capabilities to become better scientists than me. I have no words to thank Swastik, my first student, for his extraordinary help and support during the lag phase of my PhD. Swastik and I started growing together, and his cheerful, pleasant aura has always kept me happy and motivated. I owe a lot of my growth and success to their hard work and commitment, and I wish them all success and happiness.

I extend my heartfelt gratitude to my badminton friends, who brought joy and balance to my life during the rigorous journey of my Ph.D. Having an amazing friend circle outside the lab serves as an oxygen cylinder sometimes. I want to thank my badminton group: Dr. Chandershekhar, Dr. Sanjeev Kumar, Ritu Kumar, Sanjeev Kumar Yadav, Deepak, Arjun, Pankaj, Aditya, Anjali, Sneha, Gaurav, Pritam, and Dr. Dinanath. Pankaj Sahu deserves special acknowledgment for being the best badminton doubles partner, bearing all my anger, and covering all my weaknesses in court. I can't thank Deepak Yadav and Aditya enough for giving me the toughest rivalry on the court and being my all-time support outside of the court. I would like to also thank Anjali Mahadevan and Arjun Bisht for all those wonderful “Chai” outings. I would like to thank my BTech friends Yukti, Tapish, Mansi, Mridula, Aakash, and Munish for supporting me throughout my journey.

I would like to acknowledge all my PH18 batchmates, including Kajal, Gagan, Aanchal, Pooja, Deeptodeep, Mahender, Kusum, Vaibhav, and Umer. I would also like to thank Dr. Archit Gupta, a friend from IPU, a mentor for life, and a very amazing scientific collaborator. I feel very proud whenever people say that you and Archit are both carbon copies and a product from the same factory (USBT, GGSIPU).

I would like to thank Anuja Walimbe again, one of my strongest pillars of support. I have no hesitation in saying that whatever I have achieved till now, she holds a significant share in that, and I am grateful. I wish to continue this journey together, supporting each other and achieving new milestones hand in hand. I am immensely grateful for her unwavering support, patience, and understanding throughout my entire PhD journey. Her encouragement, patience, and unwavering belief in me have been the pillars that held me strong during challenging times.

Thank you for being my constant source of strength and for being by my side every single day through every high and low.

Last but not least, I extend my deepest gratitude to my family, whose unwavering support and boundless love made this journey possible. My elder brother, Deepak Joshi, and sister, Mamta Joshi, have been my pillars of strength. They never asked about my Ph.D. product despite supporting me unconditionally and keeping me protected from all the family responsibilities throughout this journey. My mother, Urmila Joshi, instilled in me the virtues of resilience and standing up for righteousness. My father, Ramesh Chand Joshi, taught me the importance of an unwavering spirit. My cousins, Garima and Gaurav, have always shown unwavering belief in me. My uncles Ajay Joshi, Vijay Joshi, and Rajender Joshi have been constant pillars of support. For everything they've done and for shaping who I am today, this thesis stands as a dedication to my family. Additionally, I want to thank myself for sustaining me during the darkest of nights and not losing belief in myself. Lastly, I would again thank my FUS group members for all their support; I dedicate this thesis to my “Fuzzy” group.

Ashish Joshi

******

Thesis Synopsis

Dissecting Molecular Events of Phase Separation of Fused in Sarcoma Using Single-Molecule FRET, HomoFRET, and Vibrational Raman Spectroscopy

Chapter 1. Introduction

The human body consists of roughly 30 trillion cells, and a single eukaryotic cell can host up to several billion protein molecules to perform their functions. These protein molecules, in combination with several nucleic acids, are involved in an array of biochemical processes within cells, such as immune protection, cell cycle regulation and differentiation, cellular trafficking, catalyzing biochemical reactions, and so on. Phase separation of biomolecules into liquid-like supramolecular assemblies has newly emerged as a critical organizing principle within living cells. The intrinsically disordered group of proteins (IDPs/IDRs) comprising low-complexity (LC), prion-like domains have been identified as the major drivers of cellular phase separation leading to the formation of membrane-less organelles (MLOs) enriched in proteins and nucleic acids. In addition to performing diverse physiological functions, these non-canonical MLOs are also known to undergo aberrant phase transitions and aggregation, resulting in a range of fatal neurodegenerative diseases. Hence, obtaining insights into critical molecular events rendering the formation of these pathological assemblies has gained significant importance. A plethora of ensemble tools have been employed to delineate the biophysical principles of phase separation and maturation. However, a detailed understanding of the fundamental molecular drivers governing phase separation and liquid-to-solid transitions remains elusive. Here, we illuminate the inner workings and chain dynamics of an archetypical prion-like, low-complexity domain of Fused in Sarcoma (FUS-LC) using an amalgamation of single-droplet, single-molecule FRET, picosecond time-resolved fluorescence anisotropy, fluorescence correlation spectroscopy in conjunction with vibrational Raman spectroscopy. Our results reveal the conformational distribution and dynamics within the monomeric and condensed phases at a single-molecule resolution in a droplet-by-droplet manner. We investigate the change in material properties accompanying a density transition coupled percolation of the monomeric FUS-LC, leading to the formation of a dense phase comprising a viscoelastic network fluid. The incorporation of a disease-associated mutation (G156E) resulted in the further increased expansion of the FUS-LC polypeptide chain, causing enhanced protein-protein interactions and an increase in dense phase concentration, leading to increased

aggregation propensity in patients. We also utilized the vibration Raman spectroscopy to capture the structural changes in the hydration water layer within liquid droplets of three archetypal phase-separating proteins, using single-droplet vibrational Raman spectroscopy, highlighting a sequence-encoded reorganization of the hydrogen bonding network of solvent molecules upon phase separation. Our study illuminates the internal restructuring of the solvent hydrogen bonding network distinctly within the condensates and the dispersed phase in a sequence-encoded manner in the absence and presence of co-solutes. Finally, we demonstrate the application of a simple and versatile technique of anisotropy imaging to study homoFRET as a reporter of molecular packaging or as a proximity ruler within the dynamic biomolecular condensates of an archetypal phase separating protein Fused in Sarcoma (FUS) both *in vitro* and *in situ*. Our homoFRET measurements capture the alteration in supramolecular organization and nanoscale architectures within condensates formed in diverse solution conditions.

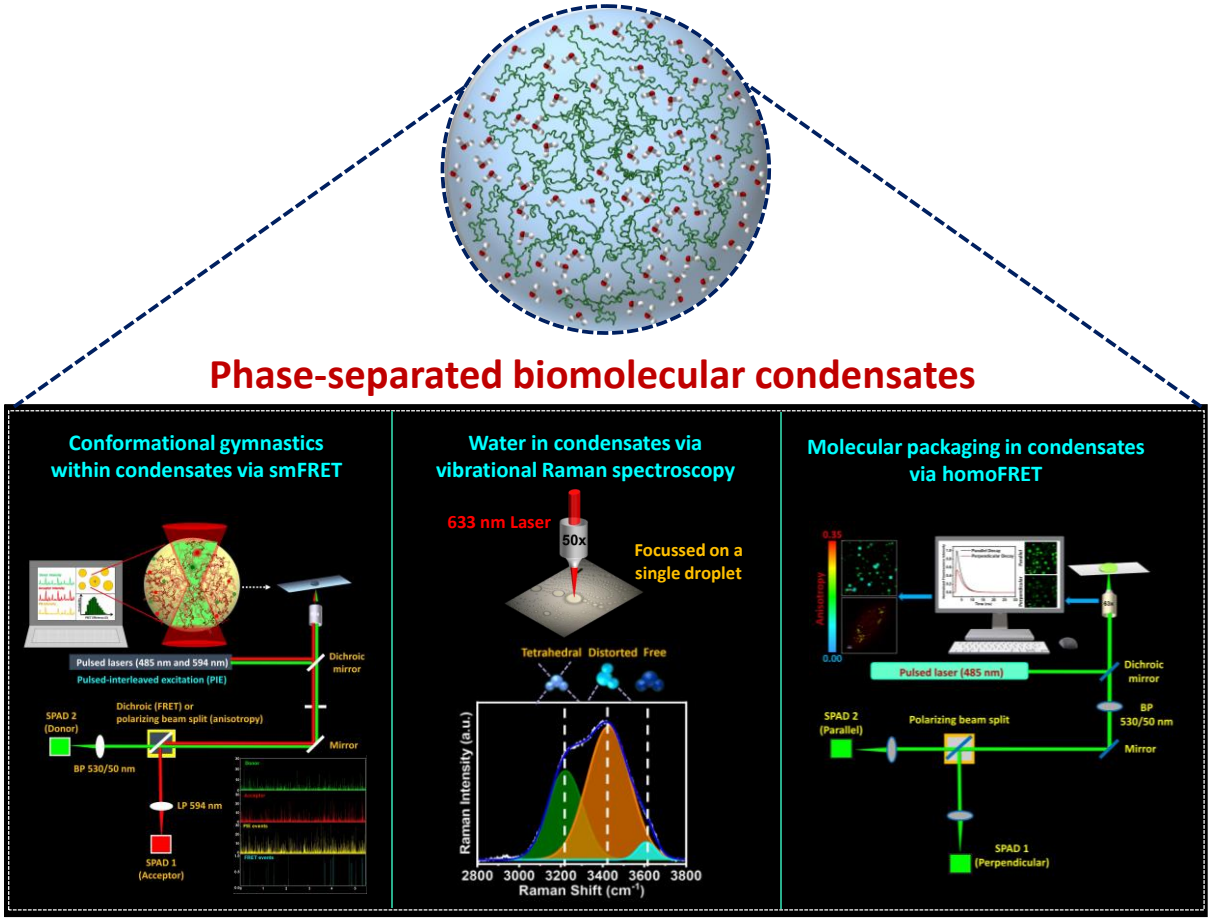

Taken together, the techniques and tools developed in this thesis can serve as a potent tool to illuminate the complex interplay of the large number of intermolecular interactions driving

phase separation and can give insights into key molecular drivers of biological phase transitions.

Chapter 2. Single-molecule FRET Unmasks Structural Subpopulations and Crucial Molecular Events During FUS Low-complexity Domain Phase Separation

Biomolecular condensates formed via phase separation of proteins and nucleic acids are thought to be associated with a wide range of cellular functions and dysfunctions. We dissect

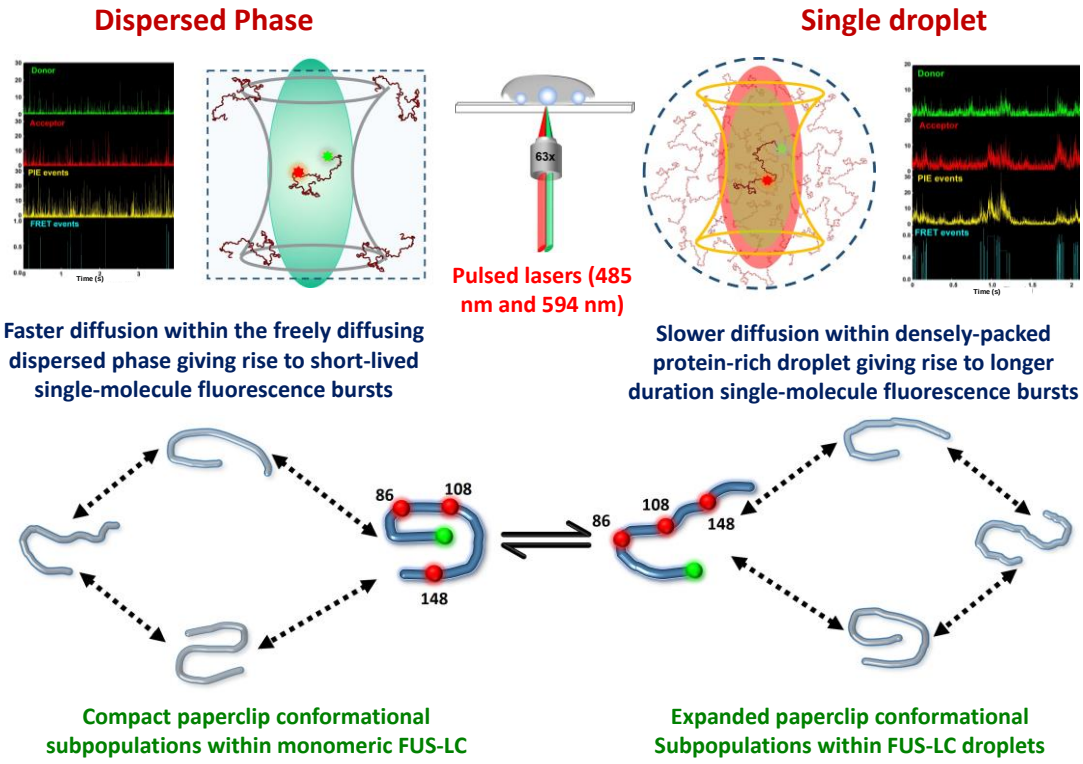

Joshi A, Walimbe A, Avni A, Rai SK, Arora L, Sarkar S, & Mukhopadhyay S. Single-molecule FRET unmasks structural subpopulations and crucial molecular events during FUS low-complexity domain phase separation. *Nat. Commun.* **2023,** 14, 7331.

critical molecular events associated with phase separation of an intrinsically disordered prion-like low-complexity domain of Fused in Sarcoma (FUS-LC) by performing single-molecule studies, permitting us to access the wealth of molecular information that is skewed in conventional ensemble experiments. Our single-molecule FRET experiments reveal the coexistence of two conformationally distinct subpopulations in the monomeric form. Single-droplet single-molecule FRET studies coupled with fluorescence correlation spectroscopy,

picosecond time-resolved fluorescence anisotropy, and vibrational Raman spectroscopy indicate that structural unwinding switches intramolecular interactions into intermolecular contacts allowing the formation of a dynamic network within condensates. We investigate the change in material properties accompanying a density transition coupled percolation of the monomeric FUS-LC, leading to the formation of a dense phase comprising a viscoelastic network fluid. A disease-related mutation G156E introduces enhanced structural plasticity and more condensed droplets, engendering greater interchain interactions that can accelerate pathological aggregation. Our findings provide key mechanistic underpinnings of sequence-encoded dynamically-controlled structural unzipping, resulting in biological phase separation.

Chapter 3. The Hydrogen-bonded Water Network in Phase-separated Biomolecular Condensates

Biomolecular condensates formed via macromolecular phase separation of intrinsically disordered proteins/regions (IDPs/IDRs) and nucleic acids into the liquid-like membraneless

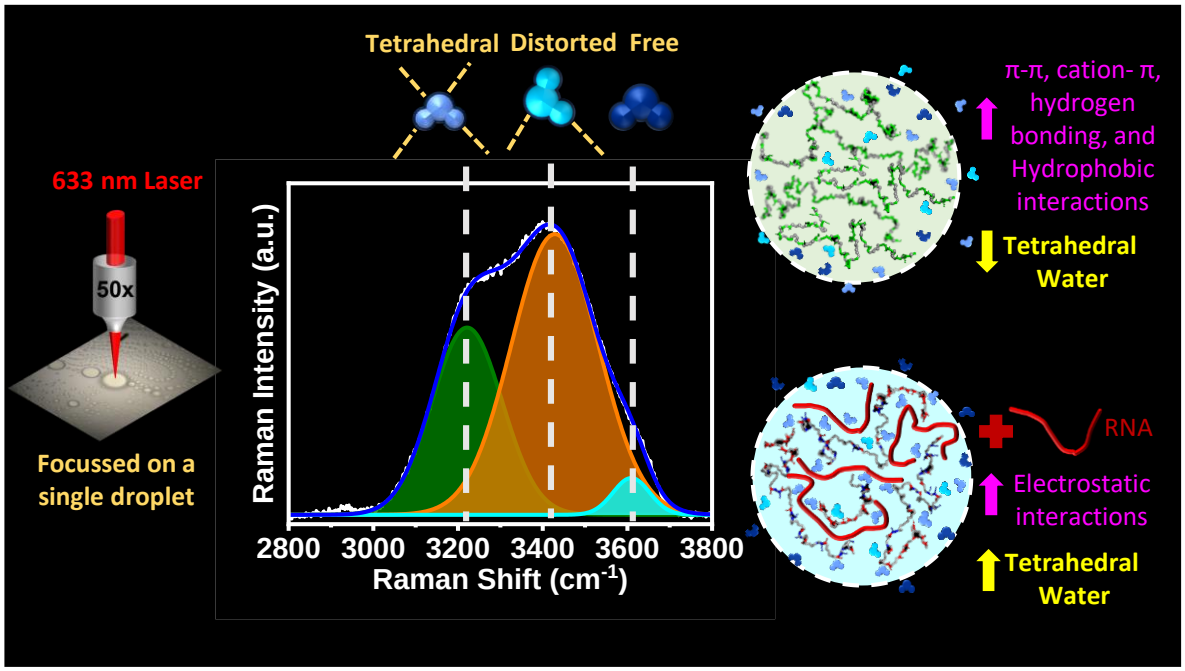

Joshi A, Avni A, Walimbe A, Rai SK, Sarkar S, & Mukhopadhyay S. The hydrogen-bonded water network in phase-separated biomolecular condensates (*manuscript submitted*).

compartments are proposed to play a critical role in spatiotemporally organizing and controlling cellular biochemistry. Water makes up for ~ 60-70 % of the condensate volume and is thought to influence the complex interplay of chain-chain and chain-solvent interactions, modulating the phase behavior of macromolecules and mesoscale material properties of condensates. The behavior of water in condensates, as well as the key structural and dynamical roles of protein hydration water in driving the phase separation process, remain poorly understood. In this study, we employ single-droplet vibrational Raman spectroscopy to illuminate the structural redistribution of water in the protein hydration water layer, facilitating the formation of a dynamic intermolecular network resulting in macromolecular phase separation of neuronal IDPs. We provide a direct observation of the changes in the water hydrogen bonding network driven by a range of molecular drivers including hydrophobic, hydrogen bonding, and electrostatic effects in directing phase separation. Single-droplet water Raman studies can offer a potent tool to shed light on the intriguing interplay of sequence-dependent chain-chain and chain-solvent interactions governing the driving force of biological phase transitions involved in physiology and disease.

Chapter 4. Intermolecular Energy Migration via HomoFRET Captures the Modulation in the Material Property of Phase-separated Biomolecular Condensates

Biomolecular condensation via phase separation of proteins and nucleic acids has emerged as a crucial mechanism underlying the spatiotemporal organization of cellular components into functional membraneless organelles. However, aberrant maturation of these dynamic, liquid-like assemblies into irreversible gel-like or solid-like aggregates is associated with a wide range of fatal neurodegenerative diseases. New tools are essential to dissect the changes in the internal material properties of these biomolecular condensates that are often modulated by a wide range of factors involving the sequence composition, truncations, mutations, post-translational modifications, and the stoichiometry of nucleic acids and other biomolecules. Here, we employ homo-Förster Resonance Energy Transfer (homoFRET) as a proximity intermolecular ruler to study intermolecular energy migration that illuminates the molecular packing in the nanometric length-scale within biomolecular condensates. We used the homoFRET efficiency, measured by a loss in the fluorescence anisotropy due to rapid depolarization, as a readout of the molecular packing giving rise to material properties of

biomolecular condensates. Using single-droplet anisotropy imaging, we recorded spatially-resolved homoFRET efficiencies of condensates formed by fluorescent protein-tagged Fused

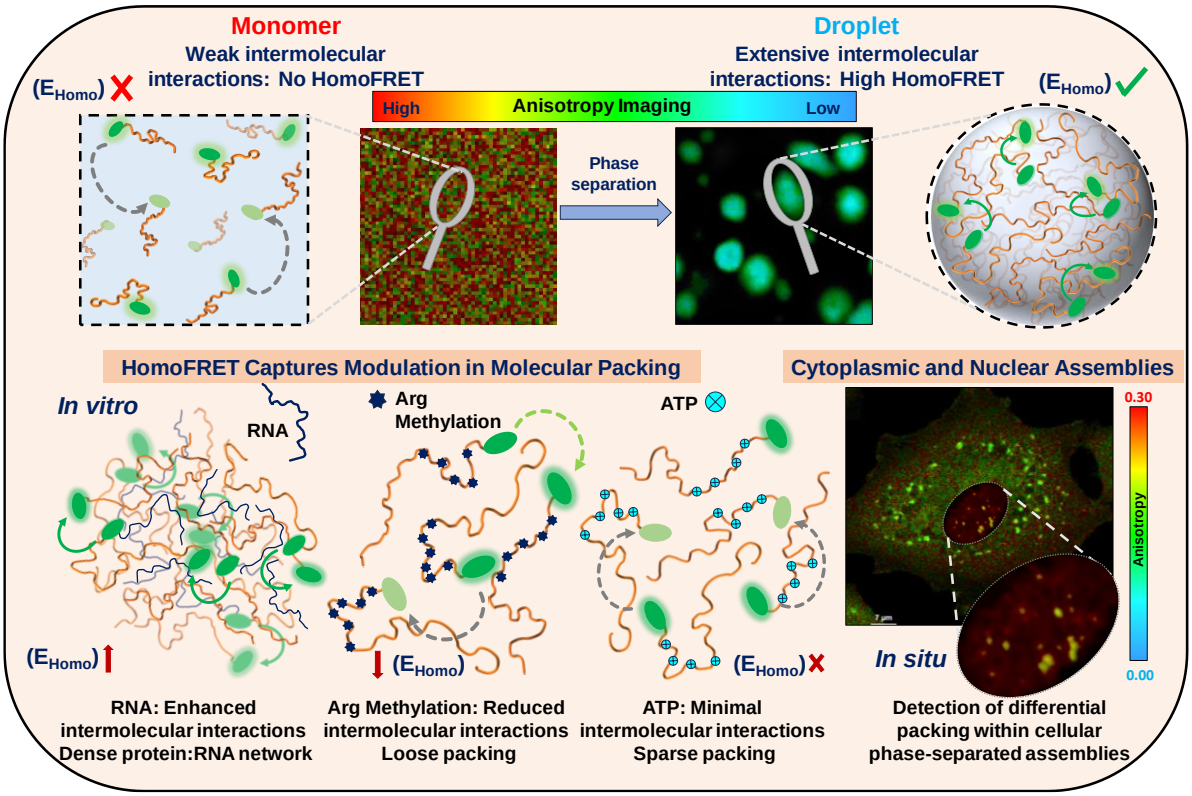

Joshi A, Walimbe A, Sarkar S, Arora L, Kaur G, Jhandai P, Chatterjee D, Banerjee I, & Mukhopadhyay S. Intermolecular energy migration via homoFRET captures the modulation in the material property of phase-separated biomolecular condensates (*bioRxiv 2024*).

in Sarcoma (FUS). By performing single-droplet picosecond time-resolved anisotropy measurements, we were able to discern various energy migration events within the dense network of polypeptide chains in FUS condensates. Our homoFRET studies also captured the modulation of material properties by RNA, ATP, and post-translational modification. We also used mammalian cell lines stably expressing FUS to study nuclear FUS and oxidative stress-induced stress granule formation in the cytoplasm. Our studies demonstrate that spatially-resolved homoFRET methodology offers a potent tool for studying intracellular phase transitions in cell physiology and disease.

Chapter 5. Conclusions and Future Directions

The work described in this thesis provides methodologies to dissect crucial molecular grammar of an archetypical phase separating protein Fused in Sarcoma (FUS) both in monomeric and droplet phases. In this chapter, we provide an overall summary of our work with certain limitations and discuss some fascinating questions for the future. The major findings of the work include (i) a single-molecule view of biomolecular condensates dissecting some crucial molecular events (Chapter 2), (ii) the role of the hydration water network structure in the formation of different types of biomolecular condensates (Chapter 3), and (iii) probing the molecular packing via homoFRET within biomolecular condensates (Chapter 4). The methodologies described in this thesis can find a broad range of applications in studying biomolecular phase transitions *in vitro* and *in situ* involved in some of the crucial physiological and pathological mechanisms.

******

List of Publications

- Rai, S. K., Khanna, R., Sarbahi, A., **Joshi, A.,** & Mukhopadhyay S. Chaperone-Mediated Phase Separation Regulates Liquid-to-Solid Phase Transitions of Tau into Amyloid Fibrils (manuscript in preparation).

- **Joshi, A.,** Walimbe, A., Sarkar, S., Arora, L., Kaur, G., Jhandai, P., Chatterjee, D., Banerjee, I., & Mukhopadhyay, S. Intermolecular Energy Migration via HomoFRET Captures the Modulation in the Material Property of Phase-Separated Biomolecular Condensates *(bioRxiv 2024).*

- **Joshi, A.,** Avni, A., Walimbe, A., Rai, S. K., Sarkar, S., & Mukhopadhyay, S. The Hydrogen-Bonded Water Network in Phase-Separated Biomolecular Condensates *(manuscript submitted).*

- **Joshi, A.,** Walimbe, A., Avni, A., Rai, S. K., Arora, L., Sarkar, S., & Mukhopadhyay, S. Single-Molecule FRET Unmasks Structural Subpopulations and Crucial Molecular Events During FUS Low-Complexity Domain Phase Separation. *Nat. Commun.*, 14, 7331 (2023).

- Avni, A., **Joshi, A.,** & Mukhopadhyay, S. Hydrogen-Deuterium Exchange Vibrational Raman Spectroscopy Distinguishes Distinct Amyloid Polymorphs Comprising Altered Core Architecture. *J. Phys. Chem. Lett.*, 14, 5592–5601 (2023).

- Mahapatra, S., Sarbahi, A., Punia, N., **Joshi, A.,** Avni, A., Walimbe, A., & Mukhopadhyay, S. ATP Modulates Self-Perpetuating Conformational Conversion Generating Structurally Distinct Yeast Prion Amyloids that Limit Autocatalytic Amplification. *J. Biol. Chem.*, 299, 104654 (2023).

- Gupta, A.,[§] **Joshi, A.,[§]** Arora, K., Mukhopadhyay, S., & Guptasarma, P. The Bacterial Nucleoid-Associated Proteins, HU and Dps, Condense DNA into Context-Dependent Biphasic or Multiphasic Complex Coacervates. *J. Biol. Chem.*, 299, 104637 (2023). **[§]Contributed equally.**

- **Joshi, A.,** & Mukhopadhyay, S. Biophysics of Biomolecular Condensates. *Biophys. J.*, 122, 737–740 (2023).

- Pattanashetty, S. G., **Joshi, A.,** Walimbe, A., & Mukhopadhyay, S. "Guidelines for Experimental Characterization of Liquid–Liquid Phase Separation in Vitro" in "***Droplets of Life***" **2022,** Volume 1, Pages 233-249. (Publisher: Elsevier; Editor: Vladimir Uversky, University of South Florida).

- Avni, A.,[§] **Joshi, A.,[§]** Walimbe, A., Pattanashetty, S. G., & Mukhopadhyay, S. Single-Droplet Surface-Enhanced Raman Scattering Decodes the Molecular Determinants of Liquid-Liquid Phase Separation. *Nature Communications*, 13, 4378 (2022). **[§]Contributed equally**.

- Dogra, P., Roy, S. S., **Joshi, A.,** & Mukhopadhyay, S. Hofmeister Ions Modulate the Autocatalytic Amyloidogenesis of an Intrinsically Disordered Functional Amyloid Domain via Unusual Biphasic Kinetics. *J. Mol. Biol.*, 432, 6173–6186 (2020).

- Dogra, P., **Joshi, A.,** Majumdar, A., & Mukhopadhyay, S. Intermolecular Charge-Transfer Modulates Liquid-Liquid Phase Separation and Liquid-to-Solid Maturation of an Intrinsically Disordered pH-Responsive Domain. *J. Am. Chem. Soc.*, 141, 20380–20389, (2019).

Presentations at Conferences

- **Ashish Joshi**, Anuja Walimbe, Anamika Avni, Sandeep K. Rai, Lisha Arora, Snehasis Sarkar, and Samrat Mukhopadhyay "Single-droplet single-molecule FRET and vibrational Raman spectroscopy unmasks structural subpopulations and crucial molecular events during FUS low-complexity domain phase separation." Presented poster at FCSXIV, the 14th National Workshop on Fluorescence and Raman Spectroscopy meeting, organized jointly by the Indian Institute of Science Education and Research Mohali (IISER Mohali) and Institute of Nanoscience and Technology (INST) from December 9-14, 2023, at Mohali, Punjab, India.

- **Ashish Joshi**, Anuja Walimbe, Anamika Avni, Sandeep K. Rai, Lisha Arora, Snehasis Sarkar, and Samrat Mukhopadhyay "Single-droplet single-molecule FRET and vibrational Raman spectroscopy unmasks structural subpopulations and crucial molecular events during FUS low-complexity domain phase separation." Presented poster at Complex Fluid International Conference (CompFlu 2023), organized by Indian Institute of Technology (IIT) Madras, Chennai, India, from December 18-20, 2023.

Table of Contents

Introduction

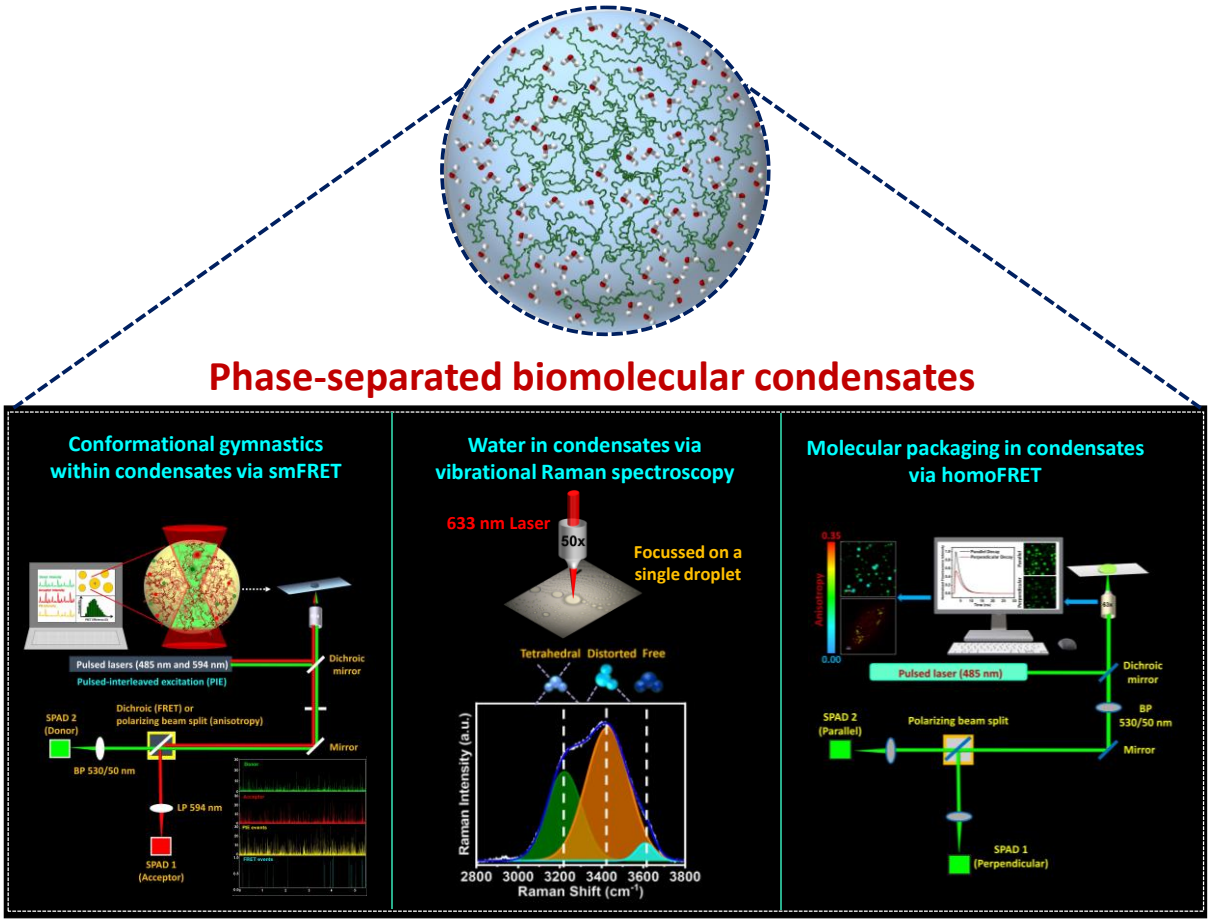

1.1 Intrinsically disordered proteins

1.1.1 Introduction to intrinsic disorder in proteins

The human body comprises approximately 30 trillion cells, and a single eukaryotic cell can host up to several billion protein molecules that perform a wide range of functions[1,2]. These protein molecules perform key biochemical processes within cells, such as immune protection, cell cycle regulation and differentiation, cellular trafficking, catalyzing biochemical reactions, and so on. For several decades, the structure-function paradigm governed the physiological function of proteins, describing that the protein function is governed by its well-defined 3D structure encoded in its amino acid sequence[3-12]. Another aspect of this viewpoint is the “lock and key” model by Emil Fischer, explaining the specificity of enzymes and the "induced fit" model suggesting the change in protein/enzyme's active site conformations to enhance its binding with the substrate[13]. However, recent studies have unveiled a novel class of proteins termed intrinsically disordered proteins (IDPs) that lack a definite three-dimensional structure and defy the traditional sequence-structure-function relationship, unlike globular proteins. These proteins perform an array of complex biological functions within the cells due to their inherent flexibility, enabling them to interact with multiple binding partners simultaneously[14-21]. On the contrary to natively folded proteins, IDPs exhibit variations in amino acid composition, hydrophobicity, charge distribution, and aromaticity. Moreover, folded proteins can also possess disordered regions/domains, namely intrinsically disordered protein regions (IDPRs), enriched in polar amino acids like Arg, Gln, Ser, Glu, and Lys, alongside structure-breaking amino acids such as Pro and Gly. This unique amino acid composition increases the protein's disorder by amplifying its hydrophobicity and net charge[22]. The existence of IDPs and IDRs is ubiquitous in nature and can be observed across all the life kingdoms and viral proteomes. Several studies highlight the common occurrence of these proteins/regions among all living beings, and the percentage of occurrence rises significantly upon increasing complexity of organisms. The eukaryotic genome constitutes nearly 25-30% of the fraction coding for IDPs or IDRs[18-24]. IDPs are highly dynamic and known for rapidly changing conformations possessing approximately equal energies[17]. IDPs possess a relatively flat free-energy surface on a folding free-energy landscape carrying multiple local energy minima separated by minor energy barriers, unlike “funnel-shaped” global energy minimum for folded/globular proteins, representing a thermodynamically favorable native state (Figure 1.1)[24-26]. Furthermore, the energy landscape model shows the binding of native complexes

within IDPs with various other partners. The unfolded polypeptide chains at the top of the 'energy funnel' represent the dynamic, rapidly interconverting conformational states.

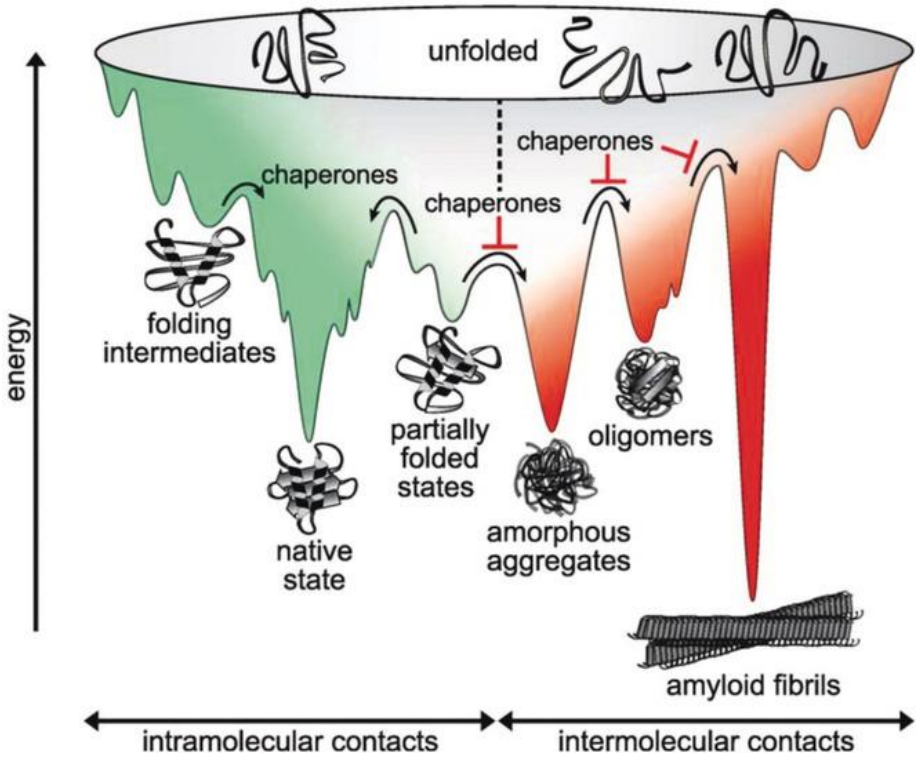

Figure 1.1. An illustration of protein folding energy landscape for native folding and aggregation, predominantly driven by intramolecular and intermolecular contacts, respectively. The native folded state is obtained by funneling down the unfolded chains to the thermodynamically favorable, low-energy states via multiple folding intermediates and the partially folded states. Similarly, the unfolded chain can enter the off-pathway, folding to form higher-order self-assemblies, including oligomers and amorphous and amyloid aggregates. Chaperones can either facilitate or inhibit the crossing of the kinetic energy barriers depending on the fate of the folding process. Reproduced with permission from reference (26).

As the protein folds, the transition from disordered intermediates to the natively folded conformational state includes the generation of a large number of partially folded states called metastable states, which get temporarily populated during this process[18,27]. These transient metastable states, upon accumulation, can lead to the formation of pathological oligomers, protofibrils, amorphous and amyloid aggregates[9,27-29]. Interestingly, nearly 33% of the human genome codes for proteins that are either IDPs or contain IDRs, which can be distinguished easily from folded/globular proteins by potential energy landscapes (Figure 1.2)[29-31]. The folded proteins exhibit a conformational landscape with a funnel-shaped global energy

minimum that defines the conformational entropy of these proteins; however, IDPs contain multiple energy minima separated by infinitesimal barriers, which results in rapidly interconverting dynamic conformational states amongst multiple local energy minima with nearly equal energies. Hence, unlike folded proteins, IDPs exist as rapidly interconverting dynamic ensembles in their native state (Figure 1.2)[18,31].

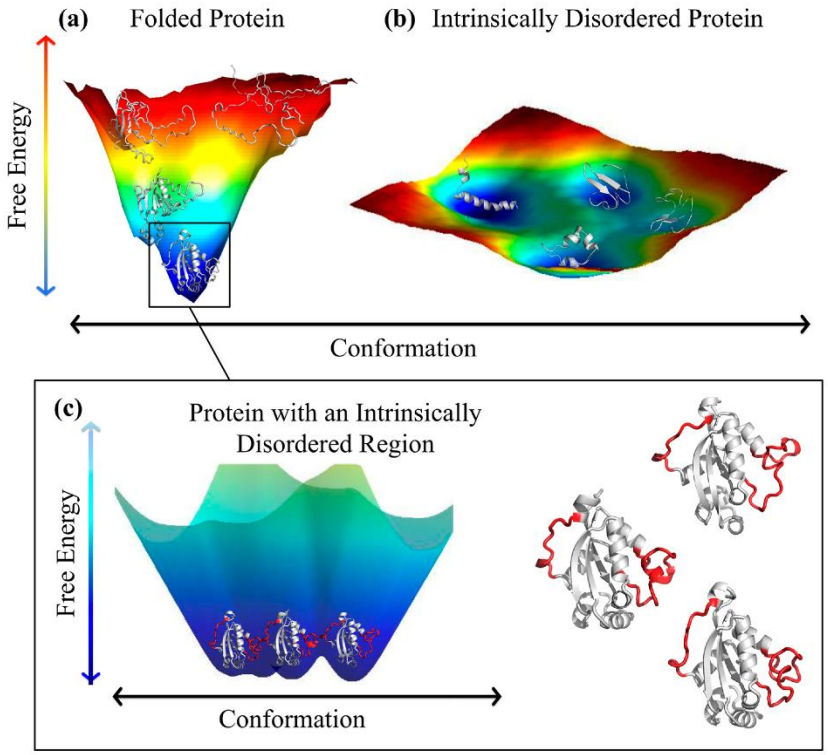

Figure 1.2. Schematic representation of the energy landscape of human nucleoside diphosphate kinase (NDPK), PDB ID: 1nsk (folded protein) a. CcdA C-terminal, PDB ID: 3tcj (intrinsically disordered **b**. The favorable conformations (local free energy minima) are represented in dark blue. The global free energy minimum in (a) is zoomed in (c) which displays the different conformations obtained by varying the disordered regions (shown in red) around the folded regions (shown in white). Reproduced with permission from reference (31).

However, despite performing a wide range of cellular functions like cell signaling, cell division, cell cycle control, replication, transcription, and translation regulation, intrinsically disordered proteins are associated with most of the pathological aggregates deposited in neurodegenerative diseases[32,33].

1.1.2 Intrinsically disordered proteins in cell physiology and disease

Intrinsically disordered proteins (IDPs) or disordered regions containing proteins (IDRs) constitute a major population of our proteome. They are known to participate in a multitude of critical events in both cellular physiology and pathology[18,30,32-34]. These proteins exhibit self-association and multivalency with a wide range of protein ligands owing to their extensive flexibility and ability to acquire a large number of different conformations within cells. IDPs are also known to function via molecular recognition using short sequences known as "molecular recognition features" (MoRF), "eukaryotic linear motifs" (ELM), or "short linear motifs" (SLiM)[11,30].

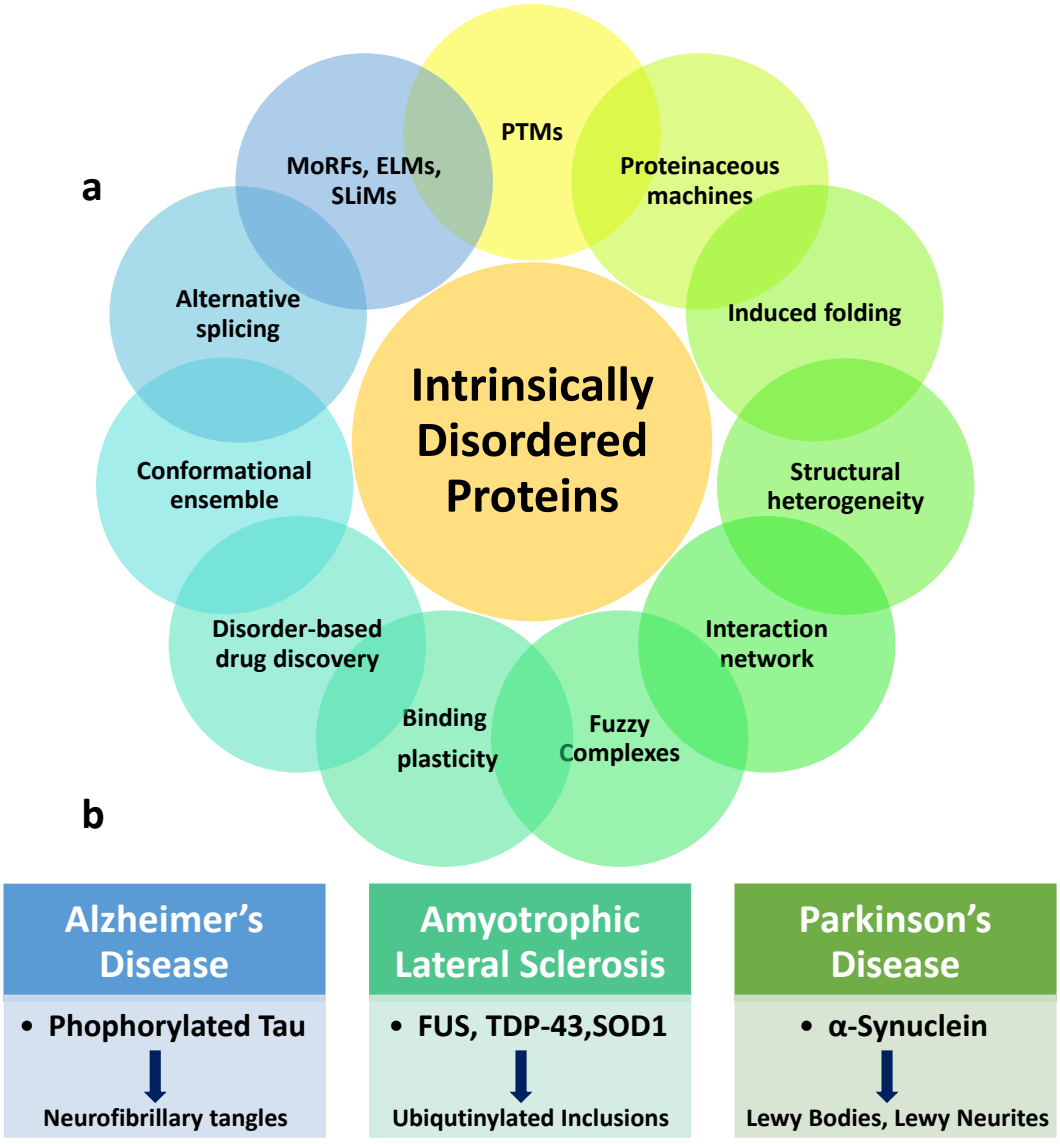

Figure 1.3. a. Diverse biological functions and molecular aspects of intrinsically disordered proteins (IDPs/IDRs) and b. IDPs associated with various neurodegenerative diseases.

IDPs can be categorized into six major categories: entropic chains, display sites, chaperones, effectors, assemblers, and scavengers. While entropic chains act as linkers and spacers due to their high conformational plasticity, others bind either transiently or may associate/dissociate like chaperones. They also harbor sites for post-translational modifications and several permanent binding sites as effectors, assemblers, or scavengers[30,34]. Furthermore, some of the IDPs are known to remain disordered upon binding with partners, forming so-called Fuzzy complexes[35].

In addition to performing vital cellular functions, dysregulation of IDPs is often linked to several pathological conditions. Mutation, alteration in structure, stress, improper shuttling, and aberrant signaling within these proteins can cause the chain to adopt misfolded/aggregation-prone conformations, leading to the formation of insoluble protein structures known as amyloid aggregates, which are hallmarks of various neurodegenerative disorders such as Amyotrophic lateral sclerosis (ALS), Alzheimer's disease, Parkinson's disease, and so on. The misfolded aggregates of these IDPs accumulate in neurons as amyloid plaques, neurofibrillary tangles, Bunina bodies, Lewy bodies, etc. (Figure 1.3)[18] and cause neuronal death[32,33]. Moreover, the mislocalization of these proteins and gene fusion are also linked to several other metabolic diseases and cancer. A growing body of extensive research has recently uncovered that IDPs containing low complexity regions undergo liquid-liquid phase separation within cells. This organizing principle is known to regulate complex biochemical reactions in cells by facilitating the compartmentalization of biomolecules within the cell cytoplasm and nucleus. The concept of biomolecular condensation will be further elaborated in the succeeding section.

1.2 Liquid-liquid phase separation (LLPS)

1.2.1 LLPS a cellular organizing principle

Cells comprise thousands of functional biomolecules, including proteins, carbohydrates, lipids, and nucleic acids within the crowded, complex cellular milieu. These biomolecules are intricately organized, and their functions are tightly regulated within the confined spaces of various membrane-limited organelles, namely the nucleus, mitochondria, Golgi complex, endoplasmic reticulum, and so on. In addition to these membrane-bounded organelles, the existence and role of a range of membrane-less organelles (MLOs) in organizing and maintaining complex cellular biochemistry by locally 'concentrating specific types of

biomolecules' is now evident across organisms[36-40]. Emerging evidence now supports the abundance and widespread occurrence of these biomolecular condensates formed via biomolecular liquid-liquid phase separation (LLPS) (Figure 1.4)[34,40].

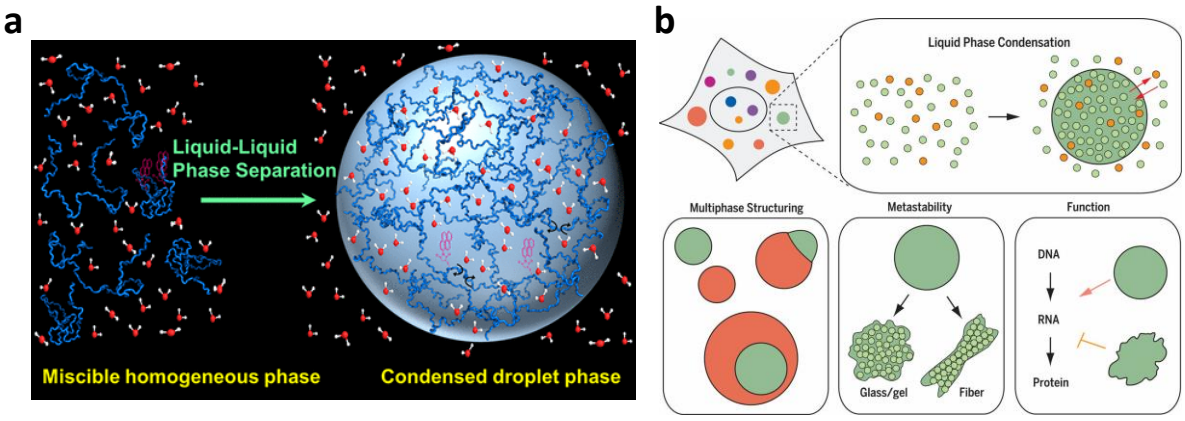

Figure 1.4. a. Schematic representation of liquid-liquid phase separation (LLPS) showing the demixing of components of a miscible, homogenous phase to form co-existing dispersed and condensed phases. The dispersed phase is depleted, and the condensed phase is enriched in the biomolecule undergoing phase separation. b. Assembly of a large number of dynamic liquid condensates via the process of phase separation of cellular biomolecules. The condensates exhibit physicochemical properties, including sequence-dictated multiphasic structuring and the formation of metastable gel-like and solid-like states. These condensates are crucial in regulating the central dogma by modulating transcription and translation. Reproduced with permission from references (34) and (40), respectively.

These biomolecular condensates or membrane-less organelles (MLOs), which include stress granules, P bodies, germ granules, Cajal bodies, nuclear paraspeckles, nucleolus, and so forth, are dynamic, liquid-like, non-stoichiometric, selectively permeable, mesoscopic assemblies with spontaneous formation and dissociation in response to a variety of cellular cues[38-48]. These assemblies are enriched in proteins and nucleic acids and facilitate the compartmentalization of hundreds of biochemical reactions progressing simultaneously inside living cells, with the added benefit of on-demand formation and reversibility. These condensates exhibit liquid-like properties, including extensive diffusion, fusion, Ostwald ripening, dripping, and surface-wetting. A growing body of research has identified intrinsically disordered proteins/regions (IDPs/IDRs) as the primary drivers of biological liquid-liquid phase separation[49-54]. These IDPs, in association with nucleic acids, are responsible for a wide variety of critical cellular functions, including genome organization, RNA metabolism, cellular signaling, regulation, and

immune responses. Due to the intrinsic disorder, low sequence complexity, structural flexibility, multivalency, and a broad range of binding partners, IDPs/IDRs are the best candidates for undergoing biological phase separation. These IDPs participate in a multitude of weak, transient intermolecular contacts that undergo constant making and breaking at a characteristic timescale, defining the material properties of these assemblies[44,48,52-54]. The molecular drivers of biological phase transitions will be discussed in the subsequent section.

1.2.2 Molecular drivers of biomolecular condensation: The role of disorder in phase separation

As described in the previous sections, the disordered class of proteins can be identified by a charge-enriched amino acid sequence (typical IDPs/IDRs), low-sequence complexity prion-like regions with repetitive amino acid sequences, and the elastin-like polypeptides (ELPs), characterized by a large proportion of the hydrophobic residues[43]. A common defining feature of these diverse classes of proteins is the overall enrichment of structure-breaking residues, namely glycine, and proline, discouraging the formation and preservation of secondary structural elements within these polypeptide chains. This conformational flexibility, concomitant with the promiscuous multivalent interaction behavior of IDPs, enables the supramolecular assembly of proteins and nucleic acid molecules, leading to phase separation[45,52,54-59]. However, condensation requires multiple states (i.e., a large number of microstates), which can either be achieved by multiple configurations of structured or disordered domains. Based on previous computational studies, the involvement of folded or structured counterparts of IDPs is generally associated with slower dynamics and reduced liquid-like behavior of the condensates[43]. On the contrary, certain folded domains, such as the RNA-recognition motifs (RRM), oligomerization domains, and interactive or catalytically active domains functioning within the condensates when separated by unstructured linker regions may enhance the overall multivalency and facilitate the assembly and activity of cellular condensates. Nevertheless, large-scale proteomic studies have established a strong association between disorderedness and a higher propensity to form proteinaceous membrane-less organelles (PMLOs)[53,55,57,58].

The weak, multivalent interactions between multiple chains of IDPs ultimately form a strong network of interactions and provide the major driving force of phase separation (Figure 1.5)[53,54]. Based on the charge composition and the post-translational modifications on the key

residues, different phase-separating systems are driven by a range of intermolecular interactions, including hydrogen bonding, electrostatic contacts, hydrophobic interactions, and aromatics or π-interactions[43,54,57]. However, if unregulated, these transient multivalent interactions can lead to strong, persistent contacts, resulting in a wide range of neuropathological conditions.

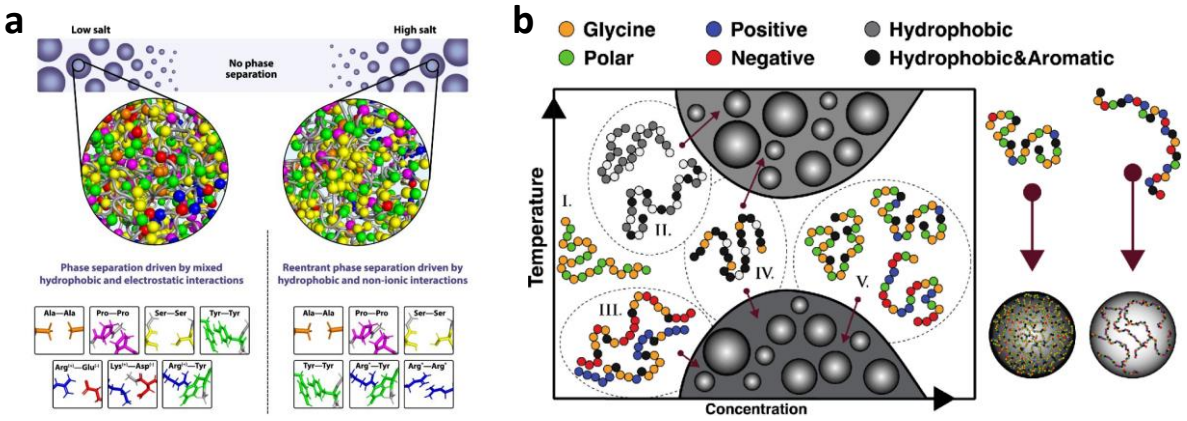

Figure 1.5. a. Depending on the solution conditions (here, salt concentration), the predominant driving interactions can vary in a given phase-separating system. At low-salt regimes, both hydrophobic and electrostatic interactions contribute towards driving the phase separation process. Meanwhile, the hydrophobic interactions are the predominant drivers at reentrant or high-salt regimes due to the unavailability of the charged amino acids due to charge screening (indicated by asterisks). b. Sequence-encoded phase behavior of low-complexity regions. The amino acid composition, primarily the balance between the charged and hydrophobic amino acids, determines the phase diagram and temperature dependence of phase separation. A charge-predominant sequence (I) exhibits solubility over a wide temperature range. A complex mixture of oppositely charged LCRs exhibits a UCST behavior. The introduction of hydrophobic amino acids (II) leads to an LCST behavior. A predominance of aromatics (IV) can exhibit either UCST or LCST behavior. Lastly, LCRs with charged residues and aromatics show a UCST behavior. Additionally, a well-spaced and charge-enriched sequence composition leads to a low-density condensed phase with a large fraction of solvent molecules. Reproduced with permission from references (53) and (54), respectively.

(A) Hydrogen Bonds: Intramolecular hydrogen bonds are well known to stabilize the secondary structural components within polypeptide chains. In addition to allowing the solvation of polar amino acids, an extensive network of hydrogen bonding between residues such as glutamine has been shown to provide one of the significant molecular driving forces in the case of Fused in Sarcoma (FUS) phase separation[60]. All residue types are essentially capable of forming hydrogen bonds, whereas the amino acids with charged or polar side chains

exhibit a higher tendency to participate in these intra- and interchain hydrogen bonds. Besides the homotypic protein-protein interactions, hydrogen bonds are crucial for protein-RNA and protein-DNA recognition and recruitment within phase-separated condensates[49,59,61].

(B) Hydrophobic interactions: Hydrophobic interactions are largely responsible for the folding and stability of structured proteins. Additionally, the hydrophobic residue-dominated polypeptide chains depend on these interactions to drive the formation and stabilization of the protein-rich condensed phase[43,62]. Moreover, hydrophobic contacts facilitate the protein-ligand-specific contacts and lead to preferential recruitment of specific client molecules into the biomolecular condensates while acting as the scaffold proteins. Hydrophobic amino acids, including valine and leucine, and polar amino acids with non-polar groups, such as glutamine (methylene groups), can participate in the formation of hydrophobic contacts, promoting phase separation[49,60,63].

(C) Electrostatic interactions: As mentioned previously, typical IDPs are generally enriched in charged amino acids, including both acidic and basic residues. Polypeptide chains with high net charge may require the presence of an oppositely charged species in order to satisfy the electrostatic charges or neutralization of the charges to initiate phase separation via electrostatic interactions[43,64]. In such cases, co-phase separation of two oppositely charged components can be facilitated by heterotypic electrostatic interactions either between two protein molecules or a protein and nucleic acid molecule, which is also known as complex coacervation. On the contrary, when both the charges are present on a single polypeptide chain, either clustered or uniformly distributed, condensation can be achieved by the homotypic interactions amongst a single species, which can be further regulated by factors such as salt, ionic strength, and polarity of the solvent, pH, post-translational modifications, and so on[43,65].

(D) π- π and cation- π interactions: In addition to the aromatic side chains such as tyrosine, tryptophan, and phenylalanine, the polypeptide chain backbone exhibits a partial π-bond character with a tendency to associate with planar interactions within sp^2-hybridized groups[43,56]. However, aromatic amino acids comprise the major participants of π- π interactions via planar π-stacking amongst these cyclic side chains. Moreover, these aromatic residues also form cation-π interactions with acidic or positively charged side chains of arginine and lysine residues. Particularly, the interaction between tyrosine and arginine is significant in driving the phase separation of proteins such as FUS and hnRNPA2, in addition to multiple other electrostatic, hydrophobic, and hydrogen bonding interactions[43,54,56]. Cation- π interactions can

potentially determine the viscoelastic properties via the non-Fickian diffusion within liquid droplets, resulting in slower dynamics on shorter length scales and faster dynamics at a larger length scale[67]. Lastly, sp^2-hybridized or π-contacts form the principal mode of interaction between the aromatic nitrogen bases of single-stranded DNA/RNA and the sp^2-hybridized aromatic and non-aromatic side chains of His, Asn, Tyr, Phe, Trp, Glu, Asp, Gln, and Arg residues[43,67].

1.2.3 Role of phase separation in physiology and pathology

Biomolecular condensation results in the concentration of specific biomolecules within protein-dense compartments, co-existing with the surrounding depleted phase in the absence of any delimiting membranes. These assemblies exhibit features such as compartmentalization, selective partitioning and concentration, specificity, reversibility, and tunability, making them suitable for a diverse range of critical cellular activities. Many complex biochemical reactions within the nucleus are spatiotemporally organized within the protein and nucleic acid-enriched nuclear condensates[49,68,69] (Figure 1.6a)[51].

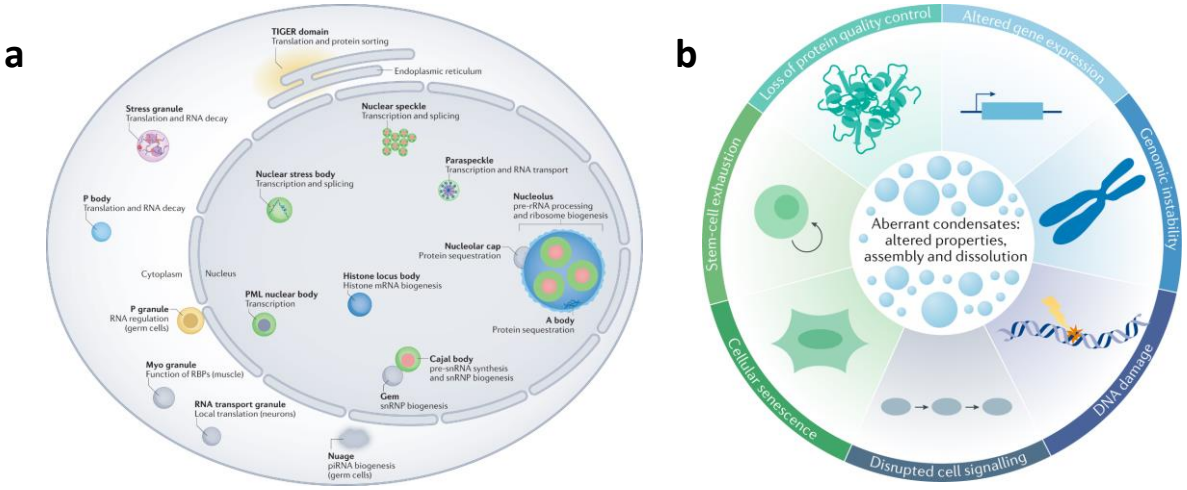

Figure 1.6. a. Illustration of a eukaryotic cell highlighting the abundance of phase-separated membraneless organelles present in both the nucleus and cytosol, associated with critical cellular functioning. b. Changes in the material properties and regulation of condensate assembly with aging is associated with excess DNA damage, altered genome stability, disrupted gene expression and cellular signaling, inefficient protein quality control, cell and stem-cell death. Reproduced with permission from references (51) and (37), respectively.

Beginning from compact packaging and maintenance of chromosome structure, nuclear condensates are implicated in replication and DNA damage repair, pre-ribosome assembly, RNA biogenesis, and metabolism within living cells. In eukaryotes, activation of innate immunity proceeds via the physical process of phase separation. A DNA-sensor enzyme termed cyclic GMP-AMP synthase (cGAS) is shown to form cytoplasmic foci in the presence of any cytoplasmic DNA (e.g., viral DNA), leading to downstream activation of interferon production in response to pathogenic infection[70]. Phase separation also provides the means for neuronal signaling via condensates formed within the neurons (pre- and post-synaptic densities) and synapses, in addition to protecting neurons from hyperactivation. In addition to providing the reaction vessels for physiological reactions, cellular condensates also function as reservoirs for the participant molecules of related biomolecular condensates. As in the case of active transcription sites, nuclear speckles harbor the components required for mRNA splicing such that cotranscriptional splicing condensates can be assembled on these nascent RNA molecules from components 'borrowed' from these nuclear speckles[70].

Despite the physiological significance of phase-separated condensates, they are also associated with a broad range of diseases (Figure 1.6b)[37]. Recently, it has been found that heterotypic condensates of viral proteins and nucleic acids are also observed at physiological conditions *in vitro* and within cells, which enhance viral replication and transmission. Similarly, dysregulation of multicomponent condensates formed via phase separation of tumor suppressor proteins with proto-oncogenic proteins leads to tumorigenesis via oncogenic accumulation of these proto-onco proteins[70,71]. Furthermore, an aberrant liquid-to-solid transition of these reversible, dynamic assemblies to irreversible solid-like aggregates is strongly implicated in several neurodegenerative diseases. Several IDPs known to phase separate, such as Fused in Sarcoma (FUS), tau, TAR-DNA binding protein 43 (TDP-43), and α-synuclein, are increasingly found in pathological aggregates within neurons. The liquid-like condensates of these neuronal IDPs, either individually or in association with related proteins, are responsible for carrying out critical activities such as RNA processing, DNA damage repair, transcription, stabilization of cytoskeleton, neuronal signaling, and so on[50,51,68]. However, any alterations such as single-point or truncation mutations, excessive post-translational modifications, defective cytoplasmic transport, etc., lead to the deposition of irreversible aggregates within the cytoplasm, which are identified as pathological hallmarks of Alzheimer's disease, Parkinson's disease, Amyotrophic lateral sclerosis (ALS), and Frontotemporal Lobar Degeneration (FTLD)[70,72].

1.3 Tools and techniques for *in vitro* characterization of phase separation

1.3.1 Sequence characterization and bioinformatic analyses

As discussed in the previous sections, the intrinsically disordered subclass of proteins forms the major drivers of phase separation. However, various factors, such as sequence composition, hydrophobicity, and charge distribution, dictate the propensity of these IDPs/IDRs to undergo phase separation[73]. Additionally, folded proteins comprising multiple folded domains separated by short stretches of disordered regions or short linear motifs (SLiMs) capable of multivalent protein-protein and protein-nucleic acid interactions are also shown to promote phase separation.

Table 1. Summary of bioinformatics tools used for sequence prediction and characterization of proteins undergoing phase separation.

Program	Link	Prediction
PONDR[74]	http://www.pondr.com/	Disorder
IUPred[75]	https://iupred.elte.hu/	Disorder
D2P2[76]	http://d2p2.pro/	Disorder
CIDER[77]	http://pappulab.wustl.edu/CIDER/	Patterning/distribution of charged/hydrophobic residues
PLAAC[78]	http://plaac.wi.mit.edu/	Prion-like low-complexity domains
SMART[79]	http://smart.embl-heidelberg.de/	Low-complexity domains
catGRANULE[80]	http://service.tartaglialab.com/update_submission/332113/29d4292474	LLPS propensity
FuzPred/ FuzDrop[81]	http://protdyn-fuzpred.org/	Fuzzy interactions and LLPS propensity

Hence, various bioinformatic tools are now widely used to predict the disorder content and resulting sequence-encoded phase separation propensities. Table 1 summarizes the bioinformatics tools widely employed for the sequence characterization of proteins under investigation.

1.3.2 *In vitro* phase separation assays

(a) Turbidity and sedimentation assays

Phase separation into coexisting light and dense phases can be readily observed by the milky or turbid appearance of the phase-separated solutions. The micron-sized liquid droplets, depending on their size, number, and density, cause variable scattering or transmittance of the solution, which can be captured as a function of protein concentration, ionic strength, pH, temperature, and so on to determine the comparative extent of phase separation. Typically, the turbidity or optical density of the phase-separated solutions is measured at a wavelength of 350 nm or 600 nm using either a nanodrop or a spectrophotometer. Turbidity assays can be employed to construct phase diagrams of homotypic or heterotypic phase-separating systems. Similarly, the threshold protein concentration beyond which phase separation begins can also be estimated by performing concentration-dependent turbidity measurements. This minimum threshold concentration (C_{sat}) necessary for phase separation can also be determined via sedimentation assay[82-84].

Sedimentation assay requires setting up large-volume phase separation reactions (generally 250– 500 µL) followed by ultracentrifugation of the droplet reactions to separate the dispersed or light and droplet or dense phases. The droplets or condensed phase are obtained as a transparent glassy pellet, depending on the number and size of droplets initially present within the solution. In the case of homotypic phase separation, the protein concentration, calculated by measuring absorbance at 280 nm within the dispersed phase, is essentially the saturation concentration (C_{sat}) under given droplet conditions. However, it should be noted that these experiments can provide a range of concentrations due to the broad regime of phase transition and the alteration in phase behavior in response to various confounding factors such as pH, ionic strength, temperature, and so on. Conversely, the condensed phase pellet can be resuspended in a fixed buffer volume, and the protein concentration can be estimated to obtain the dense phase concentration[82]. However, approximation of the pellet volume can prove to be

a difficult task. Moreover, in a multicomponent system (complex coacervation), the protein concentration cannot distinguish between individual proteins in the solution. Here, the condensed phase pellet can be further analyzed using SDS-PAGE, where band intensity can be correlated to the protein concentration by running samples with known protein concentrations simultaneously.

(b) Microscopy assays

Imaging and microscopy studies enable visualization and characterization of droplet morphologies and liquid properties when combined with fluorescence tagging. The presence of droplets indicated by the rise in turbidity is further confirmed by visualizing these solutions under a bright-field or confocal fluorescence microscope. Simple light microscopes or differential interference contrast (DIC) can be associated with certain artifacts and may present difficulties in imaging low-density droplet samples. Confocal fluorescence microscopy utilizes proteins with fluorescent protein tags such as eGFP (enhanced green fluorescent protein), mCherry, or organic fluorophores such as Alexa, Cy, or Atto dyes. Depending on the intrinsic or externally introduced (via site-directed mutagenesis) labeling site, fluorescent dyes with maleimide, NHS ester dyes, or other reactive groups can be covalently attached at specific sites within the protein of interest. This fluorescently tagged protein is used in small amounts (0.1-10 %) to visualize the liquid droplets formed via phase separation. Properties of droplets, such as their shape, size distribution, and liquid-like behavior, can be easily observed from these preliminary experiments[84,85].

1.3.3 Determination of material properties of droplet interior

The liquid-like nature can be determined based on liquid-like properties exhibited by the droplets, including surface tension, fusion, dripping, surface-wetting, and so on. The dynamic interior of these droplets can be probed by performing fluorescence recovery after photobleaching (FRAP) measurements. A near-complete and fast recovery indicates a highly liquid-like interior of the droplets, whereas a slow and incomplete recovery indicates a less liquid-like or more gel-like interior within these condensates. A whole droplet FRAP reports on the diffusion of molecules within the droplet as well as with the surrounding dispersed phase. FRAP provides qualitative or comparative information about diffusion within and exchange with the surroundings[82-85]. Further quantitative information about the diffusion properties of molecules within the monomeric and dispersed phase can be obtained by

performing fluorescence correlation spectroscopy (FCS) measurements, which provide additional details regarding the number of molecules and concentration of molecules within the femtolitre observation volume. FCS is also used to study protein diffusion, folding-unfolding, protein-ligand interactions, interaction kinetics, and so on[64,83,84,86]. Similarly, light or fluorescence microscopy-based imaging can be used to quantify the material properties by filming the droplet fusion to obtain properties such as ratio of viscosity, inverse capillary velocity, and surface tension of dense phase. Additional tools such as passive microrheology monitor the movement of beads encompassed within the droplets and calculate the mean squared displacement (MSD) of these to estimate the diffusivity within these droplets[87]. Moreover, micro-fluidics-based methodology involving the determination of sample viscosity by inserting beads into droplet phase underflow, magnetic tweezers, optical traps, and atomic force microscopy have been successfully used to investigate the viscoelasticity within the dense phase[88].

1.4 Vibrational Raman spectroscopy of proteins

1.4.1 Principle of vibrational Raman spectroscopy

The phenomenon of vibrational Raman scattering was first discovered in 1928 by the Indian physicist C.V. Raman, together with his research associate K.S. Krishnan, where they announced a new theory of radiation, which later won him a Nobel prize in 1930[89]. The origin of Raman spectroscopy lies in the ability of atoms to undergo various types of molecular vibrations via the spring-like chemical bonds connecting them. These molecular vibrations are defined by factors such as the atomic mass of constituent atoms, the three-dimensional orientation of atoms and their bonds, bond order, and so on. Thus, external energy input in the form of photons of a specific wavelength (associated with an oscillating electromagnetic field) results in the vibration of bonds within molecules[90]. The vibrations leading to a permanent change in the dipole moment of the molecule are 'IR active' and can be detected in IR spectroscopy (Figure 1.7). Meanwhile, the vibrations capable of momentarily inducing change in the polarizability of the molecules are 'Raman active' and can be detected by Raman spectroscopy. Raman spectroscopy is beneficial over IR spectroscopy for studying disordered proteins because it requires a change in molecular polarizability during vibration to detect transitions, whereas IR spectroscopy relies on changes in dipole moment, making it difficult for symmetrical molecules.

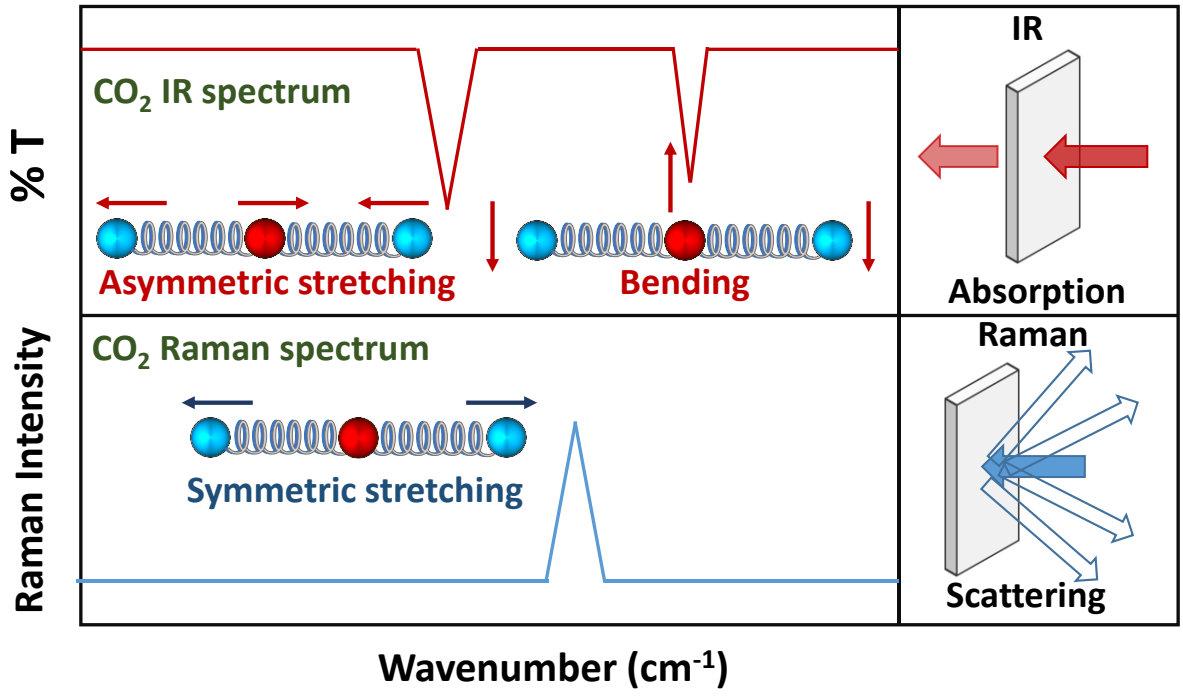

Figure 1.7. Different modes of vibrations of carbon dioxide highlight the mutually exclusive IR active and Raman active vibrations and their signals. Drawn by the author based on reference (91).

This difference allows Raman spectroscopy to provide distinct advantages in studying disordered proteins. Raman spectra typically include elastically scattered light (Rayleigh) and two equally distanced lines (Stokes and anti-Stokes) in contrast to IR spectroscopy, which shows irregular absorbance or transmittance lines depending on the material studied. Both Raman and IR spectroscopy enable label-free, noninvasive, and nondestructive structural characterization. Raman spectroscopy, with its ability to detect specific vibrational modes and provide unique spectral fingerprints, is particularly useful for identifying components within condensates in a single-droplet manner. This sensitivity and specificity make Raman spectroscopy a valuable tool for studying the composition and structure of complex biological mixtures like condensates. Thus, IR and Raman spectroscopy are complementary techniques that provide complete information[91]. Upon interaction with incident photons, molecules are transiently excited to a short-lived, virtual, higher-energy electronic state. Upon return to the ground electronic state, the photon is reemitted instantaneously in the form of scattered light. The majority of the time, the molecule is excited from and returns to the lowest vibrational energy level (v_0), which leads to elastic scattering with the emitted photon carrying the same energy as the excitation photon (Rayleigh scattering). However, at a frequency of one in 10^6

events, the emitted photon experiences either a gain or loss of energy due to the interaction of the incident electromagnetic waves with the sample molecules, termed inelastic scattering or Raman scattering. Upon excitation from the ground vibrational state (v_0), if the molecule enters into a higher vibrational state (v_1, v_2..), the photon is emitted with a lower energy and is termed Stokes photon or Stokes scattering. On the contrary, when the molecule is excited from a higher vibrational state and relaxes to a lower vibrational state, the emitted photon carries higher energy than the incident photon and is emitted at a lower wavelength. This is described as Anti-Stokes scattering (Figure 1.8)[92]. As the probability of the molecules existing in a higher vibrational state within a large population is low, Stokes scattering bands present with a higher intensity as compared to the anti-Stokes within the Raman spectrum.

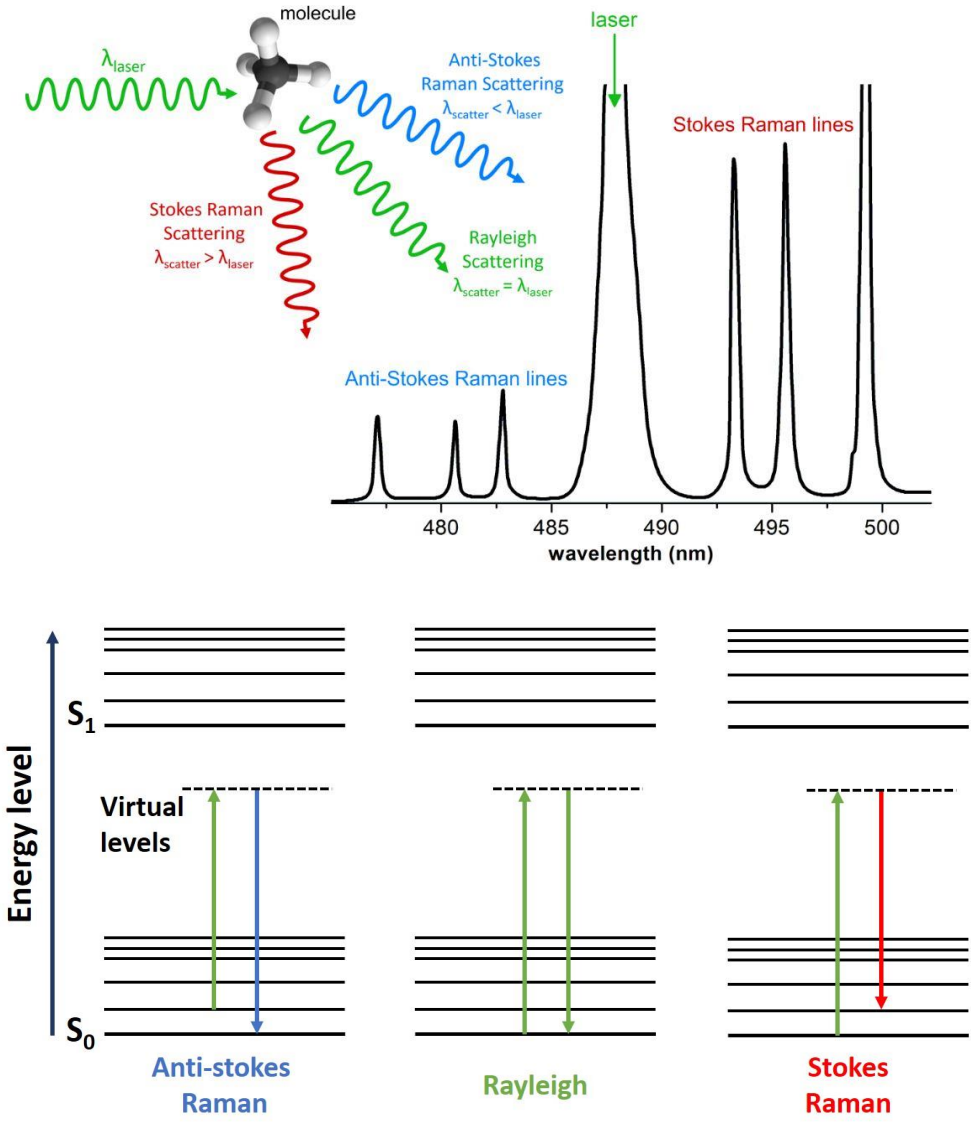

Figure 1.8. Schematic representation of different scattering modes depending on the energy of scattered photons. The photons can be emitted with the same energy as the incident photons

(same wavelength, Rayleigh scattering), with lower energy (longer wavelength, Stokes Raman), or less frequently with higher energy (lower wavelength, Anti-Stokes Raman). The energy level diagram depicts the energy transitions in Rayleigh, Anti-Stokes and Stokes Raman scattering. Reproduced with permission from reference (92).

1.4.2 Vibrational Raman bands of proteins

Vibrational Raman spectroscopy of proteins is a non-invasive, label-free technique frequently used to obtain structural information and yields a relatively complex Raman spectrum (Figure 1.9)[85,93]. The combination of these overlapping bands arises from the vibrations of the polypeptide chain backbone along with the amino acid side chains. Here, we describe the prominent signature bands and the relation between their position, intensity, and the corresponding structural features of proteins, as discussed extensively in the existing literature[94-99].

(A) Polypeptide chain backbone vibrations:

Amide I: Protein Raman spectra exhibit an intense band (1600 cm^{-1} to 1700 cm^{-1}) termed Amide I, which originates majorly (~ 80 %) from the C = O stretching vibrations with a minor contribution (~ 20%) of the out-of-plane C- N stretching[94,95]. This signature Raman band arises from the protein backbone and is responsive to hydrogen bonding strength (C=O and N-H groups), backbone torsional angles, and thus to the backbone conformation and secondary structures. For instance, the Amide I originating from a helix with less than six residues appears in the form of multiple peaks, whereas a single peak at 1655 cm^{-1} indicates a helix with more than six residues. With an increase in the helix length, the Amide I peak exhibits a downshift in the frequency due to the increasing strength of hydrogen bonding. Similarly, the characteristic Raman bands at ~ 1670 cm^{-1} and 1630 cm^{-1} assigned to the parallel β-sheet structures exhibit a blueshift for anti-parallel β-sheet. Additionally, signature Raman bands centered at ~ 1648 cm^{-1} and ~ 1680 cm^{-1} are observed in the case of protein structures with random coil conformation[94,95,100].

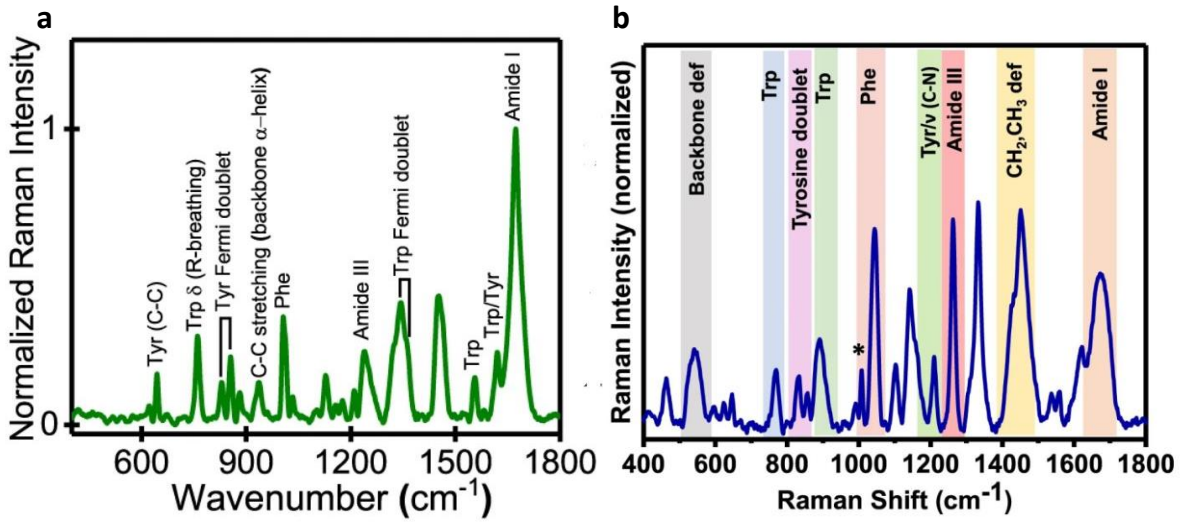

Figure 1.9. Vibrational Raman spectra obtained from proteins. The signature Raman bands originating from the protein backbone, secondary structural elements and aromatic amino acids are highlighted in the spectra. Reproduced with permission from references (93) and (85), respectively.

Amide II: This band ranges from 1480 cm^{-1} to 1580 cm^{-1} and is attributed to the out-of-phase C-N stretching and N-H bending vibrations with a minor contribution from C-C stretching and C=O bending vibrations[94,95]. In the non-resonant Raman mode, the cross-section of this band is extremely small and, hence, is more or less invisible in the Raman spectrum.

Amide III: Amide III band reports on the secondary structural components within the polypeptide chain and ranges from 1220 cm^{-1} to 1400 cm^{-1}. This signature Raman band arises majorly from the in-phase C-N stretching and N-H bending vibrations of the polypeptide chain, with a minor contribution from the in-plane C=O bending and C-C stretching vibrations. This band is completely free from any contribution from water, making it a suitable peak for the structural analysis of proteins in aqueous solutions. Amide III provides an additional benefit over the Amide I band, such that the constituent bands are well-resolved, providing a better estimation of the secondary structural elements. The α-helices show a distinct band at ~1300 cm^{-1}, the 2.51 helix at 1272 cm^{-1}, polyproline (PPI) at ~ 1252 cm^{-1}, β-sheets at 1240 cm^{-1}, and random coil structures show up at ~ 1240 cm^{-1} to 1250 cm^{-1}. Using resonance Raman, the position of the Amide III band can be used to estimate the dihedral angle (Ψ) due to the dependence of the peak position on the backbone conformation of the polypeptide chain[101,102]. Similarly, the sensitivity of Amide III to the hydrogen bonding of the polypeptide chain

backbone can be exploited to capture the changes in the H-bonding strength and, thus, the changes in secondary structural composition within protein samples[94,95,100].

Amide IV-VIII: Amide IV (625-770 cm^{-1}) originates from the OCN bending, Amide V (640 – 800 cm^{-1}) arises from NH out-of-plane bending, Amide VI (540 – 600 cm^{-1}) from the C = O out-of-plane bending, and lastly Amide VII (~ 200 cm^{-1}) due to the skeleton mode[94,95].

(B) Aromatic amino acids:

Phenylalanine: The aromatic amino acid phenylalanine exhibits six distinct bands positioned at 622, 1004, 1031, 1207, 1586, and 1606 cm^{-1}, corresponding to the six different vibrational modes. Apart from the very intense band at 1004 cm^{-1}, which arises from the benzene ring-breathing mode, all other bands of Phe are masked by the bands from other aromatic residues. Under non-resonant conditions, the band at 1004 cm^{-1} is relatively insensitive towards the changes in polypeptide chain conformation and, hence, is used as a reference for normalization of the protein Raman spectra. However, all the peaks (except 1032 cm^{-1}) are sensitive to protonation and can report changes in the pH conditions in the protein surroundings. Other changes in the solvent properties, such as hydrophobic character, can be detected by monitoring the peak intensity of the in-plane ring deformation band (621 cm^{-1}). An increase in the solvent hydrophilicity is indicated by reduced peak intensity resulting from the modified interactions of the substituted benzene ring with the solvent molecules.

Tyrosine: Multiple Raman bands positioned at 1613, 1209, 1194, 1175, 855, 835, and 643 cm^{-1} are attributed to aromatic tyrosine residue. The bands (appearing at 835 and 855 cm^{-1}) arising from the Fermi resonance of the out-of-plane fundamental mode at 420 cm^{-1} and the in-plane fundamental mode at 840 cm^{-1} are termed the 'tyrosine Fermi doublet'. This doublet marker band indicates the hydrogen bonding extent of the hydroxyl group of the tyrosine side chain. In cases where the hydroxyl non-hydrogen bonded, an intensity ratio of ~ 6.7 is observed, whereas a ratio of ~ 2.5 indicates strongly hydrogen-bonded hydroxyl. A doublet intensity ratio of 0.3 suggests the donor behavior of hydroxyl, and the ratio rises to 1.25 when it acts as both a donor and acceptor. Additionally, bands at 1177 and 1613 cm^{-1} are also used to probe the environment of the tyrosine side chain with respect to hydration and hydrogen bonding with the solvent[103].

Tryptophan: Tryptophan is characterized by various bands positioned at 1550 cm^{-1} (W3, indole-ring vibration), a doublet at 1340 and 1360 cm^{-1} (W7, Fermi resonance between multiple

out-of-plane vibrations, and a band of an in-plane N1 = C8 vibration of indole ring). The intensity ratio (I_{1360}/I_{1340}) reports on the solvent-accessibility of the Trp residue, where a value of more than one indicates a hydrophobic environment. The band at ~ 1010 cm^{-1} (W16 mode, benzene ring-breathing vibrations) indicates the strength of van der Waals interactions formed by the indole ring with residues in the vicinity. The position of the band at 1012 cm-1 suggests strong van der Waals interactions, and weak or no interactions result in a peak position at ~ 1007 -1010 cm^{-1}. The signature band at 767 cm^{-1} ascribed to the indole ring breathing mode of tryptophan indicates the presence of cation-π/CH-π interactions[104,105].

Histidine: Under non-resonant Raman conditions, histidine does not show any intense scattering bands. In resonant Raman, the protonation of the imidazole ring can be monitored by observing the band at 1408 cm^{-1}.

(C) Other amino acids: The non-aromatic amino acids show extremely weak signals in the protein Raman spectra, located in the region 500 to 1700 cm^{-1}. Depending on the abundance of these residues, the peaks for alanine, valine, glycine, lysine, leucine, isoleucine, serine, aspartate, and glutamate can be identified in the Raman spectrum when not masked by the amide I and amide III peaks.

A signature Raman band for the S-H group is observed at ~ 2500 cm^{-1} and C-S at ~ 2585 cm^{-1}, which exhibits a gradual downshift depending on the strength of hydrogen bonding where strong –SH is further downshifted from 2565 cm^{-1}. The disulfide bonds exhibit Raman bands in the range 450 to 700 cm^{-1}. The position of the band reports on the conformation of C-C-S-S-C-C moiety. A band at ~ 508 cm^{-1} indicates a gauche-gauche-gauche, ~ 525 cm^{-1} indicates gauche-gauche-trans, and ~ 544 cm^{-1} indicates a trans-gauche-trans conformation[94,95].

1.5 Single-molecule Förster resonance energy transfer (smFRET)

1.5.1 Introduction to smFRET

A plethora of techniques have been developed for investigating the underlying physical principles governing the assembly, disassembly, and material properties of biomolecular condensates formed *in vitro* and within cells. Microscopic techniques, including atomic force microscopy (AFM), super-resolution imaging, fluorescence recovery after photobleaching (FRAP), etc, are routinely used for the characterization of droplet properties such as

composition, dimensions, liquid-like nature, material properties, and so on[106]. However, these techniques are incapable of illuminating the molecular-level events and structural details of the proteins undergoing phase separation. To overcome these limitations, studies employ higher-level methodologies such as NMR, small-angle X-ray scattering (SAXS), small-angle neutron scattering (SANS), and cryo-electron microscopy, which provide atomic-level structural details within the liquid-like condensed phase and solid-like aggregates[106-110]. Nonetheless, most of these techniques require extreme processing of high-concentration samples and provide time and population-averaged ensemble information within the dispersed and condensed phases.

On the contrary, single-molecule techniques are sensitive and provide structural information at the single-molecular resolution without requiring extensive processing of high-purity, concentrated samples. Individual molecules within the dispersed and condensed phases can be investigated deeply to obtain information such as droplet morphologies, size distributions, molecular diffusion, viscoelastic properties, and so on. Moreover, single-molecule studies can further illuminate molecular details, including conformational distribution and their interconversion dynamics, in addition to heterotypic and homotypic intermolecular interactions at the nanoscopic length and time scales[111]. A variation of the single-molecule techniques, namely single-molecule Förster resonance energy transfer (smFRET), a spectroscopic ruler, has been widely used in studies involving real-time monitoring of structural changes and protein chain dynamics, such as protein folding[112-116]. The basic working principle of FRET lies in capturing the distance distributions of different regions within the same or other biomolecules labeled with a suitable pair of donor and acceptor fluorophores. The donor fluorophore, when excited, transfers the photon to the acceptor fluorophore via a non-radiative, dipole-dipole interaction in a distance-dependent manner. Hence, the change in conformation or intermolecular interactions is recorded as a change in FRET efficiency for the labeled positions for a given set of conditions. This technique allows us to delve deeper into complex biological processes such as protein folding-unfolding, membrane diffusion, protein-membrane interactions, signal transduction, enzyme-ligand binding, dynamics of protein-protein and protein-nucleic acid interactions from the aspect of macromolecular conformational dynamics and structural heterogeneity at the single-molecule resolution (Figure 1.10)[112-118]. Thus, smFRET is now emerging as a promising tool to discern the processes occurring on a wide range of timescales ranging from seconds (immobilized fluorophore) to nanoseconds (freely diffusing fluorophore).

1.5.2 Principles and instrumentation of smFRET

Single-molecule FRET experiments begin with the selection of a suitable dye pair for the FRET measurements. As single-molecule measurements require a very low concentration of fluorescent probes, choosing fluorophores with bright fluorescence (high quantum yield) and decent photostability is necessary. Preferably, bulky fluorescent tags and fluorescent proteins (GFP, RFP, YFP) are avoided in order to overcome the issue of steric hindrance and the introduction of additional structural and dynamic components from the fluorophore molecule. Thus, organic fluorophores, including Alexa, Atto, and Cyanine dyes, have emerged as the best candidates for single-molecule FRET measurements. The donor-acceptor dye pair can be

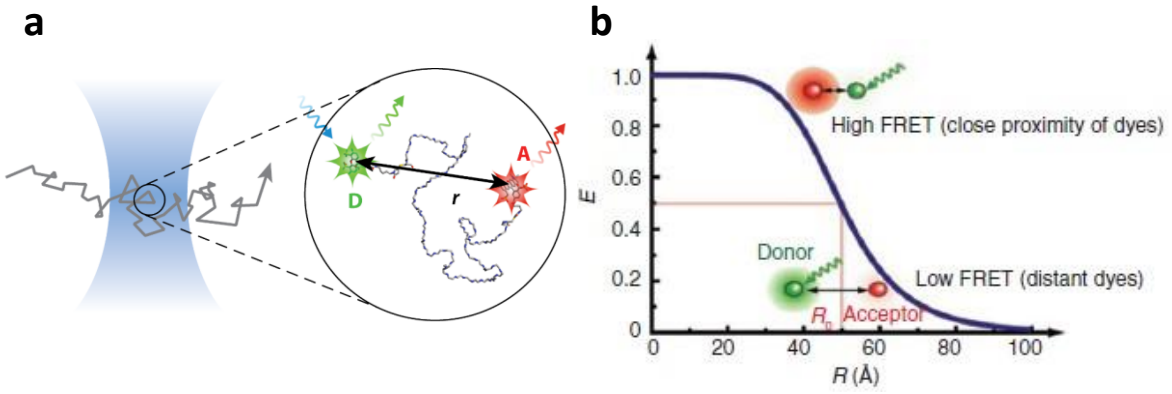

Figure 1.10 a. Diffusion of single protein molecule labeled with both donor and acceptor dye. b. Representative FRET efficiency (E) plot (R_0 = 50 Å) shows the dependence of E on the inter-dye distances. The donor dye is excited with the donor laser, which can then either emit fluorescent photons or transfer energy in a non-radiative manner to the acceptor dye, or both depending on the distance between the donor and acceptor dye. At an inter-dye distance of R_0, the FRET efficiency is obtained as 0.5, which increases non-linearly with decreasing inter-dye distance, except around R_0. Reproduced with permission from references (112) and (113), respectively.

covalently attached to the biomolecule under investigation by orthogonal labeling chemistries such as thiol-maleimide, amine-NHS ester, aldehyde-hydrazide, or azide-alkyne depending on the reactive group available or introduced at the labeling site. Dye pairs such as AlexaFluor488-AlexaFluor594, Cy3-Cy5, and Atto 425-Atto 520 are generally used for labeling at a combination of residue positions within a single polypeptide chain in the case of proteins. In certain advanced studies, three different positions are labeled with one donor and two acceptor

molecules, termed three-color FRET, which provides information on the distance distributions for two pairs of residue positions simultaneously[112-115].

After labeling, further column-based purification methods like ion-exchange or high-pressure liquid chromatography (HPLC) can be performed to maximize the proportion of dual-labeled (two-color FRET) or triple-labeled (three-color FRET) species to improve data collection. As mentioned previously, smFRET studies can be performed in two different modes, either by surface-immobilization of the molecules by using affinity tags (for, e.g., Biotin-avidin system) or by monitoring molecules diffusing freely through the femtolitre confocal volume (Figure 1.11a)[112,113]. Confocal-microscopy-based single-molecule FRET measurements have been used as the technique of choice in the case of proteins. The confocal-based single-molecule setup is equipped with a diode laser as the source of excitation, which is directed via a combination of reflective mirrors and dichroic mirrors towards a high-NA, high-magnification objective lens, which further focuses the laser to form a femtolitre confocal volume within the sample.

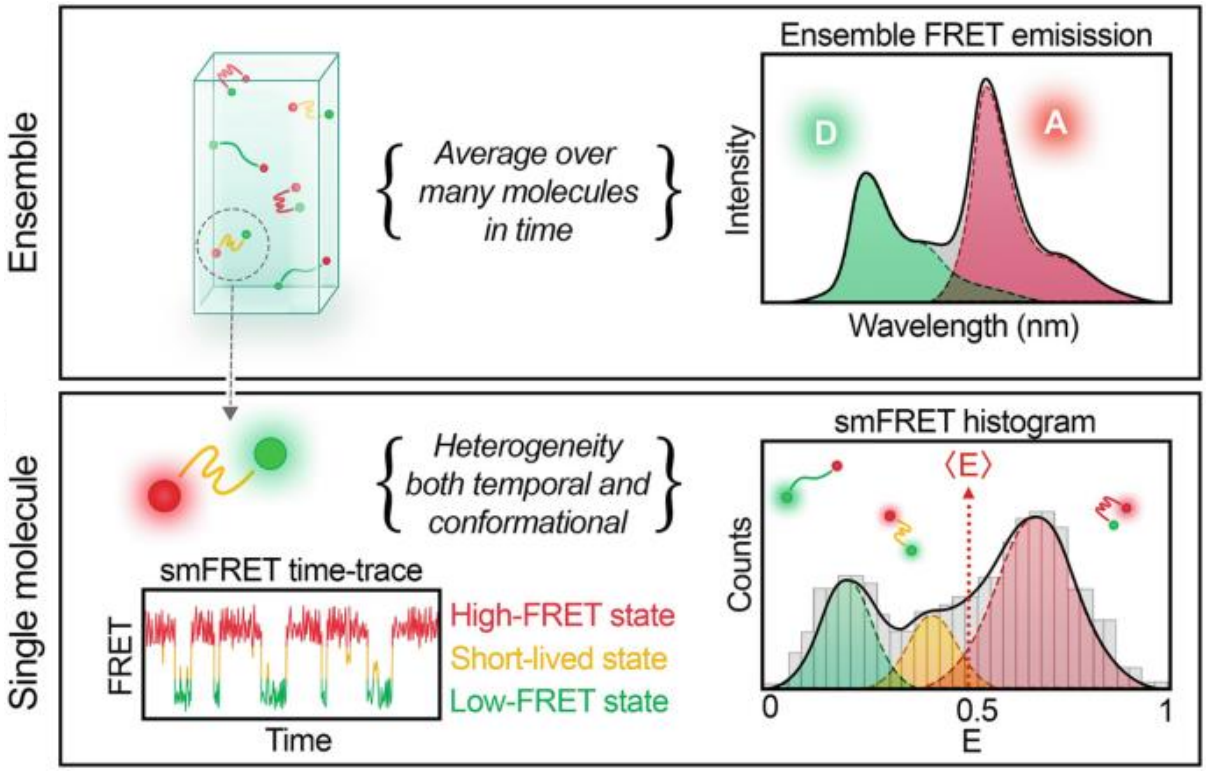

Figure 1.11. Schematic representation showing the difference between ensemble and single-molecule fluorescence FRET measurements. Reducing the dual-labeled reporter concentration and the confocal observation volume will allow monitoring of freely diffusing fluorescently labeled molecules and obtaining single-molecule fluorescent bursts. Single-molecule FRET

can capture the conformational and temporal heterogeneity within samples. Reproduced with permission from reference (118).

The system of mirrors then separates and directs the emitted photons towards the detection system. A small pinhole (~ 50-150 μm) filters the out-of-focus emission, and a dichroic mirror placed before the detectors separates the donor and acceptor emission into corresponding channels. The photons are finally detected by respective detectors, which can be either photomultiplier tubes (PMTs) or avalanche photodiodes (APD).

1.5.3 Limitations and advancements in smFRET

The presence of incompletely labeled, i.e., donor-only and acceptor-only species, can never be avoided entirely due to the occasional inactive fluorophores and the photobleaching effects. In the traditional FRET measurements, the donor-only species give rise to zero FRET efficiency peak due to the absence of acceptor dye upon excitation with the donor laser. This zero-efficiency peak interferes with and masks any low-FRET efficiency peaks, making it challenging to distinguish between low-FRET and donor-only species. A recent development in FRET measurements, termed alternative laser excitation (ALEX) or pulsed interleaved excitation (PIE-FRET), employs an alternative acceptor-exciting laser interleaved with the donor-exciting laser[113]. ALEX uses continuous-wave lasers, alternating at a rapid frequency of 10^5 Hz, multiple-fold faster than the typical diffusion time of a protein chain through the confocal volume, enabling alternate excitation of both molecules. In ALEX, the alternating of the lasers is achieved through an acoustic optic modifier, whereas PIE-FRET involves excitation by pulsed diode lasers in conjunction with APD with single-photon and time-correlated detection. This combination of pulsed lasers with time-correlated detection allows fluorescence lifetime measurements concurrently with fluorescence intensity measurements. PIE allows for advanced multiparametric fluorescence detection (MPD/MFD) incorporating fluorescence correlation spectroscopy and anisotropy measurements from the PIE-FRET data when used in a four-detector setup[112-114]. The emitted photons are time-stamped to their corresponding excitation pulses at the respective detectors. This method allows the identification of donor-only and acceptor-only species based on the fluorescence emission. The dual-labeled molecules generate fluorescent bursts in both acceptor and donor channels upon incidence of the respective acceptor and donor-excitation laser. Fluorescence bursts collected

from the dual-labeled species are then considered for the calculation of the FRET efficiency histogram.

In the confocal-based smFRET methodology, the fluorescence time trace is also dependent on the motion of the diffusing species through the confocal volume. Thus, the diffusion properties, including the characteristic diffusion time and the changes in FRET transfer efficiency, while the molecules traverse the femtolitre confocal volume. The technique of fluorescence correlation spectroscopy allows for these measurements, which provide the time-dependent variation in the fluorescence intensity and often FRET efficiency as well. Compared to smFRET, FRET-FCS data are generally collected over an extended period of time to achieve a good signal-to-noise ratio, preferably performing cross-correlation with a 50/50 beamsplitter and two detectors to eliminate the detector-associated responses.

1.5.4 Data analysis and interpretation

The raw data is obtained in the format of photon counts separated in the donor (I_D) and acceptor (I_A) channels, binned into chosen time windows depending on the characteristic diffusion time of fluorescent species, which typically range from 0.5-1 ms in the case of protein samples[112-119]. The bursts are corrected for the background counts, and a cutoff threshold of 30-50 photons is employed for the selection of the bursts over the background. The FRET efficiency is calculated using eq^n (1),

$$E = \frac{1}{1+\left(\frac{I_D}{I_A}\right)\gamma} \quad \text{--- (1)}$$

where γ accounts and corrects for the difference in the detection efficiencies of the donor and acceptor APDs and the quantum yields of the donor and acceptor dyes. Additional correction factors accounting for the direct excitation of the acceptor fluorophore with donor laser (β) and for the spectral cross-talk or bleedthrough into the acceptor channel (α) are calculated by performing some quantitative comparative measurements in a fluorescent spectrophotometer and both the channels in the sm-FRET setup.

Incorporating these corrections, the FRET transfer efficiencies are calculated and constructed into a probability distribution histogram[120-124]. Upon Gaussian fitting of the histogram, a mean transfer efficiency is obtained, which provides the distance between the fluorophores, averaged over the time of measurement (Figure 1.11b)[118].

$$E = \frac{1}{1+\left(\frac{r}{R_0}\right)^6} \quad \text{--- (2)}$$

$$r = R_0 \left[\frac{1}{E} - 1\right]^{\frac{1}{6}} \quad \text{--- (3)}$$

However, it should be noted that the distance obtained here is the separation between the fluorophores, or inter-dye distance, calculated in terms of the Förster radius (R_0) for the given dye pair. Additional corrections for the Förster radius (R_0) for the given set of measurement conditions and additional dye-linker distances need to be considered to estimate the precise residue-residue distance. Förster radius (R_0) can be corrected for dipole orientation factor (κ^2), the refractive index of the medium (η), quantum yield, and the overlap integral for the given FRET pair.

1.6 Fused in Sarcoma (FUS)

The FUS gene is situated on chromosome 16 and was discovered as a fusion oncogene, resulting from a chromosomal translocation observed in human myxoid liposarcomas. The resultant oncogenic protein presents as a translocation product of the N-terminal of FUS fused with the transcription-associated factor CHOP[125]. FUS is a prion-like, highly abundant, 15 exons encoding, 526 amino acid DNA/RNA binding protein. FUS belongs to a unique class of RNA-binding family called the FET family, which includes Ewing RNA-binding protein (EWS) and TATA-binding protein-associated factor 2N (TAF15)[126]. Additionally, FUS has been identified as one of the critical components of the heterogeneous nuclear ribonucleoprotein (hnRNP) complex. A growing body of exciting research has shown that FUS is primarily involved in DNA/RNA metabolism, including DNA repair, gene transcription, regulation, RNA/microRNA processing, RNA shearing, RNA transport, gene translation, cell proliferation, and maintenance of genomic stability[126,127]. Apart from RNA, FUS can also strongly bind to ssDNA and dsDNA. The key binding sequence for FUS with nucleic acids is GUGGU, which is abundant in the 5' untranslated regions (UTRs). FUS mutants show a unique preference for binding to sequences within the 3'-UTR and introns.

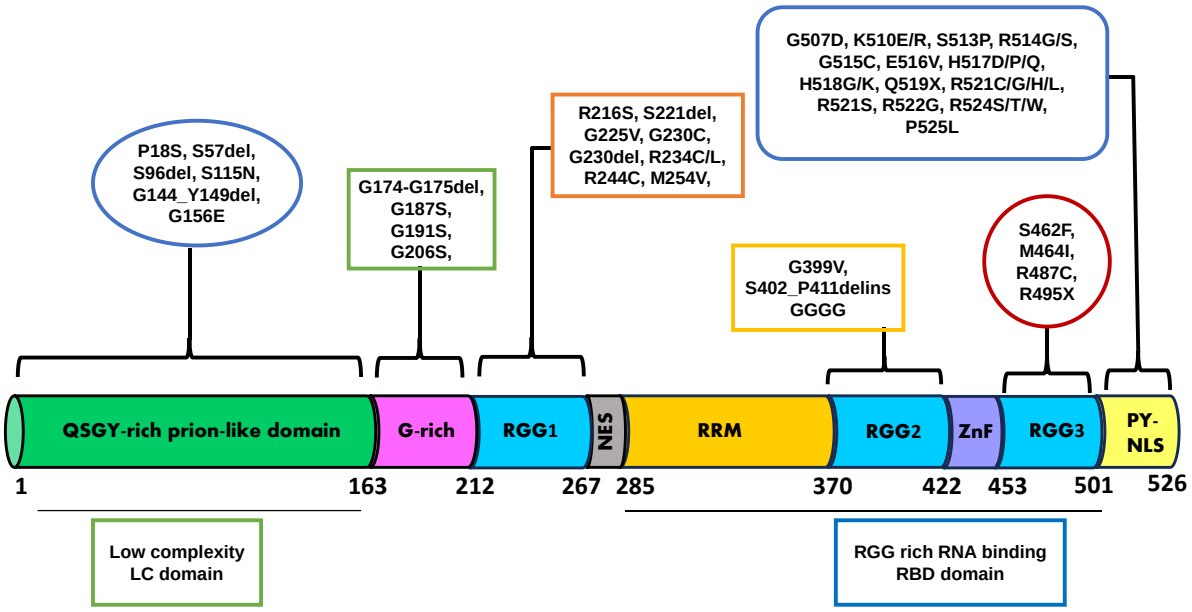

Figure 1.12. Domain architecture of human Fused in Sarcoma (FUS) proteins. FUS is a 526 amino acid long protein with a multidomain architecture comprising an SYGQ-rich prion-like low-complexity domain, multiple arginine-glycine rich RGG domains, an RRN-recognition motif, a zinc-finger domain (ZnF), and a nuclear export (E) and nuclear localization (L) signal. The disease-associated mutations implicated in amyotrophic lateral sclerosis (ALS) and frontotemporal lobar degeneration (FTLD) throughout the sequence are marked.

Interestingly, all the FET family proteins share a common multidomain architecture like FUS. FUS consists of an intrinsically disordered, QSGY-rich, low complexity N-terminal domain (LC) and a partly structured C-terminal RNA-binding domain (RBD). The RBD comprises an RNA-recognition motif (RRM), two RGG-rich domains, a folded zinc finger domain, and a 25 amino acids short nuclear localization signal (NLS) (Figure 1.12)[128]. FUS undergoes various post-transitional modifications, such as asymmetric demethylation of arginine (A216 and A218), and phosphorylation of serine at the N-terminal LC domain. These post-transcriptional modifications are known to modulate the self-assembly of FUS into oligomers, which are considered an essential step for chromatin binding. FUS protein primarily resides in the nucleus under physiological conditions, although it can shuttle from the nucleus to the cytoplasm. FUS is capable of binding nascent pre-mRNA and can serve as a molecular bridge between U1 small nuclear ribonucleoprotein and RNA polymerase II, facilitating transcription-splicing coupling.

FUS also utilizes non-sense-mediated decay of its pre-mRNA to regulate its expression in cells. In addition to this, it is known to promote the formation of a D-loop and homologous recombination during dsDNA repair. In neuronal cells, FUS is primarily involved in crucial functions such as dendritic spine development and stability, mRNA stability, RNA movement, and maintaining synaptic balance (Figure 1.13)[129].

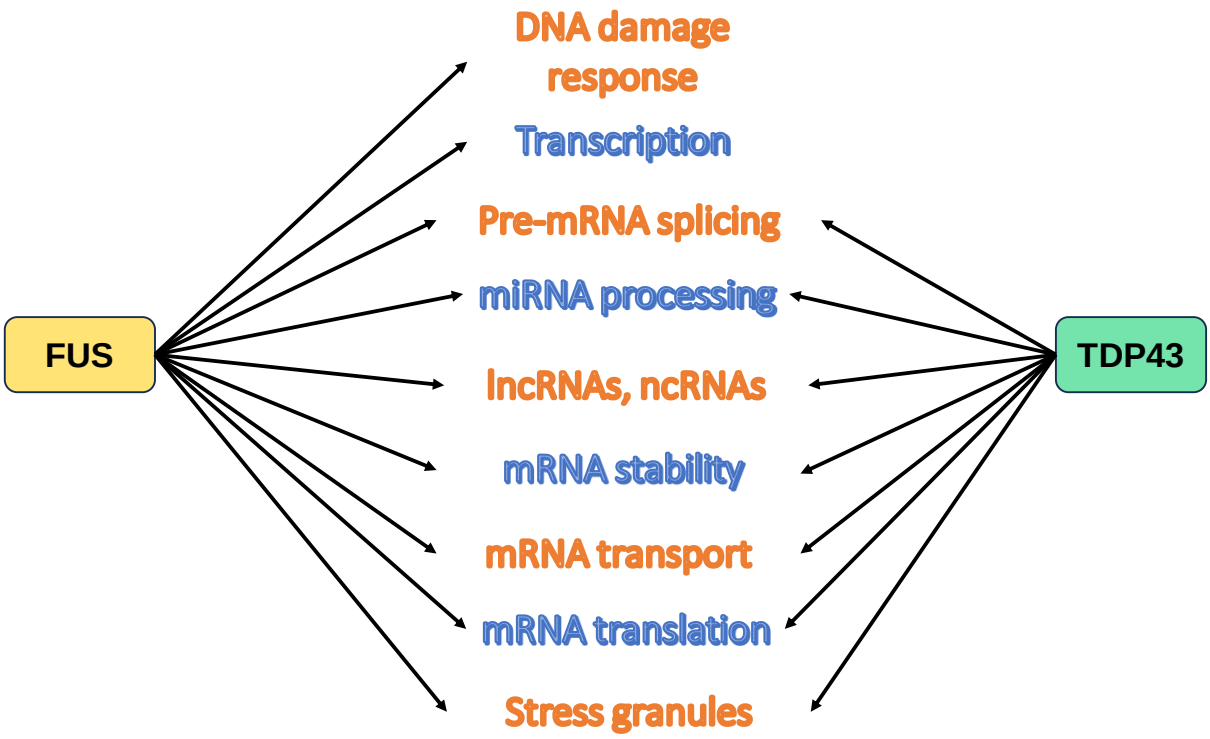

Figure 1.13. Schematic representation depicting the role of FUS and other related proteins in critical physiological functions.

FUS-associated pathology is primarily divided into two categories: first, the loss of function in the nucleus due to incorrect localization of nuclear FUS to the cytoplasm, and second, the gain of toxic function of cytoplasmic FUS[127,128,130]. The cytoplasmic FUS accumulation promotes stress granule formation characterized as non-membranous, ribonucleoproteins (RNPs) bodies containing mRNAs, translation machinery, ribosomes, and other RNA-binding proteins (RBPs). These stress granules are the primary cause of FUS-associated neurodegeneration in Amyotrophic lateral sclerosis (ALS) and Frontotemporal dementia (FTD). The stress granule formation can be induced by a wide variety of stress, such as oxidative stress, nutrient deprivation, organelle dysfunction, and pathogenic infection that inhibit protein synthesis.

Additionally, the pathological role of FUS has been verified in various other conditions, such as polyglutamine disease and intranuclear inclusion body disease. Mutations in the FUS gene cause the mislocalization of nuclear FUS and the formation of cytoplasmic inclusion bodies, eventually leading to the formation of pathological aggregates, which are the primary cause of neurodegeneration in ALS and FTD patients [127-137] (Figure 1.14).

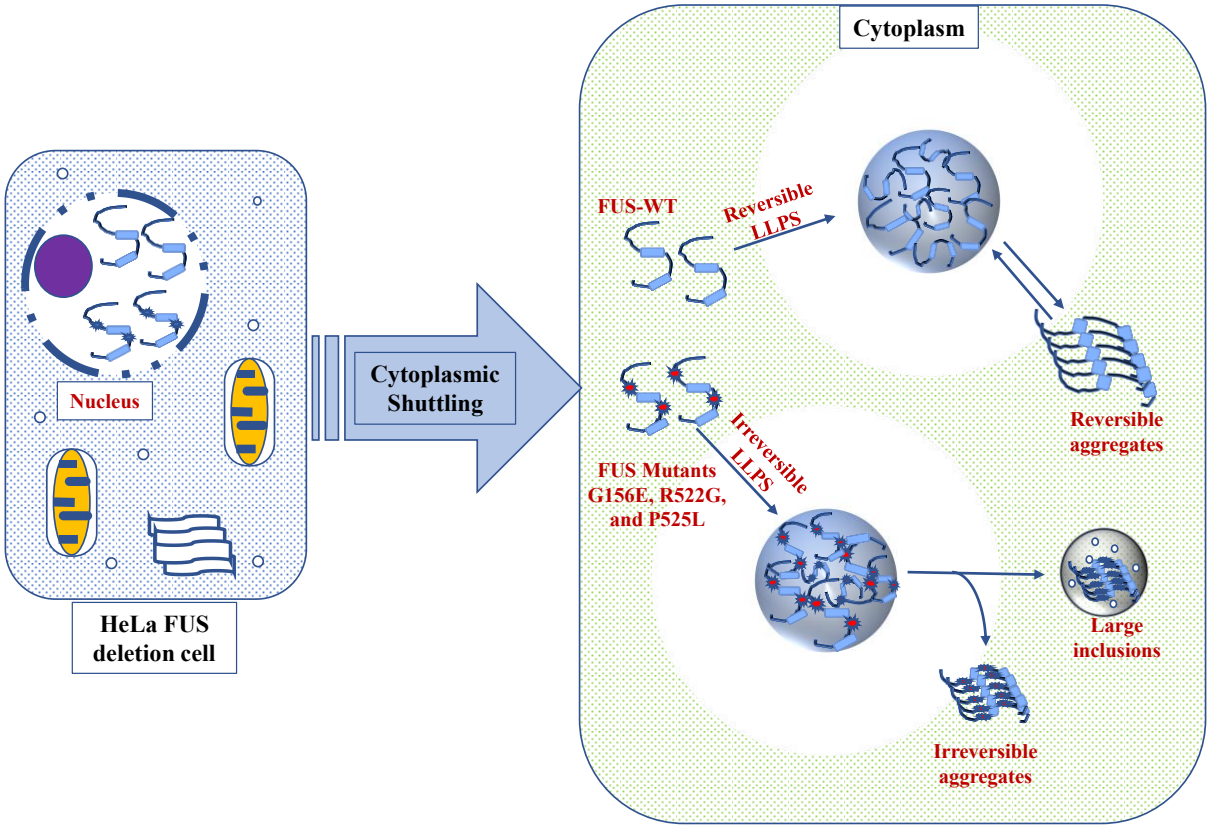

Figure 1.14. Schematic representation of the cellular assembly of FUS. Wild-type and mutant FUS can phase separate upon cytoplasmic shuttling and form irreversible aggregates.

However, some of the positive FUS cytoplasmic inclusions are still present in autopsy material and other parts of the brain like cortex, hippocampus, and motor neurons in patients with sporadic ALS and FTLD. To date, over 50 known mutations are associated with FUS pathology, primarily impacting exon 15, which contains the Nuclear Localization Signal (NLS) and the glycine-rich domain of the FUS protein (Figure 1.12)[127-131].

The human genome consists of approximately 30 FUS-like proteins, including the FET family, TDP-43, and hnRNPA1. A current flurry of research suggests proteins with low

complexity domains and RNA binding domains serve as the best candidates for biological phase separation. These proteins possess a unique capability to get demixed from the surroundings and form a protein-enriched phase via liquid-liquid phase separation[60,85,127,138-140]. These liquid condensates, if unregulated, can lead to the formation of gel-like or solid-like species, which are considered precursors of neuropathological aggregates. The phase separation of FUS is primarily governed by two interactions: electrostatic interactions amongst the charged residues and cation-pi interactions between tyrosine of the N-terminal LC domain and charged arginine of the C-terminal domain[85,107,138-140]. These interactions are also tuned by several post-translational modifications like arginine methylation, phosphorylation, and diseases-associated mutations within the FUS sequence. Recent reports suggest incomplete arginine methylation and phosphorylation are some of the key factors that can lead to the aberrant phase transition of FUS into more gel/solid-like species. Additionally, non-productive electrostatic repulsion amongst the N-terminal domain and productive electrostatic attractions amongst the C-terminal arginine-rich domain regulate the viscoelastic properties of these condensates. Although several studies shed light on the phase separation of FUS, the molecular origin and the sequence of events that regulates intracellular phase transition into these liquid-like compartments and the liquid-to-solid phase transition of FUS remain elusive.

1.7 Thesis motivation and perspective

Liquid-liquid phase separation has been identified as a new principle in the formation of liquid-like, membrane-less organelles (MLOs) or intracellular compartments across organisms. Recent investigations highlight the role of intrinsically disordered proteins and regions (IDPs/IDRs) in forming these highly dynamic mesoscopic liquid droplets. These IDPs/IDRs comprise low-complexity domains with repetitive amino acid sequences, providing multivalent transient sticker-spacers contacts or Fuzzy interactions between the different repeat domains in various combinations. These multivalent interactions involve protein-protein and protein-nucleic acid interactions, thermodynamically favoring the genesis of these MLOs. Previous studies have shown the gradual maturation of these liquid droplets to form gel-like or solid-like aggregates, which are implicated in a variety of neurodegenerative diseases such as Amyotrophic lateral sclerosis (ALS), Frontotemporal dementia (FTDs) and Alzheimer's disease. However, the molecular origin and the sequence of events that regulates these intracellular phase transitions into these liquid-like compartments and further into solid-like aggregates remain elusive. This thesis primarily aims to unveil the molecular origin and drivers

controlling the LLPS of a neuronal IDP, namely FUS (Fused in Sarcoma) and its prion-like low-complexity domain (FUS-LC). This work delves into the intricate molecular mechanisms underlying the organization of dense, liquid-like structures, exploring how subtle variations in cellular factors or sequence alterations can induce significant changes in their properties. Our findings elucidate the dynamics of microstate alterations as a fundamental phenomenon governing diverse condensation processes and offer deep insights into the intricacies of condensation events, via high-resolution spatio-temporal analysis. This detailed characterization of heterogeneity is pivotal for unraveling the biophysical determinants dictating the formation and stabilization of condensates. Notably, our research underscores the indispensable role of water in these processes, providing a comprehensive, experimentally derived narrative that intricately describes the condensation process. The biomolecular condensates of FUS are physiologically relevant within the nucleus in a wide range of functions, including DNA damage repair, RNA splicing, transport, transcription, and so on. However, aberrant phase separation and aggregation of FUS are strongly associated with neurodegeneration in humans. Using a combination of multidisciplinary approaches involving biophysical, biochemical, fluorescence, and vibrational spectroscopy, molecular, and cell biology, my work seeks insights into the role of chain dynamics during the phase transitions of RNA-binding proteins (RBPs) comprising the low-complexity domains. We aim to identify the importance of heterogeneity, the mechanism behind the making and breaking of transient bonds, nucleation, and oligomerization associated with FUS phase separation in cellular functions and diseases. For our studies, we utilize/developed state-of-the-art single-molecule fluorescence resonance energy transfer (smFRET), super-resolution imaging, picosecond time-resolved spectroscopy, fluorescence correlation spectroscopy (FCS), dynamic light scattering (DLS), vibrational Raman spectroscopy and ensemble fluorescence lifetime/anisotropy.

In chapter 2 of this thesis, we illuminate the inner workings and chain dynamics of an archetypical prion-like, low-complexity domain of Fused in Sarcoma (FUS-LC) using an amalgamation of single-droplet, single-molecule FRET, picosecond time-resolved fluorescence anisotropy, fluorescence correlation spectroscopy in conjunction with vibrational Raman spectroscopy. Our results reveal the conformational distribution and dynamics within the monomeric and condensed phases at a single-molecule resolution in a droplet-by-droplet manner. Our single-molecule measurements could capture the conformational gymnasium of the FUS-LC polypeptide chain and expansion in conformation upon phase separation. We investigate the change in material properties accompanying a density transition coupled

percolation of the monomeric FUS-LC, leading to the formation of a dense phase comprising a viscoelastic network fluid. The incorporation of a disease-associated mutation (G156E) resulted in further increased expansion of the FUS-LC polypeptide chain, causing enhanced protein-protein interactions and an increase in dense phase concentration. This, we believe, is responsible for an accelerated FUS-LC (G156E) aggregation behavior.

In Chapter 3, we utilized the vibration Raman spectroscopy to capture the structural changes in the hydration water layer within liquid droplets of three archetypal phase-separating proteins, using single-droplet vibrational Raman spectroscopy, highlighting a sequence-encoded reorganization of the hydrogen bonding network of solvent molecules upon phase separation. This chapter provides direct observation of the alterations in the internal hydrogen-bonding network and reveals a release of bound, strongly coordinated hydration water accompanying the condensate formation within three archetypal phase separation systems. To probe the effect of diverse molecular drivers of phase separation ranging from aromatics, hydrophobics, and electrostatic interactions, we studied water within the condensates of Fused in Sarcoma (FUS), the low-complexity domain of FUS (FUS-LC), and tau. The extent of the release of water could be correlated with the contribution of hydrophobic and electrostatic interactions involved in driving phase separation. This reconstitution of the hydrogen-bonding network presumably promotes extensive solute-solute intermolecular interactions, providing the thermodynamic forces enabling the entropically unfavorable process of phase separation and thus leading to condensate formation. We further shed light on the effect of small molecule modulators of phase separation, including salt and RNA, on the hydration water structure within condensates.

Finally, in Chapter 4, we demonstrate the application of a versatile methodology, namely homo-Förster Resonance Energy Transfer (homoFRET) imaging as a reporter of supramolecular packing or as a proximity ruler within the dynamic biomolecular condensates of an archetypal phase separating protein Fused in Sarcoma (FUS). We capture the rise in homoFRET upon condensate formation from anisotropy imaging, indicating the densely packed molecular organization within condensates. We also capture the effect of small-molecule modulators such as RNA, ATP, and salt, as well as post-translational modifications in altering the dynamic nanoscale packing within condensates of FUS. Our time-resolved anisotropy measurements allow us to investigate the underlying components of excitation energy migration at nanosecond and subnanosecond timescales. Lastly, we also show the utility

of anisotropy imaging within distinct assemblies of FUS formed within cells in diverse conditions. This technique of anisotropy imaging can provide a highly sensitive and potent tool for the preliminary detection of the diverse complex biomolecular condensates formed in vitro and within cells and further illuminate their heterogeneous molecular organization and molecular proximities. I believe the work presented in this thesis will broaden our current understanding of the formation and dissolution of biomolecular condensates. The techniques adopted in this thesis can serve as a potent tool to unzip a large number of complex interactions driving phase separation and can give insights into key molecular drivers of biological phase separation.

1.8 References

1. Sender, R., Fuchs, S., & Milo, R. Revised estimates for the number of human and bacteria cells in the body. *PLoS Biol.* **14**, e1002533 (2016).

2. Alberts, B., Johnson, A., Lewis, J., Raff, M., Roberts, K., Walter, P. Molecular biology of the cell*,* 4th ed.; Garland Science, Taylor & Francis Group: New York, (2002).

3. Wright, P. E.; Dyson, H. J. Intrinsically unstructured proteins: re-assessing the protein structure-function paradigm. *J. Mol. Biol.* **293**, 321-331 (1999).

4. Dobson, C. M. Šali, A., & Karplus, M. Protein Folding: A Perspective from Theory and Experiment. *Angew. Chem. Int. Ed.* **37**, 868–893 (1998).

5. Dunker, A. K., Obradovic, Z., Romero, P., Garner, E. C., & Brown, C. J. Intrinsic protein disorder in complete genomes. *Genome Inform Ser. Workshop Genome Inform*. **11**, 161-171 (2000).

6. Dunker, A. K., Lawson, J. D., Brown, C. J., Williams, R. M., Romero, P., Oh, J. S., Oldfield, C. J., Campen, A. M., Ratliff, C. M., Hipps, K. W., Ausio, J., Nissen, M. S., Reeves, R., Kang, C., Kissinger, C. R., Bailey, R. W., Griswold, M. D., Chiu, W., Garner, E. C., & Obradovic, Z. Intrinsically disordered protein. *J. Mol. Graph Model.* **19**, 26-59 (2001).

7. Dunker, A. K., Brown, C. J., Lawson, J. D., Iakoucheva, L. M., & Obradović, Z. Intrinsic disorder and protein function. *Biochemistry* **41**, 6573-6582 (2002).

8. Anfinsen, C. B. Principles that govern the folding of protein chains. *Science* **181**, 223-230 (1973).

9. Tompa, P. Intrinsically unstructured proteins. *Trends Biochem. Sci.* **27**, 527-533 (2002).

10. Dyson, H. J., & Wright, P. E. Intrinsically unstructured proteins and their functions. *Nat. Rev. Mol. Cell. Biol*. **6**, 197-208 (2005).

11. Dunker, A. K., Babu, M. M., Barbar, E., Blackledge, M., Bondos, S. E., Dosztányi, Z., Dyson, H. J., Forman-Kay, J., Fuxreiter, M., Gsponer, J., Han, K. H., Jones, D. T., Longhi, S., Metallo, S. J., Nishikawa, K., Nussinov, R., Obradovic, Z., Pappu, R. V., Rost, B., Selenko, P., Subramaniam, V., Sussman, J. L., Tompa, P., & Uversky, V. N. What's in a name? Why these proteins are intrinsically disordered: Why these proteins are intrinsically disordered. *Intrinsically Disord. Proteins.* **1**, e24157 (2013).

12. Dobson, C. M. The structural basis of protein folding and its links with human diseases. *Phil. Trans. R. Soc. Lond. B* **356**, 133-145 (2001).

13. Fischer, E. Einfluss der Configuration auf die Wirkung der Enzyme. Berichte der deutschen chemischen Gesellschaft **27**, 2985-2993 (1894).

14. Frauenfelder, H., Sligar, S. G., & Wolynes, P. G. The energy landscapes and motions of proteins. *Science* **254**, 1598–1603 (1991).

15. Turoverov, K. K., Kuznetsova, I. M., & Uversky, V. N. The protein kingdom extended: ordered and intrinsically disordered proteins, their folding, supramolecular complex formation, and aggregation. *Prog. Biophys. Mol. Biol.* **102**, 73-84 (2010).

16. Dill, K. A., & Chan, H. S. From Levinthal to pathways to funnels. *Nat. Struct. Biol.* **4**, 10-9 (1997).

17. Uversky, V. N. Intrinsically disordered proteins and their “Mysterious” (Meta)Physics. *Fron. Phys.* **7**, 1-18 (2019).

18. Wolynes, P. G., Onuchic, J. N., & Thirumalai, D. Navigating the folding routes. *Science* **267**, 1619-1620 (1995).

19. Betts, M. J., & Sternberg, M. J. An analysis of conformational changes on protein-protein association: implications for predictive docking. *Protein Eng.* **12**, 271-283 (1999).

20. Wright, P. E., & Dyson, H. J. (2015). Intrinsically disordered proteins in cellular signalling and regulation. *Nat. Rev. Mol. Cell Biol.* **16**, 18–29 (2015).

21. Uversky, V. N., & Dunker, A. K. Understanding protein non-folding. *Biochim. Biophys. Acta.* **1804**, 1231-1264 (2010).

22. Uversky, V. N., Oldfield, C. J., & Dunker, A. K. Intrinsically Disordered Proteins in Human Diseases: Introducing the D2 Concept. *Annu. Rev. Biophys*. **37**, 215–246 (2008).

23. Jahn, T. R., & Radford, S. E. The Yin and Yang of protein folding. *FEBS J*. **272**, 5962-5970 (2005).

24. Romero, P., Obradovic, Z., Kissinger, C. R., Villafranca, J. E., Garner, E., Guilliot, S., & Dunker, A. K. Thousands of proteins likely to have long disordered regions. *Pac. Symp. Biocomput.* **3**, 437-448 (1998).

25. Ke, P. C., Zhou, R., Serpell, L. C., Riek, R., Knowles, T. P. J., Lashuel, H. A., Gazit, E., Hamley, I. W., Davis, T. P., Fändrich, M., Otzen, D. E., Chapman, M. R., Dobson, C. M., Eisenberg, D. S., & Mezzenga, R. Half a century of amyloids: past, present and future. *Chem. Soc. Rev.* **49**, 5473-5509 (2020).

26. Adamcik, J., & Mezzenga, R. Amyloid Polymorphism in the Protein Folding and Aggregation Energy Landscape. *Angew. Chem. Int. Ed. Engl.* **57**, 8370-8382 (2018).

27. Ward, J. J., Sodhi, J. S., McGuffin, L. J., Buxton, B. F., & Jones, D. T. Prediction and functional analysis of native disorder in proteins from the three kingdoms of life. *J. Mol. Biol.* **337**, 635-645 (2004).

28. Fink, A. L. Natively unfolded proteins. *Curr. Opin. Struct. Biol.* **15**, 35-41 (2005).

29. Trivedi, R., & Nagarajaram, H. A. Intrinsically Disordered Proteins: An Overview. *Int. J. Mol. Sci.* **23**, 14050 (2022).

30. Gsponer, J., & Madan Babu, M. The rules of disorder or why disorder rules. *Prog. Biophys. Mol. Biol.* **99**, 94-103 (2009).

31. Burger, V. M., Gurry, T., & Stultz, C. M. Intrinsically Disordered Proteins: Where Computation Meets Experiment. *Polymers* **6**, 2684-2719 (2014).

32. Babu, M. M. The contribution of intrinsically disordered regions to protein function, cellular complexity, and human disease. *Biochem. Soc. Trans.* **44**, 1185-1200 (2016).

33. Uversky, V. N. Intrinsically disordered proteins and their (disordered) proteomes in neurodegenerative disorders. *Front. Aging Neurosci.* **7**, 18 (2015).

34. Majumdar, A., Dogra, P., Maity, S., & Mukhopadhyay, S. Liquid-Liquid Phase Separation Is Driven by Large-Scale Conformational Unwinding and Fluctuations of Intrinsically Disordered Protein Molecules. *J Phys. Chem. Lett.* **10**, 3929-3936 (2019).

35. Fuxreiter M. Fuzziness in Protein Interactions-A Historical Perspective. *J Mol. Biol*. **430**, 2278-2287 (2018).

36. Kilgore, H. R., & Young, R. A. Learning the chemical grammar of biomolecular condensates. *Nat. Chem. Biol.* **18**, 1298–1306 (2022).

37. Alberti, S., & Hyman, A. A. Biomolecular condensates at the nexus of cellular stress, protein aggregation disease and ageing. *Nat. Rev. Mol. Cell Biol.* **22**, 196–213 (2021).

38. Lyon, A. S., Peeples, W. B., & Rosen, M. K. A framework for understanding the functions of biomolecular condensates across scales. *Nat. Rev. Mol. Cell Biol.* **22**, 215–235 (2021).

39. Mittag, T., & Pappu, R. V. A conceptual framework for understanding phase separation and addressing open questions and challenges. *Mol. Cell* **82**, 2201–2214 (2022).

40. Shin, Y., & Brangwynne, C. P. Liquid phase condensation in cell physiology and disease. *Science* **357**, (2017).

41. Roden, C., & Gladfelter, A. S. RNA contributions to the form and function of biomolecular condensates. *Nat. Rev. Mol. Cell Biol.* **22**, 183–195 (2021).

42. Choi, J. M., Holehouse, A. S., & Pappu, R. V. Physical principles underlying the complex biology of intracellular phase transitions. *Annu. Rev. Biophys*. **49**, 107–133 (2020).

43. Dignon, G. L., Best, R. B., & Mittal, J. Biomolecular phase separation: From molecular driving forces to macroscopic properties. *Annu. Rev. Phys. Chem.* **71**, 53–75 (2020).

44. Yu, M., Heidari, M., Mikhaleva, S., Tan, P. S., Mingu, S., Ruan, H., Reinkemeier, C. D., Obarska-Kosinska, A, Siggel, M., Beck, M., Hummer, G., & Lemke, E. A. Visualizing the disordered nuclear transport machinery in situ. *Nature* **617**, 162-169 (2023).

45. Shapiro, D. M., Ney, M., Eghtesadi, S. A., & Chilkoti, A. Protein phase separation arising from intrinsic disorder: First-principles to bespoke applications. *J. Phys. Chem. B* **125**, 6740–6759 (2021).

46. Brangwynne, C. P. Phase transitions and size scaling of membrane-less organelles. *J. Cell Biol.* **203**, 875-881 (2013).

47. Hyman, A. A., Weber, C. A., & Jülicher, F. Liquid-liquid phase separation in biology. *Annu. Rev. Cell Dev. Biol.* **30**, 39-58 (2014).

48. Mitrea, D. M., & Kriwacki, R. W. Phase separation in biology; functional organization of a higher order. *Cell Commun. Signal*. **14**, 1 (2016).

49. Mitrea, D. M., Cika, J. A., Guy, C. S., Ban, D., Banerjee, P. R., Stanley, C. B., Nourse, A., Deniz, A. A., & Kriwacki, R. W. Nucleophosmin integrates within the nucleolus via multi-modal interactions with proteins displaying R-rich linear motifs and rRNA. *eLife* **5**, (2016).

50. Boeynaems, S., Alberti, S., Fawzi, N. L., Mittag, T., Polymenidou, M., Rousseau, F., Schymkowitz, J., Shorter, J., Wolozin, B., Van Den Bosch, L., Tompa, P., & Fuxreiter, M. Protein Phase Separation: A New Phase in Cell Biology. *Trends Cell Biol*. **28**, 420-435 (2018).

51. Hirose, T., Ninomiya, K., Nakagawa, S., & Yamazaki, T. A guide to membraneless organelles and their various roles in gene regulation. *Nat. Rev. Mol. Cell Biol.* **24**, 288–304 (2023).

52. Martin, E. W., Holehouse, A. S., Peran, I., Farag, M., Incicco, J. J., Bremer, A., Grace, C. R., Soranno, A., Pappu, R. V., & Mittag, T. Valence and patterning of aromatic residues determine the phase behavior of prion-like domains. *Science* **367**, 694-699 (2020).

53. Krainer, G., Welsh, T. J., Joseph, J. A., George-Hyslop, S. G., Hyman, A. A., Collepardo-Geuvara, R., Alberti, S., & Knowles, T. P. J. Reentrant liquid condensate phase of proteins is stabilized by hydrophobic and non-ionic interactions. *Nat. Commun.* **12**, 1085 (2021).

54. Martin, E. W. & Mittag, T. Relationship of sequence and phase separation in protein low-complexity regions. *Biochemistry* **57**, 2478–2487 (2018).

55. Brangwynne, C. P., Tompa, P., & Pappu, R. V. Polymer physics of intracellular phase transitions. *Nat. Phys.* **11**, 899–904 (2015).

56. Vernon, R. M., Chong, P. A., Tsang, B., Kim, T. H., Bah, A., Farber, P., Lin, H., & Forman-Kay, J. D. Pi-Pi contacts are an overlooked protein feature relevant to phase separation. *eLife* **7**, e31486 (2018).

57. Ruff, K. M., Choi, Y. H., Cox, D., Ormsby, A. R., Myung, Y., Ascher, D. B., Radford, S. E., Pappu, R. V., & Hatters, D. M. Sequence grammar underlying the unfolding and phase separation of globular proteins. *Mol. Cell.* **82**, 3193-3208 (2022).

58. Uversky, V. N. Intrinsically disordered proteins in overcrowded milieu: Membrane-less organelles, phase separation, and intrinsic disorder. *Curr. Opin. Struct. Biol.* **44**, 18–30 (2017).

59. Kaur, T., Raju, M., Alshareedah, I., Davis, R.B., Potoyan, D.A., & Banerjee, P. R. Sequence-encoded and composition-dependent protein-RNA interactions control multiphasic condensate morphologies. *Nat. Commun.* **12**, (2021).

60. Murthy, A. C., Dignon, G. L., Kan, Y, Zerze, G. H., Parekh, S. H., Mittal, J., & Fawzi, N. L. Molecular interactions underlying liquid-liquid phase separation of the FUS low-complexity domain. *Nat. Struct. Mol. Biol.* **26**, 637–48 (2019).

61. Cheng, A. C., Chen, W. W, Fuhrmann, C. N, Frankel, A. D. Recognition of nucleic acid bases and base-pairs by hydrogen bonding to amino acid side-chains. *J. Mol. Biol.* **327**, 781–96 (2023).

62. Rauscher, S., & Pomès, R. The liquid structure of elastin. *eLife* **6**, e26526 (2017).

63. Wang, A., Conicella, A. E., Schmidt, H. B., Martin, E. W., Rhoads, S. N., Reeb, A. N., Nourse, A., Montero, D. R., Ryan, V. H., Rohatgi, R., Shewmaker, F., Naik, M. T., Mittag, T., Ayala, Y. M., & Fawzi, N. L. A single N-terminal phosphomimic disrupts TDP-43 polymerization, phase separation, and RNA splicing. *EMBO J.* **37**, e97452 (2018).

64. Rai, S. K., Khanna, R., Avni, A., & Mukhopadhyay, S. Heterotypic electrostatic interactions control complex phase separation of tau and prion into multiphasic condensates and co-aggregates. *Proc. Natl Acad. Sci. U.S.A.* **120**, e2216338120 (2023).

65. Dogra, P., Joshi, A., Majumdar, A., & Mukhopadhyay, S. Intermolecular Charge-Transfer Modulates Liquid-Liquid Phase Separation and Liquid-to-Solid Maturation of an Intrinsically Disordered pH-Responsive Domain. *J. Am. Chem. Soc.* **141**, 20380-20389 (2019).

66. Wang, J., Choi, J. M., Holehouse, A. S., Lee, H. O., Zhang, X., Jahnel, M., Maharana, S., Lemaitre, R., Pozniakovsky, A., Drechsel, D., Poser, I., Pappu, R. V., Alberti, S., & Alberti, S. A molecular grammar governing the driving forces for phase separation of prion-like RNA binding proteins. *Cell* **174**, 688–99 (2018).

67. Shakya, A., & King, J. T. Non-Fickian molecular transport in protein–DNA droplets. *ACS Macro Lett.* **7**, 1220–25 (2018)

68. Sabari, B. R., Dall'Agnese, A., & Young, R. A. Biomolecular Condensates in the Nucleus. *Trends Biochem. Sci.* **45**, 961-977 (2020).

69. Wang, B., Zhang, L., Dai, T., Qin, Z., Lu, H., Zhang, L., & Zhou, F. Liquid–liquid phase separation in human health and diseases. *Sig. Transduct. Target Ther.* **6**, 290 (2021).

70. Boija, A., Klein, I. A., & Young, R. A. Biomolecular Condensates and Cancer. *Cancer Cell* **39**, 174-192 (2021).

71. Chandra, B., Michmerhuizen, N. L., Shirnekhi, H. K., Tripathi, S., Pioso, B. J., Baggett, D. W., Mitrea, D. M., Iacobucci, I., White, M. R., Chen, J., Park, C. G., Wu, H., Pounds, S., Medyukhina, A., Khairy, K., Gao, Q., Qu, C., Abdelhamed, S., Gorman, S. D., Bawa, S., Maslanka, C., Kinger, S., Dogra, P., Ferrolino, M. C., Giacomo, D. D., Mecucci, C., Klco, J. M., Mullighan, C. G., & Kriwacki, R. W. Phase Separation Mediates NUP98 Fusion Oncoprotein Leukemic Transformation. *Cancer Discov.* **12**, 1152-1169 (2022).

72. Zbinden, A., Pérez-Berlanga, M., De Rossi, P. & Polymenidou, M. Phase separation and neurodegenerative diseases: a disturbance in the force. *Dev. Cell* **55**, 45–68 (2020).

73. Lin, Y. H., Forman-Kay, J. D., & Chan, H. S. Theories for sequence-dependent phase behaviors of biomolecular condensates. *Biochemistry* **57**, 2499e2508 (2018).

74. Xue, B., Dunbrack, R. L., Williams, R. W., Dunker, A. K., & Uversky, V. N. PONDR-FIT: A meta-predictor of intrinsically disordered amino acids. *Biochim. Biophys. Acta* **1804**, 996–1010 (2010).

75. Dosztányi, Z. Prediction of protein disorder based on IUPred. *Protein Sci*. **27**, 331e340 (2018).

76. Oates, M. E., Romero, P., Ishida, T., Ghalwash, M., Mizianty, M. J., Xue, B., Dosztányi, S., Uversky, V. N., Obradovic, Z., Kurgan, L., Dunker, A. K., & Gough, J. D2P2: Database of disordered protein predictions. *Nucleic Acids Res.* **41**, D508eD516 (2013).

77. Holehouse, A. S., Das, R. K., Ahad, J. N., Richardson, M. O., & Pappu, R. V. CIDER: Resources to Analyze Sequence-Ensemble Relationships of Intrinsically Disordered Proteins. *Biophys. J.* **10**, 16-21 (2017).

78. Lancaster, A. K., Nutter-Upham, A., Lindquist, S., & King, O. D. PLAAC: A web and command-line application to identify proteins with prion-like amino acid composition. *Bioinformatics* **30**, 2501e2502 (2014).

79. Letunic, I., & Bork, P. 20 years of the SMART protein domain annotation resource. *Nucleic Acids Res*. **46**, D493eD496 (2018).

80. Bolognesi, B., Lorenzo Gotor, N., Dhar, R., Cirillo, D., Baldrighi, M., Tartaglia, G. G., & Lehner, B. A Concentration-Dependent Liquid Phase Separation Can Cause Toxicity upon Increased Protein Expression. *Cell Rep.* **16**, 222–231(2016).

81. Horvath, A., Miskei, M., Ambrus, V., Vendruscolo, M., & Fuxreiter, M. Sequence-based prediction of protein binding mode landscapes. *PLoS Comput. Biol.* **16**, e1007864 (2020).

82. Agarwal, A., Rai, S. K., Avni, A., & Mukhopadhyay, S. An intrinsically disordered pathological prion variant Y145Stop converts into self-seeding amyloids via liquid-liquid phase separation. *Proc. Natl. Acad. Sci. U.S.A*. **118**, e2100968118 (2021).

83. Alberti, S., Gladfelter, A., & Mittag, T. Considerations and challenges in studying liquid-liquid phase separation and biomolecular condensates. *Cell* **176**, 419e434 (2019).

84. Pattanashetty, S. G., Joshi, A., Walimbe, A., & Mukhopadhyay, S. Guidelines for in vitro Characterization of Liquid-liquid Phase Separation. In: Uversky, U. (ed.) Droplets of life:

Membrane-less Organelles, Biomolecular Condensates, and Biological Liquid-liquid Phase Separation. Elsevier 1, 233-249 (2022).

85. Avni, A., Joshi, A., Walimbe, A., Pattanashetty, S. G., & Mukhopadhyay, S. Single-droplet surface-enhanced Raman scattering decodes the molecular determinants of liquid-liquid phase separation. *Nat. Commun.* **13**, 4328 (2022).

86. Alshareedah, I., & Banerjee, P. R. Measurement of Protein and Nucleic Acid Diffusion Coefficients Within Biomolecular Condensates Using In-Droplet Fluorescence Correlation Spectroscopy. *Methods Mol. Biol.* **2563**, 199-213 (2023).

87. Elbaum-Garfinkle, S., Kim, Y., Szczepaniak, K., Chen, C. C.-H., Eckmann, C. R., Myong, S., & Brangwynne, C. P. The disordered P granule protein LAF-1 drives phase separation into droplets with tunable viscosity and dynamics. *Proc. Natl. Acad. Sci. U.S.A*. **112**, 7189e7194 (2015).

88. Taylor, N., Elbaum-Garfinkle, S., Vaidya, N., Zhang, H., Stone, H. A., & Brangwynne, C. P. Biophysical characterization of organelle-based RNA/protein liquid phases using microfluidics. *Soft Matter* **12**, 9142e9150 (2016).

89. Raman, V., & Krishnan, K. S. A New Type of Secondary Radiation. *Nature* **121**, 501- 502 (1928).

90. Smith., & Dent, G. Modern Raman Spectroscopy: A Practical Approach 1st ed., Wiley (2005).

91. Campanella, B., Palleschi, V., & Legnaioli, S. Introduction to vibrational spectroscopies. ChemTexts 7, 5 (2021).

92. Infrared and Raman Spectroscopy in Forensic Science; Chalmers, J. M., Edwards, H. G. M., Hargreaves, M. D., Eds., Wiley (2012).

93. Agarwal, A., Arora, L., Rai, S.K. et al. Spatiotemporal modulations in heterotypic condensates of prion and α-synuclein control phase transitions and amyloid conversion. *Nat. Commun.* **13**, 1154 (2022). Same as ref. 100

94. Tuma, R. Raman Spectroscopy of Proteins: From Peptides to Large Assemblies. *J. Raman Spectrosc.* **36**, 307-319 (2005).

95. Rygula, A., Majzner, K., Marzec, K. M., Kaczor, A., Pilarczyk, M., & Baranska, M. Raman Spectroscopy of Proteins: A Review. *J. Raman Spectrosc.* **44**, 1061-1076 (2013).

96. Thomas, G. J. Jr. Raman spectroscopy of protein and nucleic acid assemblies. *Annu. Rev. Biophys. Biomol. Struct.* **28**, 1-27 (1999).

97. Matousek, P., & Stone, N. Emerging concepts in deep Raman spectroscopy of biological tissue. *Analyst* **134**, 1058-1066 (2009).

98. Carey, P. R. Raman spectroscopy, the sleeping giant in structural biology, awakes. *J. Biol. Chem.* **274**, 26625-26628 (1999).

99. Dey, T. Microplastic pollutant detection by Surface Enhanced Raman Spectroscopy (SERS): a mini-review. *Nanotechnol. Environ. Eng.* **8**, 41–48 (2023).

100. Lippert, J. L.; Tyminski, D.; Desmeules, P. J. Determination of the secondary structure of proteins by laser Raman spectroscopy. *J. Am. Chem. Soc.* **98**, 7075–7080 (1976).

101. Mikhonin, A. V., Bykov, S. V., Myshakina, N. S., & Asher, S. A. Peptide secondary structure folding reaction coordinate: correlation between UV Raman amide III frequency, Psi Ramachandran angle, and hydrogen bonding. *J. Phys. Chem. B*. **110**, 1928-1943 (2006).

102. Asher, S. A., Ianoul, A., Mix, G., Boyden, M. N., Karnoup, A., Diem, M., & Schweitzer-Stenner, R. Dihedral psi angle dependence of the amide III vibration: a uniquely sensitive UV resonance Raman secondary structural probe. *J. Am. Chem. Soc.* **123**, 11775-11781 (2021).

103. Hernandez, B., Coic, Y. M., Pfluger, F., Kruglik, S. G., & Ghomi, M. All characteristic Raman markers of tryrosine and tyrosinate originate from phenol ring fundamental vibrations. *J. Raman Spectrosc.* **47**, 212–220 (2015).

104. Milan-Garces, E. A., Mondal, S., Udgaonkar, J. B., & Puranik, M. Intricate packing in the hydrophobic core of barstar through a CH- π interaction. *J. Raman Spectrosc.* **45**, 814–821 (2014).

105. Schlamadinger, D. E., Daschbach, M. M., Gokel, G. W., & Kim, J. E. UV resonance Raman study of cation-π interactions in an indole crown ether. *J. Raman Spectrosc.* **42**, 633-638 (2011).

106. Ganser, L. R., & Myong, S. Methods to Study Phase-Separated Condensates and the Underlying Molecular Interactions. *Trends Biochem. Sci.* **45**, 1004-1005 (2020).

107. Murthy, A. C., Tang, W. S., Jovic, N., Janke, A. M., Seo, D. H., Perdikari, T. M., Mittal, J., & Fawzi, N. L. Molecular interactions contributing to FUS SYGQ LC-RGG phase separation and co-partitioning with RNA polymerase II heptads. *Nat. Struct. Mol. Biol.* **28**, 923-935 (2021).

108. Tibble, R. W., & Gross, J. D. A call to order: Examining structured domains in biomolecular condensates. *J. Magn. Reson*. **346**, 107318 (2023).

109. Goetz, S. K., & Mahamid, J. Visualizing Molecular Architectures of Cellular Condensates: Hints of Complex Coacervation Scenarios. *Dev. Cell* **55**, 97-107 (2020).

110. Tollervey, F., Zhang, X., Bose, M., Sachweh, J., Woodruff, J. B., Franzmann, T. M., & Mahamid, J. Cryo-Electron Tomography of Reconstituted Biomolecular Condensates. In: Zhou, HX., Spille, JH., Banerjee, P.R. (eds) Phase-Separated Biomolecular Condensates. *Methods mol. biol.* **2563**, 297-324 (2023).

111. Ji, J., Wang, W., & Chen, C. Single-molecule techniques to visualize and to characterize liquid-liquid phase separation and phase transition. *Acta Biochim. Biophys. Sin. (Shanghai)* **55**, 1023-1033 (2023).

112. Schuler, B., Soranno, A., Hofmann, H., & Nettels, D. Single-Molecule FRET Spectroscopy and the Polymer Physics of Unfolded and Intrinsically Disordered Proteins. *Annu. Rev. Biophys.* **45**, 207-231 (2016).

113. Roy, R., Hohng, S., & Ha, T. A practical guide to single-molecule FRET. *Nat. Methods* **5**, 507-516 (2008).

114. Metskas, L. A., & Rhoades, E. Single-Molecule FRET of Intrinsically Disordered Proteins. *Annu. Rev. Phys. Chem*. **71**, 391-414 (2020).

115. Mukhopadhyay, S., Krishnan, R., Lemke, E. A., Lindquist, S., & Deniz, A. A. A natively unfolded yeast prion monomer adopts an ensemble of collapsed and rapidly fluctuating structures. *Proc. Natl. Acad, Sci. U. S. A.* **104**, 2649-2654 (2007).

116. Schuler, B. Single-molecule FRET of protein structure and dynamics - a primer. *J. Nanobiotechnology* **11**, S2 (2013).

117. Lerner, E., Barth, A., Hendrix, J., Ambrose, B., Birkedal, V., Blanchard, S. C., Börner, R., Chung, H. S., Cordes, T., Craggs, T. D., Deniz, A. A., Diao, J., Fei, J., Gonzalez, R. L., Gopich, I. V., Ha, T., Hanke, C. A., Haran, G., Hatzakis, N. S., Hohng, S., Hong, S. C., Hugel, T., Ingargiola, A., Joo, C., Kapanidis, A. N., Kim, H. D., Laurence, T., Lee, N. K., Lee, T. H., Lemke, E. A., Margeat, E., Michaelis, J., Michalet, X., Myong, S., Nettels, D., Peulen, T. O., Ploetz, E., Razvag, Y., Robb, N. C., Schuler, B., Soleimaninejad, H., Tang, C., Vafabakhsh, R., Lamb, D. C., Seidel, C. A. M., & Weiss, S. FRET-based dynamic structural biology: Challenges, perspectives and an appeal for open-science practices. *eLife* **10**, e60416 (2021).

118. Israels, B., Lund, L.M., & Birkedal, V. Single-Molecule FRET: Principles and Analysis. In: Šachl, R., Amaro, M. (eds) *Fluorescence Spectroscopy and Microscopy in Biology.* Springer Series on Fluorescence, Springer, Cham. **20**, 99-127 (2022).

119. Sasmal, D. K., Pulido, L. E., Kasal, S., & Huang, J. Single-molecule fluorescence resonance energy transfer in molecular biology. *Nanoscale* **8**, 19928-19944 (2016).

120. Galvanetto, N., Ivanović, M. T., Chowdhury, A., Sottini, A., Nüesch, M. F., Nettels, D., Best, R. B., & Schuler, B. Extreme dynamics in a biomolecular condensate. *Nature* **619**, 876-883 (2023).

121. Melo, A. M., Coraor, J., Alpha-Cobb, G., Elbaum-Garfinkle, S., Nath, A., & Rhoades, E. A functional role for intrinsic disorder in the tau-tubulin complex. *Proc. Natl. Acad. Sci. U.S.A.* **113**, 14336-14341 (2016).

122. Elbaum-Garfinkle, S., & Rhoades, E. Identification of an aggregation-prone structure of tau. *J. Am. Chem. Soc.* **134**,16607-16613 (2012).

123. Wen, J., Hong, L., Krainer, G., Yao, Q. Q., Knowles, T. P. J., Wu, S., & Perrett, S. Conformational Expansion of Tau in Condensates Promotes Irreversible Aggregation. *J. Am. Chem. Soc.* **143**,13056-13064 (2021).

124. Joshi, A., Walimbe, A., Avni, A., Rai, S. K., Arora, L., Sarkar, S., & Mukhopadhyay, S. Single-molecule FRET unmasks structural subpopulations and crucial molecular events during FUS low-complexity domain phase separation. *Nat. Commun.* **14**, 7331 (2023).

125. Crozat, A., Åman, P., Mandahl, N., & Ron, D. Fusion of CHOP to a novel RNA-binding protein in human myxoid liposarcoma. *Nature* **363**, 640–644 (1993).

126. Schwartz, J. C., Cech, T. R., & Parker, R. R. Biochemical Properties and Biological Functions of FET Proteins. *Annu Rev Biochem.* **84**, 355-379 (2015).

127. Portz, B., Lee, B. L., & Shorter, J. FUS and TDP-43 Phases in Health and Disease. *Trends Biochem. Sci.* **46**, 550-563 (2021).

128. Deng, H., Gao, K., & Jankovic, J. The role of FUS gene variants in neurodegenerative diseases. *Nat. Rev. Neurol.* **10**, 337-348 (2014).

129. Ratti, A., & Buratti, E. Physiological functions and pathobiology of TDP-43 and FUS/TLS proteins. *J Neurochem.* **138** (Suppl 1), 95-111 (2016).

130. Svetoni, F., Frisone, P., & Paronetto, M. P. Role of FET proteins in neurodegenerative disorders. *RNA Biol.* **13**, 1089–1102 (2016).

131. Tüű-Szabo, B., Hoffka, G., Duro, N., & Fuxreiter, M. Altered dynamics may drift pathological fibrillization in membraneless organelles. *Biochim. Biophys. Acta, Proteins Proteomics* **1867**, 988–998 (2019).

132. Murray, D. T., Kato, M., Lin, Y., Thurber, K. R., Hung, I., McKnight, S. L., & Tycko, R. Structure of FUS protein fibrils and its relevance to self-assembly and phase separation of low-complexity domains. *Cell* **171**, 615–627 (2017).

133. Kato, M. & McKnight, S. L. The low-complexity domain of the FUS RNA binding protein self-assembles via the mutually exclusive use of two distinct cross-β cores. *Proc. Natl Acad. Sci. U.S.A.* **118**, e2114412118 (2021).

134. Maltseva, D., Chatterjee, S., Yu, C. C., Brzezinski, M., Nagata, Y., Gonella, G., Murthy, A. C., Stachowiak, J. C., Fawzi, N. L., Parekh, S. H., & Bonn, M. Fibril formation and ordering of disordered FUS LC driven by hydrophobic interactions. *Nat. Chem.* **15**, 1146–1154 (2023).

135. Berkeley, R. F., Kashefi, M., & Debelouchina, G. T. Real-time observation of structure and dynamics during the liquid-to-solid transition of FUS LC. *Biophys. J.* **120**, 1276–1287 (2021).

136. Lee, M., Ghosh, U., Thurber, K. R., Kato, M. & Tycko, R. Molecular structure and interactions within amyloid-like fibrils formed by a low-complexity protein sequence from FUS. *Nat. Commun*. **11**, 5735 (2020).

137. Burke, K. A., Janke, A. M., Rhine, C. L., & Fawzi, N. L. Residue-by-residue view of in vitro FUS granules that bind the C-terminal domain of RNA polymerase II. *Mol. Cell* **15**, 231–241 (2015).

138. Hofweber, M., Hutten, S., Bourgeois, B., Spreitzer, E., Niedner-boblenz, A., Schifferer, M., Ruepp, M. D., Simons, M., Niessing, D., Madl, T., & Dormann, D. Phase separation of FUS is suppressed by its nuclear import receptor and arginine methylation. *Cell* **173**, 706–719 (2018).

139. Qamar, S., Wang, G., Randle, S. J., Ruggeri, F. S., Varela, J. A., Lin, J. Q., Philips, E. C., Miyashita, A., Williams, D., Ströhl, F., Meadows, W., Ferry, R., Dardov, V. J., Tartaglia, G. G., Farrer, L. A., Schierle, G. S. K., Kaminski, C. F., Holt, C. E., Fraser, P. E., Schmitt-Ulms, G., Klenerman, D., Knowles, T., Vendruscolo, M., & St George-Hyslop, P. FUS phase separation is modulated by a molecular chaperone and methylation of arginine cation-π interactions. *Cell* **173**, 720–734 (2018).

140. Monahan, Z., Ryan, V. H., Janke, A. M., Burke, K. A., Rhoads, S. N., Zerze, G. H., O'Meally, R., Dignon, G. L., Conicella, A. E., Zheng, W., Best, R. B., Cole, R. N., Mittal, J., Shewmaker, F., & Fawzi, N. L. Phosphorylation of the FUS low-complexity domain disrupts phase separation, aggregation, and toxicity. *EMBO J*. **36**, 2951-2967 (2017).

Single-Molecule FRET Unmasks Structural Subpopulations and Crucial Molecular Events During FUS Low-Complexity Domain Phase Separation

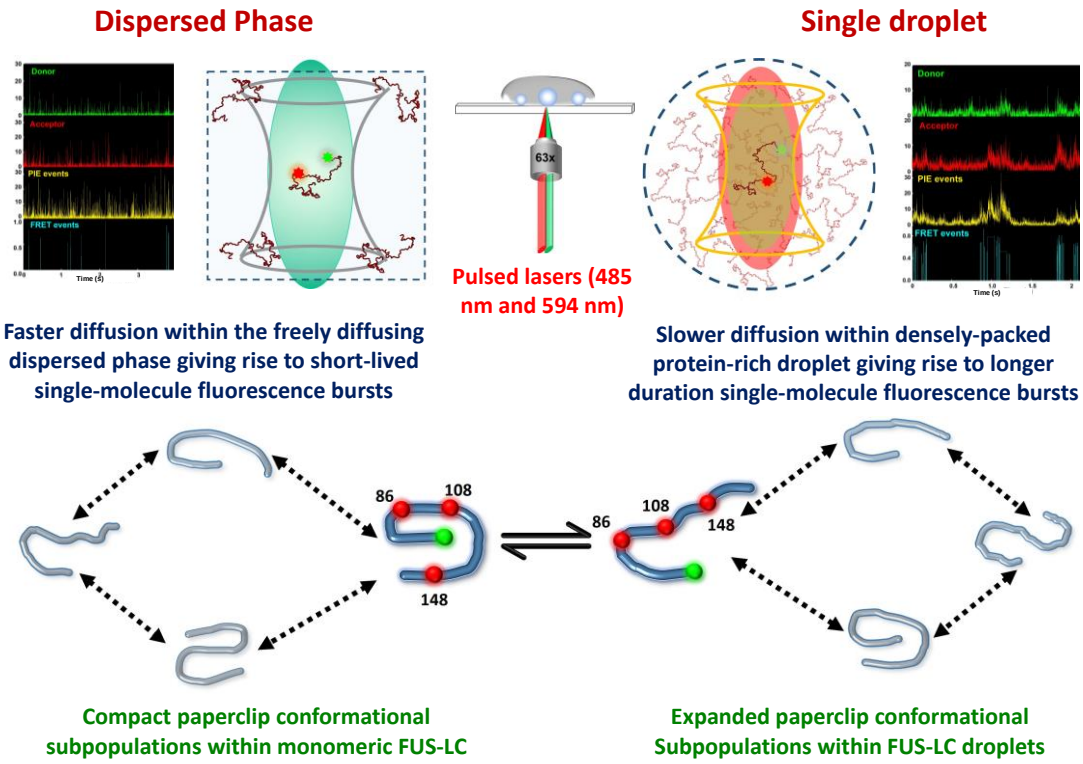

The work described in this chapter has been published in *Nature Communications.*

Joshi A, Walimbe A, Avni A, Rai SK, Arora L, Sarkar S, & Mukhopadhyay S. Single-molecule FRET unmasks structural subpopulations and crucial molecular events during FUS low-complexity domain phase separation. *Nat. Commun.,* **2023,** 14, 7331.

2.1 Introduction

Living cells compartmentalize their biochemical components and processes using well-defined membrane-bounded organelles. A growing body of rapidly evolving research reveals that in addition to such conventional membrane-bounded organelles, cells contain noncanonical membraneless organelles that are thought to be formed via liquid-liquid phase separation of proteins, nucleic acids, and other biomolecules[1-10]. These membraneless compartments, also termed biomolecular condensates, include nucleolus, stress granules, P-bodies, Cajal bodies, nuclear speckles, and so on. These membraneless bodies are highly dynamic, liquid-like, regulatable, permeable, nonstoichiometric supramolecular assemblies involved in the spatiotemporal regulation of vital cellular processes including genome organization, RNA processing, signaling, transcription, stress regulation, immune response, and so forth[11-13]. Recent studies have established that intrinsically disordered proteins/regions (IDPs/IDRs) possessing low-complexity and prion-like domains are the key candidates for biological phase separation[7,8,14-16]. These studies revealed that the presence of low-sequence complexity promotes intrinsic disorder, conformational flexibility, structural heterogeneity, and multivalency that enable the polypeptide chains to participate in a multitude of ephemeral chain-chain interactions governing the making and breaking of noncovalent interactions on a characteristic timescale. These noncovalent intermolecular interactions involve electrostatic, hydrophobic, hydrogen bonding, dipole-dipole, π–π, and cation–π interactions and yield a highly dynamic liquid-like behavior of phase-separated biomolecular condensates[17-22]. Biomolecular condensate formation involves a density transition coupled to the percolation that results in the dense phase comprising a viscoelastic network fluid[4]. Such condensates comprising viscoelastic fluids can undergo aberrant liquid-to-solid phase transitions resulting in the maturation and hardening of these assemblies into solid-like aggregates that are associated with a wide range of neurodegenerative diseases[2,12-14,23].

An archetypal phase-separating protein, Fused in Sarcoma (FUS), is a highly abundant protein belonging to the FET (FUS, EWSR1, and TAF15) family of proteins. Liquid-like condensates of FUS are thought to play crucial roles in RNA processing, DNA damage repair, paraspeckle formation, miRNA biogenesis, and the formation of stress granules. On the contrary, solid-like aggregates of FUS are identified as pathological hallmarks of several neurodegenerative diseases including Amyotrophic Lateral Sclerosis (ALS) and Frontotemporal Dementia (FTD)[24-28]. FUS exhibits a multidomain architecture comprising an

intrinsically disordered N-terminal domain and a partly structured C-terminal RNA-binding domain. The N-terminal domain contains a QSGY-rich prion-like low-complexity domain, whereas, the C-terminal RNA-binding domain (FUS-RBD) consists of an RNA-recognition motif (RRM), two RGG-rich stretches, a zinc finger domain, and a short nuclear localization signal (NLS) (Figure 2.1a). The N-terminal, intrinsically disordered, prion-like low-complexity domain, termed FUS-LC, has been identified as the major driver of self-assembly into liquid-like condensates, hydrogels, and solid-like aggregates (Figure 2.1b)[25-29]. Previous studies have established that FUS-LC serves as a model prion-like system to investigate the fundamental biophysical principles of phase separation and maturation. Structural characterizations have indicated that FUS-LC remains intrinsically disordered in both monomeric dispersed and condensed phases[25,30-37]. However, the complex interplay of the key molecular determinants and the crucial molecular events that critically govern the course of macromolecular phase separation of FUS-LC remain elusive. The key question of how sequence-encoded conformational plasticity, structural distributions, and chain dynamics control weak, multivalent, transient intermolecular interactions resulting in the formation of liquid-like condensates is of paramount importance both in normal cell physiology and disease biology.

In this work, we elucidate the structural heterogeneity, distributions, and interconversion dynamics of FUS-LC using single-molecule experiments that permit us to monitor the conformational states in a molecule-by-molecule manner. Such single-molecule experiments offer a powerful approach to accessing the incredible wealth of molecular information that is normally skewed in conventional ensemble-averaged experiments[38-44]. These single-molecule studies allow us to interrogate one molecule at a time and directly capture the hidden conformational states, characteristic conformational fluctuations, and interconversion dynamics. We utilized highly sensitive single-molecule FRET (Förster resonance energy transfer) using FUS-LC constructs site-specifically and orthogonally labeled with a donor-acceptor pair (Figure 2.1c) that allowed us to detect and characterize structurally distinct states and conformational distributions within structurally heterogeneous populations in the monomeric dispersed phase and the protein-rich condensed phase. Our single-molecule FRET studies varying the inter-residue distance in conjunction with fluorescence correlation spectroscopy (FCS), picosecond time-resolved fluorescence anisotropy, and vibrational Raman spectroscopy within individual phase-separated condensates permitted us to dissect the conformational shapeshifting events associated with phase separation of FUS-LC. We also

elucidated the impact of a clinically relevant pathological mutation on the conformational distribution and dynamics that alters the phase behavior of the low-complexity domain.

2.2 Experimental details

2.2.1 Materials

The catalog number for all the materials are mentioned in parentheses. Sodium phosphate monobasic dihydrate (P9791), sodium phosphate dibasic dihydrate (71643), 2-mercaptoethanol (BME) (M3148), 1,4-dithiothreitol (DTT) (43815), Tris(2-carboxyethyl)phosphine hydrochloride (TCEP) (C4706), and Urea (U5378) were of MB grade purity, procured from Sigma (St. Louis, MO, USA). Luria Bertani Broth, Miller (LB) (M1245), N-cyclohexyl-3-aminopropanesulfonic acid (CAPS) (MB008), sodium chloride (1.93206.0521), ethylenediaminetetraacetic acid (EDTA) (MB011), and nickel chloride (GRM1394) were procured from HiMedia Laboratories. Kanamycin (K-120-10) and isopropyl-β-thiogalactopyranoside (IPTG) (I2481) were obtained from Gold Biocom (USA). Fluorescent probes like fluorescein-5-maleimide (F-5-M) (F150), AlexaFluor488 succinimidyl ester, AlexaFluor488 (A20000), and AlexaFluor594-maleimide (A10256) were purchased from Molecular Probes, Invitrogen. Ni-NTA resin (30230) was purchased from Qiagen. Amicon membrane filters (UFC901024) for concentrating protein were obtained from Merck Millipore. PD-10 (17085101), NAP-10 (17085402), and HiLoad 16/600 Superdex-G-200 (28-9893-23) columns were purchased from GE Healthcare Life Sciences (USA). High-purity milli-Q water was used to prepare all the buffers in this study. A Metrohm 827 lab pH meter was used to adjust the pH (± 0.01) of all the buffer solutions prepared at 25 °C, and all the buffer solutions were filtered before use.

2.2.2 Bioinformatics analyses

Various bioinformatics tools were used for the sequence characterization of FUS-LC. Classification of Intrinsically Disordered Ensemble Regions (CIDER) (https://pappulab.wustl.edu/CIDERinfo.html)[45] for visualization of charged and hydrophobic amino acids and Predictor of Natural Disordered Regions (PONDR) (http://www.pondr.com/)[46] for disorder propensity prediction were used. To determine the phase separation propensity catGranule (http://www.tartaglialab.com/)[47] and PScore (http://abragam.med.utoronto.ca/~JFKlab/)[18] (based on π-π interaction propensity) were used. Disorder and phase separation propensity plots were generated using the Origin software.

2.2.3 Construct details and Site-directed mutagenesis

All single cysteine and disease mutants were created by site-directed mutagenesis using the recombinant MBP-His_6-FUS-LC WT (Addgene plasmid # 98653; https://www.addgene.org/98653/; RRID: Addgene_98653) cloned in pTHMT vector which was a kind gift from Nicolas L. Fawzi. The primer sets used for introducing these point mutations have been listed in Table 1. All mutations were confirmed by sequencing.

A16C Forward	CCCAAAGCTATGGGTGCTACCCCACCCAGC
A16C Reverse	GCTGGGTGGGGTAGCACCCATAGCTTTGGG
S86C Forward	CTATGGCAGTAGCCAGTGCTCCCAATCGTC
S86C Reverse	GACGATTGGGAGCACTGGCTACTGCCATAG
S108C Forward	CCAGCTCCCAGCTGCACCTCGGGAA
S108C Reverse	TTCCCGAGGTGCAGCTGGGAGCTGG
S148C Forward	AAAGCTATGGACAGCAGCAATGCTATAATCCCCC
S148C Reverse	GGGGGATTATAGCATTGCTGCTGTCCATAGCTTT
LC G156E Forward	GCTATAATCCCCCTCAGGGCTATGAACAGCAGAACCAGTACAACAGC
LC G156E Reverse	GCTGTTGTACTGGTTCTGCTGTTCATAGCCCTGAGGGGGATTATAGC

Table 1. Primers used for site-directed mutagenesis

2.2.4 Recombinant protein expression and purification

Wild-type and all the variants of FUS-LC were transformed in *E. coli* BL21(DE3) std cells, overexpressed, and purified using affinity chromatography, followed by gel-filtration chromatography. Bacterial cultures were grown at 37 °C, 220 rpm, to an $O.D._{600}$ of 0.8-1. Protein overexpression was induced by adding 1 mM isopropyl-β-thiogalactopyranoside (IPTG) and further growing cultures at 37 °C for 4-5 h. Bacterial cells were harvested by centrifugation at 4 °C, 3220 x g for 30 minutes, and stored at -80 °C for future use. Cell pellets were resuspended in lysis buffer (20 mM sodium phosphate, 300 mM NaCl, 10 mM imidazole, pH 7.4) and were lysed by probe sonication at 5% amplitude, 15 seconds ON, and 10 seconds OFF for 20 minutes. The lysate was centrifuged at 4 °C, 15,557 x g for 1 h to remove the cell debris, and the supernatant was loaded onto a Ni-NTA column. The column was washed, and the bound protein was eluted with elution buffer (20 mM sodium phosphate, 300 mM NaCl, 300 mM imidazole, pH 7.4).

The N-terminal MBP-His_6 tag was cleaved by adding recombinantly expressed and in-house purified TEV protease at a 1:40 molar ratio (TEV: protein), followed by incubation at 30 °C for 1.5 h. It was then subjected to overnight dialysis at room temperature. The cleaved protein was passed through the Ni-NTA column to separate the uncleaved species and TEV protease and flowthrough were collected and concentrated using a 10 kDa MWCO Amicon filter. Concentrated protein was further loaded on HiLoad 16/600 Superdex-G-200 (GE) column equilibrated with the SEC buffer (20 mM CAPS, 150 mM NaCl, pH 11). SEC elution fractions were run on an SDS-PAGE gel to determine fractions containing protein of interest. Pure protein fractions were pooled, concentrated, and buffer-exchanged into 20 mM CAPS, pH 11 buffer using a PD-10 column. Pure protein was concentrated using a 3 kDa MWCO Amicon filter, and concentration was estimated by measuring absorbance at 280 nm (ε_{280} = 30,720). Pure protein was flash-frozen and stored at - 80 °C.

2.2.5 Circular dichroism (CD) measurements

Far-UV CD spectra were recorded using a Chirascan spectrophotometer (Applied Photophysics, UK) in a quartz cuvette of 1 mm path length. Wild-type and G156E FUS-LC were diluted to 10 μM in 20 mM sodium phosphate buffer, pH 7.4. Measurements were made

for buffer and monomeric FUS-LC. Recorded absorption spectra were averaged over 10 scans, followed by blank subtraction using ProData Viewer version 4.1.9 software, and plotted using the Origin software.

2.2.6 Phase separation assays

Protein stock was thawed on ice and diluted up to 200 μM in 20 mM phosphate buffer, pH 7.4. Phase separation of wild-type and G156E FUS-LC was induced by the addition of 250 mM NaCl in the reaction mixture. Spontaneous phase separation of FUS-LC into liquid droplets was indicated by the immediate rise in turbidity upon mixing with salt.

2.2.7 Turbidity assay

The turbidity of monomeric FUS-LC and phase-separated samples of wild-type and G156E FUS-LC were monitored by measuring absorbance at 350 nm on a Multiskan Go (Thermo Scientific) plate reader. Droplet reactions of 100 μL (200 μM FUS-LC in 20 mM phosphate, 250 mM NaCl, pH 7.4) were set up and used for the turbidity measurements. The mean and standard errors were obtained from at least 3 independent sets of measurements.

2.2.8 Fluorescence labeling

Single-cysteine FUS-LC variants were labeled with fluorescein-5-maleimide (F-5-M) and AlexaFluor488-C5-maleimide under denaturing buffer conditions (8 M Urea, 20 mM phosphate, pH 7.5) for anisotropy and FRAP measurements. Pure protein was incubated with 0.3 mM tris(2-carboxyethyl)phosphine (TCEP) for 30 minutes on ice and was mixed with fluorescent dyes in a molar ratio of 1:30 (for F-5-M) and 1:3 (for AlexaFluor488-maleimide). The labeling mixture was incubated in the dark under stirring conditions at room temperature for 3 h. Following the reaction, the excess free dye was removed by buffer exchange using a NAP-10 column. For dual-labeling of FUS-LC single-cysteine variants, the pure protein was incubated under denaturing conditions (8 M Urea, 20 mM phosphate, pH 8) with the amine-reactive NHS ester of AlexaFluor488 (donor dye) in a molar ratio of 1:4 under shaking at 25 °C for 4 h. The unreacted dye was further removed using a NAP-10 column, and the eluted protein was concentrated and used for labeling with the thiol-reactive acceptor dye. The donor-labeled protein was mixed with AlexaFluor594-maleimide in a ratio of 1:4 and incubated at 25 °C with

stirring for 5 h, under denaturing conditions (8 M Urea, 20 mM phosphate, pH 7.5). The labeling reaction was then buffer exchanged with a NAP-10 column, and the remaining free dye was removed using a 3 kDa MWCO Amicon filter. All the single and dual-labeled proteins were concentrated using a 3 kDa MWCO Amicon filter. Labeling efficiencies were estimated by measuring absorbance at 280 nm ($\varepsilon_{280nm} = 30{,}720\ M^{-1}cm^{-1}$, for FUS-LC cysteine variants), 494 nm ($\varepsilon_{494} = 73{,}000\ M^{-1}\ cm^{-1}$, for AlexaFluor488 and $\varepsilon_{494} = 68{,}000\ M^{-1}\ cm^{-1}$, for F-5-M) and 590 nm ($\varepsilon_{590} = 92{,}000\ M^{-1}\ cm^{-1}$ for AlexaFluor594) to estimate the total protein and labeled protein concentrations. Using our labeling protocol, we obtained a ~ 100% labeling efficiency for the acceptor fluorophore and ~ 80% labeling efficiency for the donor fluorophore.

2.2.9 Confocal microscopy

All fluorescence microscopy imaging was performed on ZEISS LSM 980 Elyra 7 super-resolution Microscope using a 63x oil-immersion objective (N.A. 1.4) and a monochrome cooled high-resolution AxioCamMRm Rev. 3 FireWire(D) camera. Phase separation of 200 µM unlabeled FUS-LC was induced in the presence of 0.1% AlexaFluor488-labeled FUS-LC by the addition of 250 mM NaCl (20 mM phosphate, pH 7.4). Reactions were incubated at room temperature for 5 minutes and a 5-10 µL sample was placed on a glass coverslip and imaged using a 488 nm laser diode (11.9 mW). For two-color imaging, the droplet reaction was spiked with 0.05% of dual-labeled FUS-LC and imaged using 488 nm and 590 nm excitation sources, respectively. The images were acquired at 1840 x 1840 pixels and 16-bit depth resolution. Airyscan images of the fluorescently labeled droplets were acquired by utilizing the confocal laser scanning microscope via the Airyscan 2 detector equipped with 32 channels (GaAsP). Image processing and analyses were performed on in-built instrument software Zen Blue 3.2 and ImageJ (NIH, Bethesda, USA).

2.2.10 Fluorescence recovery after photobleaching (FRAP) measurements

FRAP experiments were done on ZEISS LSM 980 Elyra 7 super-resolution microscope using a 63x oil-immersion objective (N.A 1.4) and a monochrome cooled high-resolution AxioCamMRm Rev. 3 FireWire(D) camera. A region of 1 µm was bleached inside droplets doped with 0.1% AlexaFluor488-labeled FUS-LC using a 488 nm laser diode. The recovery was recorded using the Zen Blue 3.2 (ZEISS) software. FRAP measurements were performed

for at least 8 independent droplets for both wild-type and G156E FUS-LC. Fluorescence recovery curves were normalized, background corrected, and plotted using the Origin software.

2.2.11 Steady-state fluorescence measurements

Steady-state FRET experiments were performed on a Fluoromax-4 spectrofluorometer (Horiba Jobin Yvon, NJ, USA) using a 1-mm pathlength quartz cuvette. For all the experiments, 50 nM of dual-labeled FUS-LC variants were used. The donor fluorophore (AlexaFluor488) was excited at 494 nm and fluorescence emission was recorded from 515 nm to 700 nm to monitor both donor and acceptor emission spectra.

2.2.12 Single-droplet FRET imaging by acceptor photobleaching

Phase separation of 200 µM FUS-LC (20 mM phosphate, pH 7.4) was induced by the addition of 250 mM NaCl in salt in the presence of 0.05 % dual-labeled single-cysteine variants of FUS-LC. The droplet reaction was imaged on a ZEISS LSM 980 Elyra 7 super-resolution microscope using a 63x oil-immersion objective (N.A 1.4) and a monochrome-cooled high-resolution AxioCamMRm Rev. 3 FireWire(D) camera. To determine the FRET efficiency, the acceptor present in a dual-labeled droplet was photobleached using a 594 nm laser, and the increase in the donor fluorescence intensity was recorded upon bleaching the acceptor fluorophore. FRET efficiencies were estimated using the Zen Blue 3.2 (ZEISS) software.

2.2.13 Dynamic light scattering (DLS)

For estimating the hydrodynamic radii of monomeric FUS-LC, a dynamic light scattering instrument (Malvern Zetasizer) was used. All the reaction buffers were filtered using 0.02 µm filters. Monomeric FUS-LC (50 µM in 20 mM phosphate, pH 7.4) in the absence and presence of 250 mM NaCl was used for measurements at room temperature.

2.2.14 C_{sat} estimation

Droplet reactions (200 µM FUS-LC) were induced by the addition of 250 mM NaCl (in 20 mM sodium phosphate, pH 7.4 buffer) and incubated at 25 °C for 10 minutes. The reactions were then subjected to ultracentrifugation at 25 °C, 18000 x g for 30 minutes. The supernatant was

removed carefully without disturbing the pellet to estimate the dilute phase concentration. The protein saturation concentration (C_{sat}) of the dilute phase was estimated by measuring the absorbance at 280 nm (ε_{280} = 30,720).

2.2.15 Single-molecule FRET experiments and data analysis

In single-molecule FRET experiments, the ratiometric FRET efficiency (E) for each molecule is recorded from the fluorescence bursts that are separated into donor (I_D) and acceptor (I_A) signals using the following equation.

$$E = \frac{1}{1+\left(\frac{I_D}{I_A}\right)\gamma} \quad \text{--- (1)}$$

where γ is a correction factor obtained from different quantum yields of donor and acceptor dyes and the detection efficiencies for donor and acceptor channels.

Single-molecule FRET experiments were performed using a MicroTime 200 time-resolved confocal microscope (PicoQuant) in a pulsed interleaved excitation (PIE) mode. All the single-molecule FRET experiments were performed in 20 mM phosphate buffer, 250 mM NaCl, pH 7.4. Measurements in the monomeric dispersed phase were performed in the presence of 75-150 pM of dual-labeled FUS-LC, and droplet formation of 200 µM FUS-LC was performed in the presence of 5-10 pM of dual-labeled protein. Data were acquired within 15-20 min after the initiation of the phase separation. Reactions were set in a buffer containing n-propyl gallate as an oxygen scavenger to improve the photostability of the fluorophore in the solution. Pulsed laser sources (485 nm and 594 nm) at a frequency of 20 MHz were used to alternately excite the donor and the acceptor fluorophores within the dual-labeled samples using a 60x water-immersion objective (N.A.= 1.2). The laser power was fixed at 45-60 µW (40-50 µW for 485 nm and 5-10 µW for 594 nm laser) measured at the back aperture of the objective for the dispersed phase and 5.5-8.5 µW (5-7 µW for 485 nm and 0.5-1.5 µW for 594 nm laser) in order to minimize the saturation, background counts, and photobleaching of the acceptor. The lasers were focused inside the solution (50 µm from the surface) for the dispersed phase and within single droplets (2-4 µm inside) for the condensed phase to obtain fluorescence emission bursts. The emitted photons were collected and focused through a 50 µm pinhole, and a dichroic beam splitter (zt594rdc) was used to separate the donor and acceptor emission. The emission was filtered (BP 535/50 nm for the green channel and LP 594 for the red channel) and detected by the respective single-photon avalanche diode (SPAD) detectors. Data were

collected and analyzed using the SymphoTime64 software v2.7. A typical binning time used was 0.5 ms and 1 ms, and using PIE, the bursts containing both donor and acceptor signals were considered for FRET analysis. The donor and acceptor counts were corrected for the background with a minimum threshold of 35 photons used for the further selection of bursts to construct the FRET efficiency histogram. The FRET efficiencies were corrected for the spectral crosstalk between the donor and acceptor fluorophore (α = 0.05), direct excitation of the acceptor by donor laser (β = 0.003), and the correction factor in the detection efficiencies of the donor and acceptor channels (γ = 1.12) which were estimated by performing comparative measurements in both acceptor and donor channels of the instrument and a fluorescence spectrophotometer[48,49]. All the FRET efficiency histograms were constructed for > 20,000 events. The FRET efficiency histograms were plotted and fitted using a Gaussian peak function in the Origin software.

2.2.16 Distance estimation from single-molecule FRET

The inter-dye distance (r) between the N-terminally labeled AlexaFluor488 and AlexaFluor594 at a cysteine residue was estimated using the mean FRET efficiency (E) obtained from single-molecule FRET histograms using the following relationships.

$$E = \frac{1}{1+\left(\frac{r}{R_0}\right)^6} \quad \text{--- (2)}$$

$$r = R_0 \left[\frac{1}{E} - 1\right]^{\frac{1}{6}} \quad \text{--- (3)}$$

For the distance estimation in the monomeric dispersed form, a Förster radius (R_0) of 54 Å for AlexaFluor488 and AlexaFluor594 was used[50,51]. For droplets, the R_0 was corrected (52.4 Å) by taking the altered index of refraction within condensates into account. We employed the previously reported method for correction by estimating the protein concentration within the protein-rich dense phase[52]. The protein concentration within droplets was estimated by the sedimentation assay by pelleting the dense phase at 25 °C, 18000 x g for 30 minutes. Time-resolved fluorescence anisotropy decay measurements for both AlexaFluor488-labeled and AlexaFluor594-labeled FUS-LC, both in monomer and droplets, revealed considerable local fluorophore rotational dynamics validating the assumption of the orientation factor to be $^2/_3$ (Figure 2.1d, e). However, we would like to point out here that we do not rule out minor effects

of the orientation factor and photon shot noise on inter-dye distances. These effects can be more pronounced in the condensed phase than in the monomeric dispersed phase precluding us from the distance estimation in droplets.

2.2.17 Fluorescence correlation spectroscopy (FCS)

FCS measurements were performed using the same MicroTime 200 setup for the monomeric phase and the condensed phase of wild-type and G156E FUS-LC. A free dye solution of 1 nM AlexaFluor488 was used to estimate the structure parameter of confocal volume (5.52), which was used for further FCS analyses. For the dispersed phase measurements, data were acquired in the presence of 10 nM AlexaFluor488-labeled FUS-LC in the presence of salt (250 mM NaCl). For single-droplet FCS measurements, droplet reactions were set up with 1-3 nM AlexaFluor488 labeled FUS-LC, and these samples were placed on glass coverslips. Measurements were performed by focusing inside the solution for the dispersed phase and within single droplets for the condensed phase of wild-type and G156E FUS-LC. FCS data were collected, analyzed, and correlation curves were fitted with the triplet-state model using SymphoTime64 software v2.7 to obtain diffusion time within the dispersed and condensed phases.

2.2.18 Single-droplet steady-state and time-resolved fluorescence anisotropy measurements

MicroTime 200 time-resolved confocal microscope (PicoQuant) was used for performing steady-state fluorescence anisotropy measurements of dispersed and droplet phase of FUS-LC spiked with 0.1% F-5-M-labeled single-cysteine variants at residue positions 16, 86, 108, and 148. Fluorescein-5-maleimide (F-5-M) dye was used as a thiol-reactive anisotropy probe owing to its short linker length which accurately reports on the rotational dynamics of the polypeptide chain. Freshly phase-separated droplet reactions were spotted on a coverslip with a thickness of 1.5 mm placed directly on a Super Apochromat 60x water immersion objective with 1.2 NA (Olympus). Samples were excited with the 485 nm laser, and the emitted fluorescence was collected and filtered by a bandpass emission filter (BP 535/50) before entering the pinhole (50 μm). The in-focus emitted light exiting the pinhole was split into the two detector channels by a polarizing beam-splitter placed before the detectors and detected by the respective Single-Photon Avalanche Diodes (SPADs). Anisotropy imaging was performed for single-droplet

steady-state anisotropy measurements, and a point time trace was obtained for time-resolved anisotropy measurements. The correction factors were calculated by performing fluorescence measurements in a free dye solution and utilized to estimate steady-state anisotropy using the commercially available SymphoTime64 software v2.7. The fluorescence anisotropy (r_{ss}) is given by the following relationship.

$$r_{ss} = \frac{I_{\parallel} - I_{\perp}}{[1-3L2]I_{\parallel} + [2-3L1]I_{\perp}} \text{ --- (4)}$$

where $I_{\parallel}$ and $I_{\perp}$ are the background corrected parallel and perpendicular fluorescence intensities, and L1 (0.308) and L2 (0.0368) are the objective correction factors.

For time-resolved fluorescence anisotropy decay analysis, the decay profiles obtained from SymphoTime64 software v2.7 were further analyzed by global fitting using the following relationships.

$$I_{\parallel}(t) = 1/3I(t)[1 + 2r(t)] \text{ --- (5)}$$

$$I_{\perp}(t) = 1/3I(t)[1 - r(t)] \text{ --- (6)}$$

where $I_{\parallel}$(t), $I_{\perp}$(t), and $I(t)$ denote the time-dependent fluorescence intensities collected at the parallel, perpendicular, and magic angle (54.7°) geometry. The perpendicular component was always corrected using the G-factor that was intendedly obtained from free dye in the buffer. The time-resolved fluorescence anisotropy decay profiles were fitted using a biexponential decay model yielding two rotational correlation times, namely, fast (ϕ_1) and slow (ϕ_2) rotational correlation times as follows.

$$r(t) = r_0[\beta_1 e^{\left(\frac{-t}{\Phi_1}\right)} + \beta_2 e^{\left(\frac{-t}{\Phi_2}\right)}] \text{ --- (7)}$$

where r_0 denotes the (time-zero) fundamental anisotropy of the fluorophore, and β_1 and β_2 the fractional amplitudes associated with ϕ_1 and ϕ_2, respectively. The goodness of fit was estimated based on the autocorrelation function, randomness of residuals, and reduced χ^2 values.

2.2.19 Raman spectroscopy

Raman spectra of phase-separated individual droplets of wild-type and G156E FUS-LC were acquired on an inVia laser Raman microscope (Renishaw, UK) at room temperature. Freshly phase-separated samples (3-5 μL) were drop cast onto a glass slide covered with aluminum foil and spectra were obtained within 15-20 min after phase separation initiation. Single droplets were focused using a 100x long working distance objective lens (Nikon, Japan). The samples were excited with an NIR laser (785 nm) with an exposure time of 10 seconds at a laser power of 500 mW (100%), and an edge filter of 785 nm was used to block the Rayleigh scattering. The collected Raman scattering was dispersed using a diffraction grating (1200 lines/mm) and further detected by an air-cooled CCD detector. Data were acquired for 5 accumulations, after which collected spectra were background-corrected and smoothened using inbuilt software Wire 3.4. Since a tyrosine vibrational band could potentially interfere with the backbone amide band, amide I bands were separately baseline-corrected and deconvoluted to estimate the secondary structural contents. All the data were plotted and analyzed using the Origin software.

2.3 Results

2.3.1 Single-droplet FRET imaging hints at long-range intramolecular interactions in the condensed phase

FUS-LC comprising 163 residues exhibits a near-uniform distribution of amino acids, serine (S), tyrosine (Y), glycine (G), and glutamine (Q), and is characterized by a low net charge and low mean hydrophobicity (Figure 2.1b, Figure 2.2a). We began with the bioinformatics characterization using PONDR[45], which confirmed the presence of intrinsic disorder in FUS-LC (Figure 2.2b), and CIDER[46] (Classification of Intrinsically Disordered Ensemble Relationships) which provides various distinctive features of IDPs built on the sequence composition. Using CIDER, we obtained the NCPR (net charge per residue) value from the NCPR plot and the diagram of states which illustrates the distribution of positive and negative charges throughout the sequence. IDPs often possess a sequence composition that is characterized by a low mean hydrophobicity and a high net charge[53].

However, FUS-LC carries a low net charge with an NCPR value < 0.25; such a polypeptide can exist as compact globular ensembles in contrast to the well-solvated expanded conformations exhibited by charged IDPs[46,54].

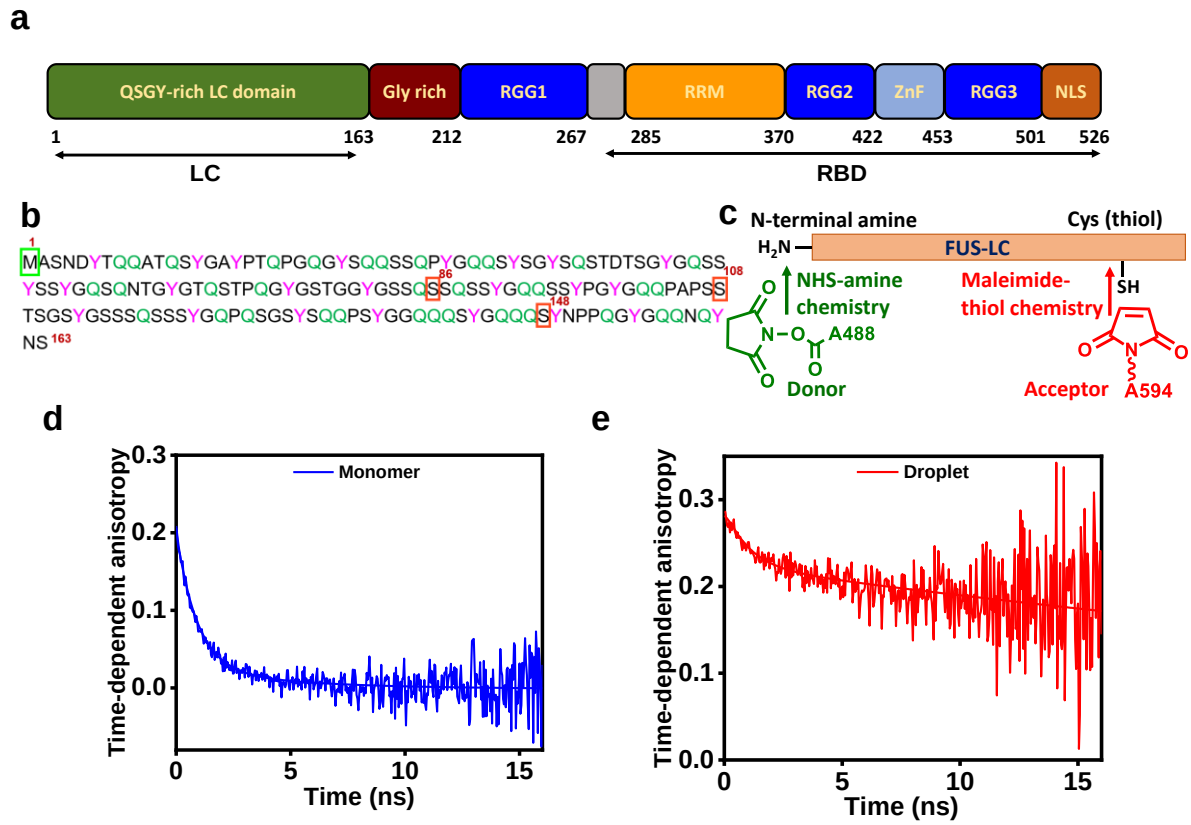

Figure 2.1 a. Domain architecture of full-length FUS. b. The amino acid sequence of FUS-LC highlighting the tyrosine and glutamine residues. Residue positions for single-cysteine mutants are underlined. c. Schematic of orthogonal labeling chemistry utilized for site-specific labeling of N-terminal with NHS ester of AlexaFluor488 and cysteine with thiol-active AlexaFluor594-maleimide. Representative picosecond time-resolved fluorescence anisotropy decay profiles for FUS-LC N-terminally labeled with AlexaFluor488 (donor) within the monomeric dispersed (d) and droplet (e) phases. Solid lines represent fits obtained from biexponential decay analysis. Fast rotational correlation times and associated fractional amplitudes obtained within the monomeric phase (~ 0.9 ns and 0.86) and condensed phase (~ 1.8 ns and 0.22) indicated considerable depolarization due to local rotational dynamics of the attached fluorophore. Similar parameters were recovered for the acceptor (AlexaFluor594)-labeled FUS-LC.

Based on the charge composition, FUS-LC is predicted to adopt a compact[55] or tadpole-like[46] structure, as also evident from the diagram of states, which predicts IDP conformations based on the fraction of positively and negatively charged residues within the sequence (Figure 2.2c). To experimentally validate, we recombinantly expressed and purified FUS-LC and performed circular dichroism (CD) spectroscopic measurements of monomeric FUS-LC which exhibited a characteristic disordered state (Figure 2.2d). Upon addition of salt, as observed previously[30-32], a homogeneous solution of FUS-LC underwent phase separation. Next, in order to directly

visualize the droplet formation, we took advantage of the fact that FUS-LC does not contain any lysine residue and selectively labeled the N-terminal amine using the amine-reactive AlexaFluor488 succinimidyl ester (NHS ester) (Figure 2.1c). This labeling strategy also allowed us to perform (selective) orthogonal dual labeling for FRET studies (see below). Using AlexaFluor488-NHS-labeled FUS-LC, we imaged the droplets using confocal microscopy (Figure 2.2e). These droplets exhibited liquid-like behavior as evident by rapid and complete fluorescence recovery after photobleaching (FRAP) (Figure 2.2f). These observations indicated that FUS-LC undergoes liquid phase condensation upon the addition of salt and are in agreement with previous reports[25,30,31]. Next, in order to elucidate the conformational changes associated with phase separation, we performed intramolecular FRET measurements both in monomeric dispersed and condensed phases. The FRET donor (AlexaFluor488) was installed using the N-terminal NHS chemistry, whereas, the acceptor (thiol-active AlexaFluor594-maleimide), was covalently linked using thiol-maleimide chemistry at a Cys position of the single-Cys variants created along the FUS-LC polypeptide chain (Figure 2.1b, c). We created three single-Cys mutants of FUS-LC (Cys residues at residue positions 86, 108, and 148) that encompassed the significant part of the polypeptide chain from the N- to the C-terminus and allowed us to record three intramolecular distances from the N-terminal end (N-to-86, N-to108, and N-to-148). The orthogonal labeling chemistries (NHS labeling at N-terminal amine and thiol-maleimide chemistry at Cys residues) yielded three FRET constructs selectively labeled with a donor (AlexaFluor488) and an acceptor (AlexaFluor594) (Figure 2.1c). As a prelude to performing more advanced single-molecule FRET experiments, we carried our ensemble steady-state FRET measurements both in spectroscopy and microscopy formats.

The dual-labeled FUS-LC constructs exhibited energy transfer both in the monomeric dispersed state (Figure 2.2g) and in the droplet phase as evident by an overlapping two-color confocal microscopy image (Figure 2.2h). We next performed single-droplet acceptor photobleaching experiments in a droplet-by-droplet manner. To determine the residue length-dependent FRET efficiency within these condensates, the acceptor was photobleached, and a subsequent increase in donor intensity was recorded (Figure 2.2i, j), which was used to extract ensemble FRET efficiency within individual condensates (Figure 2.2k). The FRET efficiency for the N-to-108 construct was significantly higher than the N-to-86 and N-to-148 constructs. A higher FRET efficiency for the N-to-108 construct hinted at the presence of some long-range interactions in the polypeptide chain within these condensates.

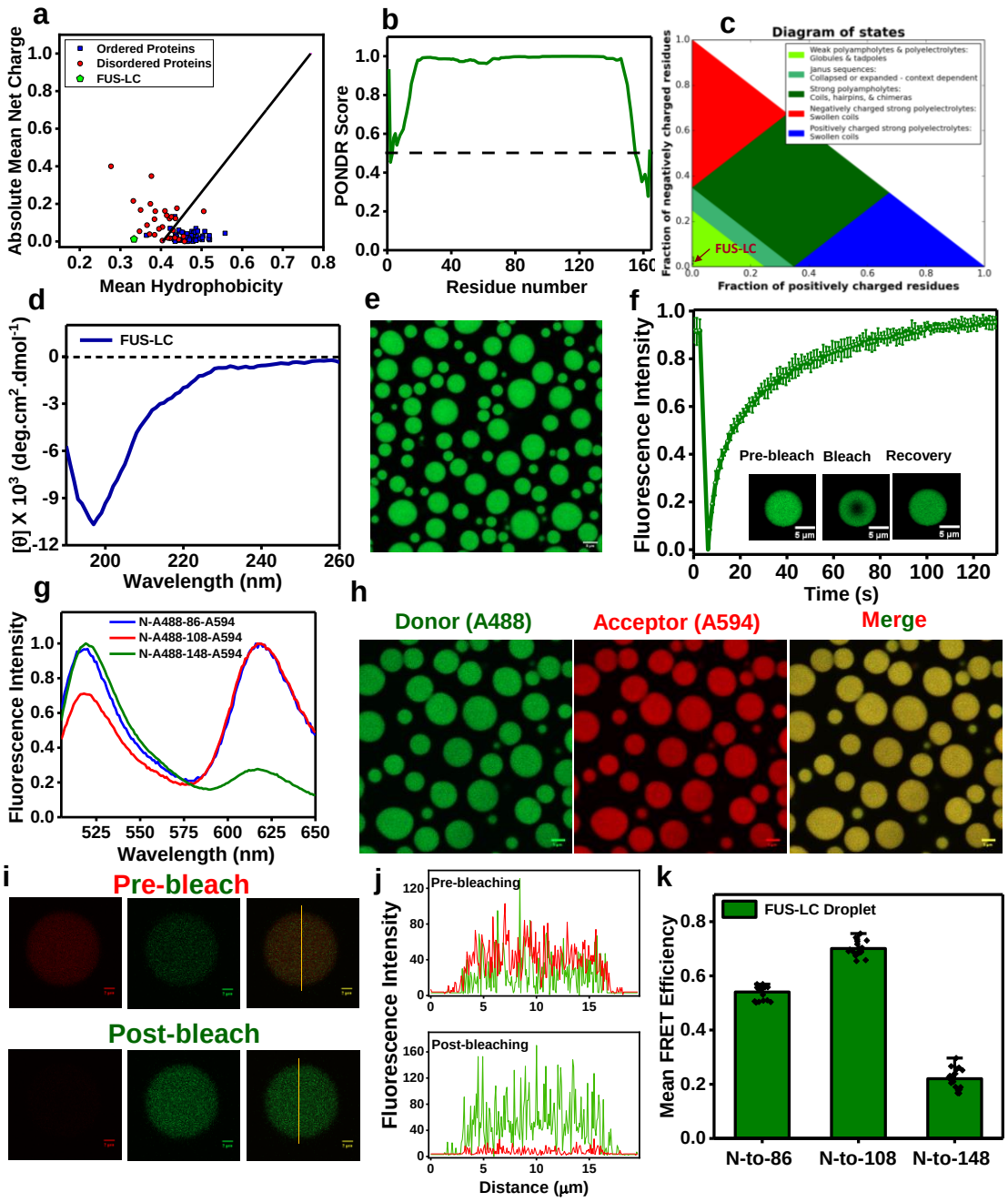

Figure 2.2 a. The mean hydrophobicity vs. the mean net charge for a range of natively ordered and disordered proteins, FUS-LC is represented in green. b. Predictor of Natural Disordered Regions (PONDR) showing unstructured FUS-LC. c. A sequence annotated diagram of IDP states based on the fraction of negative and positive charged residues shows FUS-LC as compact globules and tadpole-like conformations d. A far-UV CD spectrum of FUS-LC indicating random-coil conformation. e. Confocal image of FUS-LC droplets containing 0.1 % AlexaFluor488-labeled protein. f. FRAP kinetics of multiple droplets (n = 12) represented by the mean and standard deviation (0.1% AlexaFluor488-labeled FUS-LC was used for FRAP measurements). g. Ensemble steady-state fluorescence emission spectra of dual-labeled FUS-

LC showing donor and acceptor fluorescence upon donor excitation at 488 nm. h. Two-color Airyscan confocal image of FUS-LC droplets formed in the presence of 0.05% FUS-LC labeled with AlexaFluor488 at the N-terminal and AlexaFluor594 at Cys 86 (N-A488-86-A594) i. A representative image of acceptor photobleaching FRET of individual dual-labeled FUS-LC condensates and (j) fluorescence intensity profiles showing a decrease in the acceptor fluorescence intensity and an increase in the donor fluorescence intensity upon acceptor photobleaching. The imaging was independently repeated 5 times with similar observations. k. Mean FRET efficiencies in FUS-LC condensates were estimated from the acceptor photobleaching for three constructs varying the intramolecular distance, namely, N-to-86, N-to-108, and N-to-148. Data represent mean $\pm$ SD for n = 9 droplets.

These ensemble FRET experiments are not capable of discerning conformational distribution and dynamics but provide the groundwork for carrying out more advanced single-molecule FRET measurements. Therefore, to detect and characterize the co-existing conformationally distinct subpopulations and their interconversion, we next set out to perform our single-molecule FRET measurements both in the dispersed and condensed phases.

2.3.2 Experimental design for single-droplet single-molecule FRET

In this section, we provide a brief description of the experimental design for carrying out single-molecule experiments within individual condensates. A more detailed description of the setup, experiments, data acquisition, and data analysis are provided in experimental details. Our single-molecule FRET experiments were performed using the two-color pulsed-interleaved excitation (PIE) mode on a time-resolved confocal microscope (Figure 2.3). The PIE-FRET methodology permitted us to identify the low FRET states by eliminating the contribution of the zero-FRET efficiency peak which arises due to the acceptor photobleaching during the transit time[56]. In the case of the dispersed solutions, the dual-labeled protein concentration of 75-150 pM was sufficient to obtain single-molecule fluorescence bursts that arise due to freely diffusing fluorescently-labeled protein molecules within the femtolitre confocal volume. Photon bursts separated into the donor and acceptor channels provide the footprints of individual molecules that diffuse in and out of the confocal volume and allow us to estimate the FRET efficiencies of individual diffusion events. In order to perform such single-molecule FRET experiments on individual condensates, a much lower concentration of the dual-labeled protein (5-10 pM) was needed in the condensed phase. Phase separation was induced from a mixture of unlabeled and dual-labeled FUS-LC so that the dual-labeled protein concentration was ~ 5-10 pM and the total protein concentration was 200 μM.

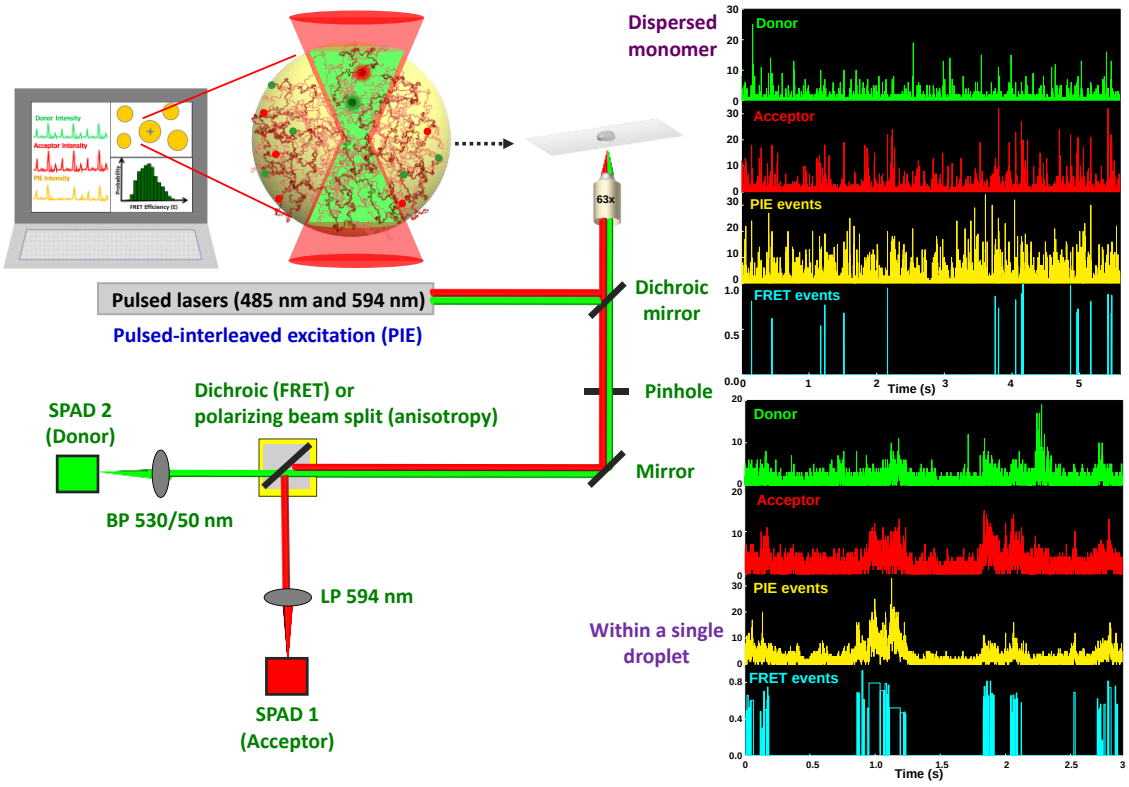

Figure 2.3 Experimental design for single-droplet single-molecule measurements. The schematic of our single-molecule microscopy setup (MicroTime 200, PicoQuant). The major components are an excitation system with two picosecond pulsed lasers (485 nm and 594 nm), an inverted microscope, and the confocal detection system consisting of an integrated system of dichroic mirrors, pinhole, bandpass filters, and single-photon avalanche diodes (SPADs) as detectors. Representative time traces displaying fluorescence bursts in donor and acceptor channels and corresponding PIE and FRET events recorded in the monomeric dispersed (top) and droplet (bottom) phases are also shown.

We placed the solution on a coverslip surface and allowed it to settle for ~ 5 min after which most droplets got immobilized onto the glass surface. We then chose large immobilized droplets (3-7 µm diameter) that are much larger than the focal spot and focused the lasers inside these droplets (~ 2 µm from the surface into the droplet). We used this procedure for single-droplet single-molecule FRET, FCS, and fluorescence anisotropy measurements. Figure 2.3 shows representative time traces containing bursts in the dispersed phase and within single droplets. Using the PIE, only the bursts originating from the dual-labeled molecules qualify as FRET events for constructing FRET-efficiency histograms. The bursts originating from the droplets have longer duration compared to the monomeric protein which is attributed to the

densely crowded environment and a slower diffusion within the condensed phase leading to a much larger number of excitation-emission cycles of the fluorophores during the transit time through the confocal volume. In the next two sections, we describe our single-molecule FRET results obtained in the monomeric and condensed phases of FUS-LC.

2.3.3 Single-molecule FRET reveals two coexisting structural subpopulations of FUS-LC in the monomeric form

We performed our single-molecule FRET experiments with three dual-labeled constructs of FUS-LC varying the intramolecular distance (N-to-86, N-to-108, and N-to-148). Under the solution condition (pH 7.4, 250 mM NaCl), FUS-LC remains monomeric up to a concentration of 50 μM as evident by our dynamic light scattering and turbidity measurements (Figure 2.4a, b, c). We performed single-molecule FRET experiments using 75-150 pM of dual-labeled FUS-LC. The single-molecule PIE-FRET efficiency histogram for the N-to-86 construct exhibited a unimodal distribution with a peak at ~ 0.76 (Figure 2.4d) that corresponds to a mean inter-dye distance of ~ 45 Å. The observed mean FRET efficiency was significantly higher than the calculated mean FRET efficiency expected for a chain in a good solvent (Table 2) suggesting that the FUS-LC chain is considerably collapsed. Next, we chose two other constructs (N-to-108 and N-to-148) having larger intramolecular distances and expected much lower FRET efficiency. In contrast to our expectation, we observed an unusual bimodal distribution in the single-molecule FRET efficiency histogram for both constructs. The construct having a 108-residue separation (N-to-108) exhibited two FRET efficiency peaks at ~ 0.97 and ~ 0.80 corresponding to distances of ~ 30 Å and ~ 43 Å, respectively. Whereas the N-to-148 construct showed peaks at ~ 0.73 and ~ 0.10 (Figure 2.4e, f) corresponding to distances of ~ 46 Å and ~ 79 Å, respectively.

These FRET efficiency histograms capture essential structural features indicating the presence of at least two predominant structural subpopulations in the monomeric conformational ensemble (Figure 2.4g). These distinct subpopulations could involve compact S-shaped/paperclip-like (high-FRET) and partially extended tadpole-like (low-FRET) conformers that are in equilibrium having an interconversion exchange rate much slower than the observation time (0.5 ms). A binning time of 1 ms did not significantly alter the histograms suggesting the conformational exchange between these structural subpopulations could even be slower than 1 ms (Figure 2.4h, i). Such structural distributions can satisfactorily explain the observed chain length-dependent inter-residue FRET efficiency histograms.

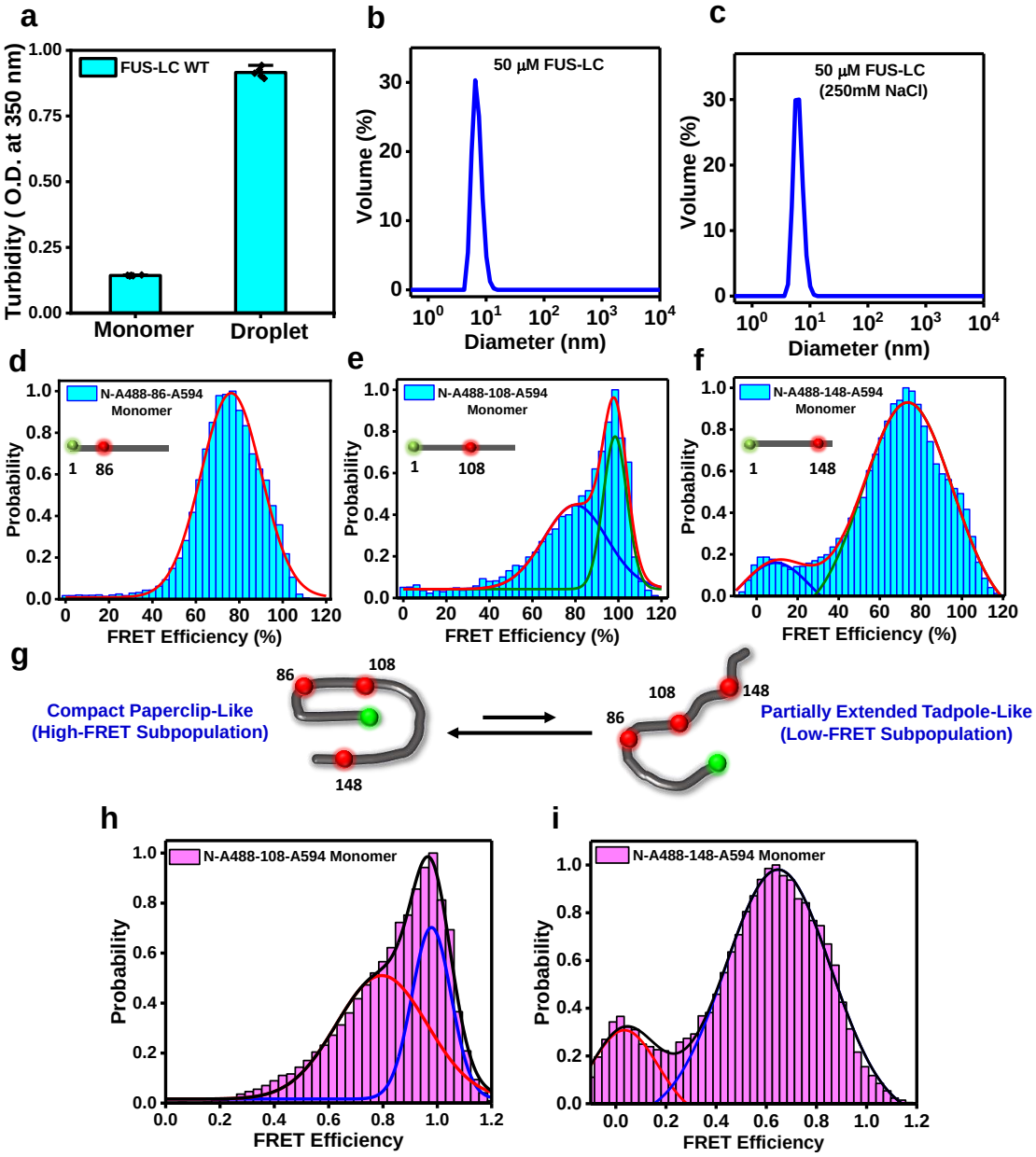

Figure 2.4. a. Turbidity plot of wild-type FUS-LC measured at 350 nm in monomeric and droplet conditions. Turbidity measurements were performed for 200 μM of FUS-LC in 20 mM phosphate buffer, pH 7.4 without salt and with 250 mM NaCl for monomer and droplet phases, respectively. Data represent mean ± SD (n = 5 independent reactions). Representative distribution of particle size obtained from dynamic light scattering (DLS) measurements of monomeric FUS-LC (50 μM protein, in 20 mM phosphate, pH 7.4) under non-phase separating (no salt) (b) and phase-separating conditions (c) (250 mM NaCl). The experiment was independently repeated 3 times with similar results. d.-f. Single-molecule FRET histogram of monomeric FUS-LC in the monomeric dispersed phase for dual-labeled (d) N-to-86, (e) N-to-108, and (f) N-to-148 constructs. The total number of events was > 20,000 and the number of events at maxima was 4217 (d), 1995 (e), and 2990 (f). g. A schematic showing the coexistence

of compact paperclip-like and extended tadpole-like conformers. Single-molecule FRET efficiency histograms obtained for the dispersed phase of N-to-108 (h) and N-to-148 (i) constructs with 1 ms time binning.

The major population comprises the high-FRET S-shaped/paperclip-like conformers that can potentially arise due to the strong intrachain interactions driven by π–π interactions between multiple tyrosine residues and hydrogen bonding between glutamine sidechains (Figure 2.1b). It is interesting to note that such compaction is observed in the N-terminal half of the polypeptide chain, whereas, the C-terminal segment adopts both compact and extended conformations possibly due to the presence of a larger number of proline residues. Taken together, our single-molecule FRET studies indicated that intrinsically disordered FUS-LC adopts two structurally distinct subpopulations having a varied extent of intrachain interactions. Next, we asked how conformational shapeshifting allows these intrachain interactions to turn into interchain interactions to promote phase separation of FUS-LC into liquid-like droplets.

2.3.4 Single-droplet single-molecule FRET reveals a structural expansion and an increase in the conformational heterogeneity upon phase separation

We performed single-droplet single-molecule FRET measurements using all of the dual-labeled FUS-LC constructs (N-to-86, N-to-108, and N-to-148). The N-to-86 construct in the droplet phase also exhibited a unimodal FRET distribution with a lower mean FRET efficiency (~0.64) with a mean inter-dye distance of ~ 48 Å (Figure 2.5a). The FRET histogram in droplets is associated with a broader distribution compared to the dispersed monomeric form that showed a mean FRET efficiency of ~ 0.76. This observation revealed the unwinding of the polypeptide chain that presumably allows the chains to participate in intermolecular interactions driving phase separation. The other two FRET constructs (N-to-108 and N-to-148) that showed bimodal FRET distribution in the monomeric form also exhibited a broadened distribution and a decrease in the energy transfer efficiencies upon phase separation (Figure 2.5b, c). In the case of the N-to-108 construct, the mean FRET efficiencies of the two populations remained largely unaltered compared to the monomeric dispersed phase; however, the contribution of the low-FRET states grew with a concomitant broadening of the distribution. These results revealed that the N-terminal end and residues near the 108th position are involved in long-range contacts that are persistent on the millisecond timescale. For the N-to-148 construct, the low-FRET states with a mean FRET efficiency of ~ 0.30 constitute a major subpopulation within the droplet phase.

Table 2. Observed FRET efficiencies varying the inter-residue length estimated from single-molecule FRET data analyses and the comparison with the calculated FRET efficiencies based on the random coil model[1]. The approximate inter-dye distances estimated from FRET peaks of single-molecule FRET histograms are shown in parenthesis.

Constructs	**Number of residues**	**Calculated FRET efficiencies**	**Experimental FRET efficiencies (Inter-dye distance in Å)**
N-to-86	86	0.32	0.76 ± 0.02 (44.6 Å)
N-to-108	108	0.16	Subpopulation 1: 0.80 ± 0.02 (42.9 Å) Subpopulation 2: 0.97 ± 0.03 (30.3 Å)
N-to-148	148	0.06	Subpopulation 1: 0.73 ± 0.01 (45.8 Å) Subpopulation 2: 0.09 ± 0.02 (79.4 Å)

It is interesting to note that these low-FRET states coexist with the high-FRET states in the condensed phase indicating conformational shapeshifting within the droplets occurs on a much slower timescale (>> 1 ms) than the typical observation time (Figure 2.5d, e). A shift in the FRET efficiency towards lower values accompanied by a growth in the lower efficiency population in the droplet phase signifies that partially extended conformers constitute the major subpopulation in the conformational ensemble along with the presence of compact paperclip-like conformers within the condensed phase.

These findings revealed that the compact FUS-LC conformational ensemble undergoes considerable unwinding engendering more structural plasticity and heterogeneity that allow the dissolution of intramolecular interactions and the formation of new intermolecular contacts promoting phase separation (Figure 2.5f). Glutamine and tyrosine residues in the condensed phase can participate in a dynamic network of intermolecular hydrogen bonding and π–π interactions within droplets giving rise to a highly condensed network fluid. These dynamic interactions can undergo making and breaking on a characteristic timescale giving rise to the internal viscoelastic behavior of these condensates. Therefore, next, we set out to study the polypeptide chain diffusion and dynamics within individual condensates on a wide range of timescales.

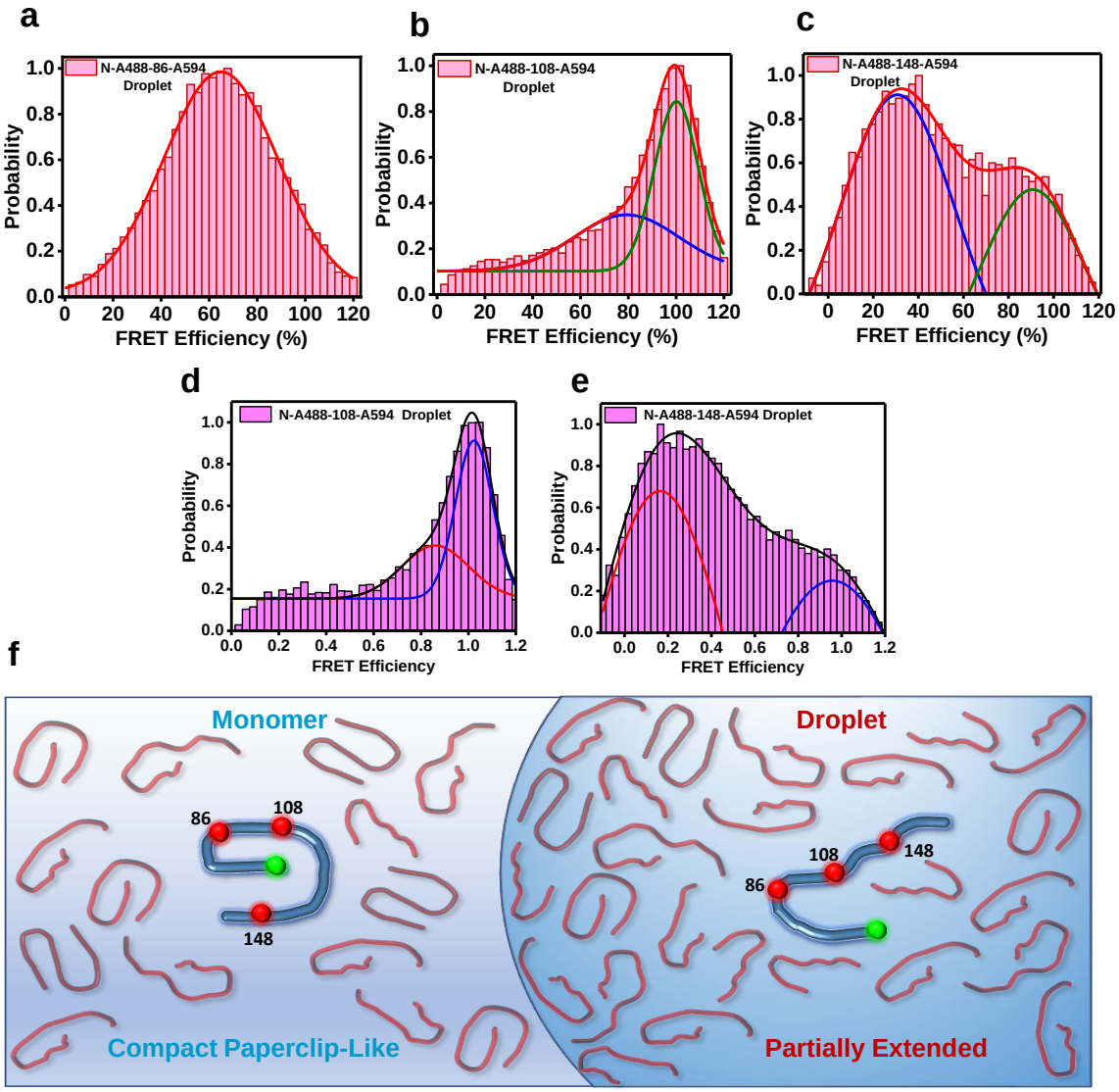

Figure 2.5. a.-c. Single-droplet single-molecule FRET histograms for FUS-LC in condensed phase for dual-labeled (a) N-to-86, (b) N-to-108, and (c) N-to-148 constructs. The total number of events was > 20,000 and the number of events at maxima was 1329 (a), 2711 (b), and 831 (c). The FRET efficiency values and estimated inter-dye distances are shown in Tables 2 and 3. The binning time was 0.5 ms. A binning time of 1 ms also yielded similar FRET histograms (Figure d, e). The Förster radius of the FRET pair (Alexa488-Alexa594) used was 54 Å. See experimental details for more information on experiments, data acquisition, data analysis, and distance estimation. f. A schematic depicting the structural unwinding of compact conformers into partially extended conformers upon phase separation.

Table 3. FRET efficiencies varying the inter-residue length estimated from single-molecule FRET data analyses for wild-type and G156E FUS-LC condensates.

Constructs	**FRET efficiencies from single-droplet single-molecule FRET studies for wild-type FUS-LC**	**FRET efficiencies from single-droplet single-molecule FRET studies for G156E FUS-LC**
N-to-86	0.64 ± 0.01	0.64 ± 0.01
N-to-108	Subpopulation 1: 0.79 ± 0.08 Subpopulation 2: 1.00 ± 0.01	Subpopulation 1: 0.86 ± 0.04 Subpopulation 2: 1.01 ± 0.01
N-to-148	Subpopulation 1: 0.30 ± 0.01 Subpopulation 2: 0.90 ± 0.02	Subpopulation 1: 0.24 ± 0.02 Subpopulation 1: 0.79 ± 0.06

2.3.5 Translational and rotational dynamics within individual condensates reveal the formation of a viscoelastic network fluid

In order to investigate the chain diffusion within individual condensates, we performed single-droplet FCS measurements using AlexaFluor488-labeled FUS-LC. FUS-LC exhibited a diffusion time of ~ 0.13 ms in the monomeric dispersed form. The translational diffusion time increased 400 times to ~ 50 ms in the droplet indicating a highly crowded and viscous environment within the droplets presumably due to the formation of a dynamic network of intermolecular interactions (Figure 2.6a, b). We envisaged such a network of interactions giving rise to the condensate formation would impede the reorientation dynamics of polypeptide chains involved in intermolecular multivalent interactions. In order to delineate the role of reorientation dynamics, we employed site-specific single-droplet fluorescence (polarization) anisotropy measurements that report the extent of rotational flexibility of the polypeptide chain. For fluorescence anisotropy experiments, we chose four sites along the polypeptide chain and labeled single-Cys variants of FUS-LC (A16C, S86C, S108C, and S148C) using thiol-active fluorescein-5-maleimide that contains a shorter linker than Alexa dyes, and therefore, can report the rotational flexibility of the polypeptide chain without exhibiting a significant local depolarization. All residue locations exhibited a sharp increase in the steady-state fluorescence anisotropy in the condensed phase compared to the dispersed

monomeric phase (Figure 2.6c, d). These results indicated dampening of the rotational flexibility of the FUS-LC chain within droplets. Notably, the 108th position exhibited a higher anisotropy value in both the monomer and droplet phases suggesting the possibility of some persistent long-range contacts that are in accordance with our single-molecule FRET data. Although steady-state fluorescence anisotropy measurements suggested reorientation restraints within condensates, these measurements do not allow us to discern the contributions of distinct modes of rotational dynamics. Next, we employed single-droplet picosecond time-resolved fluorescence anisotropy measurements that can discern the various modes of rotational dynamics. In order to temporally resolve the distinct molecular events, we utilized the highly sensitive picosecond time-resolved fluorescence anisotropy decay measurements that permit us to probe the depolarization kinetics of fluorescence anisotropy from the time-zero anisotropy value due to various modes of rotational relaxation[57,58]. In the case of monomeric IDPs, the depolarization kinetics follow a typical multiexponential decay function. Such anisotropy decay functions typically involve a fast rotational correlation time representing the local wobbling-in-cone motion of the fluorophore and slow rotational correlation times corresponding to backbone dihedral angle fluctuations and long-range reorientation dynamics[59-61]. As expected, the anisotropy decay profiles for monomeric FUS-LC recorded at different residue locations were satisfactorily described by a biexponential decay model giving rise to two well-separated correlation times: fast rotational correlation time representing a local probe motion (~ 1 ns) and a slow rotational correlation time (~ 4-5 ns) corresponding to dihedral and long-range reorientation motions (Figure 2.6e-j). We then measured fluorescence anisotropy decay kinetics within individual droplets and observed that the depolarization kinetics slowed down considerably. The fast local correlation time exhibited a slight increase, whereas, the slow rotational correlation displayed a sharp increase from ~ 5 ns to ~ 60 ns at all residue locations (Figure 2.6e-j). Such an increase in the slow correlation time within condensates indicated a dampening of the chain reorientation dynamics presumably due to the formation of a network via interchain physical crosslinks. Based on the previous studies on FUS-LC indicating the role of the glutamine and tyrosine residues in hydrogen bonding, π-sp^2, and hydrophobic interactions[25], we postulate that these intermolecular contacts form a dense network of physical crosslinks within the FUS-LC condensates (Figure 2.1b). The PScore analysis[18] that quantifies the π–π contacts in proteins revealed a high propensity of π–π interactions mediated phase separation of FUS-LC which contains 24 tyrosine and 37 glutamine residues (Figure 2.6k). Taken together, our results on chain dynamics coupled with

structural subpopulations indicate the presence of a network of intermolecular interactions as depicted in our schematic (Figure 2.6l).

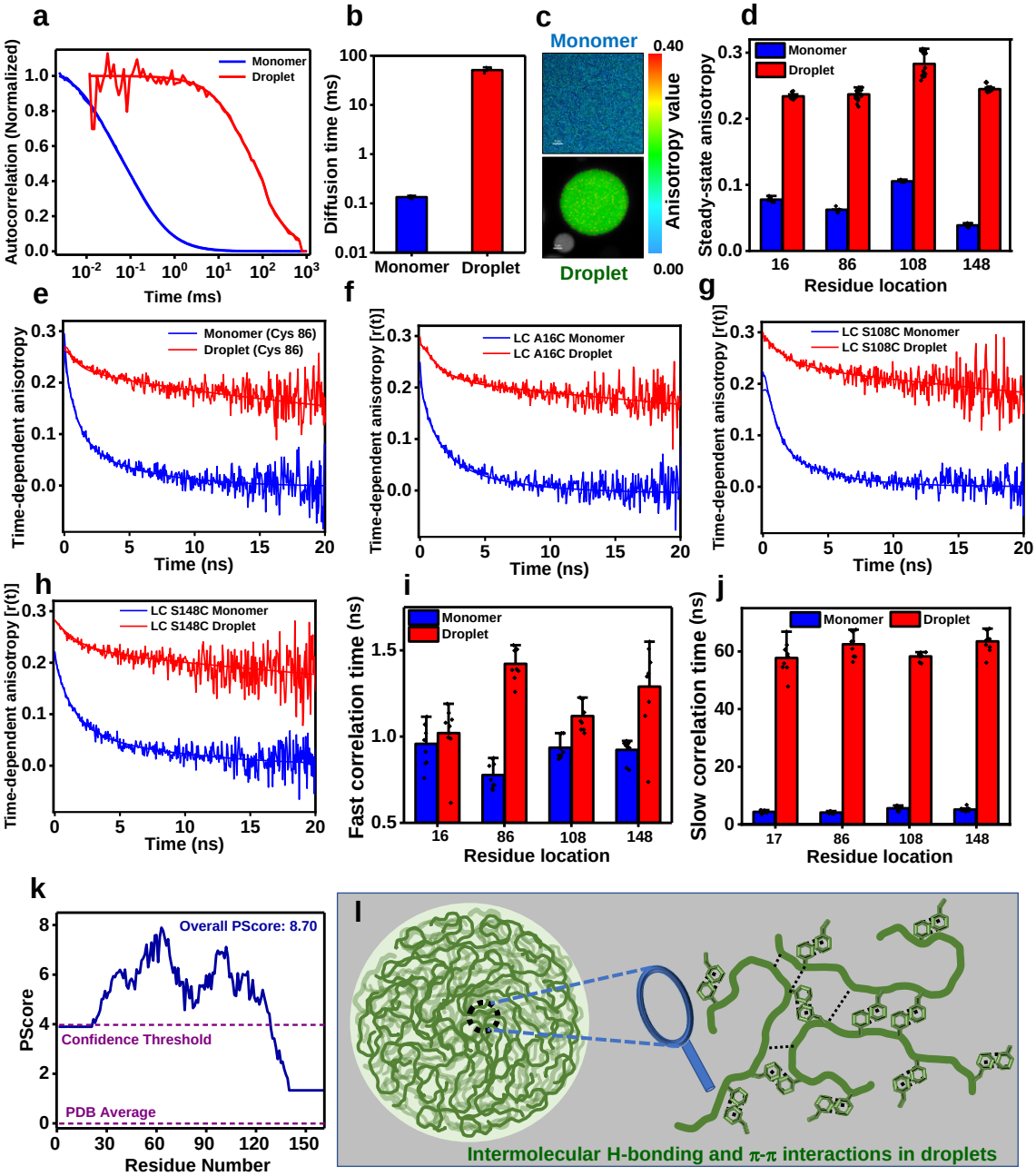

Figure 2.6. a. Autocorrelation plots (normalized) acquired from FCS measurements performed for AlexaFluor488 labeled FUS-LC in monomer and within single droplets. b. The diffusion time of FUS-LC in monomeric and condensed phases estimated from FCS. Data represent mean ± SD for n = 5 independent samples. FCS measurements were performed in the presence of 10 nM (in dispersed monomer) and 1-3 nM (in droplet) of AlexaFluor488-labeled FUS-LC. c. Representative fluorescence anisotropy images for a dispersed phase and a single droplet showing anisotropy heatmap. d. Steady-state fluorescence anisotropy values for FUS-LC in

monomeric and within individual condensates. Fluorescence anisotropy was measured using fluorescein-5-maleimide-labeled FUS-LC at residue positions 16, 86, 108, and 148. Data represent mean ± SD for n = 6, 5, 8, 8 independent samples at positions 16, 86, 108, and 148 respectively, for monomers and n = 24 for droplets. The fluorescence lifetime did not exhibit a significant change from monomeric dispersed to condensed phase. e-h. Representative picosecond time-resolved fluorescence anisotropy decay profiles for FUS-LC labeled at residue position 86, 16, 108, and 148 in monomer and droplets. Solid lines are fits obtained from biexponential decay analysis. i. Fast rotational correlation times and j. slow rotational correlation times for residue locations 16, 86, 108, and 148 recovered from decay analyses. Data represent mean ± SD (n = 9 independent samples). Rotational correlation times are included in Table 4. k. Predictor of phase separation of IDPs based on the propensity to form long-range planar π-π contacts calculated as Pscore value for FUS-LC. l. A schematic representing a dense network of intermolecular π-π contacts and hydrogen bonding within FUS-LC condensates.

Such a network of dynamic physical crosslinks can slow down translational and rotational diffusion ensuing a viscoelastic network fluid within the condensates. Next, we asked if our unique structural and dynamical readouts of wild-type FUS-LC can detect and distinguish the altered phase behavior of a disease-associated mutation.

2.3.6 A disease-associated mutant alters the phase behavior by modifying conformational distribution and dynamics

Several mutations in the disordered LC domain, RNA-binding domain, and NLS are associated with various neurodegenerative diseases. One such mutation in the LC domain (G156E) is a patient-derived, clinically relevant mutation that functions by modulating the phase behavior and aggregation propensity of FUS[34,62,63]. Thus, we next set out to study the effect of this disease-related mutation on the conformational characteristics and phase behavior of FUS-LC. We created a single-point mutant (G156E) and recombinantly expressed this construct. The CD spectrum of G156E FUS-LC indicated a disordered conformation and showed no significant changes in the secondary structural contents as compared to the wild-type FUS-LC (Figure 2.7a). Next, we began with the phase separation assay of G156E FUS-LC. A rise in turbidity values of the protein solution in the presence of salt (Figure 2.7b) indicated the formation of droplets capable of recruiting dual-labeled wild-type FUS-LC as confirmed by our two-color confocal fluorescence imaging (Figure 2.7c). To predict the effect of this mutation on the phase behavior of FUS-LC, we employed a bioinformatics analysis tool

namely catGranule[47], which computes the phase separation propensity of proteins based on their FG and RG contents, disorder, and RNA-binding propensity.

Table 4. Rotational correlation times and associated amplitudes recovered by fitting fluorescence anisotropy decay kinetics using a biexponential decay model for the monomeric dispersed phase and individual droplets.

Residue position		**Fast rotational correlation time (ϕ_1) and amplitude (β_1)**	**Slow rotational correlation time ($\phi 2$) and amplitude ($\beta 2$)**
16	Monomer	0.95 ± 0.12 ns (0.66 ± 0.08)	4.34 ± 0.45 ns (0.33 ± 0.08)
	Droplet	1.02 ± 0.16 ns (0.29 ± 0.12)	57.73 ± 5.44 ns (0.74 ± 0.01)
86	Monomer	0.77 ± 0.07 ns (0.66 ± 0.05)	4.11 ± 0.32 ns (0.33 ± 0.05)
	Droplet	1.42 ± 0.09 ns (0.26 ± 0.00)	62.49 ± 4.29 ns (0.73 ± 0.00)
108	Monomer	0.93 ± 0.06 ns (0.65 ± 0.02)	5.61 ± 0.81 ns (0.34 ± 0.02)
	Droplet	1.11 ± 0.08 ns (0.23 ± 0.01)	58.26 ± 1.37 ns (0.76 ± 0.01)
148	Monomer	0.92 ± 0.06 ns (0.79 ± 0.05)	5.16 ± 0.70 ns (0.20 ± 0.05)
	Droplet	1.29 ± 0.24 ns (0.21 ± 0.02)	63.50 ± 3.92 ns (0.78 ± 0.02)

As predicted by catGranule[47] (Figure 2.7d), the phase separation propensity of G156E FUS-LC was slightly lower in comparison to the wild-type FUS-LC as indicated by relatively lower turbidity (Figure 2.4a, 2.7b) and a higher saturation concentration compared to wild-type FUS-

LC (Figure 2.7e). Unlike for the low-complexity domain of FUS, the phase separation propensity of full-length FUS appears to remain unaffected by the G156E mutation[62,63].

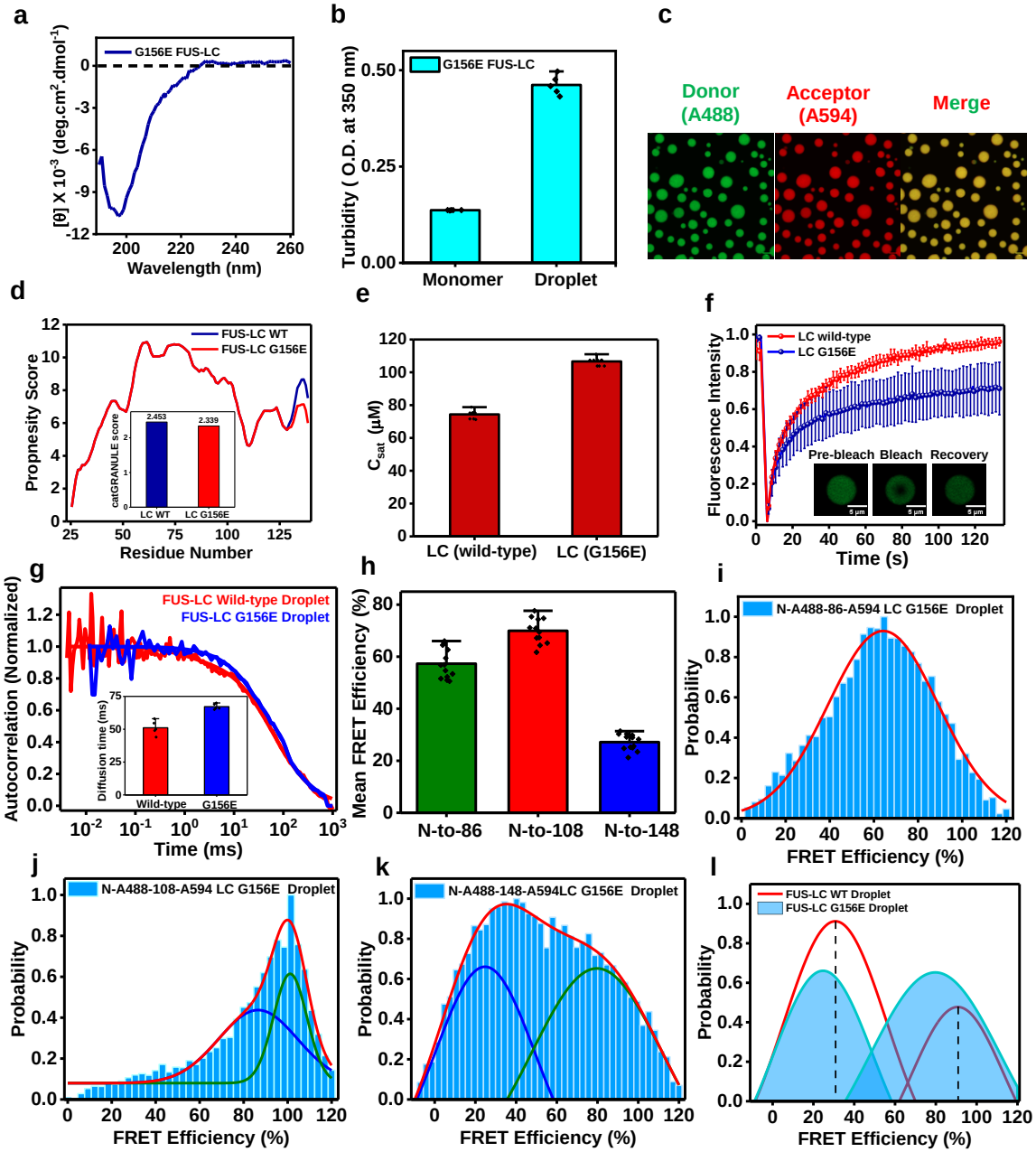

Figure 2.7. a. The circular dichroism spectrum of G156E FUS-LC shows similar structural features to wild-type FUS-LC. CD measurements were performed for 10 µM G156E FUS-LC in 20 mM phosphate, pH 7.4. b. The solution turbidity plot of G156E FUS-LC (200 µM protein in 20 mM phosphate, pH 7.4) indicates phase separation in the presence of 250 mM salt. Data represent mean ± SD (n = 5 independent samples). c. Airyscan confocal imaging showing G156E FUS-LC droplets recruit wild-type dual-labeled FUS-LC. d. Comparison of phase separation propensity plots of wild-type and mutant G156E FUS-LC using bioinformatics tool catGranule shows a slightly lower propensity of G156E FUS-LC. Inset shows a comparison of

catGranule score for wild-type and G156E FUS-LC. e. Saturation concentrations (C_{sat}) of wild-type and G156E FUS-LC were estimated using centrifugation. Data represent mean ± SD (n = 9 independent reactions). f. FRAP kinetics of AlexaFluor488-labeled FUS-LC within wild-type and G156E mutant droplets. Data represent mean ± SD (n = 8 droplets). g. Normalized FCS autocorrelation plots with mean diffusion times (Inset) for wild-type and G156E droplets. Data represent mean ± SD (n = 5 droplets). h. Mean FRET efficiency obtained from acceptor photobleaching of G156E FUS-LC droplets. Data represent mean ± SD (n = 13 droplets). Single-droplet single-molecule FRET histograms in G156E FUS-LC droplets using dual-labeled (i) N-to-86, (j) N-to-108, and (k) N-to-148 constructs. The total number of events was > 20,000 and the number of events at maxima was 1019 (i), 1725 (j), and 698 (k). l. Overlay of fitted subpopulations for wild-type and G156E FUS-LC droplets (shaded) for the N-to-148 construct showing a shift towards a lower FRET efficiency within G156E FUS-LC droplets.

However, this mutation accelerates aggregation of full-length FUS and can potentially change the physical properties of condensates. To further characterize these G156E FUS-LC droplets, we performed FRAP measurements which showed a slower and lower fluorescence recovery compared to wild-type FUS-LC (Figure 2.7f). In order to get insights into the polypeptide chain diffusion within individual droplets, we performed single-droplet FCS measurements which indicated a slightly slower translational diffusion (~ 70 ms) in comparison to wild-type FUS-LC droplets (~ 50 ms) (Figure 2.7g,). These results suggested that the G156E mutation alters the phase behavior and the condensed phase exhibits more restrained diffusion.

Next, in order to gain structural insights into the wild-type FUS-LC chain within G156E FUS-LC condensates, we performed ensemble single-droplet FRET using acceptor photobleaching in the confocal fluorescence microscopy format. Ensemble single-droplet FRET indicated the retention of long-range contacts between the N-terminal and residue location 108 similar to the wild-type FUS-LC droplets (Figure 2.7h). To obtain insights into the structural subpopulations and conformational dynamics, we then performed single-droplet single-molecule FRET measurements (Figure 2.7i-k). The wild-type FRET-pair-labeled LC acts as a reporter of the environment, the extent of interactions, and conformational distributions of the densely packed surrounding polypeptide chains within condensates of mutant FUS-LC (G156E). FRET efficiency histograms for the N-to-86 and N-to-108 constructs within G156E droplets were similar to those observed for wild-type FUS-LC droplets. Interestingly, the FRET efficiency histogram for the N-to-148 construct exhibited a slight shift towards lower FRET efficiency compared to the wild-type FUS-LC droplets (Figure 2.7l, Table 3). This reduction in FRET efficiency of both populations indicated more expansion of the C-

terminal segment of the chain that facilitates the formation of a network of intermolecular contacts within the G156E FUS-LC condensates. Such a conformational unwinding in the mutant, presumably due to the presence of an additional negative charge, can offer a larger number of multivalent interactions leading to a more densely packed interior of the condensate and more dampened translational and rotational dynamics. This observation is consistent with a slower internal diffusion corroborating our FRAP and FCS results. Taken together, our results revealed an unraveling of the polypeptide chain within condensates of the G156E mutant promoting increased interchain interactions and a dense network which can further facilitate pathological aggregation of the mutant FUS-LC as previously observed[34,62,63]. Next, we wanted to distinguish the secondary structural features that govern the condensate properties of wild-type and mutant FUS-LC.

2.3.7 Single-droplet vibrational Raman spectroscopy supports the altered phase behavior of the disease-associated mutant

In order to probe the secondary structural features of FUS-LC, we performed single-droplet vibrational Raman spectroscopy that allowed us to obtain insights into polypeptide structure and organization within individual droplets[64,65]. Focusing a laser beam into a droplet permits us to obtain a Raman spectrum that contains the characteristic vibrational signatures corresponding to the polypeptide backbone (amide I and amide III) and side chains (aromatic and aliphatic residues). These vibrational signatures provide us with vital information on the secondary structural distributions and intermolecular interactions within a single condensate (Figure 2.8a). Amide I vibrational band (1630-1700 cm^{-1}) originates primarily due to the C=O stretching vibrations of the polypeptide backbone, while the amide III band (1230-1320 cm^{-1}) involves a combination of C-N stretch and N-H bending motions of the backbone. Together these amide bands constitute the secondary structural marker bands highlighting the secondary structural elements present in the proteins[25,64-67]. We observed a broad amide I band for wild-type FUS-LC droplets indicating the presence of disordered conformations and considerable conformational heterogeneity in the condensed phase (Figure 2.8b) corroborating our single-molecule FRET results. Deconvolution of the baseline-corrected amide I indicated the presence of two major peaks representing extended/unordered (~ 1692 cm^{-1}) and some ordered structural elements in the protein-rich dense phase. The peak at ~ 1671 cm^{-1} corresponds to ordered structural elements that might contain β-sheet with some minor α-helical contents (~ 1652 cm^{-1}) and can represent the signature of compact S-shaped/paperclip-like states as observed in our

FRET experiments (Figure 2.8c). On the contrary, the deconvolution analysis of the amide peak for G156E FUS-LC droplets revealed a largely unstructured state (~ 1666 cm^{-1} and ~ 1692 cm^{-1}) within droplets corroborating our FRET data (Figure 2.8d).

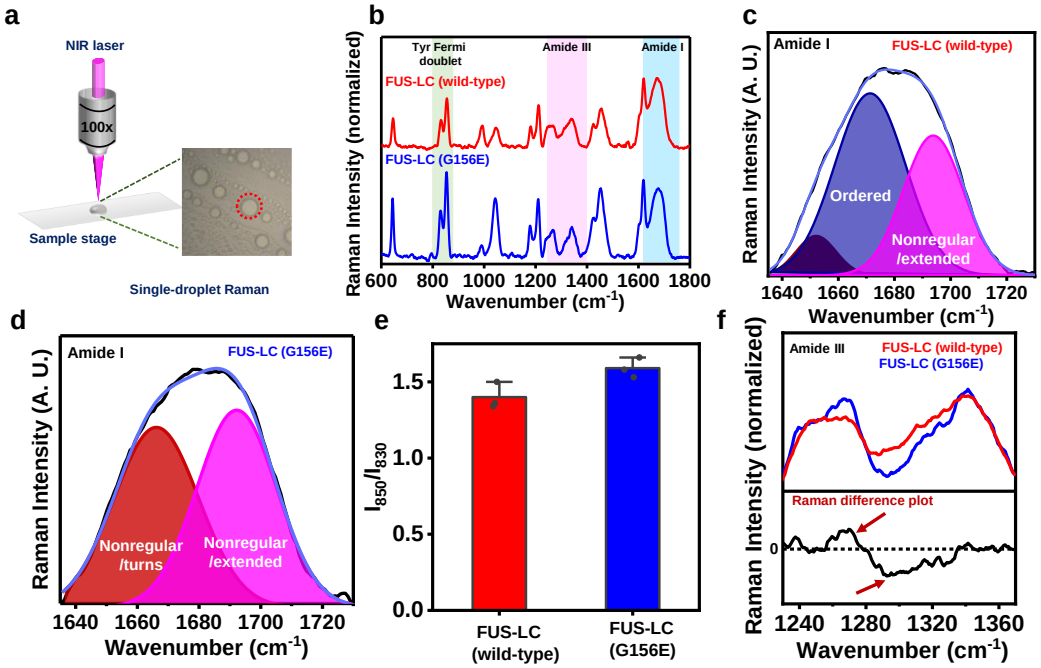

Figure 2.8. a. A schematic for our single-droplet Raman measurements by focusing a near-infrared (NIR) laser into a single droplet of FUS-LC. b. Mean Raman spectra for wild-type and G156E FUS-LC droplets. (n = 3 droplets.) Raman spectra are normalized with respect to the amide I band at ~ 1673 cm^{-1}. c, d. Gaussian deconvolution of separately baseline-corrected amide I of wild-type FUS-LC (c) and G156E FUS-LC (d) to estimate the percentage composition of various secondary structural elements. The black and blue solid lines represent the actual data and the cumulative fit, respectively. The colored solid lines represent the Gaussian peaks obtained after deconvolution. e. The ratio of the tyrosine Fermi doublet (I_{850}/I_{830}) estimated from the peak intensities. Data represent mean ± SD (n = 3 droplets). f. The Raman difference plot of the amide III bands of FUS-LC and G156E FUS-LC droplets (arrow indicates the difference of interest). See Table 5 for the peak assignment.

Nevertheless, a small increase in the full width at half maximum (FWHM) of the amide I band from wild-type (49.6 ± 0.6 cm^{-1}) to mutant droplets (51.4 ± 0.6 cm^{-1}) could further support more conformational heterogeneity in the case of the G156E mutant. More structural unzipping and heterogeneity in the case of the mutant allows a much denser network of interaction as observed in our single-molecule FRET, FCS, and anisotropy measurements. This is also

supported by the Raman intensity ratio of the tyrosine Fermi doublet (I_{850}/I_{830}), which indicates the hydrogen bonding propensity of the phenolic hydroxyl group of tyrosine with surrounding water molecules or in other words, determines the average solvent accessibility of tyrosine residues.

Table 5. Raman shift values and tentative band assignments of single-droplets of LC WT and LC G156E based on the previous studies.

LC WT (cm^{-1})	**LC G156E (cm^{-1})**	**Peak Assignment***
645	644	Tyr [γ(C-C)]
831	829	Tyr Fermi Doublet
855	853	Tyr Fermi Doublet
992	990	Dibasic Phosphate (buffer)
1046	1042	Proline CH_2 wagging
1180	1178	Tyr, ν(C-N)
1212	1210	Tyr [ν(C-C)]
1255	1256	Amide III
1338	1341	δ(CαH)
1424	1424	ν(C-H)
1455	1453	δ(CH_2/CH_3)
1620	1619	Tyr (R stretch)
1671	1676	Amide I

*δ, bending; ν, stretching; γ, twisting.

This ratio exhibited a small but measurable change from ~ 1.4 for wild-type droplets to ~ 1.6 for mutant droplets suggesting a slightly higher solvent exposure of tyrosine residues within

G156E FUS-LC droplets resulting from relatively expanded conformers facilitating a larger extent of intermolecular π-π contacts between more expanded chains within G156E FUS-LC droplets (Figure 2.8e). We further zoomed into the amide III region for wild-type and G156E droplets and constructed a Raman difference plot for the comparison. A positive band centered at ~ 1270 cm^{-1} (nonregular/turns) and a negative band at ~ 1300 cm^{-1} highlighted a higher content of disordered conformations within mutant droplets as compared to wild-type droplets (Figure 2.8f). Our single-droplet vibrational Raman studies capture the key structural differences between wild-type and mutant FUS-LC droplets and are in agreement our single-molecule FRET, FCS, FRAP, and anisotropy results. Taken together, the disease-associated mutant (G156E) of FUS-LC exhibits higher disorder facilitating more intermolecular association with altered material properties that can potentially promote aberrant phase transitions into solid-like pathological aggregates compared to the wild-type form.

2.4 Discussion

In this work, we showed that the polypeptide chain of FUS-LC undergoes conformational shapeshifting from the monomeric dispersed phase to the condensed phase. We summarized all our observations in a schematic illustration in Figure 2.9. By employing single-molecule FRET, we characterized the conformational distribution and dynamics of FUS-LC, site-specifically and orthogonally labeled with donor and acceptor fluorophores. Such single-molecule studies carried out at ultralow concentrations (~ 100 pM) allow us to unambiguously interrogate and characterize the monomeric form of the protein in a molecule-by-molecule manner that is not generally achievable by most other conventional structural tools. Our single-molecule FRET studies for freely diffusing molecules revealed that intrinsically disordered FUS-LC monomer exists as a heterogeneous ensemble of structures comprising chiefly two distinct, well-resolved, structural subpopulations. These subpopulations include compact S-shaped/paperclip-like conformers and partially extended tadpole-like conformers exchanging on a much slower timescale (>> 1 ms) than the observation time. Such slower conformational exchanges between extended and compact states can further be studied using surface-immobilized single-molecule FRET. The compaction of the disordered FUS-LC chain we observed in this study can be ascribed to the presence of extensive intramolecular interactions arising due to π–π stacking interactions between multiple tyrosine residues and hydrogen

bonding interactions between glutamine side chains, which have previously been shown to drive phase separation of FUS-LC[25].

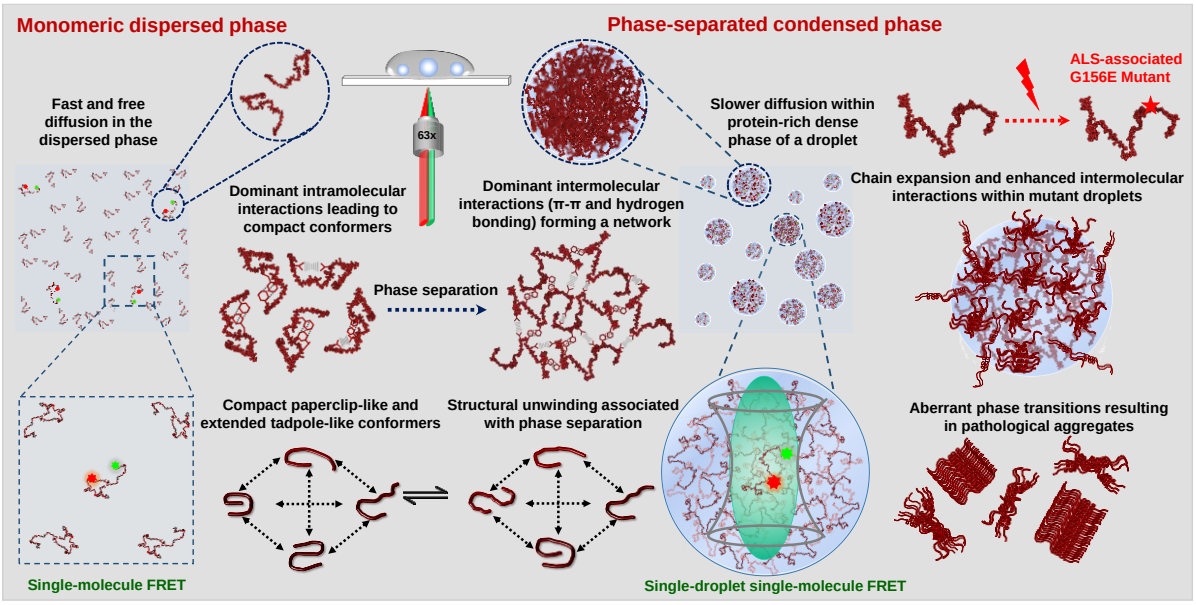

Figure 2.9. A summary of our single-molecule FRET, FCS, fluorescence anisotropy, Raman spectroscopy experiments, and the impact of a pathological mutation in the phase behavior of FUS-LC.

We propose that a large number of proline and glycine residues promote partial expansion, especially at the C-terminal part of the polypeptide chain. Such making and breaking of intramolecular noncovalent contacts give rise to rapidly fluctuating, intrinsically disordered, heterogeneous conformational ensemble in the monomeric form of FUS-LC. This conformational equilibrium in the infinitesimally dilute condition changes quite dramatically when the protein concentration is raised beyond a threshold concentration also known as the saturation concentration. Above this concentration, intermolecular chain-chain interactions become more dominant than intramolecular contacts, and thus, unzipping of compact conformers becomes facile due to the more favorable intermolecular multivalent interactions driving liquid phase condensation. In the case of full-length FUS, electrostatic and cation-π interactions between the arginine-rich C-terminal and tyrosine-rich N-terminal domains function as the major drivers of FUS phase separation[68]. On the contrary, extensive computational and mutagenesis studies on the N-terminal domain of FUS revealed the role of multiple glutamine and tyrosine residues in the formation of hydrogen bonding, hydrophobic,

and π-sp^2 contacts within FUS-LC condensates[25]. The slow conformational exchange between the conformers allows more interaction lifetime yielding a network of intermolecular interactions in the condensed phase. Such dynamically controlled conformational gymnastics can play a pivotal role in driving protein phase transitions. Additionally, previous studies have identified persistent secondary cross-β core structures within gel-like states of FUS-LC,[36] which appear to be absent in liquid droplets. Our observation is consistent with the previous computational and structural studies on FUS-LC highlighting the presence of a compact state in the monomeric form and the role of conformational disorder in phase separation [25,31,35,55].

Indeed, our single-droplet single-molecule FRET studies revealed a symphony of conformational shapeshifting events within the dense phase of individual condensates as depicted in Figure 2.9. Some of these unique molecular features involving distinct subpopulations generally remain skewed in traditional bulk experiments and can only be directly observed using a single-molecule tool. Single-molecule FRET coupled with FCS and picosecond time-resolved fluorescence anisotropy measurements allowed us to directly decipher the conformational distribution and dynamics within the dense phase. The solvent quality within this protein-rich dense phase is likely to be better than that in the monomeric form of the protein dispersed in water which is a poor solvent for a polypeptide chain. A better solvent quality, and hence a higher Flory scaling exponent, in the dense phase is expected to favor the conformational expansion. Such expanded conformers can also turn intramolecular contacts into transient intermolecular contacts favoring the condensed phase. The presence of a subpopulation of compact states suggests that the conformational interconversion is possibly associated with the making and breaking of multivalent interactions giving rise to liquid-like behavior within droplets. An interesting hypothesis can be posited based on the radial gradient of the physicochemical properties with a complex interplay of intra-chain, inter-chain, and chain-solvent interactions in the condensed phase[69]. These droplets could possess a radial distribution of conformational subpopulations based on the spatial locations within the condensate. Previous simulation studies on intrinsically disordered prion-like low-complexity domains have indicated such conformational heterogeneity within the dense phase[69,70]. Recent studies revealed that a small-world percolated network comprising a varied density of physical crosslinks can give rise to distinct conformational states and molecular orientations varying spatial location from the center to the interface of the condensates[69]. Similar studies on the full-length FUS showed pathological aggregation via phase separation by onset at the condensate interface and investigated the material properties and multiphasic nature of condensates from

the core to the interface[71,72]. The spatial resolution of the confocal microscopy-based format used in our single-molecule experiments is inadequate for dissecting the radial distribution of conformers. The FRET efficiency distribution displayed by our observed single-molecule FRET histograms could potentially comprise such conformational distributions across the droplet locations. We would also like to point out that although we observed much broader peaks in the FRET efficiency histograms in droplets, we are unable to comment on the exact distances and the width of individual peaks since there can be some contributions from the shot noise due to low photon counts and the dye orientation factor that can potentially contribute to the widths of the distribution. Our single-droplet FCS and fluorescence anisotropy results revealed that both translational diffusion and rotational chain reorientation dynamics are considerably slowed down within condensates. These findings hinted at the formation of a network of physical crosslinks giving rise to viscoelastic network fluid. Our results on a disease-associated mutant (G156E) indicated a more conformational plasticity promoting a denser network of intermolecular contacts as observed by single-molecule FRET, FRAP, FCS, and anisotropy measurements. Additionally, single-droplet vibrational Raman spectroscopy corroborated our results on altered conformational distribution for the mutant. Raman signatures for both backbone and sidechain markers indicated slightly more extended conformers and greater participation in chain-chain association within condensates. Such interactions can potentially promote aberrant liquid-to-solid phase transitions and accelerated aggregation associated with the pathological hallmark of the G156E mutant of FUS (Figure 2.9).

In summary, our single-molecule experiments directly unveiled an intriguing interplay of conformational heterogeneity, structural distribution, and dynamics that crucially governs the course of phase transitions of prion-like low-complexity domains. Such low-complexity domains are present in FUS and other FET-family proteins and are essential in mediating the homotypic and heterotypic interactions driving the assembly into liquid-like functional condensates and solid-like pathological aggregates[71-73]. Post-translational modifications and mutations can alter the interplay between intra- and intermolecular interactions shifting the conformational equilibria both in the dispersed and condensed phases. Such altered interactions can give rise to changes in the viscoelastic material properties of biomolecular condensates, promoting aberrant phase transitions associated with ALS and FTD. Single-molecule FRET in combination with mutagenesis can offer a potent approach to discern the impact of disease-associated mutations and post-translational modifications on the conformational preference

and phase behavior of IDPs/IDRs. Our findings on the role of conformational excursion in phase separation can have much broader implications for a wide range of phase-separating proteins involved in physiology and disease. For instance, tau, an intrinsically disordered neuronal protein associated with Alzheimer's disease, exhibits conformational subpopulations comprising compact paperclip/S-shaped and expanded states[43,50,74,75]. Phase separation of tau studied at the single-molecule resolution also revealed an increased conformational heterogeneity. We suggest that the sequence-encoded structural unwinding coupled with a dynamic control can expose the multivalency of polypeptide chains that promote ephemeral interactions resulting in biomolecular condensate formation. Deriving general principles from single-molecule studies on a wide range of phase-separating proteins and artificial polypeptides can provide the key mechanistic underpinning of macromolecular phase separation and pave the way for novel synthetic biology applications. Additionally, the development of multi-color, multi-parameter, super-resolved, single-droplet single-molecule FRET can offer unprecedented spatiotemporal resolution in studying intracellular heterotypic, multicomponent, and multiphasic biomolecular condensates and for exploring unchartered territories of biological phase transitions.

2.5 References

1. Kilgore, H. R. & Young, R. A. Learning the chemical grammar of biomolecular condensates. *Nat. Chem. Biol*. **18,** 1298–1306 (2022).

2. Alberti, S. & Hyman, A. A. Biomolecular condensates at the nexus of cellular stress, protein aggregation disease and ageing. *Nat. Rev. Mol. Cell Biol.* **22,** 196–213 (2021).

3. Lyon, A. S., Peeples, W. B., & Rosen, M. K. A framework for understanding the functions of biomolecular condensates across scales. *Nat. Rev. Mol. Cell Biol.* **22,** 215–235 (2021).

4. Mittag, T. & Pappu, R. V. A conceptual framework for understanding phase separation and addressing open questions and challenges. *Mol. Cell* **82,** 2201–2214 (2022).

5. Boeynaems, S., Alberti, S., Fawzi, N. L., Mittag, T., Polymenidou, M., Rousseau, F., Schymkowitz, J., Shorter, J., Wolozin, B., Van Den Bosch, L., Tompa, P., & Fuxreiter, M. Protein Phase Separation: A New Phase in Cell Biology. *Trends Cell Biol*. **28,** 420-435 (2018).

6. Roden, C., & Gladfelter, A. S. RNA contributions to the form and function of biomolecular condensates. *Nat. Rev. Mol. Cell Biol.* **22**, 183–195 (2021).

7. Choi, J. M., Holehouse, A. S., & Pappu, R. V. Physical principles underlying the complex biology of intracellular phase transitions. *Annu. Rev. Biophys.* **49**, 107–133 (2020).

8. Dignon, G. L., Best, R. B., & Mittal, J. Biomolecular phase separation: From molecular driving forces to macroscopic properties. *Annu. Rev. Phys. Chem.* **71**, 53–75 (2020).

9. Yu, M., Heidari, M., Mikhaleva, S., Tan, P. S., Mingu, S., Ruan, H., Reinkemeier, C. D., Obarska-Kosinska, A, Siggel, M., Beck, M., Hummer, G., & Lemke, E. A. Visualizing the disordered nuclear transport machinery in situ. *Nature* **617,** 162-169 (2023).

10. Shapiro, D. M., Ney, M., Eghtesadi, S. A., & Chilkoti, A. Protein phase separation arising from intrinsic disorder: First-principles to bespoke applications. *J. Phys. Chem. B* **125,** 6740–6759 (2021).

11. Mitrea, D. M., Cika, J. A., Guy, C. S., Ban, D., Banerjee, P. R., Stanley, C. B., Nourse, A., Deniz, A. A., & Kriwacki, R. W. Nucleophosmin integrates within the nucleolus via multi-modal interactions with proteins displaying R-rich linear motifs and rRNA. *eLife* **5**, (2016).

12. Shin, Y. & Brangwynne, C. P. Liquid phase condensation in cell physiology and disease. *Science* **357**, (2017).

13. Mitrea, D. M., & Kriwacki, R. W. Phase separation in biology; functional organization of a higher order. *Cell Commun. Signal.* **14,** (2016).

14. Martin, E. W., Holehouse, A. S., Peran, I., Farag, M., Incicco, J. J., Bremer, A., Grace, C. R., Soranno, A., Pappu, R. V., & Mittag, T. Valence and patterning of aromatic residues determine the phase behavior of prion-like domains. *Science* **367**, 694-699 (2020).

15. Mukhopadhyay, S. The dynamism of intrinsically disordered proteins: Binding induced folding, amyloid formation, and phase separation. *J. Phys. Chem. B* **124**, 11541–11560 (2020).

16. Martin, E. W. & Mittag, T. Relationship of sequence and phase separation in protein low-complexity regions. *Biochemistry* **57,** 2478–2487 (2018).

17. Brangwynne, C. P., Tompa, P., & Pappu, R. V. Polymer physics of intracellular phase transitions. *Nat. Phys.* **11**, 899–904 (2015).

18. Vernon, R. M., Chong, P. A., Tsang, B., Kim, T. H., Bah, A., Farber, P., Lin, H., & Forman-Kay, J. D. Pi-Pi contacts are an overlooked protein feature relevant to phase separation. *eLife* **9**, (2018).

19. Ruff, K. M., Choi, Y. H., Cox, D., Ormsby, A. R., Myung, Y., Ascher, D. B., Radford, S. E., Pappu, R. V., & Hatters, D. M. Sequence grammar underlying the unfolding and phase separation of globular proteins. *Mol. Cell.* **82**, 3193-3208 (2022).

20. Uversky, V. N. Intrinsically disordered proteins in overcrowded milieu: Membrane-less organelles, phase separation, and intrinsic disorder. *Curr. Opin. Struct. Biol.* **44,** 18–30 (2017).

21. Kaur, T., Raju, M., Alshareedah, I., Davis, R.B., Potoyan, D.A., & Banerjee, P. R. Sequence-encoded and composition-dependent protein-RNA interactions control multiphasic condensate morphologies. *Nat. Commun.* **12,** (2021).

22. Bhopatkar, A. A., Dhakal, S., Abernathy, H. G., Morgan, S. E., & Rangachari, V. Charge and redox states modulate granulin-TDP-43 coacervation toward phase separation or aggregation. *Biophys. J.* **121,** 2107-2126 (2022).

23. Vendruscolo, M., & Fuxreiter, M. Protein condensation diseases: therapeutic opportunities. *Nat. Commun.* **13,** (2022).

24. Svetoni, F., Frisone, P. & Paronetto, M. P. Role of FET proteins in neurodegenerative disorders. *RNA Biol.* **13,** 1089–1102 (2016).

25. Murthy, A. C., Dignon, G. L., Kan, Y., Zerze, G. H., Parekh, S. H., Mittal, J., & Fawzi, N. L. (2019). Molecular interactions underlying liquid-liquid phase separation of the FUS low-complexity domain. *Nat. Struct. Mol. Biol.* **26,** 637–648 (2019).

26. Loughlin, F. E., Lukavsky, P. J., Kazeeva, T., Reber, S., Hock, E. M., Colombo, M., Von Schroetter, C., Pauli, P., Cléry, A., Mühlemann, O., Polymenidou, M., Ruepp, M. D., & Allain, F. H. The Solution Structure of FUS Bound to RNA Reveals a Bipartite Mode of RNA Recognition with Both Sequence and Shape Specificity. *Mol. Cell* **73,** 490–504 (2019).

27. Hofweber, M., Hutten, S., Bourgeois, B., Spreitzer, E., Niedner-Boblenz, A., Schifferer, M., Ruepp, M. D., Simons, M., Niessing, D., Madl, T., & Dormann, D. Phase Separation of FUS Is Suppressed by Its Nuclear Import Receptor and Arginine Methylation. *Cell* **173,** 706-719 (2018).

28. Qamar, S., Wang, G., Randle, S. J., Ruggeri, F. S., Varela, J. A., Lin, J. Q., Phillips, E. C., Miyashita, A., Williams, D., Ströhl, F., Meadows, W., Ferry, R., Dardov, V. J., Tartaglia, G. G., Farrer, L. A., Kaminski Schierle, G. S., Kaminski, C. F., Holt, C. E., Fraser, P. E., Schmitt-Ulms, G., Klenerman, D., Knowles, T., Vendruscolo, M., & St George-Hyslop, P. FUS Phase Separation Is Modulated by a Molecular Chaperone and Methylation of Arginine Cation-π Interactions. *Cell* **173,** 720–734 (2018).

29. Murray, D. T., Kato, M., Lin, Y., Thurber, K.R., Hung, I., McKnight, S. L., & Tycko, R. Structure of FUS Protein Fibrils and Its Relevance to Self-Assembly and Phase Separation of Low-Complexity Domains. *Cell.* **171,** 615-627 (2017).

30. Burke, K. A., Janke, A. M., Rhine, C. L., & Fawzi, N. L. Residue-by-Residue View of In Vitro FUS Granules that Bind the C-Terminal Domain of RNA Polymerase II. *Mol. Cell* **15,** 231-41(2015).

31. Murthy, A. C., Tang, W. S., Jovic, N., Janke, A. M., Seo, D. H., Perdikari, T. M., Mittal, J., & Fawzi, N. L. Molecular interactions contributing to FUS SYGQ LC-RGG phase separation and co-partitioning with RNA polymerase II heptads. *Nat. Struct. Mol. Biol.* **28,** 923-935 (2021).

32. Monahan, Z., Ryan, V. H., Janke, A. M., Burke, K. A., Rhoads, S. N., Zerze, G. H., O'Meally, R., Dignon, G. L., Conicella, A. E., Zheng, W., Best, R. B., Cole, R. N., Mittal, J., Shewmaker, F., & Fawzi, N. L. Phosphorylation of the FUS low-complexity domain disrupts phase separation, aggregation, and toxicity. *EMBO J.* **36,** 2951-2967 (2017).

33. Lee, M., Ghosh, U., Thurber, K. R., Kato, M., & Tycko, R. Molecular structure and interactions within amyloid-like fibrils formed by a low-complexity protein sequence from FUS. *Nat. Commun.* **11,** (2020).

34. Berkeley, R. F., Kashefi, M., & Debelouchina, G. T. Real-time observation of structure and dynamics during the liquid-to-solid transition of FUS LC. *Biophys. J.* **120,** 1276-1287 (2021).

35. Emmanouilidis, L., Esteban-Hofer, L., Damberger, F. F., de Vries, T., Nguyen, C. K. X., Ibáñez, L. F., Mergenthal, S., Klotzsch, E., Yulikov, M., Jeschke, G., & Allain, F. H. NMR and EPR reveal a compaction of the RNA-binding protein FUS upon droplet formation. *Nat. Chem. Biol.* **17,** 608-614 (2021).

36. Kato, M., & McKnight, S. L. The low-complexity domain of the FUS RNA binding protein self-assembles via the mutually exclusive use of two distinct cross-β cores. *Proc. Natl. Acad. Sci. USA* **19,** (2021).

37. Maltseva, D., Chatterjee, S., Yu, C., Brzezinski, M., Nagata, Y., Gonella, G., Murthy, A. C. Stachowiak, J. C., Fawzi, N. L., Parekh, S. H., & Bonn, M. Fibril formation and ordering of disordered FUS LC driven by hydrophobic interactions. *Nat. Chem.* (2023).

38. Schuler, B., & Hofmann, H. Single-molecule spectroscopy of protein folding dynamics--expanding scope and timescales. *Curr. Opin. Struct. Biol.* **23,** 36-47 (2013).

39. Agam, G., Gebhardt, C., Popara, M., Mächtel, R., Folz, J., Ambrose, B., Chamachi, N., Chung, S. Y., Craggs, T. D., de Boer, M., Grohmann, D., Ha, T., Hartmann, A., Hendrix, J., Hirschfeld, V., Hübner, C. G., Hugel, T., Kammerer, D., Kang, H. S., Kapanidis, A. N., Krainer, G., Kramm, K., Lemke, E. A., Lerner, E., Margeat, E., Martens, K., Michaelis, J., Mitra, J., Moya Muñoz, G. G., Quast, R. B., Robb, N. C., Sattler, M., Schlierf, M., Schneider, J., Schröder, T., Sefer, A., Tan, P. S., Thurn, J., Tinnefeld, P., van Noort, J., Weiss, S., Wendler, N., Zijlstra, N., Barth, A., Seidel, C. A. M., Lamb, D. C., & Cordes, T. Reliability and accuracy of single-molecule FRET studies for characterization of structural dynamics and distances in proteins. *Nat. Methods.* **20,** 523-535 (2023).

40. Brucale, M., Schuler, B., & Samorì, B. Single-molecule studies of intrinsically disordered proteins. *Chem. Rev.* **26,** 3281-317 (2014).

41. Nasir, I., Bentley, E. P., & Deniz, A. A. Ratiometric Single-Molecule FRET Measurements to Probe Conformational Subpopulations of Intrinsically Disordered Proteins. *Curr. Protoc. Chem. Biol.* **12,** (2020).

42. Feng, X. A., Poyton, M. F., & Ha, T. Multicolor single-molecule FRET for DNA and RNA processes. *Curr. Opin. Struct. Biol.* **70,** 26-33 (2021).

43. Elbaum-Garfinkle, S., & Rhoades, E. Identification of an aggregation-prone structure of tau. *J. Am. Chem. Soc.* **10,** 16607-13 (2012).

44. Galvanetto, N., Ivanović, M. T., Chowdhury, A., Sottini, A., Nüesch, M. F., Nettels, D., Best, R. B., & Schuler, B. Extreme dynamics in a biomolecular condensate. *Nature*, **619** (7971), 876–883 (2023).

45. Holehouse, A. S., Das, R. K., Ahad, J. N., Richardson, M. O., & Pappu, R. V. CIDER: Resources to Analyze Sequence-Ensemble Relationships of Intrinsically Disordered Proteins. *Biophys. J.* **10,** 16-21 (2017).

46. Xue, B., Dunbrack, R. L., Williams, R. W., Dunker, A. K., & Uversky, V. N. PONDR-FIT: A meta-predictor of intrinsically disordered amino acids. *Biochim. Biophys. Acta* **1804,** 996–1010 (2010).

47. Bolognesi, B., Lorenzo Gotor, N., Dhar, R., Cirillo, D., Baldrighi, M., Tartaglia, G. G., & Lehner, B. A Concentration-Dependent Liquid Phase Separation Can Cause Toxicity upon Increased Protein Expression. *Cell Rep.* **16,** 222–231(2016).

48. Schuler, B., Lipman, E. A., & Eaton, W. A. Probing the free-energy surface for protein folding with single-molecule fluorescence spectroscopy. *Nature* **419**, 743-7 (2002).

49. Kudryavtsev, V., Sikor, M., Kalinin, S., Mokranjac, D., Seidel, C. A., & Lamb, D. C. Combining MFD and PIE for accurate single-pair Förster resonance energy transfer measurements. *ChemPhysChem* **13**, 1060-78 (2012).

50. Melo, A. M., Coraor, J., Alpha-Cobb, G., Elbaum-Garfinkle, S., Nath, A., & Rhoades, E. A. Functional role for intrinsic disorder in the tau-tubulin complex. *Proc. Natl. Acad. Sci. USA* **13,** 14336-14341 (2016).

51. Mukhopadhyay, S., Krishnan, R., Lemke, E. A., Lindquist, S., Deniz, A. A. A natively unfolded yeast prion monomer adopts an ensemble of collapsed and rapidly fluctuating structures. *Proc. Natl. Acad. Sci. USA* **104**, 2649-2654 (2007).

52. Zhao, H., Brown, P. H., & Schuck, P. On the distribution of protein refractive index increments. *Biophys. J.* **100**, 2309–2317 (2011).

53. Uversky, V. N., Gillespie, J. R., & Fink, A. L. Why are "natively unfolded" proteins unstructured under physiologic conditions? *Proteins* **15,** 415-27 (2000).

54. Newcombe, E. A., Ruff, K. M., Sethi, A., Ormsby, A. R., Ramdzan, Y. M., Fox, A., Purcell, A. W., Gooley, P. R., Pappu, R. V., & Hatters, D. M. Tadpole-like Conformations of Huntingtin Exon 1 Are Characterized by Conformational Heterogeneity that Persists regardless of Polyglutamine Length. *J. Mol. Biol.* **11,** 1442-1458 (2018).

55. Perdikari, T. M., Jovic, N., Dignon, G. L., Kim, Y. C., Fawzi, N. L., & Mittal, J. A predictive coarse-grained model for position-specific effects of post-translational modifications. *Biophys. J.* **6**, 1187-1197 (2021).

56. Müller, B. K., Zaychikov, E., Bräuchle, C., & Lamb, D. C. Pulsed interleaved excitation. *Biophys. J.* **89,** 3508-22 (2005).

57. Majumdar, A., Mukhopadhyay, S. Fluorescence Depolarization Kinetics to Study the Conformational Preference, Structural Plasticity, Binding, and Assembly of Intrinsically Disordered Proteins. *Methods Enzymol.* **611,** 347-381 (2018).

58. Das, D., Arora, L., & Mukhopadhyay, S. Short-Range Backbone Dihedral Rotations Modulate Internal Friction in Intrinsically Disordered Proteins. *J. Am. Chem. Soc.* **144**, 1739-1747 (2022).

59. Rai, S. K., Khanna, R., Avni, A., & Mukhopadhyay S. Heterotypic electrostatic interactions control complex phase separation of tau and prion into multiphasic condensates and co-aggregates. *Proc. Natl. Acad. Sci. USA* **120,** (2023).

60. Agarwal, A., Arora, L., Rai, S. K., Avni, A., & Mukhopadhyay, S. Spatiotemporal modulations in heterotypic condensates of prion and α-synuclein control phase transitions and amyloid conversion. *Nat. Commun.* **13,** 1154 (2022).

61. Ray, S., Singh, N., Kumar, R., Patel, K., Pandey, S., Datta, D., Mahato, J., Panigrahi, R., Navalkar, A., Mehra, S., Gadhe, L., Chatterjee, D., Sawner, A. S., Maiti, S., Bhatia, S., Gerez, J. A., Chowdhury, A., Kumar, A., Padinhateeri, R., Riek, R., Krishnamoorthy, G., & Maji, S. K. α-Synuclein aggregation nucleates through liquid-liquid phase separation. *Nat. Chem.* **12,** 705-716 (2020).

62. Patel, A., Lee, H. O., Jawerth, L., Maharana, S., Jahnel, M., Hein, M. Y., Stoynov, S., Mahamid, J., Saha, S., Franzmann, T. M., Pozniakovski, A., Poser, I., Maghelli, N., Royer, L. A., Weigert, M., Myers, E. W., Grill, S., Drechsel, D., Hyman, A. A., & Alberti, S. A Liquid-to-Solid Phase Transition of the ALS Protein FUS Accelerated by Disease Mutation. *Cell* **27,** 1066-77 (2015).

63. Rhine, K., Makurath, M. A., Liu, J., Skanchy, S., Lopez, C., Catalan, K. F., Ma, Y., Fare, C. M., Shorter, J., Ha, T., Chemla, Y. R., & Myong, S. ALS/FTLD-Linked Mutations in FUS Glycine Residues Cause Accelerated Gelation and Reduced Interactions with Wild-Type FUS. *Mol. Cell* **19,** 666-681(2020).

64. Agarwal, A., Rai, S. K., Avni, A., & Mukhopadhyay, S. An intrinsically disordered pathological prion variant Y145Stop converts into self-seeding amyloids via liquid-liquid phase separation. *Proc. Natl. Acad. Sci. USA* **9,** (2021).

65. Avni, A., Joshi, A., Walimbe, A., Pattanashetty, S. G., & Mukhopadhyay, S. Single-droplet surface-enhanced Raman scattering decodes the molecular determinants of liquid-liquid phase separation. *Nat. Commun.* **28,** (2022).

66. Rygula, A., Majzner, K., Marzec, K. M., Kaczor, A., Pilarczyk, M., & Baranska, M. Raman spectroscopy of proteins: a review. *J. Raman Spectrosc.* **44,** 1061–1076 (2013).

67. Tuma, R. Raman spectroscopy of proteins: from peptides to large assemblies. *J. Raman Spectrosc.* **36,** 307–319 (2005).

68. Wang, J., Choi, J. M., Holehouse, A. S., Lee, H. O., Zhang, X., Jahnel, M., Maharana, S., Lemaitre, R., Pozniakovsky, A., Drechsel, D., Poser, I., Pappu, R. V., Alberti, S., & Hyman, A. A. A Molecular Grammar Governing the Driving Forces for Phase Separation of Prion-like RNA Binding Proteins. *Cell* **174** (3), 688–699 (2018).

69. Farag, M., Cohen, S. R., Borcherds, W. M., Bremer, A., Mittag, T., & Pappu, R.V. Condensates formed by prion-like low-complexity domains have small-world network structures and interfaces defined by expanded conformations. *Nat. Commun.* **13,** (2022).

70. Zheng, W., Dignon, G. L., Jovic, N., Xu, X., Regy, R. M., Fawzi, N. L., Kim, Y. C., Best, R. B., & Mittal, J. Molecular Details of Protein Condensates Probed by Microsecond Long Atomistic Simulations. *J. Phys. Chem. B.* **24,** 11671-11679 (2020).

71. Chen, Y. S. A., Wang, W., Shen Y., Ruggeri, F. S., Aime, S., Wang, Z., Qamar, S., Espinosa, J. R., Garaizar, A., St George-Hyslop, P., Collepardo-Guevara, R., Weitz, D. A., Vigolo, D., and Knowles, T. P. J. The liquid-to-solid transition of FUS is promoted by the condensate surface. *Proc. Natl. Acad. Sci. USA* 120 (33), e2301366120 (2023).

72. Garaizar, A., Espinosa, J. R., Joseph, J. A., Krainer, G., Shen, Y., Knowles, T. P. J., & Collepardo-Guevara, R. Aging can transform single-component protein condensates into multiphase architectures. *Proc. Natl. Acad. Sci. USA* **119**(26), e2119800119 (2022).

73. Dhakal, S., Robang, A. S., Bhatt, N., Puangmalai, N., Fung, L., Kayed, R., Paravastu, A. K., & Rangachari, V. Distinct neurotoxic TDP-43 fibril polymorphs are generated by heterotypic interactions with α-Synuclein. *J. Biol. Chem.* **298,** (2022).

74. Wen, J., Hong, L., Krainer, G., Yao, Q. Q., Knowles, T. P. J., Wu, S., & Perrett, S. Conformational Expansion of Tau in Condensates Promotes Irreversible Aggregation. *J. Am. Chem. Soc.* **25,** 13056-13064 (2021).

75. Weickert, S., Wawrzyniuk, M., John, L. H., Rüdiger, S. G. D., & Drescher, M. The mechanism of Hsp90-induced oligomerization of Tau. *Sci. Adv.* **6,** (2020).

******

The Hydrogen-Bonded Water Network in Phase-Separated Biomolecular Condensates

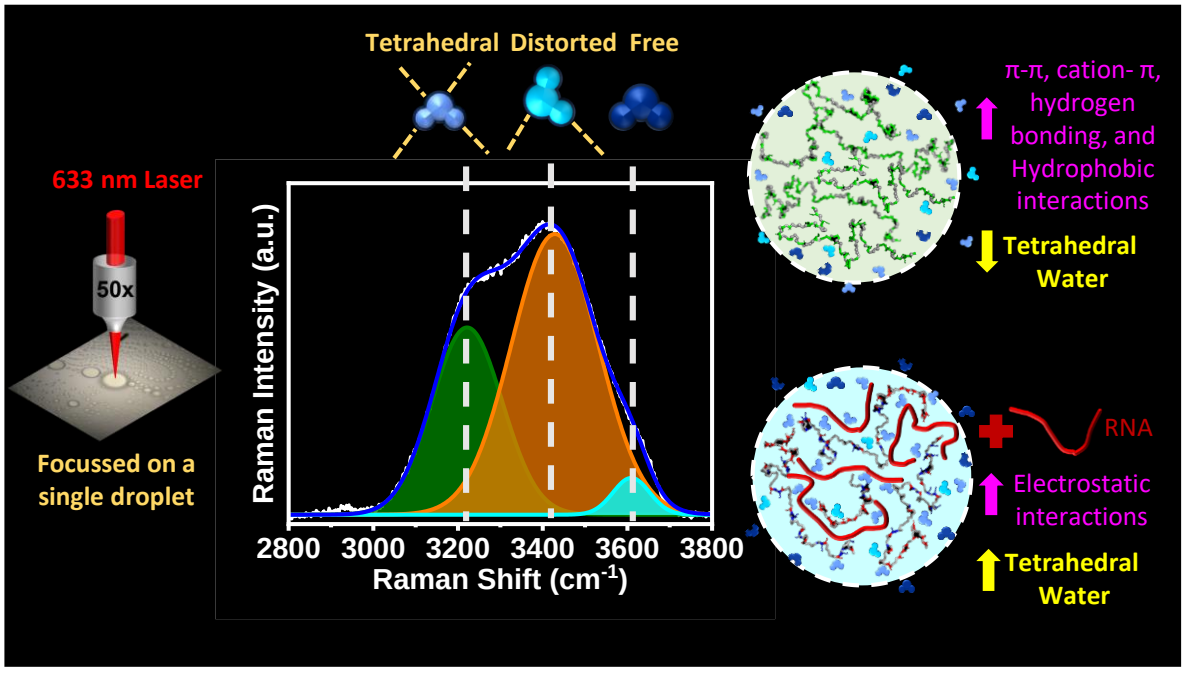

Joshi A, Avni A, Walimbe A, Rai SK, Sarkar S, & Mukhopadhyay S. The hydrogen-bonded water network in phase-separated biomolecular condensates (*manuscript submitted*).

3.1 Introduction

Macromolecular phase separation of biomolecules into biomolecular condensates, also known as membraneless organelles, is being now recognized as the key biophysical principle of spatiotemporal regulation of intracellular biochemistry[1-11]. Intrinsically disordered proteins/regions (IDPs/IDRs) along with nucleic acids are identified as the key candidates in the formation of these highly dynamic, selectively permeable, non-stoichiometric, higher-order mesoscopic assemblies which are involved in a range of vital physiological and pathological mechanisms[2-5,7,10,12-20]. Therefore, discerning the governing principles of these phase transitions has recently garnered significant attention. Recent studies highlight the role of weak, transient, multivalent contacts such as electrostatic, hydrophobic, dipole-dipole, and hydrogen bonding in driving the assembly of biomolecular condensates. The dynamic, liquid-like nature of these condensates is attributed to the dynamic relay of making and breaking of noncovalent interactions between the protein-protein and protein-solvent molecules[13,15,21-25]. Water constitutes a significant proportion (~ 60-70 %) of biomolecular condensates and undergo local readjustments leading to a disruption of the hydrogen-bonded network of water molecules in order to accommodate the crowded environment of the participating protein and nucleic acids[26,27]. Previous theoretical and experimental studies have attempted to investigate the role of this protein-bound hydration water in determining the structure, function, and protein-protein interactions by modulating the protein-solvent interactions[27-34]. This balance between protein-protein and protein-solvent interactions is thought to dictate biomolecular phase transitions. The physicochemical properties of the hydration water layer, also known as biological water, significantly differ from that of the bulk water in solution[35,36]. However, the role of this hydration water in phase transitions has remained elusive in the context of condensate biology.

Previous experimental and computational studies have attempted to probe the changes in the water network accompanying biomolecular phase separation[26,36,37]. Experimental methods have traditionally employed environment-sensitive solvatochromic dyes to explore hydration water in disordered proteins[31]. More recently, ATR-FTIR (Attenuated total reflection-Fourier transform infrared spectroscopy) has been used to study the role of water in the phase separation of Fused in Sarcoma (FUS) in the terahertz range[37]. These studies highlight the thermodynamic forces that drive phase separation and provide evidence of the synergistic effect of water and biomolecules in phase separation. While these techniques have

probed the water structure in phase separation, such measurements can only provide an average information of water molecules present in both the dense and light phases and require close contact between the sample and the ATR crystal, providing information from the sample in proximity to the internal reflective element. On the contrary, vibrational Raman spectroscopy is a label-free and non-destructive technique to study biological systems and has been extensively used to study the conformation as well as the concentration of biomolecules within the condensed phase using the water Raman band as an intensity standard[38,39]. Since the concentration of water within the condensed phase is extremely high, Raman spectroscopy can readily detect the O-H molecular vibrations representing the various hydrogen bonding modes in water clusters[40].

In this work, we have utilized vibrational Raman spectroscopy to directly observe the changes in hydration water upon phase separation mediated by various interactions comprising a complex interplay of enthalpic and entropic contributions. Such single-droplet Raman measurements allow us to distinguish between the hydrogen-bonding network in both the condensed phase and the dilute phase and permit us to discern the influence of additives on biological phase separation. To delineate the nature of water inside the condensates formed by different intermolecular interactions such as hydrogen bonding, electrostatic, hydrophobic, and aromatic interactions, we chose three model phase-separating protein systems. These proteins are the low-complexity domain of Fused in Sarcoma (FUS-LC), full-length FUS, and tau. Phase separation of FUS-LC is primarily driven by aromatic π-π, hydrogen bonding, and hydrophobic interactions, whereas tau undergoes phase separation via electrostatic interactions. On the contrary, phase separation of full-length FUS involves a more complex interplay of intermolecular interactions involving hydrophobic, π-π, cation-π, hydrogen bonding, and electrostatic interactions. Our study also illuminates the structural reorientations of water clusters surrounding the protein molecules upon the addition of regulatory small molecules such as salt, and RNA, thereby demonstrating the changes in the hydration water structure associated with diverse phase separating systems. Our work provides direct evidence of the changes in the hydration water structure associated with diverse phase-separating protein systems.

3.2 Experimental details

3.2.1 Materials

Sodium phosphate monobasic dihydrate, sodium phosphate dibasic dihydrate, 2-(N-morpholino) ethanesulfonic acid (MES), glacial acetic acid, ammonium sulfate, 4-(2-Hydroxyethyl) piperazine-1-ethanesulfonic acid (HEPES), 2-mercaptoethanol (BME), 1,4-dithiothreitol (DTT), Tris(2-carboxyethyl) phosphine hydrochloride (TCEP), phenylmethylsulfonyl fluoride (PMSF), PolyU sodium salt, Poly(ethylene glycol 8K) (PEG) and Urea were of MB grade purity, procured from Sigma (St. Louis, MO, USA). Luria Bertani Broth, Miller (LB), sodium chloride, N-cyclohexyl-3-aminopropanesulfonic acid (CAPS), ethylenediaminetetraacetic acid (EDTA), and nickel chloride were obtained from HiMedia Laboratories (MB grade). Ampicillin, Kanamycin, streptomycin sulfate, and Isopropyl-β-thiogalactopyranoside (IPTG) were purchased from Gold Biocom (USA). NiNTA resin and SP Sepharose were procured from Qiagen. Amylose resin was purchased from New England Biolabs. PD-10, NAP-10, and HiLoad 16/600 Superdex-G-200 columns were obtained from GE Healthcare Life Sciences (USA). Amicon MWCO membrane filters were purchased from Merck Millipore. In this study, all the buffers were freshly prepared using Mili-Q water and filtered before use. At 25 °C, the pH (±0.02) of all the buffer solutions was adjusted using a Metrohm 827 Lab pH meter.

3.2.2 Construct details and site-directed mutagenesis

The variant of full-length tau was created using the Tau 6x-Histag-2N4R-17C plasmid, a kind gift from Prof. Elizabeth Rhoades (University of Pennsylvania, USA). Using the Quick-change site-directed mutagenesis kit (Stratagene) native cysteines were replaced by serine (C291S, C322S). Further, the 6x-Histidine tag was removed by cloning. This null-cysteine variant was used for all our experiments. The recombinant construct of MBP-FUS FL-His_6 was a kind gift from Prof. Dorothee Dormann (IMB Mainz, Germany). The disease mutant of FUS-LC was created by site-directed mutagenesis (KOD Hotstart Mix) using the MBP-His_6-FUS-LC WT plasmid (Addgene plasmid # 98653; https://www.addgene.org/98653/; RRID: Addgene_98653), which was a kind gift from Prof. Nicolas L. Fawzi. The primers used for creating the respective mutations have been listed in Table 1.

Table 1. List of primers used for site-directed mutagenesis.

S291C Forward	GCAACGTCCAGTCCAAGTGCGGCTCAAAGG
S291C Reverse	CCTTTGAGCCGCACTTGGACTGGACGTTGC
S322C Forward	GAGCAAGGTGACCTCCAAGTGCGGCTCATTAGGC
S322C Reverse	GCCTAATGAGCCGCACTTGGAGGTCACCTTGCTC
LC G156E Forward	GCTATAATCCCCCTCAGGGCTATGAACAGCAGAACCAGTACAACAGC
LC G156E Reverse	GCTGTTGTACTGGTTCTGCTGTTCATAGCCCTGAGGGGGATTATAGC

3.2.3 Recombinant protein expression and purification

The null-cysteine variant of tau full-length was transformed into *E. coli* BL21(DE3) std strain, overexpressed and purified using cation-exchange chromatography on an SP-Sepharose column followed by gel filtration using a HiPrep 16/60 Superdex-G-75 (GE) column. The bacterial cell cultures were grown at 37 °C, 220 rpm till $O.D._{600}$ = 0.6, then overexpression was induced using 0.5 mM isopropyl-β-thiogalactopyranoside (IPTG) for 1h at 37 °C. Cultures were pelleted at 4 °C 3220 x g for 30 mins and were stored in -80 °C. Cell pellets were resuspended in lysis buffer (20 mM MES, 500 mM NaCl, 1 mM EDTA, 2 mM DTT, 1 mM $MgCl_2$, 1 mM PMSF, pH 6.5). Cell lysis was done using a probe sonicator (5% amplitude, 15 seconds ON and 15 seconds OFF for 25 mins). The lysate was boiled for 15 mins, and to remove cell debris, centrifugation was performed at 4 °C 15,557 x g for 30 mins. The supernatant was treated with streptomycin sulfate and glacial acetic acid to eliminate nucleic acid contamination. Further, high-speed centrifugation was done to remove the residue. Ammonium sulfate (60%) treatment was given to the supernatant, and the precipitated tau protein was obtained by high-speed centrifugation at 4 °C 15,557 x g for 30 mins. The dried protein pellets were dissolved in buffer A (20 mM MES, 50 mM NaCl, 1 mM EDTA, 1 mM

$MgCl_2$, 2 mM DTT, 1 mM PMSF, pH 6.5), followed by loading onto the cation-exchange column. Using a linear gradient of 100 % buffer B (20 mM MES, 50 mM NaCl, 1 mM EDTA, 2 mM DTT, 1 mM $MgCl_2$, 1 mM PMSF, 1M NaCl, pH 6.5). Pure protein fractions were pooled and further refined by gel filtration in buffer C (20 mM MES, 50 mM NaCl, pH 7.4). The purity of the protein was ensured by running an SDS-PAGE gel. Pure protein was concentrated in a 10 KDa MWCO Amicon filter, and concentration was estimated by measuring absorbance at 280 nm (ε_{280} = 6400). Small aliquots were made, flash-frozen, and stored at -80 °C.

MBP-FUS FL-His_6 plasmid transformed in *E. coli* BL21(DE3) RIPL strain were overexpressed and purified using affinity chromatography. Briefly, bacterial cultures were grown at 37 °C, 220 rpm till $O.D._{600}$= 0.6-0.8 and induced using 0.1 mM isopropyl-β-thiogalactopyranoside (IPTG) at 12 °C for 22 h. Pellets were dissolved in lysis buffer (50 mM sodium phosphate, 300 mM NaCl, 40 mM imidazole, 10 μM $ZnCl_2$, 4 mM BME, 10 % v/v glycerol, pH 8.0) and lysed using a probe sonicator at 5 % amplitude for 25 mins. The soluble fraction was isolated by high-speed centrifugation and incubated with pre-equilibrated Ni-NTA beads at 4 °C for 1.5 h. The beads were washed, and protein was eluted with 250 mM imidazole, then bound to the amylose column. The amylose beads were washed, and the protein was eluted in 20 mM maltose elution buffer (50 mM sodium phosphate, 800 mM NaCl, 40 mM imidazole, 10 μM $ZnCl_2$, 20 mM maltose, 1 mM DTT pH 8.0). An SDS-PAGE gel was run to confirm the purity of the protein.

His_6-TEV protease plasmid transformed in *E. coli* BL21(DE3) pLysS strain was overexpressed and purified using affinity chromatography. For overexpression, bacterial cultures growing at 37 °C, 220 rpm were induced with 0.35 mM IPTG at 16 °C for 20 h. Cultures were harvested and stored at -80 °C. Cell pellets were thawed at 30 °C and resuspended in lysis buffer (25 mM HEPES, 150 mM NaCl, 20 mM KCl, 20 mM $MgCl_2$, 1 mM PMSF, pH 7.4). Cell lysis was done using a probe sonicator in the presence of lysozyme to facilitate enhanced cell lysis. The cell lysate was centrifuged, and the supernatant was passed through the Ni-NTA column twice. The beads were washed, and protein was eluted in 300 mM imidazole. Excess imidazole was removed by overnight dialysis at 4 °C and the protein concentrated in 10 KDa MWCO Amicon filter and stored at -80 °C for future use.

All the variants of FUS-LC plasmids were transformed in BL21(DE3) std cells and were overexpressed and purified. For overexpression, bacterial cultures were grown at 37 °C, 220 rpm and induced with 1 mM IPTG at 37 °C for 4-5 h. For purification, pellets were

resuspended in lysis buffer (20 mM sodium phosphate, 300 mM NaCl, 10 mM imidazole, pH 7.4). Cell lysis was performed using a probe sonicator (5% amplitude, 15 sec ON, 10 sec OFF) for 20 min. The supernatant was isolated after high-speed centrifugation and loaded onto the Ni-NTA column. Beads were washed, and bound protein was eluted in 300 mM imidazole. The N-terminal MBP-His_6 tag was cleaved with TEV protease in a 1:40 molar ratio at 30 °C for 1.5 h, followed by overnight dialysis at room temperature. The reaction was passed through the Ni-NTA column to bind the MBP tag, uncleaved protein, and TEV protease, and the flowthrough containing cleaved FUS-LC was collected. The protein was further loaded on a gel-filtration column (HiLoad 16/600 Superdex-G-200) equilibrated with SEC buffer (20 mM CAPS, 150 mM NaCl, pH 11.0). Fractions containing pure protein were pooled as determined by running an SDS-PAGE gel. The pooled protein was concentrated and further buffer-exchanged into 20 mM CAPS, pH 11.0, using a PD-10 column. Finally, the pure protein was concentrated in a 3 KDa MWCO Amicon filter, and concentration was estimated by measuring absorbance at 280 nm (ε_{280} = 30,720). Small protein aliquots were made, flash-frozen, and stored at -80 °C.

3.2.4 Phase separation assays

FUS phase separation was induced by TEV cleavage in a 1:10 molar ratio (TEV protease: Protein) at room temperature in 20 mM sodium phosphate, pH 7.4. FUS-LC WT and FUS-LC G156E were diluted up to 200 μM in 20 mM sodium phosphate buffer, pH 7.4. Phase separation was initiated by the addition of 250 mM NaCl in the reaction mixture. The phase separation buffer for tau protein was 20 mM HEPES, 10% PEG, pH 7.4. Phase separation was induced by adding 10 μM protein to the reaction mixture. For phase separation with RNA, the respective concentration of RNA was added to the reaction mixture for FUS and tau droplets.

3.2.5 Raman spectroscopy

Raman spectra were obtained from the single-droplets and dispersed phase. Droplet reactions (2 μL) were placed onto a glass slide covered with aluminum foil and focused using a 50x long working distance objective lens (Nikon, Japan). The samples were excited using a 633 nm laser with an exposure of 10 sec and 50 mW laser power (100 %), and the spectra were recorded on an inVia laser Raman microscope (Renishaw, UK) at ~ 25 °C. The Raman scattering was collected and detected by an air-cooled CCD detector upon dispersion using a diffraction

grating (1800 lines/mm). Multiple Raman spectra were recorded with different batches of freshly purified protein as well, and several droplets from multiple reactions from the same stock were focused. Raman spectra (2800-3800 cm^{-1}) were acquired using Wire 3.4 software provided with the Raman spectrometer. The Raman spectra were baseline corrected using the cubic spline interpolation method provided by the software and plotted using the Origin software. The generalized polarization function $GP_{tetra/di}$ was calculated as shown previously[41,42] from the intensity contributions of the bands corresponding to the tetra- and di-coordinated water molecules at 3225 and 3432 $cm^{-1,}$ respectively, using the following relation.

$$GP_{tetra/di} = \frac{I_{3225} - I_{3432}}{I_{3225} + I_{3432}} \quad \ldots\ldots (1)$$

3.3 Results

3.3.1 Single-droplet vibrational Raman spectroscopy captures different hydrogen bonding states of water molecules

Using our laser micro-Raman setup, a laser beam is focused onto each phase-separated protein droplet as depicted in Figure 3.1. Illuminating individual droplets using a laser allowed us to capture a broad water Raman band arising due to asymmetric and symmetric stretching modes of O-H vibrations (3100-3700 cm^{-1}).

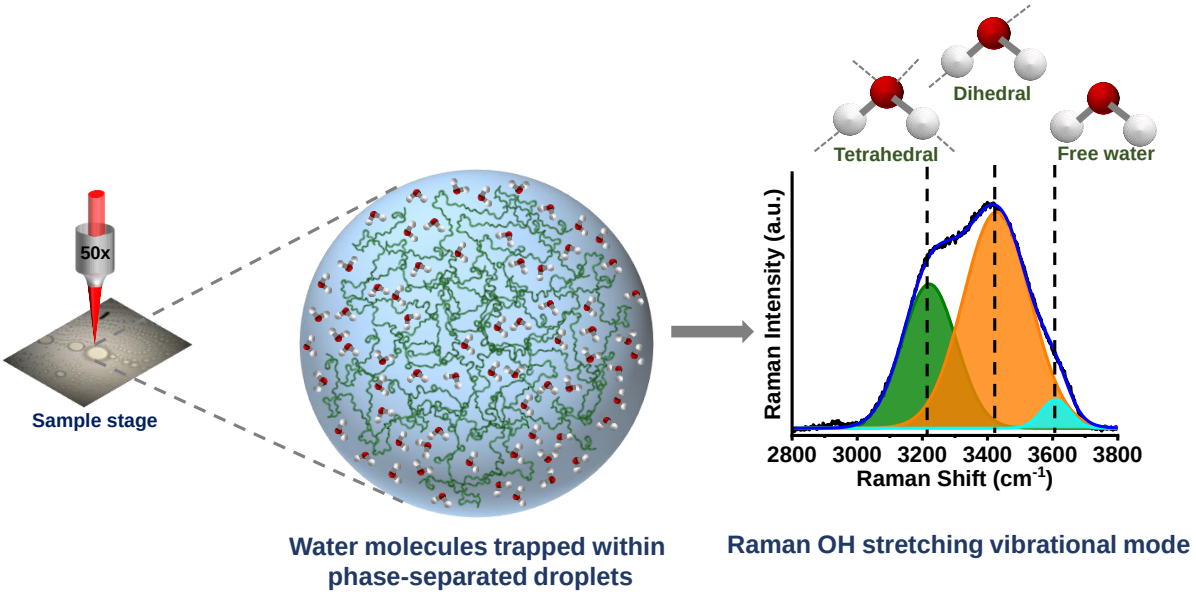

Figure 3.1. Representative Raman spectra showing the OH stretching vibrational mode for water trapped within the phase-separated protein-rich droplets. Single droplets focused using a 50x objective are illuminated with a 633 nm laser (50 mW laser power).

Spectral deconvolution of the O-H stretching Raman band gives rise to three broad overlapping O-H Gaussian peaks at ~ 3240 cm^{-1}, ~ 3440 cm^{-1}, and ~ 3600 cm^{-1} corresponding to strong H-bonded (tetrahedral/bound/hydrophilic), weak H-bonded (wrap/hydrophobic/distorted/dihedral) structures of water, and free water (bulk/non-bonded) respectively (Figure 1)[40,43-47]. These O-H Raman bands correspond to hydrogen-bonded water molecules with different donor and acceptor hydrogen bonds namely, (i) the double donor-double acceptor band (DDAA-OH) at 3240 cm^{-1} (also known as ice-like water representing a tight hydrogen-bonded network), (ii) single donor-single acceptor (DA-OH) band at 3440 cm^{-1} representing the liquid water, and (iii) the non-bonded (gas-like) water at 3600 cm^{-1} (free OH)[43]. In addition to these bands, there are more complex hydrogen bonding interactions that determine the water structure, including single donor-double acceptor band (DAA-OH) at 3040 cm^{-1} and double donor-single acceptor band (DDA-OH) at 3470 cm^{-1}. The band at 3600 cm^{-1} typically arises due to the DDA-OH and free-OH, representing the vibration of the weakly hydrogen-bound water and is often termed weakly bound water[40]. However, we assign the band at ~ 3600 cm^{-1} to free water throughout our study. We would like to note here that while these bands exist, they are possibly masked/superimposed under the three visible broad bands at ~ 3240, ~ 3440, and ~ 3600 cm^{-1}, representing the more common hydrogen-bonding states of water. We next set out to perform vibrational Raman experiments within the protein-rich condensed phase having significantly different local environments in the vicinity of water molecules to decipher the hydrogen bonding states of water.

3.3.2 Water structure and hydrogen bonding within FUS-LC droplets

We next set out to study a model phase separating protein FUS-LC to gain insights into water in condensates. FUS-LC phase separation is primarily driven by intermolecular aromatic π-π, hydrogen bonding, and hydrophobic interactions. The N-terminal domain of FUS comprises a prion-like, low-complexity sequence overrepresented in glutamine (Q), tyrosine (Y), serine (S), and glycine (G) and has been established as the primary driver of the self-assembly of the full-length FUS into phase-separated droplets and aggregates *in vitro* and *in vivo*[48-53]. As a prelude, we recorded the Raman spectra of FUS-LC droplets formed at 250 mM NaCl in a droplet-by-droplet manner and the outside light phase. The Raman spectra indicated a collective change in the water structure upon phase separation (Figure 3.2a). Spectral deconvolution of the OH

stretching band gives three Raman bands at ~ 3240 cm^{-1}, ~ 3440 cm^{-1}, and ~ 3600 cm^{-1} corresponding to tetra-coordinated, di-coordinated distorted wrap, and free water, respectively.

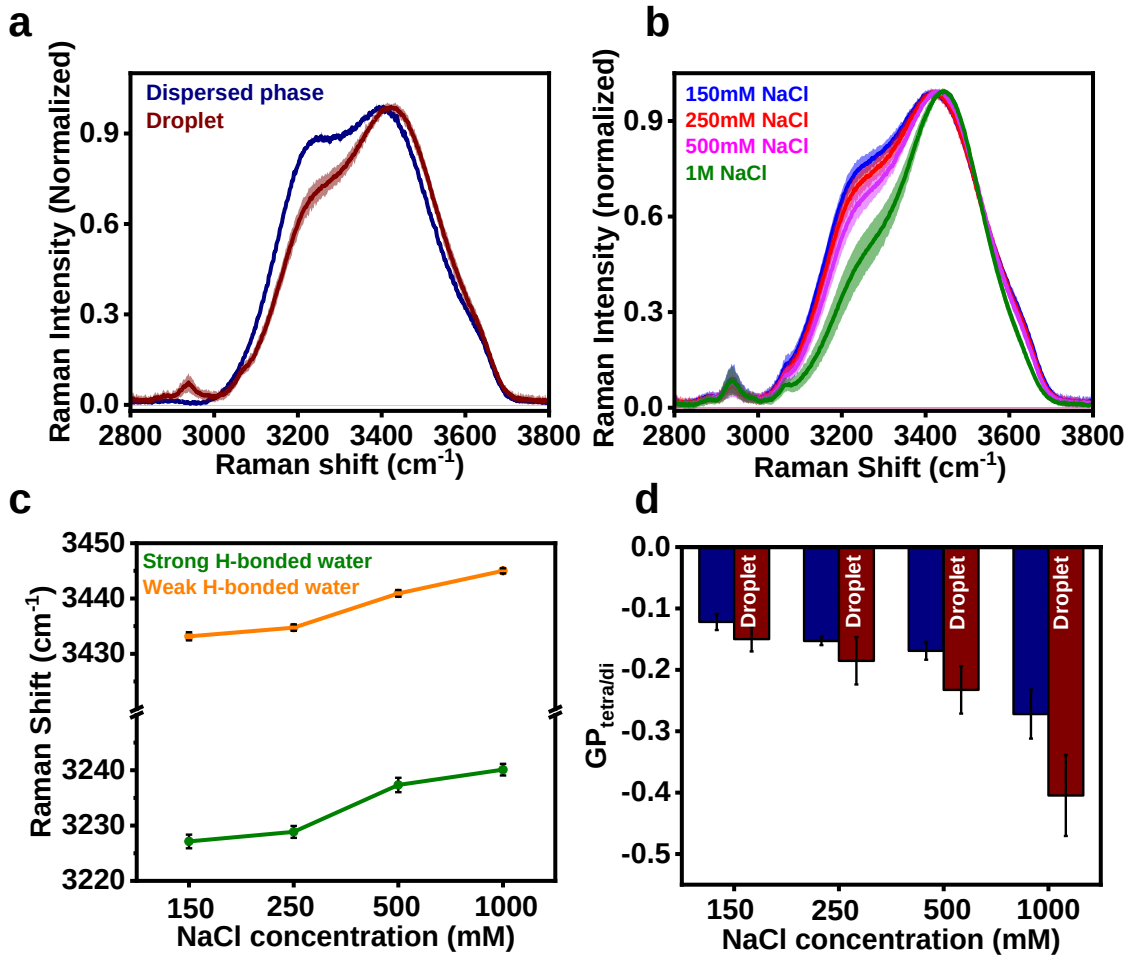

Figure 3.2. a. Water Raman spectra of the FUS-LC dispersed phase and single droplets (n = 15 for droplets and n = 10 for the dispersed phase). b. Water Raman spectra of FUS-LC single droplets formed as a function of salt concentrations (n = 15). c. Raman shift of band maxima for the strong and weak H-bonded structures of water within FUS-LC single droplets formed as a function of salt concentration. Olive represents the strongly H-bonded/tetra-coordinated water structures, whereas orange represents the weakly H-bonded/di-coordinated water structures. d. Spectral changes are quantified with the generalized polarized (GP) function calculated from the intensity contributions of the bands at 3225 and 3432 cm^{-1} ($GP_{tetra/di}$), corresponding respectively to tetra-coordinated and di-coordinated water molecules engaged in hydrogen bonds within the dispersed and the condensed phases as a function of salt concentration.

We then induced FUS-LC phase separation at different salt concentrations and recorded the water Raman spectra of the FUS-LC condensed phase in a single droplet fashion (Figure 3.2b).

Upon increasing the salt concentration from 150 mM NaCl to 1 M NaCl, we observed a measurable spectral blue shift of about 15 cm^{-1} for strong H-bonded structures and 10 cm^{-1} for weak H-bonded structures of water (Figure 3.2c). In order to obtain a better idea of the overall changes in the structure of water upon phase separation, we estimated the generalized polarization function ($GP_{tetra/di}$) for the FUS-LC condensed phase as a function of salt concentration (Figure 3.2d)[41,42]. This function considers the intensity of the Raman water band at 3225 cm^{-1} and 3432 cm^{-1} corresponding to the tetra-coordinated and di-coordinated water molecules. The $GP_{tetra/di}$ function of the FUS-LC droplets decreased as we increased the salt concentration, indicating a reduction in the tetra-coordinated water.

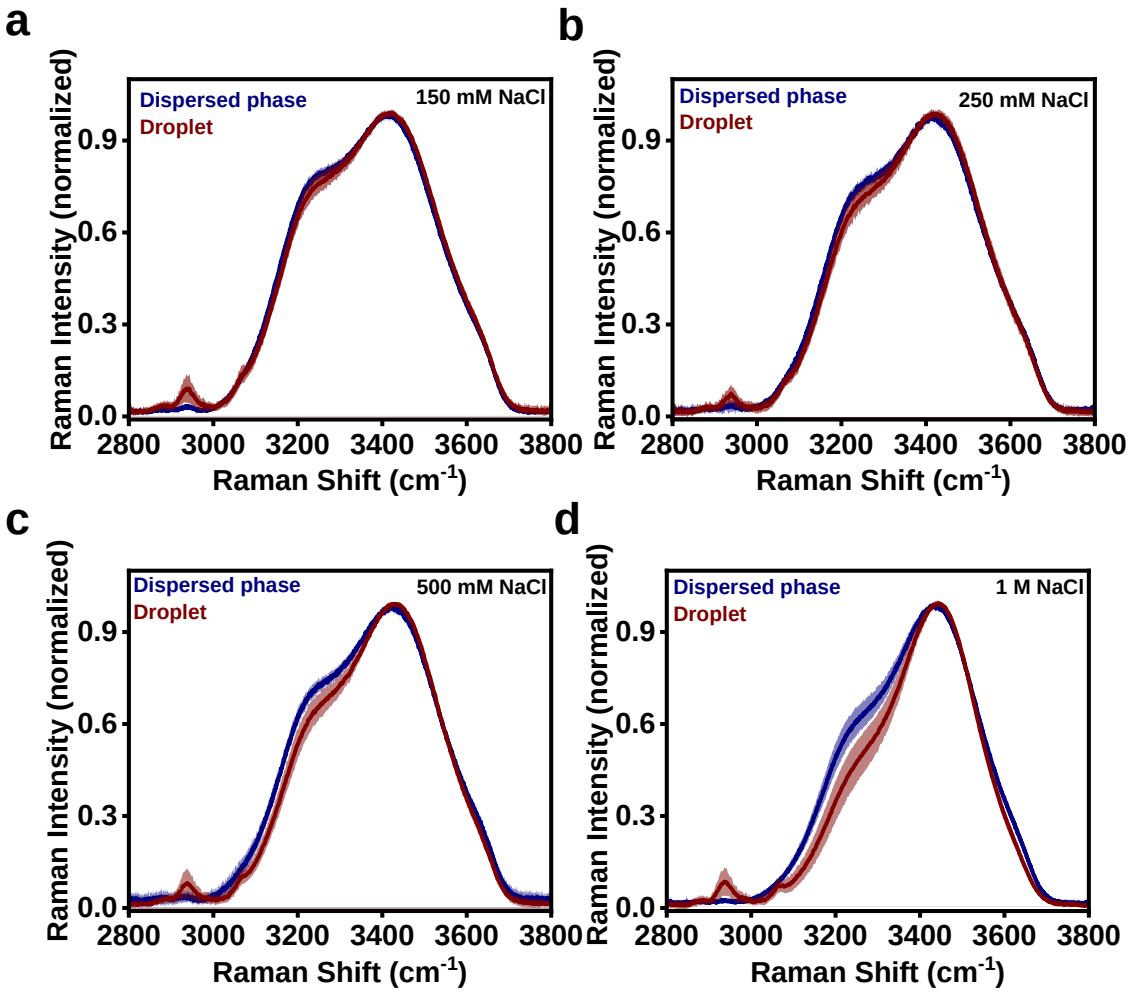

Figure 3.3. (a-d) Water Raman spectra of FUS-LC droplets and the surrounding dispersed phase at different concentrations of salt (n = 15 for droplets and n = 10 for the dispersed phase).

This observation revealed a phase separation-dependent modulation in the extent of water hydrogen bonding. Since phase separation in FUS-LC is principally driven by a combination of π-π contacts, hydrogen bonding, and hydrophobic interactions, an increase in the salt concentration can offer stronger hydrophobic effects, further increasing the extent of the π-π interactions and hydrogen bonding. These intermolecular interactions result in the desolvation of the participating residues, such as tyrosine and glutamine, which are previously solvated by the tetra-coordinated water molecules in the dispersed phase. This loss in hydrophilic-bound water leads to a reduced contribution of tetra-coordinated protein hydration water as captured in the gradual reduction in polarization function ($GP_{tetra/di}$) with increasing salt concentration (Figure 3.2d). Additionally, ions themselves are known to exert an effect on the hydrogen-bonded structure of water and can behave as water structure breakers or makers[54]. To rule out the possibility of any changes in the water structure due to the addition of salt; we recorded Raman spectra from the outer protein-deficient dispersed phase (Figure 3.3 a-d). We observed water structures distinct from the inner protein-rich phase suggesting that alterations in the hydrogen-bonding state of water within the dense phase can be attributed to the changed protein-protein and protein-solvent interactions within the condensates (Figure 3.2d). Taken together, our data indicates the entropic release of tetra-coordinated hydration water, promoting the formation of a network of hydrogen bonding, π-π and hydrophobic contacts driving FUS-LC phase separation.

3.3.3 The impact of a disease-associated mutation on water structure

The LC domain harbors several point mutations of full-length FUS implicated in a range of neurodegenerative diseases, including Amyotrophic lateral sclerosis and Frontotemporal lobar degeneration. The glycine-to-glutamate mutation at the 156th residue position (G156E) is one such disease-associated mutant known to expedite the aggregation of full-length FUS[55-57]. Hence, we next wanted to investigate how this disease-associated single-point mutation in the LC domain (G156E FUS-LC) alters the water structure within the phase-separated droplets (Figure 3.4a). The Raman O-H stretching band corresponding to the tetra-coordinated and di-coordinated water molecules showed a blue shift from 3229 cm^{-1} to 3255 cm^{-1} and 3435 cm^{-1} to 3446 cm^{-1}, respectively, for the single droplets of wild-type FUS-LC and G156E FUS-LC (Figure 3.4b, c). This suggests a partial weakening of the H-bonded structure of water within the diseased mutant droplets (Figure 3.4c). We next estimated $GP_{tetra/di}$ for the mutant droplets

and observed a reduced value compared to wild-type droplets, indicating a higher release of tetrahedrally coordinated water molecules (Figure 3.4d, e).

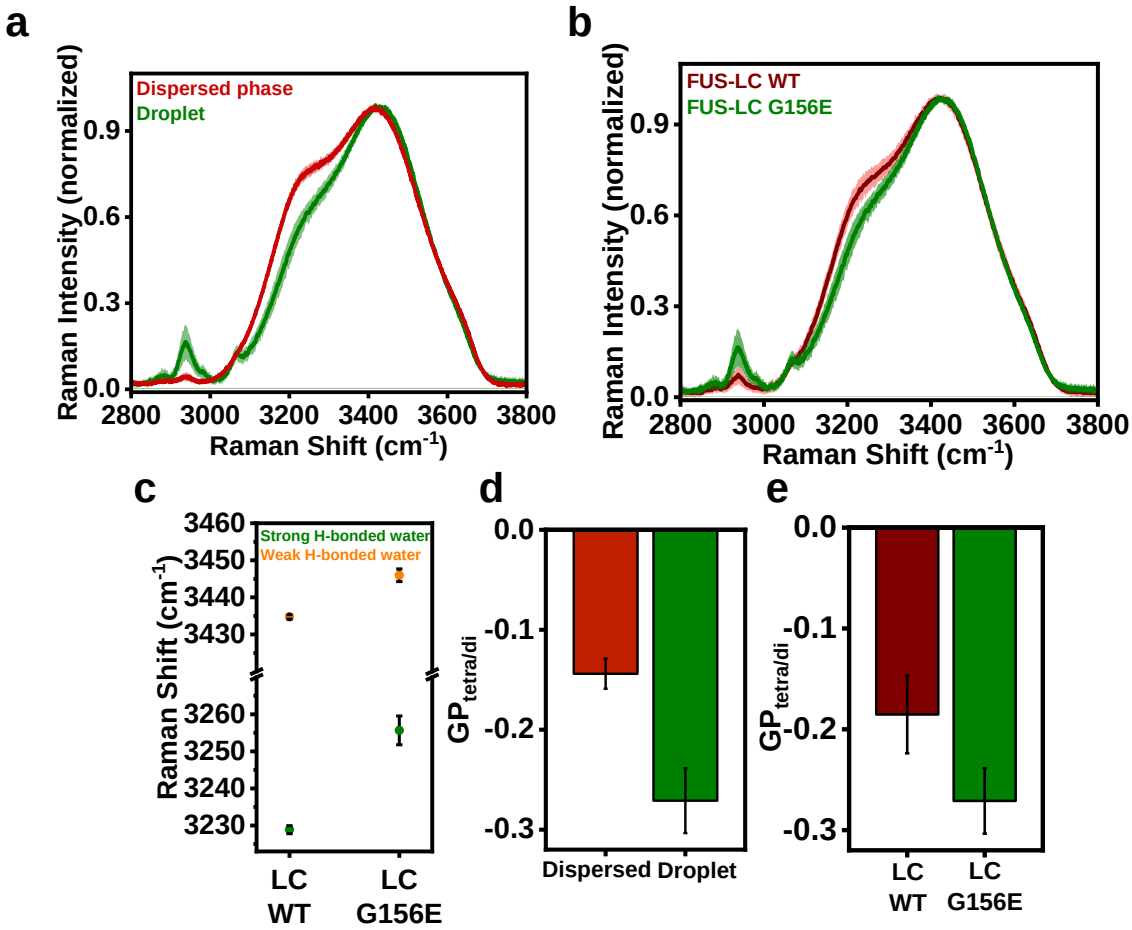

Figure 3.4. a. Water Raman spectra of FUS-LC (G156E) droplets and the surrounding dispersed phase formed at 250mM NaCl (n = 10). b. Comparison of water Raman spectra of FUS-LC (G156E) single droplets formed at 250 mM salt concentration and FUS-LC single droplets at 250 mM salt concentration [similar spectra shown in (a)] (n = 15 droplets for FUS-LC and n = 10 droplets for FUS-LC (G156E)). c. Raman shift of band maxima for the strong and weak H-bonded structures of water within FUS-LC and FUS-LC (G156E) single droplets at 250mM NaCl. Olive represents the strongly H-bonded/tetra-coordinated water structures, whereas orange represents the weakly H-bonded/di-coordinated water structures. d. $GP_{tetra/di}$ function calculated from the intensity contributions of the bands at 3225 cm^{-1} and 3432 cm^{-1} for FUS-LC (G156E) droplets and the dispersed phase. e. Comparison of the $GP_{tetra/di}$ function for single droplets of FUS-LC and FUS-LC (G156E). All Raman spectra are recorded at 50 mW laser power, 50x objective, and normalized with respect to the water Raman band at ~ 3400 cm^{-1}.

Our previous observation indicated that G156E mutation introduces chain expansion that allows an increase in intermolecular interaction resulting in a denser network of polypeptide chains within condensates[58]. Such a strong network formed via aromatic interactions between tyrosine residues and hydrogen bonding interactions between glutamine residues is accompanied by a more significant release of (bound) tetrahedrally coordinated water molecules directly interacting with the polar side chains of the protein. Therefore, our Raman studies show a smaller contribution of tetra-coordinated protein hydration water and capture this enhanced release of entropically unfavorable, highly coordinated water molecules within the condensates of the G156E FUS-LC mutant.

3.3.4 The nature of intermolecular interactions governs changes in the water structure in condensates

The structural distributions of protein hydration water are highly context-dependent and are expected to vary according to the amino acid composition, conformation, and interactions, as shown previously[27-34]. Hence, we next asked whether the introduction of a combination of cation-π, hydrogen bonding, and electrostatics, in addition to hydrophobic interactions into our phase-separating system, was capable of significantly altering the proportions of the bound and wrap hydration water within the protein-rich condensates. FUS is a model phase separating protein enriched in tyrosine, arginine, glycine, and glutamine, and its phase separation is known to be facilitated synergistically by cation-π, hydrophobic, hydrogen-bonded, and electrostatic interactions[59-63]. Thus, we next set out to investigate the water structure and hydrogen bonding within the condensates of full-length FUS. To study these droplets, we set up phase separation reactions of FUS and induced droplet formation by TEV-mediated cleavage of the solubilizing MBP tag. Our single-droplet water vibrational Raman experiments indicated a reduction in the tetrahedrally coordinated bound water within the protein-rich phase as compared to the outer dilute phase which is also evident from the spectral blue shift of ~ 10 cm^{-1} for strongly H-bonded water and ~ 12 cm^{-1} for weak H-bonded water structures (Figure 3.5a, b). We next calculated the $GP_{tetra/di}$ function for the phase-separated droplets and the surrounding dispersed phase, and observed a decreased value for the droplet state in comparison to the outer light phase akin to FUS-LC droplets (Figure 3.5c). Although this decrease in bound water content in the case of FUS-LC can be ascribed to the predominance of aromatics and hydrogen bonding in driving phase separation, full-length FUS phase transitions, on the other hand, involve an interesting interplay of majorly cation-π, electrostatic, and hydrophobic interactions. A large-

scale release of bound water from hydrophilic groups, including the positively charged arginine and aromatic tyrosine residues, is crucial for forming the cation-π interactions[64]. This entropically favorable release of tetrahedrally coordinated water, as indicated by our data, can be thus postulated to further promote the enthalpically favorable protein-protein interactions driving the phase separation of full-length FUS.

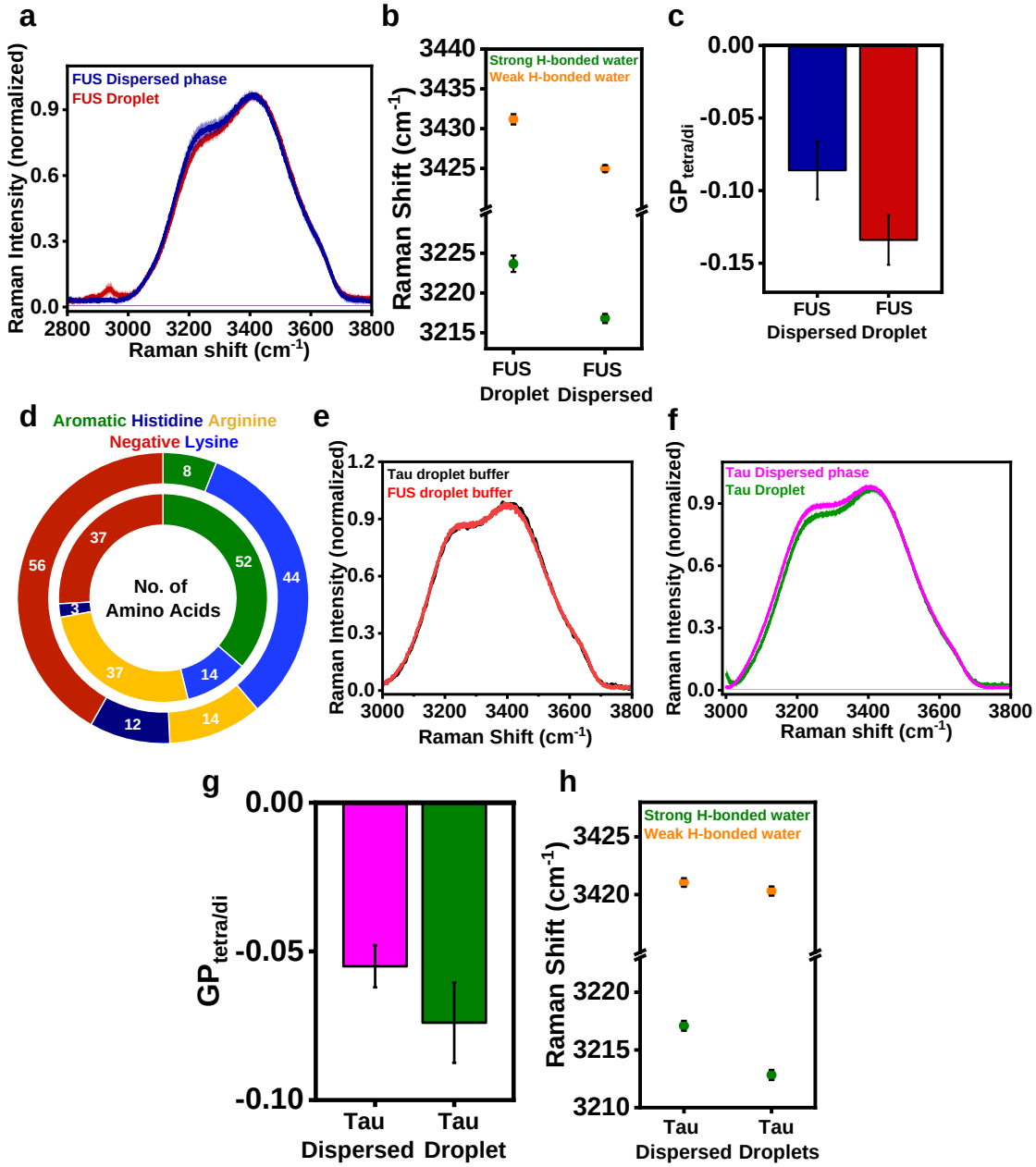

Figure 3.5. a. Water Raman spectra of the full-length FUS dispersed phase and single droplets (n = 10 for both dispersed phase and droplets). b. Raman shift of band maxima for the strong and weak H-bonded structures of water within full-length FUS droplets and the surrounding

dispersed phase. Olive represents the strongly H-bonded/tetra-coordinated water structures, whereas orange represents the weakly H-bonded/di-coordinated water structures. c. Comparison of the $GP_{tetra/di}$ function for full-length FUS dispersed phase and single droplets. d. Pie chart showing the comparison of aromatic residues, positively charged, and negatively charged residues in full-length FUS and tau. e. Water Raman spectra of full-length FUS and Tau droplet buffer (n = 10). f. Water Raman spectra of tau dispersed phase and single droplets (n = 10 for both dispersed phase and droplets). g. Comparison of the $GP_{tetra/di}$ function for tau dispersed phase and single droplets. h. Raman shift of band maxima for the strong and weak H-bonded structures of water within Tau droplets and the surrounding dispersed phase. Olive represents the strongly H-bonded/tetra-coordinated water structures, whereas orange represents the weakly H-bonded/di-coordinated water structures.

To further probe the effect of electrostatic interactions on the hydration water structure, we switched to a primarily electrostatically driven phase-separating protein, namely tau. Tau is a microtubule-associated neuronal intrinsically disordered protein known to undergo phase separation under physiological conditions, *in vitro* and *in vivo*[65-72]. Tau comprises a large number of positively and negatively charged residues distributed non-uniformly throughout the polypeptide chain, as opposed to FUS, where in addition to charged residues, aromatic amino acids constitute a significant proportion (Figure 3.5d). The electrostatic interactions between these oppositely charged residues are identified as the major contributor towards the phase separation of tau into biomolecular condensates[67,73,74]. Droplet formation of tau was induced by a molecular crowding agent (polyethylene glycol, PEG), and single-droplet Raman spectra were acquired by focusing the laser inside individual droplets. Prior to performing Raman experiments on tau droplets, we recorded Raman spectra for the droplet reaction buffers of full-length FUS and tau, which ruled out the possibility of any significant alteration in the structure of water due to the presence of molecular crowding agent and salt (Figure 3.5e). Tau droplets showed a decrease in tetrahedrally coordinated water, as indicated in the water Raman spectra, and we observed a significant blue shift of ~ 10 cm^{-1} for the strongly H-bonded structures of water and this modification in the structure of hydration water is evident in the $GP_{tetra/di}$ ratio (Figure 3.5f, g, h). Further, we compared the water Raman spectra for full-length FUS and tau and observed that the $GP_{tetra/di}$ values for the two phase-separating systems are concomitant with the observation that the condensed phase of tau has a greater proportion of bound water as compared to the full-length FUS condensed phase that can potentially aid in the water-mediated electrostatic interactions between the charged domains of the polypeptide chains (Figure 3.6a). We further deconvoluted the water Raman band from 3000 cm^{-1} to 3800 cm^{-1} and interestingly observed that the intensity of the free OH band at ~ 3610 cm^{-1} for tau droplets

reduced to nearly half of the intensity for full-length FUS droplets (Figure 3.6b, c). The area under this band also showed that the proportion of weakly bound water (accessible OH) decreased significantly for tau droplets (1.71 ± 0.07 %) as compared to the FUS (full-length/LC) droplets (3.30 ± 0.20 % for full-length FUS).

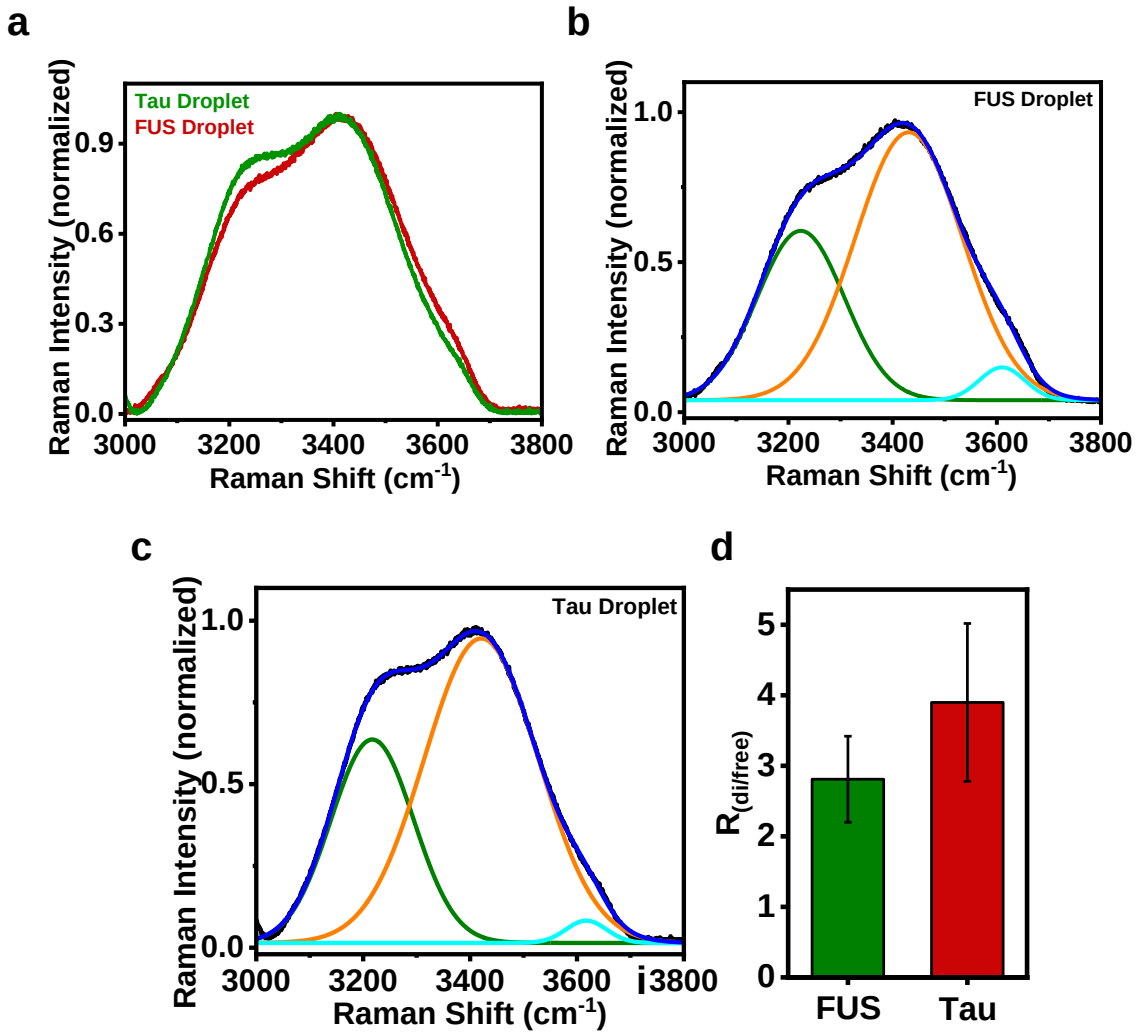

Figure 3.6. a. Comparison of the water Raman spectra of the condensed phases of full-length FUS and tau as shown. All Raman spectra are recorded at 50 mW laser power, 50x objective, and normalized with respect to the water Raman band at ~ 3400 cm^{-1}. Gaussian deconvolution of water Raman band (3000-3800 cm^{-1}) for full-length FUS (b) and tau droplets (c) to analyze the percentage composition of various secondary structural elements. The black and blue solid lines represent the actual data and the cumulative fit, respectively. The other colored solid lines represent the Gaussian peaks obtained after deconvolutions. d. Bar plot representing the intensity ratios of the bands corresponding to the di-coordinated and free water after Gaussian deconvolution for full-length FUS and tau droplets. All Raman spectra are recorded at 50 mW laser power, 50x objective, and normalized with respect to the water Raman band at ~ 3400 cm^{-1}.

To quantify this observation, we plotted the intensity ratio for the di-coordinated water and free water (Figure 3.6d), which further supported the fact that tau phase transitions are predominantly driven by electrostatic interactions where most of the water molecules are tightly bound to the protein's hydrophilic and hydrophobic groups constituting the bound and the wrap/distorted water. This further reduces the free water available in the demixed phase, and the solvent can facilitate the electrostatic interactions[75], making the enthalpically driven protein-protein interactions more favorable than the entropic release of water molecules. Taken together, this set of results highlights the role of distinct molecular drivers in modulating the structural characteristics and hydrogen bonding of the hydration water network within biomolecular condensates.

3.3.5 The role of RNA in modulating water structure within protein: RNA heterotypic condensates

We next directed our efforts to monitor the structural changes in the hydration water layer upon introducing RNA in biomolecular condensates using Raman spectroscopy. RNA is a well-known modulator of phase separation of multiple RNA-binding proteins, including FUS and tau, into dense protein-RNA-rich condensates[8,25,76-78].

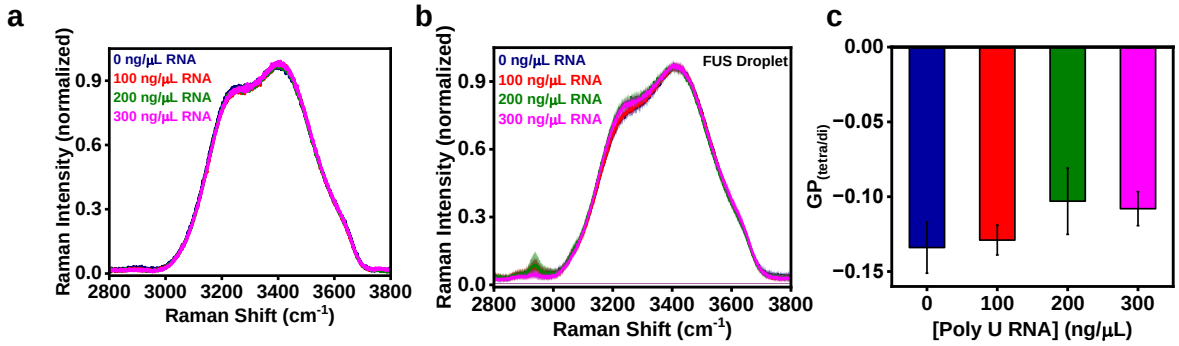

Figure 3.7. a. Water Raman spectra of full-length FUS droplet reaction buffer in the presence of different concentrations of polyU RNA (n = 10). b. Water Raman spectra of full-length FUS droplets in the presence of 0 ng/µL, 100 ng/µl, 200 ng/µl, and 300 ng/µl polyU RNA (n = 10). c. $GP_{tetra/di}$ function calculated from the intensity contributions of the bands at 3225 and 3432 cm^{-1} for full-length FUS droplets as a function of RNA concentration.

Based on the varying binding affinities of nucleic acids originating from the sequence, charge, and structure-dependent specificity towards these interacting proteins, RNA uniquely alters the protein-protein and protein-RNA interactions and, thus, phase separation within different systems. As a result, RNA tunes properties like phase separation propensity (C_{sat}), condensate constitution, and material properties, including internal diffusion, concentration, and viscoelasticity within biomolecular condensates. Based on the sequence composition, proteins can interact with RNA via electrostatic or π-π, and cation-π interactions[79,80].

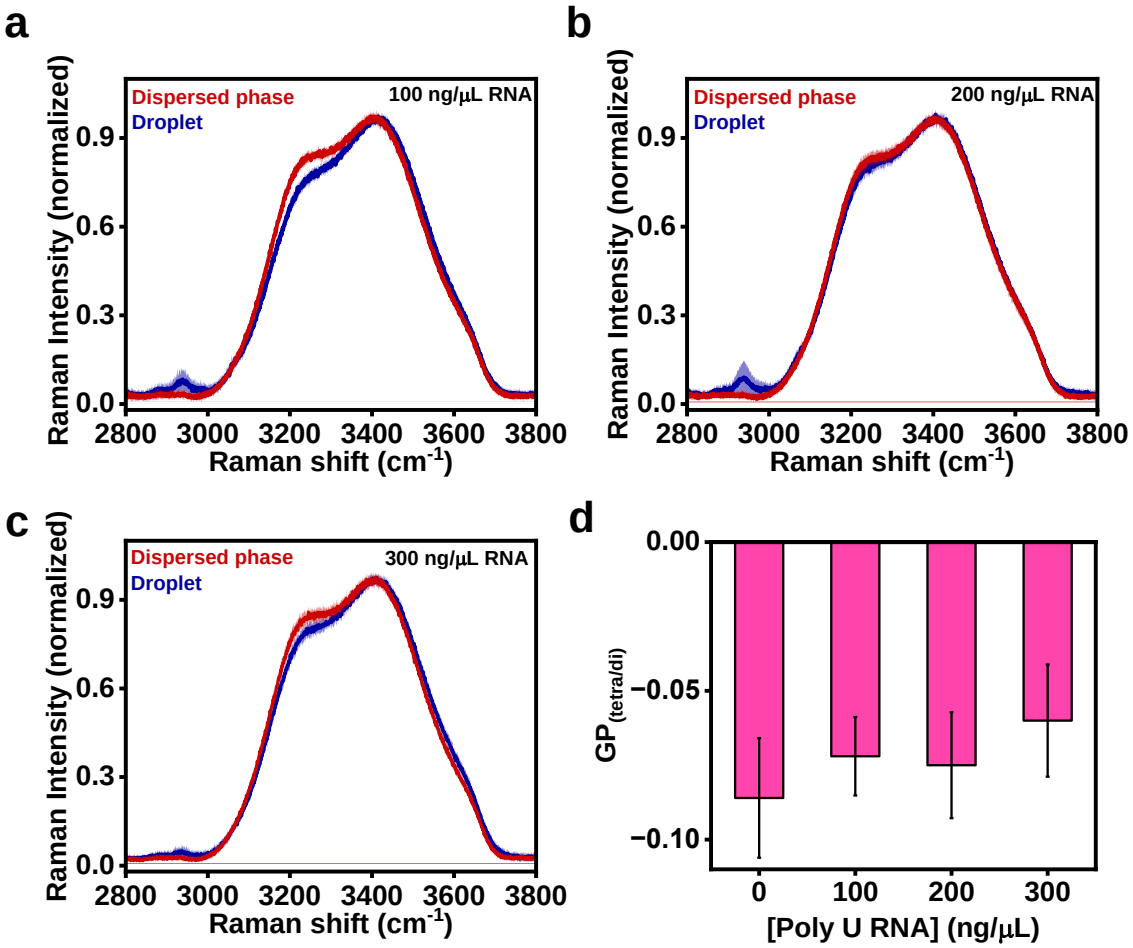

Figure 3.8. (a,b,c) Water Raman spectra of full-length FUS droplets and the surrounding dispersed phase at different concentrations of polyU RNA (n = 10). d. $GP_{tetra/di}$ function calculated from the intensity contributions of the bands at 3225 cm^{-1} and 3432 cm^{-1} for the surrounding dispersed phase as a function of RNA concentration. All Raman spectra are recorded at 50 mW laser power, 50x objective, and normalized with respect to the water Raman band at ~ 3400 cm^{-1}.

Prior to our Raman experiments within protein-rich droplets, we ensured that RNA itself did not impact the water structure by recording Raman spectra in the droplet reaction buffer for various concentrations of RNA (Figure 3.7a). Next, we recorded a Raman spectrum in the OH stretching vibration region for full-length FUS droplets formed at increasing RNA concentrations (Figure 3.7b). $GP_{tetra/di}$ values suggested a sequential increase in the strongly bound tetrahedrally coordinated water, within FUS: RNA condensates (Figure 3.7c). Based on the amino acid composition, FUS can associate with RNA via a combination of electrostatic, cation-π, or π-π interactions between the negatively charged RNA and the positively charged arginine residues in FUS[79,80], ensuing a tug-of-war between the release and retention of hydration water to assist these protein-protein interactions by forming a network within the condensates.

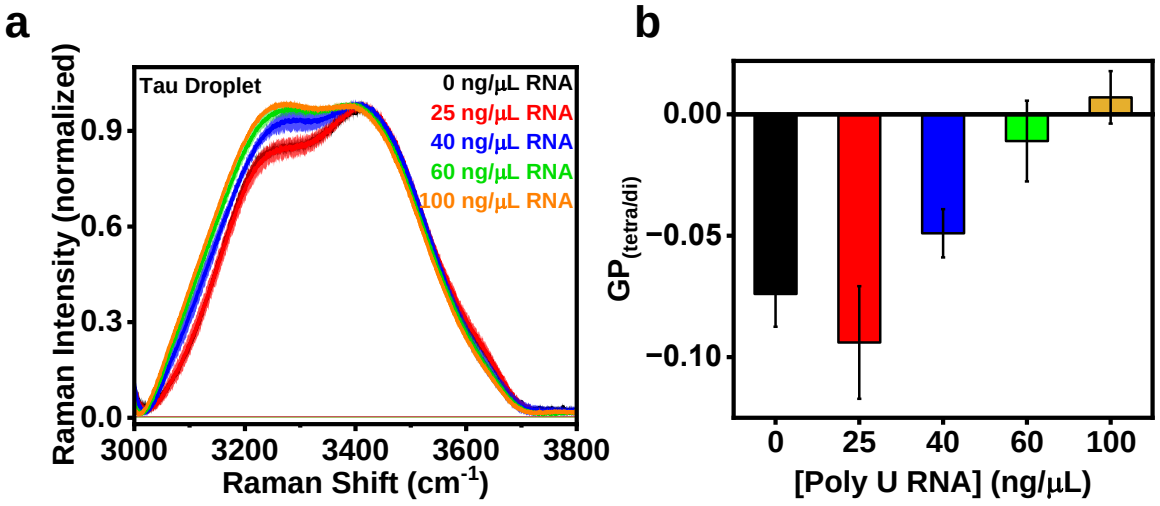

Figure 3.9. a. Water Raman spectra of tau droplets in the presence of 0 ng/µL, 25 ng/µl, 40 ng/µl, 60 ng/µl, and 100 ng/ul polyU RNA (n = 10). b. $GP_{tetra/di}$ function calculated from the intensity contributions of the bands at 3225 cm^{-1} and 3432 cm^{-1} for tau droplets as a function of RNA concentration. All Raman spectra are recorded at 50 mW laser power, 50x objective, and normalized with respect to the water Raman band at ~ 3400 cm^{-1}.

Therefore, an increased bound water content with an increasing concentration of RNA agrees well with the idea of enhanced phase separation with greater RNA concentration, resulting from the increasing strength of intermolecular interactions. Interestingly, we observed only a marginal change in the structure of water in the dispersed phase surrounding the droplets, implying that free RNA, at our concentrations in particular, is insufficient to induce any water

structural changes (Figure 3.8a-d). Next, we intended to study the distribution of water structure in a system principally driven by electrostatic interactions. We recorded water Raman spectra for tau single droplets at different concentrations of RNA from 25 to 100 ng/µL (Figure 3.9a).

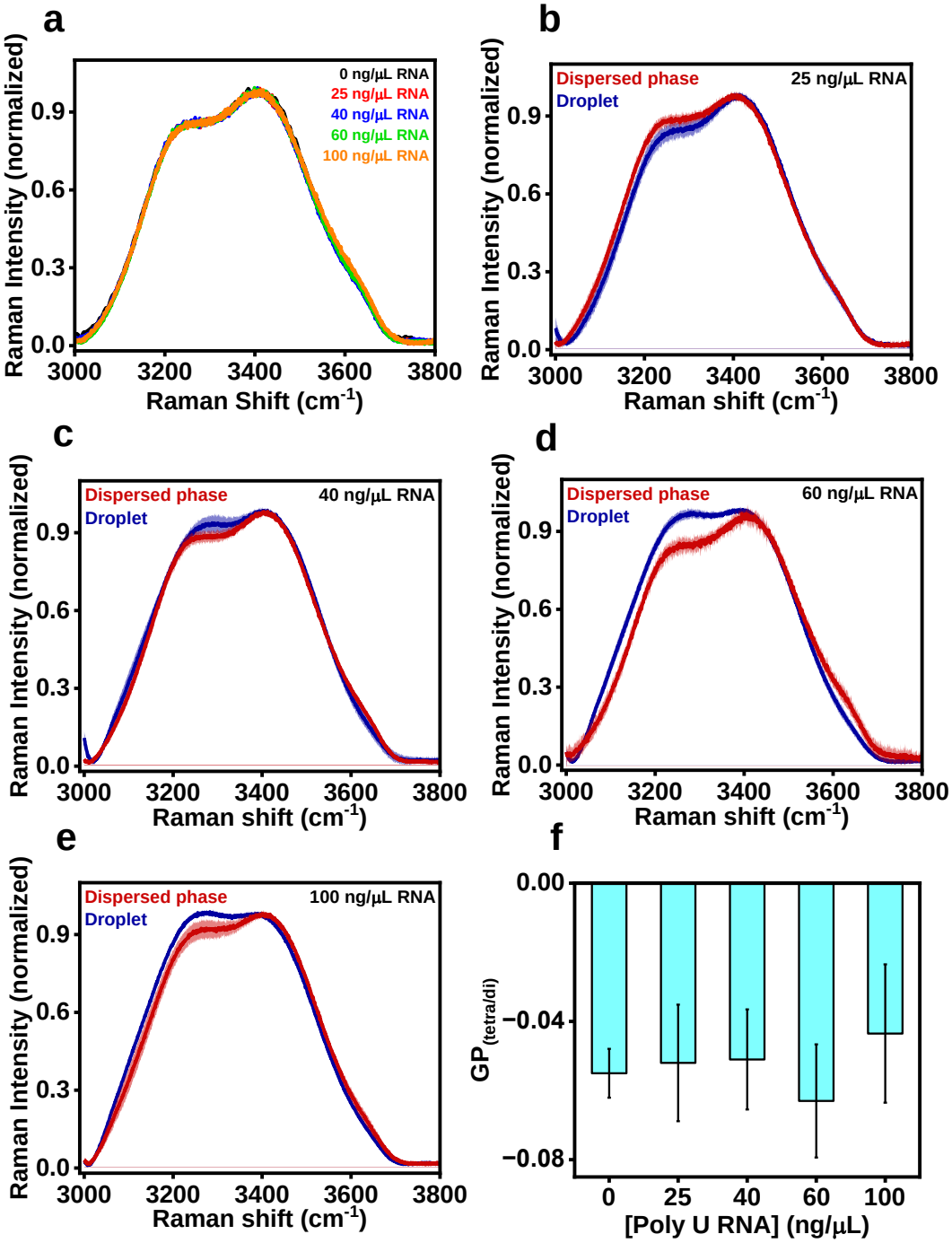

Figure 3.10. a. Water Raman spectra of Tau droplet reaction buffer in the presence of different concentrations polyU RNA (n = 10). (b-e) Water Raman spectra of full-length FUS droplets

and the surrounding dispersed phase at different concentrations of polyU RNA (n = 10 droplets). f. $GP_{tetra/di}$ function calculated from the intensity contributions of the bands at 3225 cm^{-1} and 3432 cm^{-1} for the surrounding dispersed phase as a function of RNA concentration. All Raman spectra are recorded at 50 mW laser power, 50x objective, and normalized with respect to the water Raman band at ~ 3400 cm^{-1}.

Contrary to full-length FUS droplets, the magnitude of change in the structure of water is significantly large in the case of tau droplets. At 25 ng/µL RNA, tau droplets showed a slight decrease in the bound water content as indicated by the $GP_{tetra/di}$ values, which increased sharply upon increasing RNA up to 100 ng/µL (Figure 3.9b). Our water Raman measurements in the tau dispersed phase revealed a similar hydrogen bonding network in the presence of varying concentrations of RNA (Figure 3.10a-f). Phase transitions in tau are majorly driven by electrostatic interactions, and RNA can further be involved in the heterotypic, electrostatic protein-RNA interactions enhancing condensation of tau. Here, the strongly hydrogen-bonded water bound to the polypeptide chains can facilitate the electrostatic interactions by forming a water-bound network, thereby favoring protein condensation on increasing RNA concentration. Interestingly, upon deconvolution of the water Raman band, we observed a complete band disappearance at ~ 3610 cm^{-1} originating from the free non-hydrogen bound water contrary to the full-length FUS data (Figure 3.11a, b).

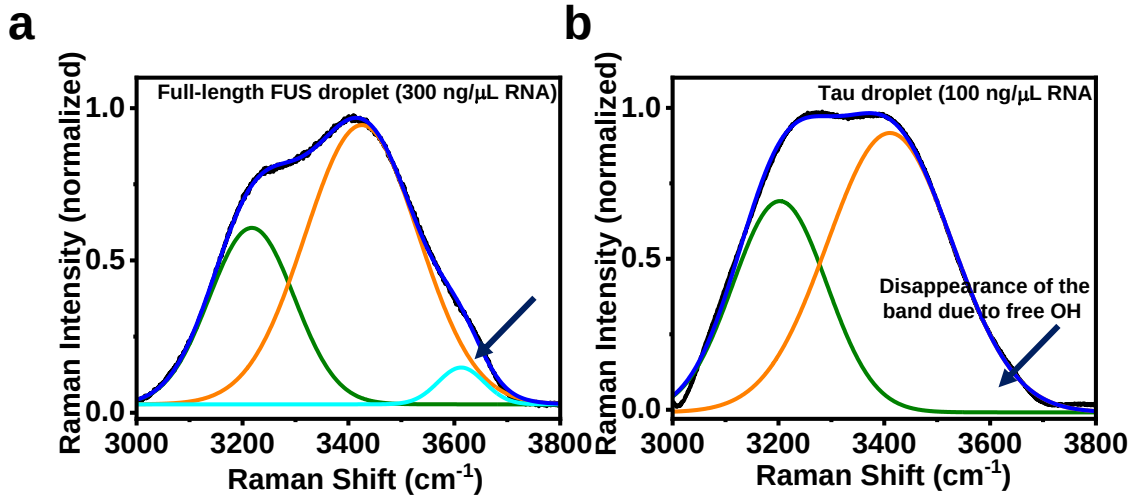

Figure 3.11. Gaussian deconvolution of water Raman band (3000-3800 cm^{-1}) for full-length FUS (a) and tau (b) droplets at highest polyU RNA concentration to analyze the percentage composition of various secondary structural elements. The black and blue solid lines represent the actual data and the cumulative fit, respectively. The other colored solid lines represent the

Gaussian peaks obtained after deconvolutions. Arrowheads show the complete disappearance of the band due to free OH vibrations for tau droplets.

This observation further suggests a strongly hydrogen-bound water network within the tau droplet phase. Taken together, these results suggest a strong influence of RNA on the hydrogen-bonded structures of water within the protein-rich dense phase and, therefore, underscore the role of tetracoordinated water in mediating the electrostatic protein-protein and protein-RNA interactions in driving the phase separation.

3.4 Discussion

Biomolecular condensates contain approximately 60-70% of water within the densely packed protein-RNA-rich droplets[26,35-37]. The water molecules in the vicinity of these biomolecules assemble into a hydration shell, providing a favorable medium for intermolecular interactions[26,27,30-33]. The demixing of these biomolecules into protein-rich dense phase and dispersed phase is associated with a considerable reorganization of the continuous network of densely H-bonded water. This change in the water structure leads to the formation of localized water clusters with characteristic hydrogen bonding network is thought to facilitate the process of phase separation[27,35,36]. However, deciphering the water structure and monitoring the water dynamics throughout this intricate process of biomolecular condensation has proved challenging despite the advent of various sophisticated experimental and computational tools[26,37,81,82]. In this work, we employed single-droplet vibrational Raman spectroscopy as a tool for the direct observation of the hydration water structure and monitor the changes accompanying condensate formation via phase separation. The hydration water within biomolecular condensates displayed significant differences when compared to the hydrogen bonding network in pure water. Our studies allowed us to investigate this dynamic hydration network within condensates formed via phase separation originating from a wide range of molecular drivers including hydrophobics, aromatics, hydrogen bonding, and electrostatic interactions (Figure 3.12). In the presence increasing salt concentrations, phase separation of FUS-LC is accompanied by a greater degree of release of tetra-coordinated water molecules that were bound to the polar tyrosine and glutamine residues in the dispersed phase. The disease-associated mutant G156E FUS-LC showed an additional weakening of the water hydrogen bonding network and a reduction in the contribution of hydrophilic bound water.

This entropic loss of bound water enables the more expanded polypeptide chain of G156E FUS-LC to participate in the formation of a relatively stronger intermolecular interactions within the dense, viscoelastic interior of mutant FUS-LC droplets, which is in accordance with previous studies[58,83]. Similarly, the condensates of full-length FUS involving a combination of cation-π, hydrogen bonding, and electrostatic interactions, showed a slightly reduced but measurable loss of the tetrahedrally coordinated water. The formation of cation-π and π-π interactions between the aromatic tyrosine residues and positively charged arginine residues necessitates the release of the bound water molecules hydrating these residues to undergo phase separation.

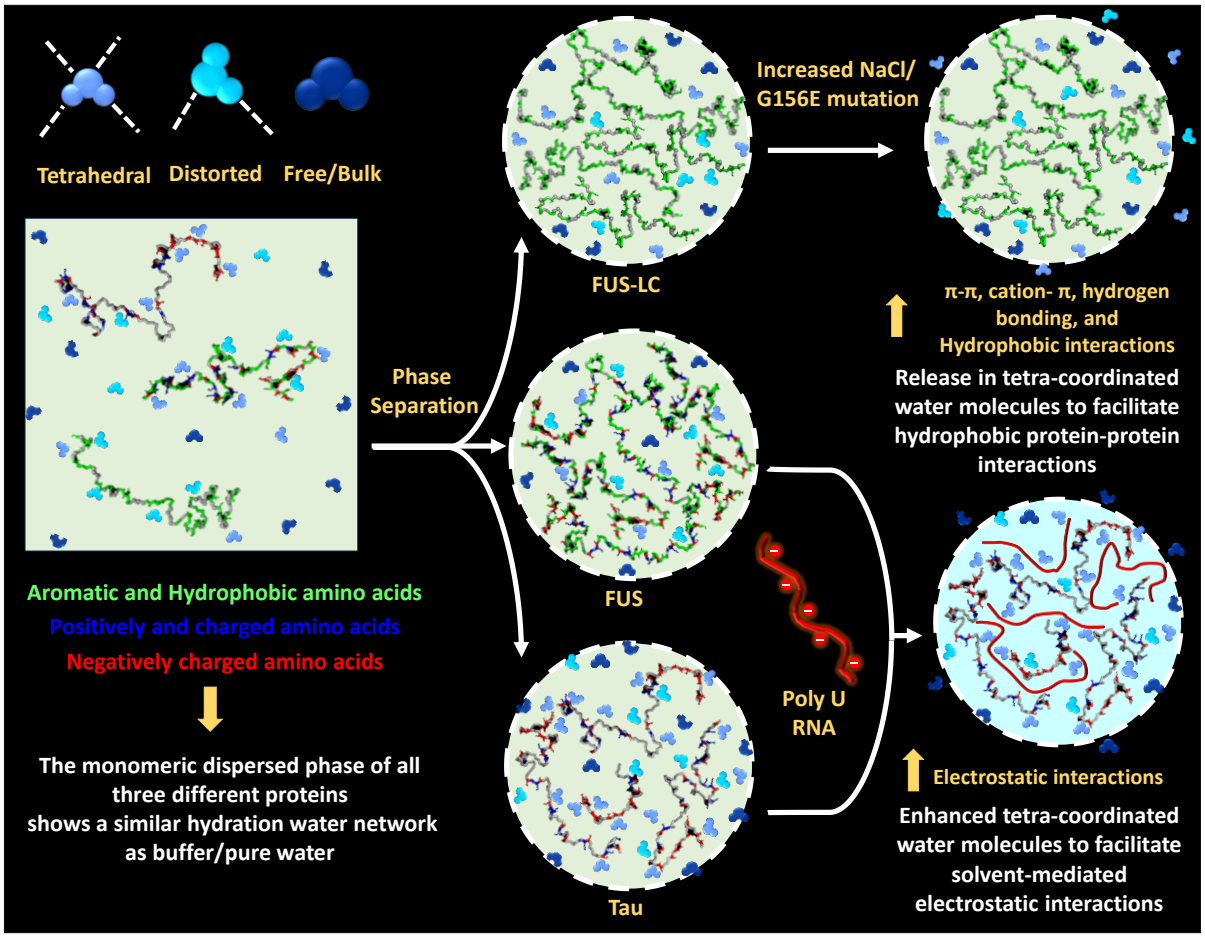

Figure 3.12. An overview of our single-droplet vibrational Raman spectroscopy illustrating the sequence-dependent changes in hydrogen bonding states of water molecules within the condensates of FUS-LC, full-length FUS, and tau.

Thus, in the case of phase separation dominated by aromatics (π-π and cation-π contacts) and hydrogen bonding interactions, the entropic gain associated with the release of this bound water

can, in turn, provide the thermodynamic driving force for the entropically unfavorable process of condensate formation. Surprisingly, we obtained a similar reduction in tetra-coordinated water molecules within the condensates of tau, where electrostatic interactions constitute the major intermolecular contacts governing phase separation. However, this release was significantly reduced compared to the FUS droplets, indicating partial retainment of tetrahedral water molecules bound to the polypeptide chain within tau condensates. This retention of structured water accompanied by a reduction in the free water content within condensates of tau is associated with a loss of entropy and is not thermodynamically favorable by itself. However, the entropic costs for this process can be compensated for by the formation of enthalpically favorable solvent-mediated ionic interactions in the case of proteins highly enriched in oppositely charged residues, such as tau. For both FUS and tau, an enhanced coordination of water molecules was observed for condensates formed in the presence of increasing polyanion concentration, i.e., polyU RNA. The heterotypic tau:RNA condensates exhibited a relatively higher retention of tetra-coordinated water compared to the FUS-RNA condensates. This can be explained as the combined effect of homotypic and heterotypic electrostatic interactions within tau condensates[84] and a tug-of-war between the diverse protein-protein and electrostatic protein-RNA interactions within the condensates of FUS. Taken together, the release of water molecules within the hydration shell of the hydrophilic and hydrophobic amino acids of protein polypeptide chains can be expected to be a general phenomenon facilitating the formation of an extensive network of intermolecular contacts, which can potentially assist in overcoming the percolation threshold eventually leading to phase separation[6]. In summary, our work elucidates the sequence-directed reorganization of the hydrogen bonding network of water molecules within biomolecular condensates of archetypal phase-separating proteins. These observations can be further extended to derive generalized principles regarding the hydration water network and decode the role of hydration water dynamics in altering various aspects of biomolecular condensates.

These single-droplet vibrational Raman measurements can serve as a potent tool for further detailed studies of the hydrogen bonding and structure of water in the form of a depth profile within droplets using a confocal Raman microscopy. The water structure can be employed as a reporter of the droplet interior and the nature of intermolecular interactions as a function of radial distribution within the condensates. By determining the water signature obtained in dynamic, liquid-like condensates and gel or solid-like aggregates, water vibrational Raman can act as a sensitive methodology to capture the spatial heterogeneity within

condensates. This can further assist in monitoring the inhomogeneous liquid-to-solid transition within condensates concerning the initiation and propagation of the conversion from dynamic liquid-like to irreversible, solid-like aggregates[85]. Several studies have employed short synthetic peptides (homo or heteropolymers of charged, aromatic or hydrophobic residues) for unraveling the complex interplay of sequence-encoded molecular drivers of phase separation[25,86]. Water vibrational Raman measurements within these condensates can illuminate the characteristic hydration water structures and the extent of hydrogen bonding within distinct condensates dominated by aromatic, hydrophobic, and electrostatic drivers. The protein sequence composition and interaction-dependent tuning of the hydration water network can be exploited to characterize the droplet interior due to point mutations, post-translational modifications, and other solution conditions such as pH, salt, temperature, and so forth. Owing to the direct noninvasive observation, vibrational water Raman signature can be successfully extended to probe the nature of such hydration water within a wide range of membraneless organelles formed within cells both of physiological and pathological significance.

3.5 References

1. Kilgore, H. R., & Young, R. A. Learning the chemical grammar of biomolecular condensates. *Nat. Chem. Biol*. **18,** 1298–1306 (2022).

2. Boeynaems S, Chong S, Gsponer J, Holt L, Milovanovic D, Mitrea DM, Mueller-Cajar O, Portz B, Reilly JF, Reinkemeier CD, Sabari BR, Sanulli S, Shorter J, Sontag E, Strader L, Stachowiak J, Weber SC, White M, Zhang H, Zweckstetter M, Elbaum-Garfinkle S, & Kriwacki R. Phase Separation in Biology and Disease; Current Perspectives and Open Questions. *J. Mol. Biol. **435,*** 167971 (2023).

3. Lyon, A. S., Peeples, W. B., & Rosen, M. K. A framework for understanding the functions of biomolecular condensates across scales. *Nat. Rev. Mol. Cell Biol.* **22,** 215–235 (2021).

4. Alberti, S., & Hyman, A. A. Biomolecular condensates at the nexus of cellular stress, protein aggregation disease and ageing *Nat. Rev. Mol. Cell Biol.* **22,** 196–213 (2021).

5. Boeynaems, S., Alberti, S., Fawzi, N. L., Mittag, T., Polymenidou, M., Rousseau, F., Schymkowitz, J., Shorter, J., Wolozin, B., Van Den Bosch, L., Tompa, P., & Fuxreiter, M. Protein Phase Separation: A New Phase in Cell Biology. *Trends Cell Biol*. **28,** 420-435 (2018).

6. Mittag, T., & Pappu, R. V. A conceptual framework for understanding phase separation and addressing open questions and challenges. *Mol. Cell* **82,** 2201–2214 (2022).

7. Choi, J. M., Holehouse, A. S., & Pappu, R. V. Physical principles underlying the complex biology of intracellular phase transitions. *Annu. Rev. Biophys.* **49,** 107–133 (2020).

8. Roden, C., & Gladfelter, A. S. RNA contributions to the form and function of biomolecular condensates. *Nat. Rev. Mol. Cell Biol.* **22,** 183–195 (2021).

9. Yu, M., Heidari, M., Mikhaleva, S., Tan, P. S., Mingu, S., Ruan, H., Reinkemeier, C. D., Obarska-Kosinska, A, Siggel, M., Beck, M., Hummer, G., & Lemke, E. A. Visualizing the disordered nuclear transport machinery in situ. *Nature* **617,** 162-169 (2023).

10. Dignon, G. L., Best, R. B., & Mittal, J. Biomolecular phase separation: From molecular driving forces to macroscopic properties. *Annu. Rev. Phys. Chem.* **71,** 53–75 (2020).

11. Shapiro, D. M., Ney, M., Eghtesadi, S. A., & Chilkoti, A. Protein phase separation arising from intrinsic disorder: First-principles to bespoke applications. *J. Phys. Chem. B* **125,** 6740–6759 (2021).

12. Mitrea, D. M., Cika, J. A., Guy, C. S., Ban, D., Banerjee, P. R., Stanley, C. B., Nourse, A., Deniz, A. A., & Kriwacki, R. W. Nucleophosmin integrates within the nucleolus via multi-modal interactions with proteins displaying R-rich linear motifs and rRNA. *eLife* **5,** (2016).

13. Martin, E. W., & Mittag, T. Relationship of sequence and phase separation in protein low-complexity regions. *Biochem.* **57,** 2478–2487 (2018).

14. Shin, Y., & Brangwynne, C. P. Liquid phase condensation in cell physiology and disease. *Science* **357,** (2017).

15. Martin, E. W., Holehouse, A. S., Peran, I., Farag, M., Incicco, J. J., Bremer, A., Grace, C. R., Soranno, A., Pappu, R. V., & Mittag, T. Valence and patterning of aromatic residues determine the phase behavior of prion-like domains. *Science* **367,** 694-699 (2020).

16. Mitrea, D. M., & Kriwacki, R. W. Phase separation in biology; functional organization of a higher order. *Cell Commun. Signal.* **14,** (2016).

17. Mukhopadhyay, S. The dynamism of intrinsically disordered proteins: Binding induced folding, amyloid formation, and phase separation. *J. Phys. Chem. B* **124,** 11541–11560 (2020).

18. Vendruscolo, M., & Fuxreiter, M. Protein condensation diseases: therapeutic opportunities. *Nat. Commun.* **13,** (2022).

19. Bhopatkar, A. A., Dhakal, S., Abernathy, H. G., Morgan, S. E., & Rangachari, V. Charge and redox states modulate granulin-TDP-43 coacervation toward phase separation or aggregation. *Biophys. J.* **121,** 2107-2126 (2022).

20. Dhakal, S., Wyant,C. E.,George, H. E.,Morgan, S. E., & Rangachari, V. Prion-like C-terminal domain of TDP-43 and α-synuclein interact synergistically to generate neurotoxic hybrid fibrils. *J. Mol. Biol.* **433,** 166953 (2021).

21. Ruff, K. M., Choi, Y. H., Cox, D., Ormsby, A. R., Myung, Y., Ascher, D. B., Radford, S. E., Pappu, R. V., & Hatters, D. M. Sequence grammar underlying the unfolding and phase separation of globular proteins. *Mol. Cell.* **82,** 3193-3208 (2022).

22. Brangwynne, C. P., Tompa, P., & Pappu, R. V. Polymer physics of intracellular phase transitions. *Nat. Phys.* **11,** 899–904 (2015).

23. Uversky, V. N. Intrinsically disordered proteins in overcrowded milieu: Membrane-less organelles, phase separation, and intrinsic disorder. *Curr. Opin. Struct. Biol.* **44,** 18–30 (2017).

24. Vernon, R. M., Chong, P. A., Tsang, B., Kim, T. H., Bah, A., Farber, P., Lin, H., & Forman-Kay, J. D. Pi-Pi contacts are an overlooked protein feature relevant to phase separation. *eLife* **9,** e31486 (2018).

25. Kaur, T., Raju, M., Alshareedah, I., Davis, R. B., Potoyan, D. A., & Banerjee, P. R. Sequence-encoded and composition-dependent protein-RNA interactions control multiphasic condensate morphologies. *Nat. Commun.* **12,** 872 (2021).

26. Lorenz-Ochoa K., & Baiz, C. Ultrafast Spectroscopy Reveals Slow Water Dynamics in Biocondensates. *J. Am. Chem. Soc.* **145,** 27800-27809 (2023).

27. Mondal, S., & Bagchi, B. From structure and dynamics to biomolecular functions: The ubiquitous role of solvent in biology. *Curr. Opin. Struct. Biol.* ***77,*** 102462 (2022).

28. Xi, E., Venkateshwaran, V., Li, L., Rego, N., Patel, A. J., & Garde, S. Hydrophobicity of proteins and nanostructured solutes is governed by topographical and chemical context. *Proc. Natl. Acad. Sci. U.S.A.* **114,** 13345-13350 (2017).

29. Shin, S., & Willard, A. P. Characterizing Hydration Properties Based on the Orientational Structure of Interfacial Water Molecules. *J. Chem. Theory Comput*. **14,** 461-465 (2018).

30. Conti, Nibali, V., & Havenith, M. New insights into the role of water in biological function: studying solvated biomolecules using terahertz absorption spectroscopy in conjunction with molecular dynamics simulations. *J. Am. Chem. Soc*. **136,** 12800-12807 (2014).

31. Arya, S., Singh, A. K., Bhasne, K., Dogra, P., Datta, A., Das, P., & Mukhopadhyay, S. Femtosecond Hydration Map of Intrinsically Disordered α-Synuclein. *Biophys. J*. **114,** 2540-2551 (2018).

32. Laage, D., Elsaesser, T., & Hynes, J. T. Water Dynamics in the Hydration Shells of Biomolecules. *Chem. Rev.* ***117,*** 10694–10725 (2017).

33. Reid, K. M., Singh, A. K., Bikash, C. R., Wei, J., Tal-Gan, Y., Vinh, N. Q., & Leitner, D. M. The origin and impact of bound water around intrinsically disordered proteins. *Biophys. J.* ***121,*** 540–551 (2022).

34. Arya, S., Singh, A. K., Khan, T., Bhattacharya, M., Datta, A., & Mukhopadhyay, S. Water Rearrangements upon Disorder-to-Order Amyloid Transition. *J. Phys. Chem. Lett.* ***7,*** 4105–4110 (2016).

35. Zaslavsky, B. Y., & Uversky, V. N. In aqua veritas: the indispensable yet mostly ignored role of water in phase separation and membrane-less organelles. *Biochem.* ***57,*** 2437–2451 (2018).

36. Ribeiro, S. S., Samanta, N., Ebbinghaus, S., & Marcos, J. C. The synergic effect of water and biomolecules in intracellular phase separation. *Nat. Rev. Chem.* **3,** 552–561 (2019).

37. Ahlers, J., Adams, E. M., Bader, V., Pezzotti, S., Winklhofer, K. F., Tatzelt, J., & Havenith, M. The key role of solvent in condensation: Mapping water in liquid-liquid phase-separated FUS. *Biophys. J.* ***120,*** 1266–1275 (2021).

38. Yokosawa, K., Kajimoto, S., Shibata, D., Kuroi, K., Konno, T., & Nakabayashi, T. Concentration quantification of the low-complexity domain of fused in sarcoma inside a single droplet and effects of solution parameters. *J. Phys. Chem. Lett.* **13,** 5692-5697 (2022).

39. Yokosawa, K., Tsuruta, M., Kajimoto, S., Sugimoto, N., Miyoshi, D., & Nakabayashi, T. Quantification of the concentration in a droplet formed by liquid–liquid phase separation of G-quadruplex-forming RNA, *Chem. Phys. Lett.* **826,** 140634 (2023).

40. Choe, C., Lademann, J., & Darvin, M. E. Depth profiles of hydrogen bound water molecule types and their relation to lipid and protein interaction in the human stratum corneum in vivo. *Analyst* **141,** 6329-6337 (2016).

41. Mangiarotti, A., Siri, M., Tam, N. W., Zhao, Z., Malacrida, L., & Dimova, R. Biomolecular condensates modulate membrane lipid packing and hydration. *Nat. Commun.* **14,** 6081 (2023).

42. Mangiarotti, A., & Bagatolli, L. A. Impact of macromolecular crowding on the mesomorphic behavior of lipid self-assemblies. *Biochim. Biophys. Acta. Biomembr.* **1863,** 183728 (2021).

43. Hu, Q., Zhao, H., & Ouyang, S. Understanding water structure from Raman spectra of isotopic substitution H2O/D2O up to 573 K. *Phys. Chem. Chem. Phys.* **19,** 21540-21547 (2017).

44. Ahmed, M., Namboodiri, V., Singh, A. K., Mondal, J. A., & Sarkar, S. K. How ions affect the structure of water: a combined Raman spectroscopy and multivariate curve resolution study. *J. Phys. Chem. B.* **117,** 16479-85 (2013).

45. Malfait, B., Moréac, A., Jani, A., Lefort, R., Huber, P., Fröba, M., & Morineau, D. Structure of Water at Hydrophilic and Hydrophobic Interfaces: Raman Spectroscopy of Water Confined in Periodic Mesoporous (Organo)Silicas. *J. Phys. Chem. C* **126,** 3520–3531 (2022).

46. Hu, Q., Lü., X., Lu, W., Chen, Y., & Liu, H. An extensive study on Raman spectra of water from 253 to 753K at 30MPa: A new insight into structure of water. *J. Mol. Spectrosc.* **292,** 23-27 (2013).

47. Sun, Q. Local statistical interpretation for water structure. *Chem. Phys. Lett.* **568,** 90–94 (2013).

48. Svetoni, F., Frisone, P. & Paronetto, M. P. Role of FET proteins in neurodegenerative disorders. *RNA Biol.* **13,** 1089–1102 (2016).

49. Murthy, A. C., Dignon, G. L., Kan, Y., Zerze, G. H., Parekh, S. H., Mittal, J., & Fawzi, N. L. Molecular interactions underlying liquid-liquid phase separation of the FUS low-complexity domain. *Nat. Struct. Mol. Biol.* **26,** 637–648 (2019).

50. Burke, K. A., Janke, A. M., Rhine, C. L., & Fawzi, N. L. Residue-by-Residue View of In Vitro FUS Granules that Bind the C-Terminal Domain of RNA Polymerase II. *Mol Cell.* **60**, 231–241 (2015).

51. Murthy, A. C., Tang, W. S., Jovic, N., Janke, A. M., Seo, D. H., Perdikari, T. M., Mittal, J., & Fawzi, N. L. Molecular interactions contributing to FUS SYGQ LC-RGG phase separation and co-partitioning with RNA polymerase II heptads. *Nat Struct Mol Biol.* **28**, 923–935 (2021).

52. Qamar, S., Wang, G., Randle, S. J., Ruggeri, F. S., Varela, J. A., Lin, J. Q., Phillips, E. C., Miyashita, A., Williams, D., Ströhl, F., Meadows, W., Ferry, R., Dardov, V. J., Tartaglia, G. G., Farrer, L. A., Kaminski Schierle, G. S., Kaminski, C. F., Holt, C. E., Fraser, P. E., Schmitt-Ulms, G., Klenerman, D., Knowles, T., Vendruscolo, M., & St George-Hyslop, P. FUS phase separation is modulated by a molecular chaperone and methylation of arginine cation-π interactions. *Cell* **173,** 720–734 (2018).

53. Murray, D. T., Kato, M., Lin, Y., Thurber, K.R., Hung, I., McKnight, S. L., & Tycko, R. Structure of FUS protein fibrils and its relevance to self-assembly and phase separation of low-complexity domains. *Cell* **171,** 615-627 (2017).

54. Li, R., Jiang, Z., Guan, Y., Yang, H., & Liu, B. Effects of metal ion on the water structure studied by the Raman O-H stretching spectrum. *J. Raman Spectrosc*. **40,** 1200-1204 (2009).

55. Berkeley, R. F., Kashefi, M., & Debelouchina, G. T. Real-time observation of structure and dynamics during the liquid-to-solid transition of FUS LC. *Biophys. J.* **120,** 1276-1287 (2021).

56. Rhine, K., Makurath, M. A., Liu, J., Skanchy, S., Lopez, C., Catalan, K. F., Ma, Y., Fare, C. M., Shorter, J., Ha, T., Chemla, Y. R., & Myong, S. ALS/FTLD-linked mutations in FUS glycine residues cause accelerated gelation and reduced interactions with wild-type FUS. *Mol. Cell* **19,** 666-681 (2020).

57. Patel, A., Lee, H. O., Jawerth, L., Maharana, S., Jahnel, M., Hein, M. Y., Stoynov, S., Mahamid, J., Saha, S., Franzmann, T. M., Pozniakovski, A., Poser, I., Maghelli, N., Royer, L. A., Weigert, M., Myers, E. W., Grill, S., Drechsel, D., Hyman, A. A., & Alberti, S. A liquid-to-solid phase transition of the ALS protein FUS accelerated by disease mutation. *Cell* **27,** 1066-77 (2015).

58. Joshi, A., Walimbe, A., Avni, A., Rai, S. K., Arora, L., Sarkar, S., & Mukhopadhyay, S. Single-molecule FRET unmasks structural subpopulations and crucial molecular events during phase separation of a prion-like low-complexity domain. *Nat. Commun.* **14,** 7331 (2023).

59. Wang, J., Choi, J. M., Holehouse, A. S., Lee, H. O., Zhang, X., Jahnel, M., Maharana, S., Lemaitre, R., Pozniakovsky, A., Drechsel, D., Poser, I., Pappu, R. V., Alberti, S., & Hyman, A. A. A molecular grammar governing the driving forces for phase separation of prion-like RNA binding proteins. *Cell* **174,** 688–699 (2018).

60. Svetoni, F., Frisone, P., & Paronetto, M. P. Role of FET proteins in neurodegenerative disorders. *RNA Biol.* **13,** 1089–1102 (2016).

61. Krainer, G., Welsh, T. J., Joseph, J. A., Espinosa, J. R., Wittmann, S., de Csilléry, E., Sridhar, A., Toprakcioglu, Z., Gudiškytė, G., Czekalska, M. A., Arter, W. E., Guillén-Boixet, J., Franzmann, T. M., Qamar, S., George-Hyslop, P. S., Hyman, A. A., Collepardo-Guevara, R., Alberti, S., & Knowles, T. P. J. Reentrant liquid condensate phase of proteins is stabilized by hydrophobic and non-ionic interactions. *Nat. Commun.* **12**, 1085 (2021).

62. Loughlin, F. E., Lukavsky, P. J., Kazeeva, T., Reber, S., Hock, E. M., Colombo, M., Schroetter, C. V., Pauli, P., Cléry, A., Mühlemann, O., Polymenidou, M., Ruepp, M. D., & Allain, F. H. T. The solution structure of FUS bound to RNA reveals a bipartite mode of RNA recognition with both sequence and shape specificity. *Mol. Cell* **73,** 490–504.e6 (2019).

63. Hofweber, M., Phase separation of FUS is suppressed by its nuclear import receptor and arginine methylation. *Cell* **173**, 706–719 (2018).

64. Park, S., Lee, Y., Jho, Y., & Hwang, D. S. Molecular Hydration Tunes the Cation–π Interaction Strength in Aqueous Solution. *Adv. Mater. Interfaces* **10,** 2201732 (2023).

65. Limorenko, G., & Lashuel, H. A. Revisiting the grammar of Tau aggregation and pathology formation: How new insights from brain pathology are shaping how we study and target Tauopathies. *Chem. Soc. Rev.* **51,** 513–565 (2022).

66. Guo, T., Noble, W., & Hanger, D. P. Roles of tau protein in health and disease. *Acta Neuropathol.* **133,** 665–704 (2017).

67. Rai, S. K., Savastano, A., Singh, P., Mukhopadhyay, S., & Zweckstetter, M. Liquid-liquid phase separation of tau: From molecular biophysics to physiology and disease. *Protein Sci.* **30,** 1294–1314 (2021).

68. Mandelkow, E. M., & Zandelkow, E. Biochemistry and cell biology of tau protein in neurofibrillary degeneration. *Cold Spring Harb. Perspect. Med.* **2,** a006247 (2012).

69. Wen, J., Hong, L., Krainer, G., Yao, Q. Q., Knowles, T. P. J., Wu, Si., & Perrett, S. Conformational expansion of tau in condensates promotes irreversible aggregation. *J. Am. Chem. Soc.* **143,** 13056–13064 (2021).

70. Ambadipudi, S., Biernat, J., Riedel, D., Mandelkow, E., & Zweckstetter, M. Liquid-liquid phase separation of the microtubule-binding repeats of the Alzheimer-related protein Tau. *Nat. Commun.* **8,** 275 (2017).

71. Majumdar, A., Dogra, P., Maity, S., Mukhopadhyay, S. Liquid-liquid phase separation is driven by large-scale conformational unwinding and fluctuations of intrinsically disordered protein molecules. *J. Phys. Chem. Lett.* **10,** 3929–3936 (2019).

72. Wegmann, S., Eftekharzadeh, B., Tepper, K., Zoltowska, K. M., Bennett, R. E., Dujardin, S., Laskowski, P. R., MacKenzie, D., Kamath, T., Commins, C., Vanderburg, C., Roe, A. D., Fan, Z., Molliex, A. M., Hernandez-Vega, A., Muller, D., Hyman, A. A., Mandelkow, E., Taylor, J. P., & Hyman, B. T. Tau protein liquid-liquid phase separation can initiate tau aggregation. *EMBO J.* **37,** e98049 (2018).

73. Kanaan, N. M., Hamel, C., Grabinski, T., & Combs, B. Liquid-liquid phase separation induces pathogenic tau conformations in vitro. *Nat. Commun.* **11,** 2809 (2020).

74. Rai, S. K., Khanna, R., Avni, A., & Mukhopadhyay S. Heterotypic electrostatic interactions control complex phase separation of tau and prion into multiphasic condensates and co-aggregates. *Proc. Natl. Acad. Sci. U.S.A.* **120,** e2216338120 (2023).

75. Sabarinathan, R., Aishwarya, K., Sarani, R., Vaishnavi, M. K., & Sekar, K. Water-mediated ionic interactions in protein structures. *J. Biosci.* **36,** 253-63 (2011).

76. Sabari, B. R., Dall'Agnese, A., & Young, R. A. Biomolecular condensates in the nucleus. *Trends Biochem. Sci.* **45,** 961–977 (2020).

77. Sanders, D. W., Kedersha, N., Lee, D. S. W., Strom, A. R., Drake, V., Riback, J. A., Bracha, D., Eeftens, J. M., Iwanicki, A., Wang, A., Wei, M. T., Whitney, G., Lyons, S. M., Anderson, P., Jacobs, W. M., Ivanov, P., & Brangwynne, C. P. Competing protein-RNA interaction networks control multiphase intracellular organization. *Cell* **181,** 306-324 (2020).

78. Silva, J. L., & Cordeiro, Y. The "Jekyll and Hyde" actions of nucleic acids on the prion-like aggregation of proteins. *J. Biol. Chem.* **291,** 15482-15490 (2016).

79. Zhang, H., Li, C., Yang, F., Su, J., Tan, J., Zhang, X., & Wang, C. Cation-pi interactions at non-redundant protein–RNA interfaces. *Biochemistry **79,*** 643–652 (2014).

80. Wilson, K. A., Holland, D. J., & Wetmore, S. D. Topology of RNA-protein nucleobase-amino acid π-π interactions and comparison to analogous DNA-protein π-π contacts. *RNA **22,*** 696–708 (2016).

81. Mukherjee, S., & Schäfer, L. V. Thermodynamic forces from protein and water govern condensate formation of an intrinsically disordered protein domain. *Nat. commun. **14,*** 5892 (2023).

82. Pezzotti, S., König, B., Ramos, S., Schwaab, G., & Havenith, M. Liquid-Liquid Phase Separation? Ask the Water! *J. Phys. Chem. Lett. **14,*** 1556–1563 (2023).

83. Thirumalai D, Kumar A, Chakraborty D, Straub JE, Mugnai ML. Conformational fluctuations and phases in fused in sarcoma (FUS) low-complexity domain. *Biopolymers,* (2023).

84. Ukmar-Godec, T., Hutten, S., Grieshop, M. P., Rezaei-Ghaleh, N., Cima-Omori, M. S., Biernat, J., Mandelkow, E., Söding, J., Dormann, D., & Zweckstetter, M. Lysine/RNA-interactions drive and regulate biomolecular condensation. *Nat. commun.* ***10,*** 2909 (2019).

85. Shen, Y., Chen, A., Wang, W., Shen, Y., Ruggeri, F. S., Aime, S., Wang, Z., Qamar, S., Espinosa, J. R., Garaizar, A., St George-Hyslop, P., Collepardo-Guevara, R., Weitz, D. A., Vigolo, D., & Knowles, T. P. J. The liquid-to-solid transition of FUS is promoted by the condensate surface. *Proc. Natl. Acad. Sci. U.S.A.* ***120,*** e2301366120 (2023).

86. Abbas, M., Lipiński, W. P., Nakashima, K. K., Huck, W. T. S., & Spruijt, E. A short peptide synthon for liquid-liquid phase separation. *Nat. Chem*. **13**, 1046-1054 (2021).

******

Intermolecular Energy Migration via HomoFRET Captures the Modulation in the Material Property of Phase-Separated Biomolecular Condensates

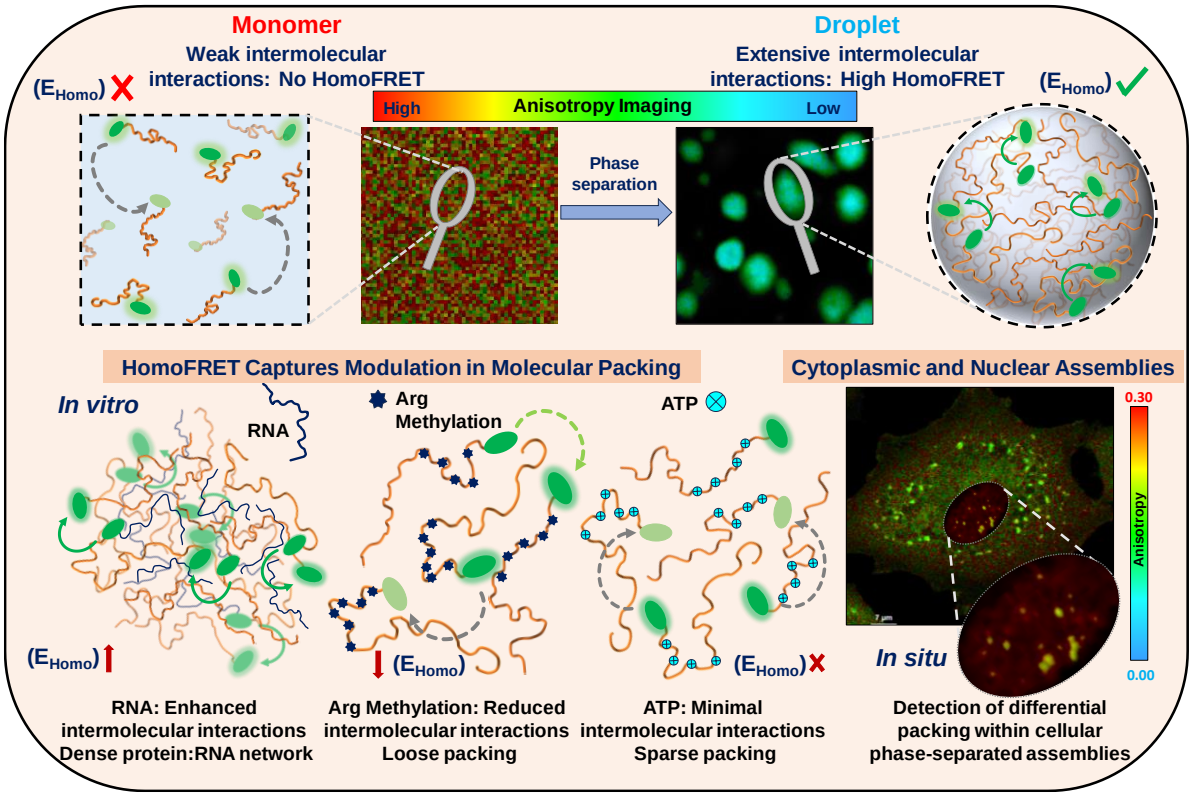

Joshi A, Walimbe A, Sarkar S, Arora L, Kaur G, Jhandai P, Chatterjee D, Banerjee I, & Mukhopadhyay S. Intermolecular energy migration via homoFRET captures the modulation in the material property of phase-separated biomolecular condensates (*bioRxiv 2024*).

4.1 Introduction

Biomolecular condensation involves the formation of dynamic, liquid-like assemblies via the phase separation of proteins in association with nucleic acids. These membraneless organelles or MLOs achieve cellular compartmentalization and facilitate the spatiotemporal organization of an array of critical cellular processes across organisms[1-10]. The class of proteins termed intrinsically disordered proteins or regions (IDPs/IDRs) with or without nucleic acids form dynamic, liquid-like, selectively permeable, non-stoichiometric assemblies such as stress granules, germ granules, P bodies, Cajal bodies, nuclear paraspeckles, etc., which are closely associated with critical cellular functions, including cellular signaling, regulation, genome organization, transcription translation, and immune responses[6,8,11-18]. These tightly regulated assemblies, when dysregulated, lead to the formation of irreversible solid-like aggregates associated with several neuropathological disorders, including Alzheimer's disease, amyotrophic lateral sclerosis (ALS), and frontotemporal lobar degeneration (FTLD), so on[14,15,19,20]. Thus, the need to uncover the molecular drivers that govern the fate of these supramolecular assemblies by modulating their material properties has led to the development of a multitude of techniques for investigating their diffusion characteristics, viscoelasticity, molecular packaging, nanoscale organization, and so on. Several microscopic techniques like fluorescence recovery after photobleaching (FRAP), fluorescence loss in photobleaching (FLIP), atomic force microscopy (AFM), etc., have been adapted to probe condensate properties, such as morphology, fusion, size distribution, and diffusion properties[21,22]. Additionally, certain microfluidic-based approaches, along with passive microrheology, monitor the diffusion of beads within the condensates or dense phase. These techniques can be successfully performed within condensates of significantly larger sizes or the ensemble condensed phase after the careful selection and processing of the beads[21,22]. However, majority of the aforementioned methodologies lack non-invasive, broader application and the ability to illuminate the condensate organization at the nanoscale, crucial in dictating the mesoscopic properties and the fate of condensates.

Similarly, Förster Resonance Energy Transfer (FRET) is an alternative technique to study the protein-protein interactions quantitively[23-25]. The typically used heteroFRET utilizes two FRET-compatible fluorophores covalently linked at specific positions to the protein chain, which proves a cumbersome task, especially when performing cellular studies. On the contrary, tagging the proteins of interest with fluorescent proteins is an extensively used methodology for studies investigating the expression, localization, functioning, and protein-

protein interactions within cells. Along these lines, homoFRET, a special case of FRET, utilizes a single fluorophore with a small Stokes' shift and a significant overlap between its fluorescence excitation and emission spectrum and has been previously captured in the form of fluorescence depolarization or loss in anisotropy as a function of local fluorophore densities[26-30]. Thus, homoFRET can be employed to investigate the proximal and distal molecular packaging within mesoscopic supramolecular assemblies such as phase-separated biomolecular condensates. Here, we demonstrate the application of a simple and versatile technique of anisotropy imaging to study homoFRET as a readout for the internal architecture and supramolecular packing governed by the intermolecular interactions and nanoscale clustering within the dynamic biomolecular condensates. HomoFRET imaging captures the enhanced excited state energy migration indicating the reduced intermolecular distances and densely-packed organization within the condensates of an archetypal phase separating protein Fused in Sarcoma (FUS). In conjunction to anisotropy imaging, our picosecond time-resolved anisotropy measurements allow us to discern the components of fluorescence depolarization originating from diverse modes of energy migration. Our steady-state anisotropy imaging also sheds light on the role of small-molecule phase-separation modulators such as RNA and ATP, along with post-translational modifications in altering the protein-protein associations and thus, the molecular packaging within these dynamic assemblies of FUS. The anisotropy decay kinetics and corresponding time constants obtained within these droplets further illuminate molecular events and condensate properties responsible for facilitating energy migration via homoFRET. Lastly, we also show the utility of anisotropy imaging within phase-separated assemblies of FUS formed *in situ*, under diverse cellular conditions. The anisotropy imaging tool to detect homoFRET in condensates can provide a highly sensitive and potent tool for the preliminary detection of the diverse complex biomolecular condensates formed *in vitro* and within cells and further illuminate their internal molecular organization and packaging.

4.2 Experimental details

4.2.1 Materials

The catalog numbers for all the materials are mentioned in parentheses. Sodium phosphate monobasic dihydrate (P9791), sodium phosphate dibasic dihydrate (71643), 2-mercaptoethanol (β-mercaptoethanol) (M3148), 1,4-dithiothreitol (DTT) (43815), sodium meta arsenite (S7400), S-adenosyl-L-methionine (SAM) (A2408), polyuridylic acid potassium salt (polyU

RNA of 800–1000 kDa molecular weight; P9528), adenosine-5′-triphosphate disodium salt hydrate (ATP) (A26209), tris-HCl (trizma hydrochloride; T3253), polybrene infection/transfection reagent (TR-1003), paraformaldehyde (158127), polyethylenimine (PEI), branched (408727), Lysozyme from chicken egg white (L4919), molecular biology grade purity, were procured from Sigma (St. Louis, MO, USA). Luria Bertani broth, miller (LB) (M1245), magnesium chloride hexahydrate (MB040), ethylenediaminetetraacetic acid (EDTA) (MB011), and nickel chloride (GRM1394), D-(+)- maltose monohydrate (GRM3050), zinc chloride (MB046), HEPES (MB016), imidazole (GRM559), glycerol (MB060), PIPES (PCT1530), EGTA (MB130) were purchased from HiMedia Laboratories. Kanamycin (K-120-10), Ampicillin (A-301-100), Chloramphenicol (C-105-25), and Streptomycin (S-150-100) were obtained from Gold Biocom (USA). VWR® Micro Cover Glasses 12 mm, Round, No. 2 (89015-725), glass coverslips were used for cell culture. GeneJET Plasmid Miniprep Kit (K0503), GeneJET Gel Extraction Kit (K0692), Lipofectamine LTX with PLUS Reagent (A12621), 3500 MWCO SnakeSkin Dialysis Tubing (68035) Gibco™ DMEM High Glucose (11965092), Gibco™ fetal bovine serum heat inactivated (FBS HI; A5256801), Invitrogen DAPI (4′,6-diamidino-2-phenylindole, Dihydrochloride; D1306), Invitrogen Fluoromount-G™ Mounting Medium (00-4958-02), Gibco™ GlutaMAX supplement (35050061), Gibco™ Sodium pyruvate 100 mM (11360070), Gibco™ MEM NEAA 100X (Non-Essential Amino Acids; 11140050), Gibco™ HEPES 1M (15630080), Gibco™ Antibiotic-Antimycotic 100X (15240062) were obtained from Thermo Fisher SCIENTIFIC. Corning T25 Flask (CLS430639), Corning 6 well plate (CLS3516), PMSF (phenylmethylsulfonyl fluoride, Roche - 11359061001), sodium chloride (1.93206.0521), potassium chloride (1.93238.0521) were purchased from Merck. Amicon® Ultra Centrifugal Filter, 10 kDa MWCO (UFC9010) for concentrating protein were obtained from Merck Millipore. Isopropyl-β- thiogalactopyranoside (IPTG; RC1113A) was obtained from G-Biosciences.

4.2.2 Construct details

The plasmids for full-length FUS (pMal-*Tev*-FUS-*Tev*-His_6), FUS-eGFP (pMal-*Tev*-FUS-EGFP-*Tev*-His_6), and PRMT1 (pET28b-PRMT1) were a kind gift from Prof. Dorothee Dormann (Johannes Gutenberg University of Mainz, Germany).

4.2.3 Recombinant protein expression and purification

The plasmids pMal-*Tev*-FUS-*Tev*-His_6 and pMal-*Tev*-FUS-EGFP-*Tev*-His_6 were transformed into *E. coli* BL21(DE3) RIPL bacterial strain, for overexpressing MBP-*Tev*-FUS-*Tev*-His_6 (referred to as FUS hereafter) and MBP-*Tev*-FUS-EGFP-*Tev*-His_6 (referred as FUS-eGFP hereafter) respectively. Overexpressed recombinant FUS and FUS-eGFP were purified by using tandem Ni-NTA and amylose resin affinity chromatography. For FUS and FUS-eGFP overexpression, bacterial cultures were grown in LB media at 37 °C, 220 rpm till an $O.D._{600}$ of 0.8–1, and protein expression was induced by adding 0.1 mM isopropyl-β-thiogalactopyranoside (IPTG) at 12 °C, 220 rpm for 22 h. Bacterial cells were harvested by centrifuging at 4 °C, 3220 × *g* for 40 min. Cell pellets were stored at −80 °C for further use. For purification, pellets were resuspended in lysis buffer (50 mM sodium phosphate, 300 mM NaCl, 40 mM imidazole, 10 µM $ZnCl_2$, 4 mM BME, and 10% v/v glycerol, pH 8.0), and bacterial cells were lysed by probe sonication at 5% amplitude, 15 s ON and 10 s OFF for 25 minutes. This bacterial whole-cell lysate was centrifuged at 4 °C, 15,557 × *g* for 1 h, to obtain the supernatant, which was then incubated with lysis buffer equilibrated Ni-NTA agarose beads for 1.5 h at 4 °C. The beads were washed with lysis buffer and protein was eluted in lysis buffer added with 250 mM imidazole, followed by binding to the amylose resin. Protein was eluted from amylose resin with 20 mM maltose elution buffer (50 mM sodium phosphate, 800 mM NaCl, 40 mM imidazole, 10 µM $ZnCl_2$, 20 mM maltose, and 1 mM 1,4-dithiothreitol, pH 8.0). The concentration of FUS and FUS-eGFP was estimated by measuring absorbance at 280 nm (ε_{280} FUS = 1,30,670 M^{-1} cm^{-1}, and ε_{280} FUS-eGFP = 1,50,560 M^{-1} cm^{-1}). Purified protein samples were run on SDS-PAGE gel to check protein purity. Purified proteins were temporarily stored at 4 °C and freshly concentrated for *in vitro* phase separation assays.

The pET28b-PRMT1 plasmid was transformed into *E. coli* BL21(DE3) std bacterial strain, for overexpressing His_6-PRMT1. For overexpression, bacterial cultures were grown in LB media till $O.D._{600}$ of 1, and protein expression was induced by adding 1 mM isopropyl-β-thiogalactopyranoside (IPTG) at 20°C, 220 rpm for 16 h. Bacterial cells were harvested by centrifuging at 4 °C, 3220 × *g* for 40 min, and pellets were stored at −80 °C for further use. For protein purification, pellets were resuspended in lysis buffer (50mM Tris-HCl pH 7.5, 150 mM NaCl, 20 mM imidazole, 4 mM BME, 20% glycerol), and bacterial cells were lysed by probe sonication at 5% amplitude, 15 s ON and 10 s OFF for 25 minutes. The cell lysate was centrifuged at 4 °C, 15,557 × *g* for 1 h, for separation of the insoluble cellular debris. The supernatant was passed through pre-equilibrated Ni-NTA agarose beads. The beads were

washed with a gradient of imidazole, and the protein was eluted in elution buffer (50 mM Tris-HCl pH 7.5, 1 M NaCl, 500 mM imidazole, 1 mM DTT). Protein was further purified and buffer exchanged by size exclusion chromatography using HiLoad 16/600 Superdex-G-200 (GE Healthcare) gel filtration column to storage buffer (50mM Tris-HCl pH 7.5, 150 mM NaCl, 20 mM imidazole, 4 mM BME, 20% glycerol) and stored at -80 °C for future use.

4.2.4 Phase separation assays

Phase separation of FUS and FUS-eGFP was induced by the addition of TEV protease (TEV: protein molar ratio of 1:10) in the phase separation buffer (20 mM HEPES, 1 mM DTT, pH 7.4) and incubated at room temperature for 10 min. For all phase separation experiments, total protein concentration was fixed at 10 μM, and for ratiometric measurements, the fraction of FUS-eGFP was varied from 1% to 100% (FUS-eGFP only droplet). For RNA-dependent anisotropy measurements, phase separation of 10 μM FUS (2 μM FUS-eGFP + 8 μM FUS) was set up in the presence of varying RNA concentrations (0 ng/μL, 25 ng/μL, 50 ng/μL, 75 ng/ μL, and 100 ng/μL polyU). To monitor the effect of methylation, phase separation of methylated FUS-eGFP was set up at a protein concentration of 10 μM for anisotropy measurements. For phase separation in the presence of ATP, FUS-eGFP droplet formation was induced in a buffer supplemented with $MgCl_2$ in the presence of 0 mM, 2.5 mM, 5 mM, and 10 mM ATP.

4.2.5 Steady-state anisotropy imaging

Anisotropy imaging was performed using our confocal-based MicroTime 200 time-resolved microscope to obtain single-droplet steady-state anisotropy values. A pulsed laser (485 nm, 20 MHz) and a Super Apochromat water immersion 60x objective (Olympus, NA 1.2) were used for performing anisotropy measurements in the dispersed and droplet phases. Droplet formation was induced under varying solution conditions (RNA, ATP, methylation) and incubated at room temperature for 10 min. Droplet reaction were spotted on a glass coverslip and allowed to settle on the surface. Upon excitation with the laser, the emitted fluorescence was split into two separate channels using a polarizing beam-splitter and directed to the single-photon counting avalanche diodes (SPADs). Anisotropy images were generated from the parallel and perpendicular counts after incorporating the correction factors using SymphoTime64 software v2.7. The steady-state anisotropy was calculated using eq^n (1) as follows;

$$r_{ss} = \frac{I_{\parallel} - I_{\perp}}{[1-3L2]I_{\parallel} + [2-3L1]I_{\perp}} \quad \ldots\ldots\ldots (1)$$

where $I_{\parallel}$ and $I_{\perp}$ are the parallel and perpendicular fluorescence intensities after background correction, and L1 (0.0308) and L2 (0.0368) account for the objective correction factors.
Based on the steady-state anisotropy values, energy migration efficiencies (E_{Homo}) within the condensates were calculated using eq^{n} (2) as follows[26];

$$E_{Homo} = 1 - \left(\frac{r}{r_0}\right) \ldots\ldots\ldots (2)$$

where r_0 and r are the calculated steady-state anisotropy values in the absence and presence of homoFRET. For FRET efficiency calculations, we used the monomeric steady-state anisotropy (non-homoFRET condition) value as the r_0.

4.2.6 Time-resolved anisotropy measurements

For the picosecond time-resolved fluorescence anisotropy measurements, freshly phase-separated FUS-eGFP droplets were settled, and fluorescence intensity was obtained in a droplet-by-droplet manner by focusing the pulsed laser inside individual droplets. The parallel and perpendicular intensity decay profiles were obtained and extracted using SymphoTime64 software v2.7 for further decay analysis to perform global fitting using eq^{n} (3) and (4),

$$I_{\parallel}(t) = 1/3I(t)[1 + 2r(t)] \quad \ldots\ldots\ldots (3)$$

$$I_{\perp}(t) = 1/3I(t)[1 - r(t)] \ldots\ldots\ldots (4)$$

where $I_{\parallel}$(t), $I_{\perp}$(t), and $I(t)$ can be defined as the time-dependent fluorescence intensities collected at the parallel, perpendicular, and magic angle (54.7°) geometry. The G-factor correction was incorporated for the perpendicular decay component, estimated by collecting the fluorescence intensity of free dye in the parallel and perpendicular channels using the anisotropy setup. The picosecond time-resolved fluorescence anisotropy decay were fitted using the suitable decay model (mono/bi/triexponential) based on the goodness of fit estimated from the autocorrelation function, randomness of residuals, and reduced $\chi 2$ values. The anisotropy decay kinetics were used to obtain energy migration time constants (ϕ_{EM}) and rotational correlation time (ϕ_r) as follows;

$$r(t) = r_0[\beta_r e^{\left(\frac{-t}{\phi_r}\right)} + \beta_{EM1} e^{\left(\frac{-t}{\phi_{EM1}}\right)} + \beta_{EM2} e^{\left(\frac{-t}{\phi_{EM2}}\right)} + \beta_{EM3} e^{\left(\frac{-t}{\phi_{EM3}}\right)}] \ldots\ldots\ldots (5)$$

where r_0 denotes the (time-zero) fundamental anisotropy of eGFP, and β_r, β_{EM1}, β_{EM2}, and β_{EM3} are the amplitudes associated with the rotational correlation time (ϕ_r), fast (ϕ_{EM1}), intermediate (ϕ_{EM2}), and slow (ϕ_{EM3}) energy migration time constants, respectively.

4.2.7 Time-dependent photobleaching anisotropy imaging

Phase separation of 10 μM FUS-eGFP was set up and incubated at room temperature for 10 min. Droplet solution (~ 50 μL) was spotted on the glass coverslip, and anisotropy imaging was performed at maximum laser power at fixed time intervals for up to 10 min. Steady-state anisotropy values were obtained for three independent reactions. Data represent the mean and standard deviation (n = 3).

4.2.8 *In vitro* methylation

Prior to setting up the methylation reaction, PRMT1 was buffer exchanged to the *in vitro* methylation buffer (IVM) (50 mM Na_2HPO_4, 150 mM NaCl, 5% glycerol, 1 mM EDTA, 1 mM DTT, pH 8.0) using a PD-10 column. Pure PRMT1 was concentrated using 10 KDa MWCO Amicon filters and used for the methylation of FUS-eGFP. Freshly purified FUS-eGFP was concentrated and washed with the IVM buffer prior to methylation. The methylation reaction was set up at a molar ratio of 1:2 (FUS-eGFP: PRMT1) in the presence of 1mM S-adenosyl-L-methionine (SAM) as the methyl donor in the IVM buffer and incubated at room temperature overnight. Methylated FUS-eGFP was concentrated freshly for droplet anisotropy measurements.

4.2.9 Fluorescence Recovery after Photobleaching (FRAP) Measurements

Phase separation of 10 μM FUS-eGFP was induced by the addition of TEV in the phase separation buffer (20 mM HEPES, 1 mM DTT, pH 7.4). Reactions were incubated at room temperature for 10 min, and a 10 μL sample was placed on a glass coverslip. FRAP experiments were performed on the ZEISS LSM 980 instrument using a 63× oil-immersion objective (NA 1.4). Droplets were allowed to settle, following which a region of diameter 1 μm was selected and bleached with the help of the green laser (488 nm laser diode) and the fluorescence was

monitored with time using a monochrome cooled high-resolution AxioCamMRm Rev. 3 FireWire(D) camera. The fluorescence recovery was recorded with the Zen Blue 3.2 (ZEISS) software, corrected for the background fluorescence, and plotted using the Origin software. FRAP measurements were obtained within the droplets of FUS-eGFP formed in the absence and presence of ATP and polyU RNA.

4.2.10 Cell culture, transfection, arsenite stress

A549 and HEK293T/17/17 cells for overexpression and stable expression of wild-type FUS and FUS ΔNLS were provided by Dr. Indranil Banerjee's lab (IISER Mohali). Cell preparation is not a part of this thesis.

4.3 Results

4.3.1 Mechanism and detection of excitation energy migration via HomoFRET

HomoFRET can be defined as energy migration from the excited state of a donor fluorophore to an acceptor fluorophore of similar chemical identity when two or more of them are placed proximally (Figure 4.1a). Excitation energy migration via homoFRET can be observed in the case of fluorophores with a small Stokes' shift and a significant overlap between the excitation and emission spectrum. HomoFRET involves energy transfer in a non-radiative but reversible manner, giving rise to a donor lifetime indistinguishable from the donor lifetime obtained in the absence of energy transfer. Hence, unlike heteroFRET, homoFRET cannot be detected by measuring a change in the donor lifetime as we observe an identical acceptor molecule in the same spectral region. Excitation with polarized light leads to similarly polarized emission in the case of zero energy transfer. However, in the case of homoFRET, energy migration to a fluorophore with a non-identically oriented dipole leads to a rapid depolarization of the emitted fluorescence. This fluorescence depolarization or loss in anisotropy can be easily captured by anisotropy imaging, where the overall extent of depolarization is determined by the local crowding or packing and is independent of the rotational diffusion of the fluorophore molecules (Figure 4.1a). This loss in anisotropy due to homoFRET is accompanied by the introduction of an additional faster component in the fluorescence anisotropy decay. This faster component is absent in the anisotropy decay observed under non-homoFRET conditions, provided by time-resolved fluorescence anisotropy measurements.

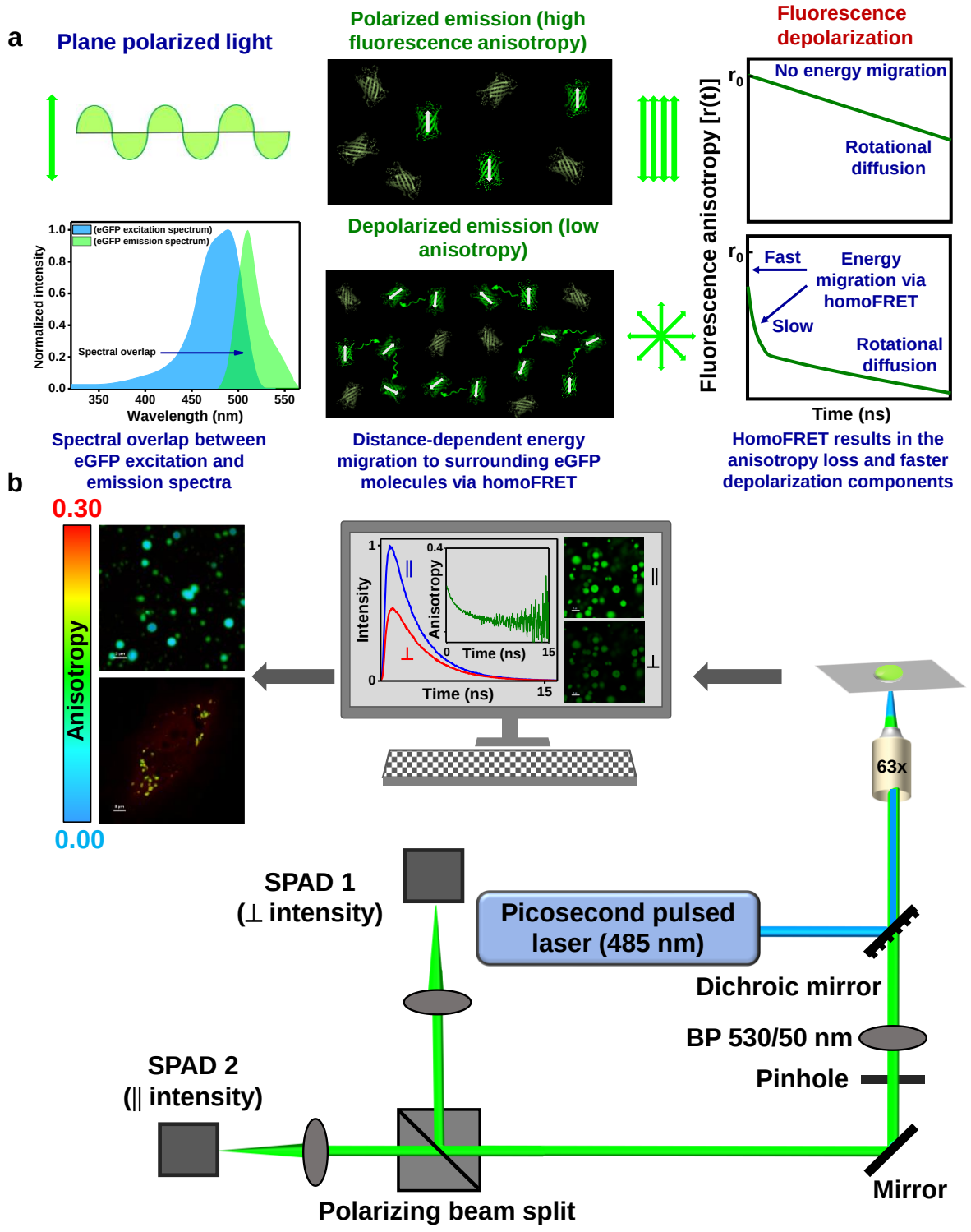

Figure 4.1. Schematic illustration depicting the a. Principle of energy migration via homoFRET. Fluorescent proteins with spectral overlap between their excitation and emission spectrum can exhibit a non-radiative excitation energy migration via homoFRET. At larger fluorophore concentrations and smaller intermolecular distances, the transfer of energy to differently oriented fluorophores in proximity leads to a depolarization of the emitted

fluorescence. The magnitude of anisotropy loss indicates the extent of homoFRET and, indirectly, the local fluorophore densities. HomoFRET introduces a faster decay component in time domain anisotropy measurements. b. Confocal microscopy setup (MicroTime 200, PicoQuant) used for our single-droplet anisotropy imaging and picosecond time-resolved measurements. Our setup constitutes a pulsed laser (485 nm), an inverted microscope, and a main optical unit comprising a dichroic mirror, pinhole, polarizing beamsplitter, and avalanche photodiodes with single-photon detection efficiency. After filtering out the out-of-focus light by pinhole, the emitted fluorescence is further separated and directed into the parallel and perpendicular channels (SPADs) by the polarizing beamsplitter.

The class of fluorescent proteins comprising green fluorescent protein (GFP) and its genetically encoded variants, including the yellow fluorescent protein (YFP), blue fluorescent protein (BFP), cyan fluorescent protein (CFP), etc., can serve as suitable candidates for homoFRET, owing to their much slower rotational mobility and thus high intrinsic anisotropy due to their bulky volume. Here, we used the enhanced green fluorescent protein (eGFP) as a homoFRET reporter and study FUS tagged with eGFP in both the mixed (dispersed) and demixed (condensed) phases using fluorescence anisotropy imaging and picosecond time-resolved anisotropy measurements. Our microscopy setup consists of a polarized excitation source (485 nm pulsed laser), an inverted microscope, and an integrated detection system comprising a dichroic mirror, bandpass filter, pinhole, polarizing beamsplitter, and detectors with single-photon detection (single-photon avalanche diodes; SPADs) (Figure 4.1b). For anisotropy imaging, the emitted fluorescence is separated into parallel and perpendicular channels, which are then used to construct images after incorporating the respective correction factors for the objective lens and differential detector efficiencies. Utilizing this setup, we began with our anisotropy imaging to explore the molecular packaging and organization within individual condensates of FUS formed under different phase separation conditions, in a droplet-by-droplet manner. The pulsed laser, in combination with time-gated single-photon detection, allowed us to perform picosecond time-resolved fluorescence anisotropy measurements within single droplets to resolve and capture the distinct energy migration rates or time constants, which otherwise remain inaccessible in the time-averaged steady-state measurements. Lastly, using this setup, we extended this technique of anisotropy imaging to detect and investigate the nuclear and cytoplasmic liquid-like assemblies or puncta of FUS-eGFP formed *in situ* in a puncta-by-puncta manner.

4.3.2 HomoFRET imaging as a proximity ruler for biomolecular condensation

FUS comprises a multidomain architecture with a low-complexity (LC) prion-like N-terminal domain and a partially structured RNA-binding C-terminal domain (Figure 4.2a)[31,32]. In order to probe phase separation of FUS via homoFRET, we utilized C-terminally eGFP tagged FUS (MBP-tev-FUS-eGFP) for our homoFRET measurements. As a prelude, we began with anisotropy imaging in the dispersed phase and condensed phases of FUS to obtain steady-state anisotropy values. In the monomeric condition (200 nM FUS-eGFP), we obtained a higher anisotropy value corresponding to the absence of homoFRET due to the low fluorophore densities in the lightly packed dispersed state (Figure 4.2b, c). Next, to monitor the condensed phase, droplet formation was initiated by the addition of TEV protease for cleavage of the solubilizing MBP tag. Upon phase separation, we obtained a large dip in the steady-state anisotropy value within individual droplets, indicating higher excited state energy migration due to the dense, closely-packed organization of FUS-eGFP molecules, as expected, within the condensed phase (Figure 4.2b, c). This increase in the local density of the FUS-eGFP molecules could be quantified by estimating the energy migration or homoFRET efficiency ($E_{homoFRET}$) based on relative change in steady-state anisotropy values from the dispersed (non-homoFRET) to condensed (homoFRET) phases, or the loss in steady-state fluorescence anisotropy value due to homoFRET (Δr_0). Using eq^n (2), we could calculate an apparent energy migration efficiency ($E_{homoFRET}$) of ~ 0.66 within the condensates of FUS-eGFP (Figure 4.2d). Next, to validate that this drop in fluorescence anisotropy was indeed a consequence of the increased homoFRET within condensates, we subjected these droplets to photobleaching with a high-intensity laser for a longer duration and monitored the fluorescence intensity for recovery of anisotropy value with time. As expected, we obtained a gradual recovery of the anisotropy values within the condensates to that of non-homoFRET conditions upon bleaching the samples (Figure 4.2e). Next, to probe the depolarization kinetics originating from homoFRET, we set out to perform picosecond time-resolved anisotropy measurements. In the monomeric phase, the anisotropy decay followed a typical monoexponential kinetics with a fundamental anisotropy (r_0 ~ 0.31) and a correlation time (ϕ_r) of ~ 30 ns, corresponding to the rotational dynamics of FUS-eGFP in the dispersed state (Figure 4.2f). On the contrary, we obtained three different components of anisotropy depolarization from the decay kinetics within droplet phase. The ultrafast component presented in the form of a loss in the fundamental anisotropy (ϕ_{EM1} with amplitude β_{EM1} ~ 0.26), where the rate of energy migration was much faster (subnanosecond) than our experimental temporal resolution. The anisotropy decay profile

exhibited characteristic biexponential decay kinetics with an intermediate time constant (ϕ_{EM2}) of ~ 1.5 ns and a slow time constant (ϕ_{EM3}) of ~ 25 ns (Figure 4.2f). These nanosecond time constants represent the intermediate and slower rates of excitation energy migration, which in association with the ultrafast subnanosecond component, collectively contribute toward the emission depolarization captured in our homoFRET measurements.

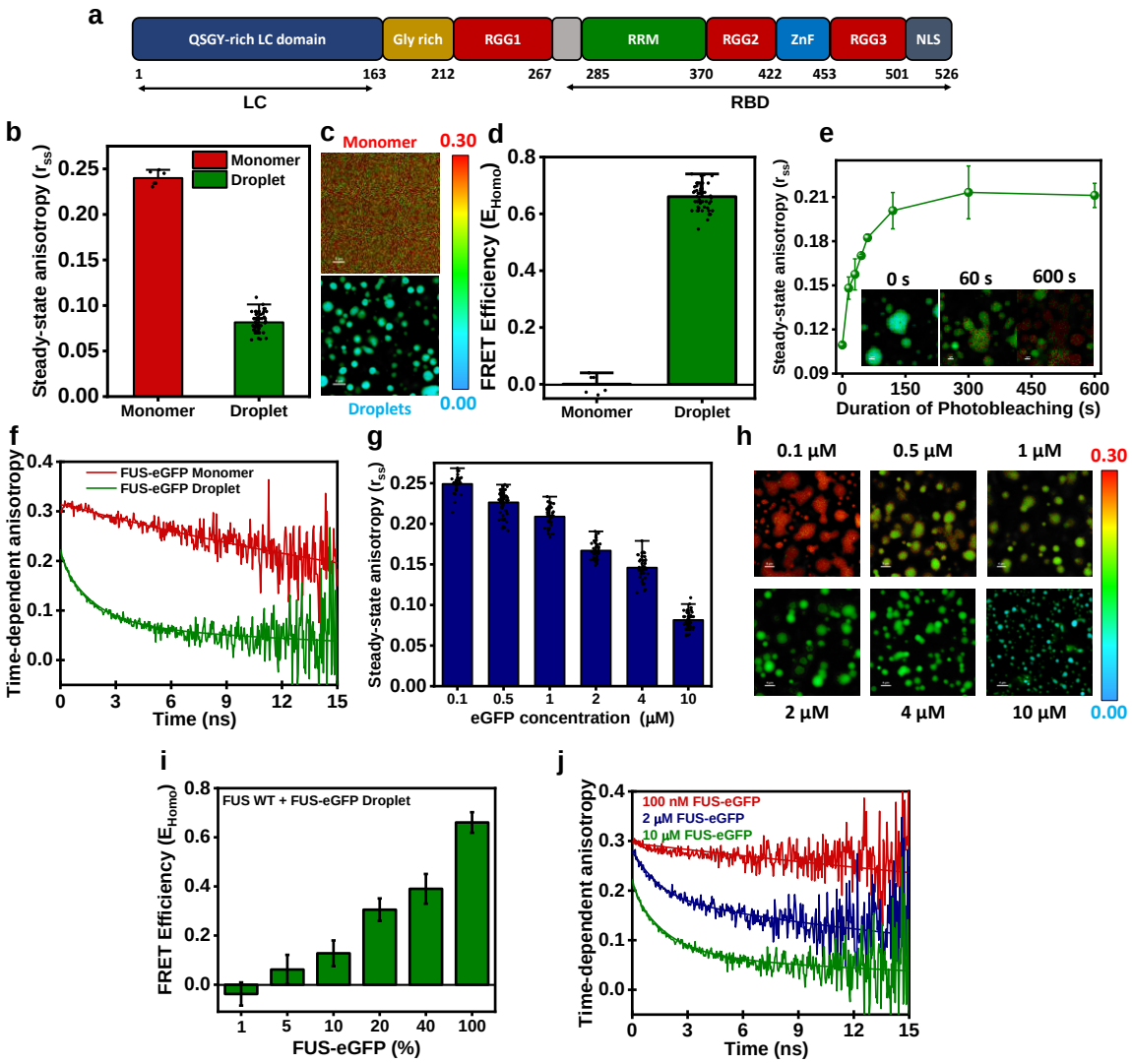

Figure 4.2. a. Sequence architecture of Fused in Sarcoma (FUS) depicting the N-terminal SYGQ-rich low-complexity domain (LC), the Arg-Gly rich RGG domains, an RNA-recognition motif (RRM), a zinc-finger domain (ZnF) and a C-terminal nuclear localization signal (NLS). b. Steady-state anisotropy values and c. the representative anisotropy images obtained from the monomeric phase and single droplets of FUS-eGFP. d. The calculated FRET efficiencies obtained from steady-state anisotropy values indicate the extent of molecular packaging in the dispersed phase and single droplets. Data represent mean ± SD (n = 6 and 60

for monomeric samples and droplets, respectively). e. Steady-state anisotropy values and their representative images (inset) obtained at high laser intensity as a function of time. Data represent mean ± SD (n = 3 independent reactions). f. Picosecond time-resolved fluorescence anisotropy decay obtained in the monomeric phase, and single droplets of FUS-eGFP fitted using monoexponential decay kinetics (no homoFRET) and a biexponential decay kinetics (high-homoFRET). g. Steady-state anisotropy values, their representative anisotropy images (h), and corresponding homoFRET efficiencies (i) as a function of varying FUS-eGFP concentration within FUS droplets. Data represent mean ± SD (n ≥ 30 for single droplets). j. Representative time-resolved anisotropy decay at varying fluorophore concentrations yielded monoexponential decay kinetics (100 nM FUS-eGFP) and biexponential decay kinetics (2 μM and 10 μM FUS-eGFP) with individual energy migration time constants. Rotational correlation time and energy migration time constants are included in Table 1.

Table 1. Excitation energy migration time constants and rotational correlation times with associated amplitudes recovered by fitting fluorescence anisotropy decay kinetics obtained from time-resolved measurements.

	Ultrafast energy migration time constant (Loss in fundamental anisotropy) ($\beta_{EM1} = \Delta r_0/r_0$)	**Intermediate energy migration time constant (ϕ_{EM2}) and amplitude (β_{EM2})**	**Slow energy migration time constant (ϕ_{EM3}) and amplitude (β_{EM3})**	**Rotational correlation time (ϕ_r) and amplitude (β_r)**
Monomer	-	-	-	31.34 ± 0.82 ns
1% FUS-eGFP in 10 μM FUS Droplet	0.06	-	-	67.92 ± 5.01 ns
20% FUS-eGFP in 10 μM FUS Droplet	0.06	1.61 ± 0.21 ns (0.37 ± 0.03)	19.86 ± 3.11 ns (0.28 ± 0.08)	58.34 ± 12.35 ns (0.37 ± 0.06)
10 μM FUS-eGFP Droplet	0.26	1.73 ± 0.14 ns (0.65 ± 0.04)	18.74 ± 4.75 ns (0.35 ± 0.04)	-

Methylated 10 μM FUS-eGFP Droplet	0.23	1.11 ± 0.11 ns (0.39 ± 0.05)	9.03 ± 1.10 ns (0.61 ± 0.04)	-
10 mM ATP 10 μM FUS-eGFP Droplet	0.01	1.60 ± 0.24 ns (0.16 ± 0.03	-	49.63 ± 7.02 ns (0.84 ± 0.03)

To further explore the sensitivity of homoFRET imaging towards differential intermolecular distances, we set out to perform anisotropy measurements over a wide range of fluorophore densities by varying the fraction of FUS-eGFP within the condensates of FUS. Beginning with one percent, we increased the fraction of FUS-eGFP and captured an incremental loss in the steady-state anisotropy values (Figure 4.2g, h) corresponding to the enhanced energy migration efficiencies (apparent homoFRET efficiencies, $E_{homoFRET}$) between the progressively closely-packed FUS-eGFP molecules (Figure 4.2i). At a low fluorophore concentration (1%), local densities of FUS-eGFP molecules resulted in steady-state anisotropy values reminiscent of non-homoFRET conditions, due to the large average intermolecular distances within condensates, leading to negligible or no energy migration. This absence of excitation energy migration was evident from our picosecond time-resolved measurements, which exhibited a typical monoexponential decay kinetics (Figure 4.2j). The correlation time constant obtained from monoexponential fitting (~ 65 ns) corresponds to the rotational dynamics of FUS-eGFP (ϕ_r) within the viscoelastic interior of FUS droplets. This slower depolarization component could be captured within these droplets as a result of the un-depolarized axis left due to the absence of faster decaying homoFRET components. This slower rotational correlation time could also be captured by fitting the anisotropy decay of droplets with a 20% labeled fraction with triexponential decay kinetics. At this fraction of FUS-eGFP, we could obtain a very small amplitude of the ultrafast component represented by the loss in r_0 (ϕ_{EM1} with amplitude β_{EM1} ~ 0.06), an intermediate time constant (ϕ_{EM2}, ~ 1.6 ns), the slow time constant (ϕ_{EM3}, ~ 20 ns), and the slower correlation time (ϕ_r) corresponding to the slower rotational diffusion (~ 60 ns) within droplets. These time constants shed light on the multiple modes of excitation energy migration originating from the array of dynamic molecular events, comprising the transient making and breaking of contacts, conformational fluctuations, translational diffusion, etc., operating at their characteristic timescales, in turn determining the rate of energy migration within condensates. These multivalent fuzzy interactions contribute to determining the mesoscopic attributes, including material properties, viscoelasticity, supramolecular

packaging, and nanoscale organization within biomolecular condensates. We next asked whether homoFRET imaging can capture the effect of RNA on the droplet interior of FUS-RNA heterotypic condensates.

4.3.3 Illuminating internal architecture of FUS-RNA heterotypic condensates using homoFRET imaging

In association with proteins, nucleic acids form the primary constituents of the vast majority of cellular biomolecular condensates[6,33-35]. FUS is a well-known RNA-binding protein involved in some of the critical DNA/RNA-associated cellular functions, where RNA is known to modulate the phase behavior and properties of FUS condensates[36-38]. RNA is capable of tuning the assembly, droplet interior (material properties), and dissolution of condensates of RNA-binding proteins in a concentration-dependent manner. Hence, we next set out to investigate the effect of RNA on the condensates of FUS using homoFRET imaging. Due to the high concentration and densely packed droplet interior, even in the absence of RNA, FUS-eGFP droplets exhibit extremely low anisotropy values, as shown in our previous results. Upon the addition of RNA, we captured a further dip in the anisotropy values (Figure 4.3a), indicating the enhanced molecular interactions and closer packaging, in agreement with the phase separation-promoting behavior of RNA. However, due to the initially borderline values, we shifted to an intermediate fluorophore fraction to monitor the effect of a wider range of RNA concentrations and to assess the changes in fluorophore densities with higher precision. Thus, we proceeded with our RNA-dependent homoFRET measurements at a 20% fluorophore concentration doped within the heterotypic FUS:RNA condensates formed in the presence of varying concentrations of polyU RNA. With increasing RNA concentration, the anisotropy imaging showed an increase in the emission depolarization (Figure 4.3b, c), originating from the enhanced excitation energy migration (Figure 4.3d), presumably due to the increasingly compact packaging within FUS:RNA condensates. While facilitating and participating in multivalent protein-RNA interactions, RNA possibly enables the formation of dense intermolecular protein-protein and protein-RNA networks, leading to a reduction in the average intermolecular distances between the FUS-eGFP molecules inside condensates. This condensing effect of RNA has been well-established for multiple phase-separating RNA-binding proteins[39,40], corroborating our FRAP measurements, which showed a slower diffusion

within the densely crowded droplet interior in the presence of lower concentrations of RNA (Figure 4.3e).

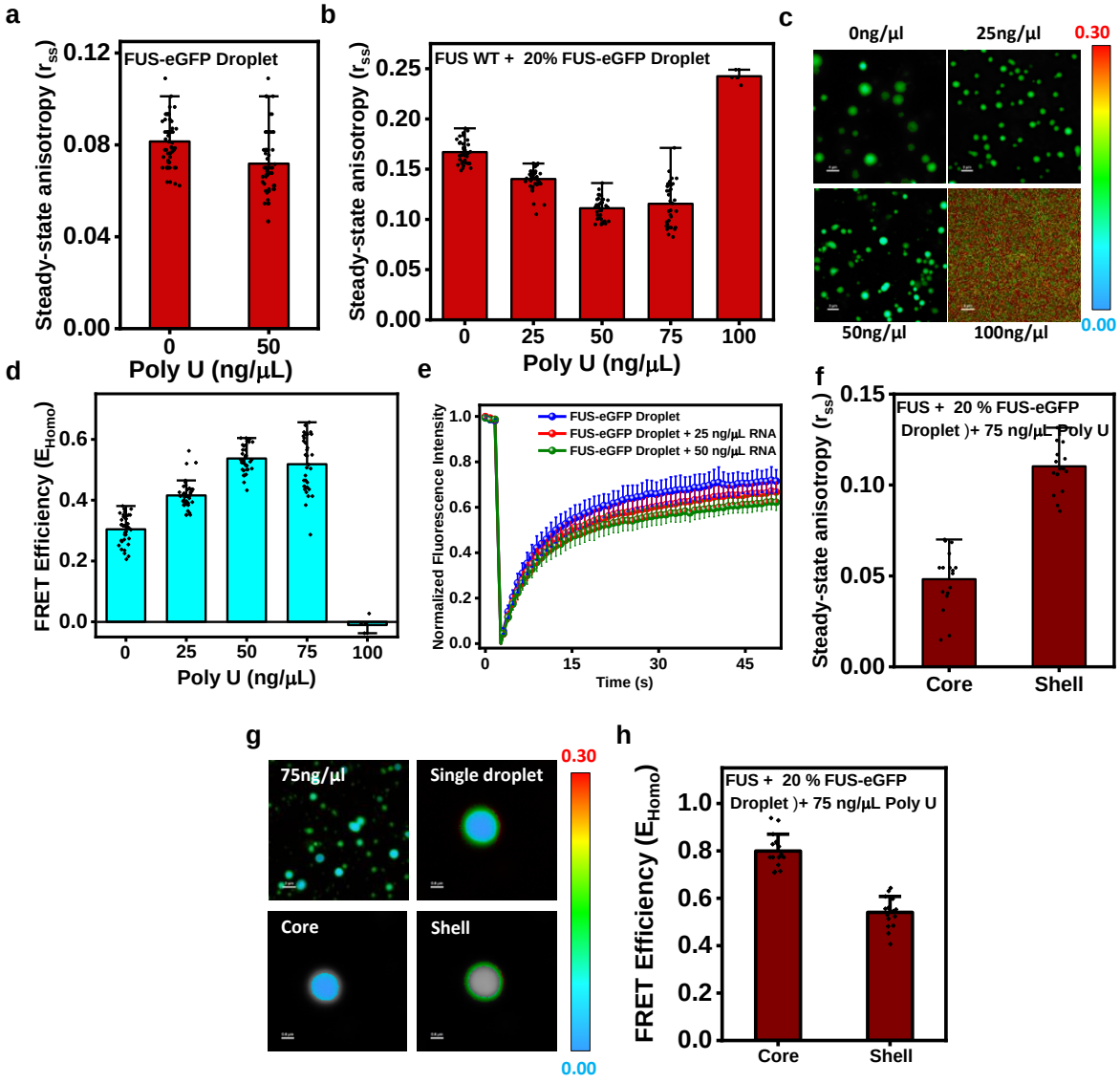

Figure 4.3. a. Steady-state anisotropy plot indicating the slight dip in anisotropy within single droplets of FUS-eGFP in the presence of RNA. Data represent mean ± SD (n = 60 for single droplets). Data for 0 ng/µL RNA is shown for comparison, same as in 4.2b, g) b. Single-droplet steady-state anisotropy plot of FUS droplets doped with 20 % FUS-eGFP with varying RNA. Data represent mean ± SD (n ≥ 30 for 0, 25, 50, 75 ng/µL RNA and n = 6 for 100 ng/µL RNA). c. Representative anisotropy images of FUS droplets in the range of RNA concentrations plotted in (b). d. Apparent homoFRET efficiencies as a function of RNA concentrations. estimated from (b). e. Fluorescence recovery after photobleaching (FRAP) kinetics of FUS-eGFP droplets in the absence and presence of RNA. Data represent mean ± SD (n = 5, 5, and 7 for 0 ng/µL, 25 ng/µL, and 50 ng/µL RNA, respectively). f. Steady-state anisotropy plots and

g. representative images showing the core-shell morphology of droplets formed at a polyU concentration of 75 ng/μL. Data represent mean ± SD (n = 17 single droplets). h. The calculated FRET efficiency values suggest a densely packed protein core enclosed within a lightly packed shell.

Upon further increasing the concentration, homoFRET imaging revealed a slight reduction followed by a complete abrogation of excitation energy migration as evident from the corresponding anisotropy values obtained for 75 and 100 ng/μL RNA, respectively (Figure 4.3b, c). The lower FRET efficiency indicated a decrease in the droplet compaction, ensuing a complete dissolution of the droplets at 100 ng/μL RNA (Figure 4.3d). This was reflected in the complete recovery of steady-state anisotropy to that of the non-homoFRET conditions. Interestingly, the anisotropy imaging of condensates in the presence of 75 ng/μL RNA exhibited density variations and a specialized nanoscale organization inside the majority of the droplets. The droplet core showed consistently lower anisotropy, as compared to the periphery, as visible in the representative anisotropy images (Figure 4.3f, g). Upon closer examination and analysis, we obtained significantly distinct protein packaging and molecular organization as suggested by the higher energy migration efficiency at the center, as opposed to the peripheral regions of these droplets (Figure 4.3h). Our homoFRET studies hint towards the existence of a typical core-shell architecture, with a comparatively denser core (high local protein densities) surrounded by a relatively lightly-packed shell inside the heterotypic FUS:RNA condensates. These peculiar droplet morphologies originate from the variable density distributions, where the densely packed core harbors a large number of protein and RNA molecules enmeshed in an extensive network of heterotypic protein-RNA interactions. These multiphasic architectures have previously been reported *in vitro* for multicomponent co-phase separation systems[41-43]. Such immiscible multiphasic morphologies originating from heterogeneous nanoscale architecture within cellular condensates can be readily captured by this robust methodology of homoFRET imaging. Taken together, our homoFRET imaging provides a readout for the local molecular clustering and the average intermolecular distances of protein molecules within the heterotypic FUS:RNA condensates. Further, we sought to probe the alterations in droplet organization within FUS-eGFP condensates as a result of other phase separation modulators, such as post-translational modification and ATP.

4.3.4 HomoFRET captures the altered molecular packaging due to post-translational methylation and ATP

The partially structured C-terminal domain of FUS is enriched in amino acids arginine and glycine (RGG-rich domains) (Figure 4.2a) and is identified to play an essential role in the RNA-binding activity and biomolecular condensation of FUS[33,36,37,44]. In healthy neurons, the arginine residues in the CTD of FUS are post-translationally modified by extensive methylation and can harbor either one (monomethylated Arg) or two (dimethylated Arg) methyl groups[45,46]. Several reports show that post-translational methylation is disrupted in the pathology of FTLD-FUS, leading to the formation and deposition of insoluble cytoplasmic aggregates of hypomethylated FUS[45,46]. Furthermore, methylation has been shown to alter the phase behavior and retain the liquid-like dynamics within FUS condensates, highlighting the significance of investigating the role of methylation in determining the material properties and internal organization of FUS condensates. With this objective, we next aimed to capture this change in droplet interior within FUS-eGFP condensates upon methylation. In this direction, we performed *in vitro* methylation using a previously established protocol employing S-adenosyl-methionine (SAM) as the methyl-group donor and the enzyme protein arginine methyltransferase 1 (PRMT1) to catalyze the reaction[45]. We began with anisotropy imaging of methylated FUS-eGFP droplets, which revealed an increased steady-state anisotropy value in comparison to the unmethylated FUS-eGFP droplets, as evident in the representative anisotropy images (Figure 4.4a, b). The calculated homoFRET efficiency (Figure 4.4c) showed a significant dip in the energy migration, indicating a reduced protein density or lesser clustering of protein molecules inside the condensates of methylated FUS-eGFP. This alteration in the molecular packaging within these methylated FUS-eGFP condensates can be explained by the reduced protein-protein interactions originating from the methylation of the positively charged arginine residues for participation in the cation-π interactions. This reduced propensity of intermolecular cation- π interaction, the principal driver of FUS phase separation, results in reduced phase separation and lesser recruitment of FUS-eGFP into the relatively more liquid-like condensates, in contrast to the unmethylated FUS-eGFP condensates. Our anisotropy imaging readily captures this low protein density in the form of higher anisotropy values due to the diminished energy migration within these lightly packed, liquid-like condensates, as also indicated by our FRAP measurements (Figure 4.4d). The picosecond time-resolved measurements (Figure 4.4e) provided us with a subnanosecond component (ϕ_{EM1} with amplitude $\beta_{EM1} \sim 0.23$), in addition to the intermediate and slow time constants ($\phi_{EM2} \sim 1.1$ ns

and ϕ_{EM3} ~ 9 ns) originating from the excited state energy migration within condensates. The faster energy migration rates (both ϕ_{EM2} and ϕ_{EM3}) as compared to the unmethylated droplets can be attributed to the faster dynamics of the conformational fluctuations, making and breaking of contacts, and translational diffusion as a result of highly dynamic, liquid-like and reversible nature of intermolecular contacts and droplet interior within the condensates of methylated FUS. Phase separation into physiological and pathological biomolecular condensates is known to be modulated by a range of physicochemical and biochemical factors, in addition to sequence-encoded and genetic parameters. Non-peptide small molecules are being extensively studied for their ability to modulate the phase behavior and mesoscopic properties of biomolecular condensates for their potential applicability in therapeutics[47,48]. Adenosine triphosphate (ATP) is a well-known modulator of phase behavior and is shown to tune properties of biomolecular condensates in a concentration-dependent manner[49-52]. The cellular physiological concentration for ATP has been estimated to be in the range of 2-12 mM, whereas the ATP concentration of ~ 8- 10 mM is shown to cause the dissolution of protein condensates, as also in the case of FUS[49-51]. Thus, to capture the effect of ATP on the material properties of condensates through anisotropy imaging, we set up phase separation reactions of FUS-eGFP in the presence of ATP, within the physiological concentration range. Our anisotropy imaging data showed a gradual rise in anisotropy with increasing ATP concentration, and we obtained a complete recovery to the monomeric anisotropy (non-homoFRET condition) at the ATP concentration of 10 mM, above which droplet dissolution is observed (Figure 4.4f, g). The dissolution effect of ATP could be monitored from the calculated homoFRET efficiency values even at the intermediate ATP concentration, where the drop in FRET efficiency suggested a gradual unpacking within condensates due to the predominance of protein-ATP interactions over the protein-protein interactions. Further, the droplets formed in the presence of 10 mM ATP exhibited no or zero-homoFRET due to the formation of extremely less dense and loosely packed condensates just prior to dissolution (Figure 4.4h). This dynamic, liquid-like droplet interior just prior to dissolution was also evident from the fast and complete FRAP recovery obtained with 10 mM ATP FUS-eGFP droplets (Figure 4.4i). Our time-domain fluorescence anisotropy measurements obtained within these droplets yielded biexponential decay kinetics with a minimal contribution of the intermediate energy migration time constant (ϕ_{EM2} ~ 1.6 ns) and a major contribution from the rotational correlation time component (ϕ_r ~ 50 ns) (Figure 4.4j).

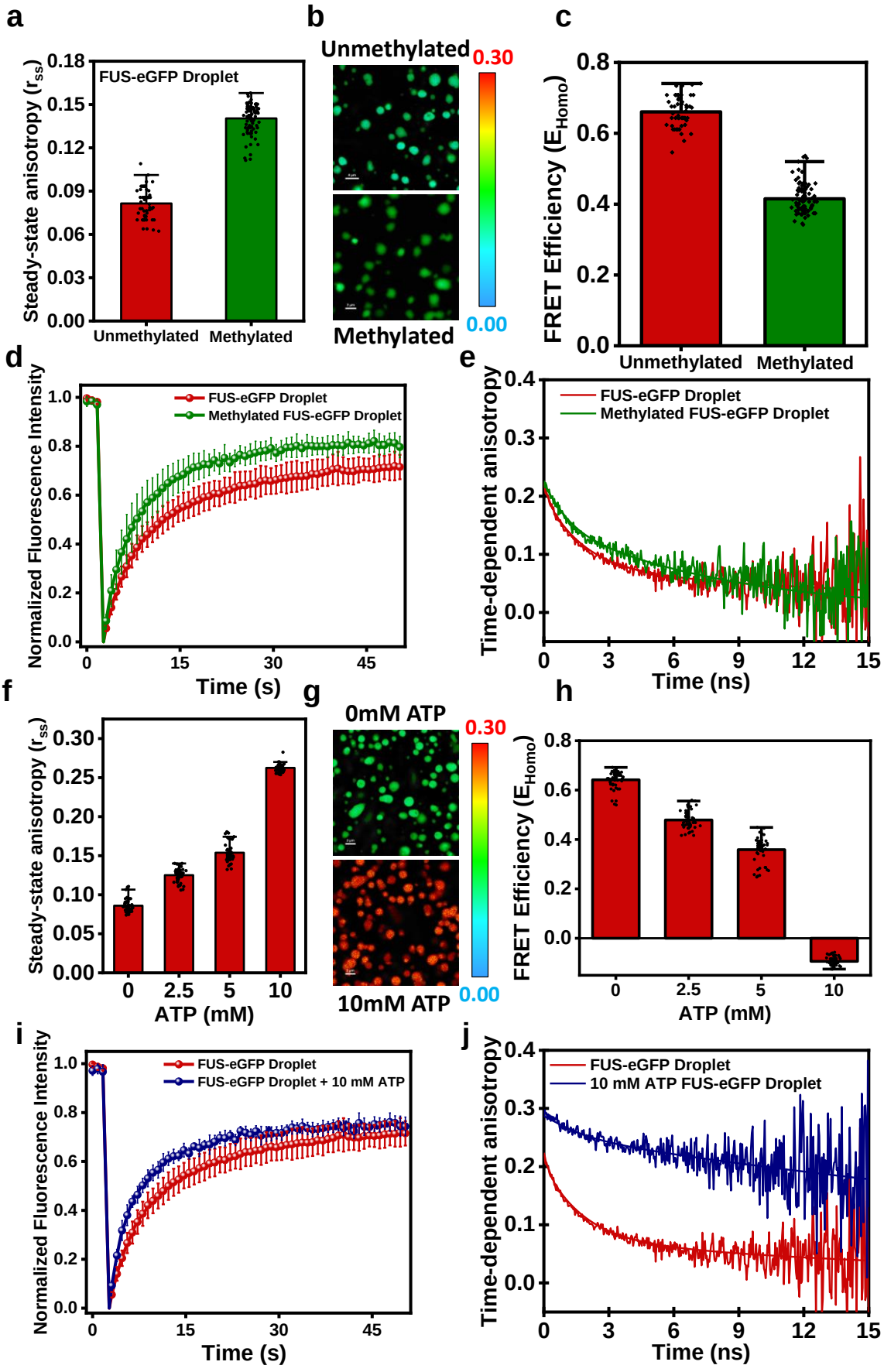
a
Steady-state anisotropy (r_{ss})
FUS-eGFP Droplet
Unmethylated
Methylated
b
Unmethylated
0.30
0.00
Methylated
c
FRET Efficiency (E_{Homo})
Unmethylated
Methylated
d
Normalized Fluorescence Intensity
FUS-eGFP Droplet
Methylated FUS-eGFP Droplet
Time (s)
e
Time-dependent anisotropy
FUS-eGFP Droplet
Methylated FUS-eGFP Droplet
Time (ns)
f
Steady-state anisotropy (r_{ss})
ATP (mM)
g
0mM ATP
0.30
0.00
10mM ATP
h
FRET Efficiency (E_{Homo})
ATP (mM)
i
Normalized Fluorescence Intensity
FUS-eGFP Droplet
FUS-eGFP Droplet + 10 mM ATP
Time (s)
j
Time-dependent anisotropy
FUS-eGFP Droplet
10 mM ATP FUS-eGFP Droplet
Time (ns)

Figure 4.4. a. Single-droplet steady-state anisotropy plots and b. representative images obtained from unmethylated and methylated FUS-eGFP droplets. Data represent mean ± SD (n > 50 independent reactions). c. Calculated energy migration efficiencies show a reduced homoFRET efficiency within the condensates of methylated FUS-eGFP. d. Fluorescence recovery after photobleaching (FRAP) kinetics shows a faster recovery, indicating a more liquid-like dynamic interior within condensates of methylated FUS-eGFP. Data represent mean ± SD (n = 5 and 7 for unmethylated and methylated droplets, respectively) e. Representative time-resolved anisotropy decay kinetics obtained within the unmethylated and methylated FUS-eGFP droplets. f. Single-droplet steady-state anisotropy as a function of increasing ATP concentration measured within FUS-eGFP condensates. Data represent mean ± SD (n = 50 single droplets). g. Representative anisotropy images of FUS-eGFP droplets formed in the presence of 0 mM and 10 mM ATP. h. The respective FRET efficiency plot calculated from the single-droplet steady-state anisotropy values in the absence and presence of varying ATP concentrations. i. FRAP kinetics of FUS-eGFP obtained from multiple FUS-eGFP droplets in the absence and presence ATP. Data represent mean ± SD (n = 5 and 9 for 0 mM and 10 mM ATP concentration, respectively). j. Representative time-resolved anisotropy decay kinetics measured within FUS-eGFP droplets with and without ATP. Rotational correlation time and energy migration time constants are included in Table 1.

This relatively faster rotational diffusion also suggests the enhanced diffusivity and liquid-like interior of the FUS-eGFP droplets formed in 10 mM ATP, as compared to the FUS droplets formed in the absence of ATP (ϕ_r ~ 60-70 ns) (Figure 4.2j). After evaluating the sensitivity of homoFRET imaging for condensates formed under a wide range of solution conditions, we next aimed to utilize homoFRET to study cellular phase-separated assemblies.

4.3.5 Mapping intermolecular organization within phase-separated assemblies of FUS *in situ*

Fluorescently tagging proteins of interest with fluorescent proteins such as GFP, CFP, YFP, mCherry, etc., is a standard practice employed for cellular studies investigating the localization, conformational changes, protein-protein association, and so on. The majority of these fluorescent proteins exhibit a significant spectral overlap between their own absorption and emission spectra, making them a suitable candidate for such homoFRET studies. Thus, we next asked whether anisotropy imaging could be employed to detect the formation of these dynamic liquid-like assemblies within the crowded, complex cellular milieu. To explore this idea, we began with the transient expression of eGFP-tagged wild-type FUS in A549 lung epithelial cells. The amino acid sequence of FUS harbors a nuclear localization signal (NLS) at the C-term end (Figure 4.2a) and, hence, primarily resides in the nucleus, where it is involved in

functions such as genome organization, DNA damage repair, transcription, RNA splicing, translational regulation, and so on[36,37,44]. Upon overexpressing eGFP-FUS in the cells, FUS readily localized to the nucleus and was more or less uniformly distributed throughout the nucleoplasm, as seen in our confocal microscopy imaging (Figure 4.5a). However, a significant proportion of the cells also showed the formation of small nuclear puncta or foci, presumably as a consequence of the overexpression stress within cells. To probe the distinct molecular packaging and distribution of eGFP-FUS within the dispersed nucleoplasm and condensed foci, we began with anisotropy imaging of these cells overexpressing wild-type eGFP-FUS (Figure 4.5b, c).

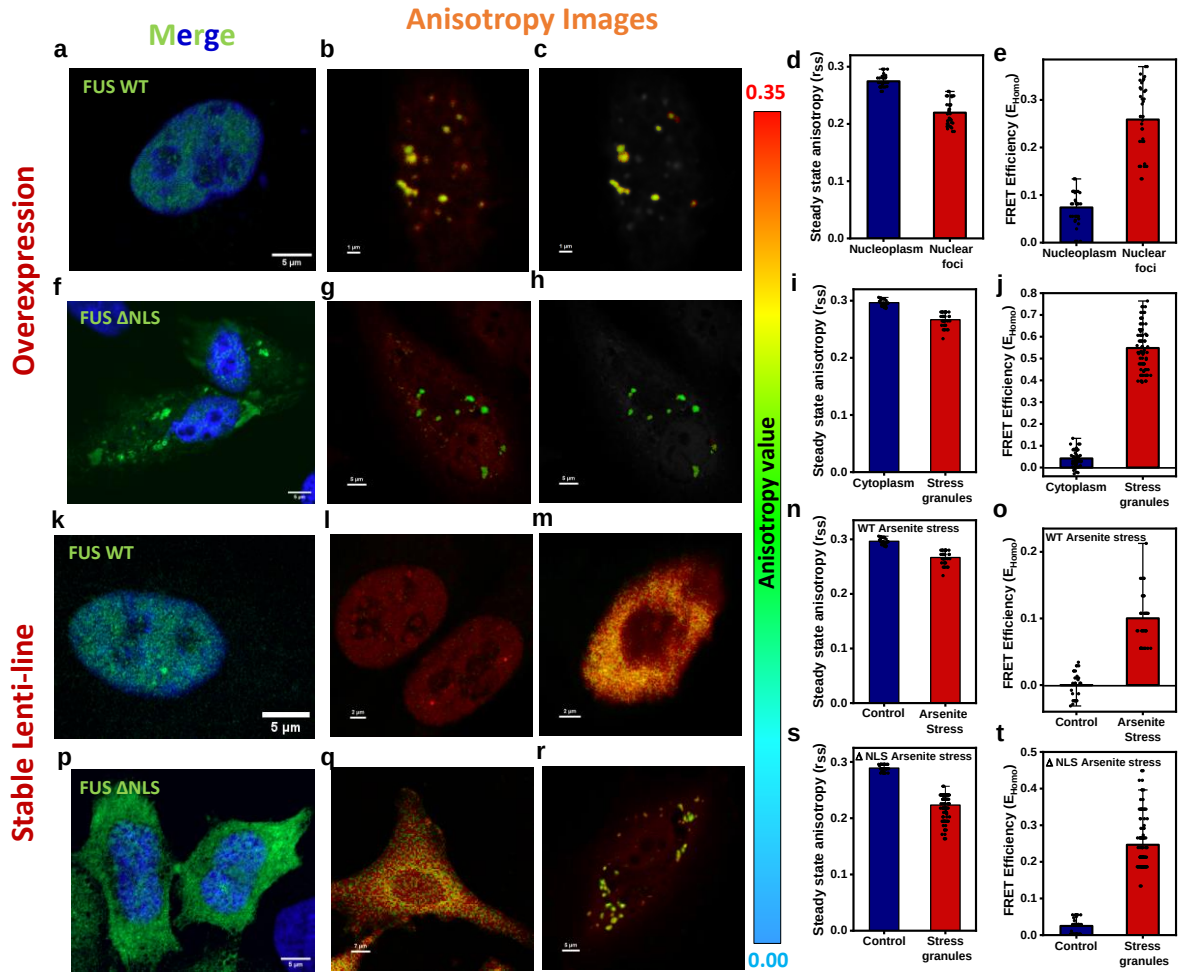

Figure 4.5. a. Representative confocal airyscan image of A549 cells overexpressing wild-type eGFP-FUS (green) show diffused localization of eGFP-FUS inside the nucleus. b. Anisotropy images of eGFP-FUS overexpression highlighting the nuclear foci (c). d. Steady-state anisotropy plots obtained from the diffused nucleoplasm and condensed nuclear foci with corresponding FRET efficiencies (e). Data represent mean ± SD (n > 30 measurements). f. Representative confocal airyscan image of A549 cells transiently expressing eGFP-FUS ΔNLS

mutant showing cytoplasmic localization along with recruitment into cytoplasmic granules (Scale bar 5 μm). g. Representative anisotropy image of cells transiently expressing mutant eGFP-FUS indicating a loss in anisotropy within the cytoplasmic granules (h). i. Steady-state anisotropy plots obtained from the diffused cytoplasm and stress granules. j. HomoFRET efficiency plot showing energy migration efficiency within the diffused cytoplasm and cytoplasmic granules. Data represent mean ± SD ($n \geq 30$ measurements). k. Representative airyscan confocal image of A549 cells with stable expression of wild-type eGFP-FUS with nuclear localization. Representative anisotropy images of cell nuclei in the absence (l) and presence of (m) arsenite stress. Cells stably expressing eGFP-FUS WT and eGFP-FUS ΔNLS were treated with 300 μM sodium arsenite for 1 h to induce stress granule formation. n. Steady-state anisotropy plot and the corresponding FRET efficiency plot (o), obtained from the nucleus of cells expressing wild-type eGFP-FUS in the non-stressed and stressed conditions. Data represent mean ± SD ($n \geq 30$ measurements). p. Airycan confocal image of A549 cells with stable eGFP-FUS ΔNLS expression showing mislocalization of mutant eGFP-FUS into the cytoplasm, without the formation of cytoplasmic granules. Representative anisotropy images of cells expressing the eGFP-FUS ΔNLS mutant showing q. diffused in non-stressed conditions and r. cytoplasmic stress granules upon exposure to arsenite stress. Corresponding steady-state anisotropy plot (s) and FRET efficiency plot (t) comparing the non-stressed and arsenite stress conditions. Data represent mean ± SD ($n > 40$ measurements).

In line with our hypothesis, the steady-state anisotropy value showed a significant change in the nucleoplasm and foci comprising eGFP-FUS (Figure 4.5d). The loss in anisotropy within the nuclear foci suggested clear compaction and approximately more than 3 times denser packaging in comparison to the surrounding dispersed phase, as indicated by our apparent energy migration efficiencies (Figure 4.5e). As mentioned previously, FUS is associated with the pathology of ALS, where a significant fraction of familial ALS cases is attributed to point mutations within FUS NLS, resulting in the accumulation of insoluble pathological aggregates due to cytoplasmic mislocalization[38,45,53-55]. Thus, with the objective of recapitulating the ALS-associated cytoplasmic mislocalization, we next overexpressed a ΔNLS mutant of eGFP-FUS (FUS ΔNLS) in these cells to visualize the cytoplasmically localized eGFP-FUS. Our fluorescence microscopy imaging revealed the mislocalization of eGFP-FUS in the cytoplasm, in addition to the formation of stress granules, as a response to the overexpression stress (Figure 4.5f). Our steady-state anisotropy imaging captured a drastic change in the molecular packaging within the cytoplasmic stress granules and the cytoplasmically dispersed FUS (Figure 4.5g-i). The calculated FRET efficiencies indicated a nearly 13 fold increased compaction in the phase-separated cytoplasmic stress granules, representing the condensed phase of FUS ΔNLS (Figure 4.5j).

One of the well-studied functions of FUS is its assembly and recruitment in stress granules in response to stress conditions. Upon exposure to various kinds of stress, cells attempt to protect themselves from stress-related damage and death by halting the ongoing energy-consuming processes, including transcription and translation[53-55]. Stress granules provide a sink for the sequestration of translationally stalled mRNAs, ribosomes, translation initiation, and elongation factors, along with several other RNA-binding proteins in the form of membraneless, dynamic, liquid-like RNP granules to facilitate cell survival[53-55]. We next sought to capture this altered localization, packaging, and protein-protein interaction of eGFP-FUS within the liquid-like phase-separated stress granules assembled in response to cellular stress. With this objective, we began with the stable expression of wild-type FUS and FUS ΔNLS. To invoke a stress damage response, we subjected the cells to arsenite exposure, which has previously been shown to induce FUS-containing stress granule formation within cells[55-58]. Confocal fluorescence imaging revealed completely diffused eGFP-FUS in the nucleus in the absence of arsenite stress and correspondingly high anisotropy due to the non-compact packaging of eGFP-FUS within the healthy nucleus (Figure 4.5k). Upon incubation with sodium arsenite, cells expressing wild-type eGFP-FUS exhibited nuclei with diffused FUS, however, with a relatively denser packaging, presumably due to enhanced nuclear oligomerization owing to arsenite-induced stress response (Figure 4.5l, m). Steady-state anisotropy measurements provided a slightly reduced anisotropy value, suggesting a relatively higher density or protein-protein association within the nuclei of stressed cells, leading to a larger energy migration efficiency (Figure 4.5n, o). Lastly, we sought to probe the organization and packaging inside stress granules formed within cells with stable expression of the FUS ΔNLS mutant. The mutant FUS showed mislocalization of eGFP-FUS into the cytoplasm, which was recruited into phase-separated stress granules in response to arsenite stress (Figure 4.5p-r). Comparative anisotropy measurements revealed an approximately 6-fold increase in the compactness and protein association within the stress granules formed upon arsenite stress (Figure 4.5s, t). Taken together, our data underscore the efficacy of homoFRET imaging as a direct readout for condensate formation and further investigations into the interior organization of supramolecular protein assemblies formed *in situ* via phase separation.

4.4 Discussion

Unique supramolecular assemblies of proteins and nucleic acids formed via the process of biomolecular condensation carry great physiological and pathological significance across organisms. The prime distinguishing factor between the majority of these functional, phase-separated, reversible condensates and irreversible pathological deposits or aggregates that are associated with aging is their internal material properties. These characteristics are determined by the internal organization and intermolecular interactions within these assemblies. Our work demonstrates the utilization of homoFRET, as a potent tool for discerning the material characteristics of condensates formed *in vitro* and *in situ* while assessing the extent of molecular packaging and intermolecular association quantitatively. By performing anisotropy imaging, we obtained steady-state anisotropy values as a measure of excitation energy migration via homoFRET. Energy migration from the excited state of one fluorophore to a chemically identical, proximally placed fluorophore leads to a depolarization of the emitted fluorescence, which is measured by the loss in the anisotropy. The extent of energy transfer via homoFRET depends on the clustering density or the higher-order packing of the fluorophore molecules, which can be readily determined from the magnitude of emission depolarization. In this work, we demonstrate the utility of anisotropy imaging to elucidate the dynamic internal architecture and obtain a quantitative measure of molecular proximities ($E_{homoFRET}$) within biomolecular condensates of a neuronal protein FUS, formed in the absence and presence of multiple phase separation modulators *in vitro* and *in situ*.

Fused in Sarcoma (FUS) is an RNA-binding protein with a prion-like low-complexity domain associated with various functional and pathological aspects and known to undergo phase separation within cells[31-33,45,46]. Anisotropy imaging of FUS tagged with eGFP resulted in a sharp dip in the steady-state anisotropy upon phase separation, corresponding to the multiple-fold increase in energy migration efficiency due to the extensive molecular crowding and compact packaging in the demixed or condensed phase. This anisotropy loss could be completely recovered upon photobleaching of the droplets verifying homoFRET as the origin of emission depolarization. Further, our picosecond time-resolved measurements yielded mono and biexponential decay kinetics, depending on the contribution of homoFRET towards fluorescence depolarization. The depolarization decay in homoFRET conditions could be further differentiated into multiple energy migration components and rotational dynamics of FUS-eGFP with their corresponding time constants and amplitudes. These energy migration rates provide a readout for the diverse molecular level events and their distinct timescales

contributing to the multiple energy migration modes facilitating homoFRET. Steady-state anisotropy values exhibited remarkable sensitivity to the variation in local densities of FUS-eGFP, as evident in our ratiometric droplet measurements. Our anisotropy imaging also captured the effect of RNA on the droplet architecture and higher-order packaging of FUS condensates, doped with 20 % FUS-eGFP, as a homoFRET reporter. At lower concentrations, RNA enhances the protein-protein association, as shown previously, leading to a relatively dense droplet interior with increasing homoFRET efficiency. At higher concentrations, just prior to dissolution, the droplets exhibit a heterogeneous organization reminiscent of the core-shell morphology previously shown for other phase-separating systems. The core showed comparatively higher molecular proximities (high $E_{homoFRET}$) corresponding to the visibly low steady-state anisotropy values with respect to the lightly-packed periphery. This was followed by the sudden rise in anisotropy values to that of the dispersed monomeric protein upon dissolution of the condensates. We also captured the effect of post-translational methylation and small-molecule phase separation modulator, namely ATP, on the internal packaging and droplet properties of FUS-eGFP. Methylation resulted in sparsely packed droplets with a more liquid-like interior, suggesting diminished clustering and intermolecular interactions in comparison to the unmethylated FUS-eGFP condensates. Similarly, with increasing ATP concentration, anisotropy values showed a gradual recovery to that of the non-homoFRET conditions, in agreement with the previously established dissolution effect of ATP[49,50]. This unpacking of FUS-eGFP condensates upon methylation and in the presence of ATP can be ascribed to the altered propensity of arginine to associate with the N-terminal tyrosine residues via cation-π interactions. Lastly, we utilized our methodology to investigate the condensate formation and higher-order packing within phase-separated assemblies of FUS-eGFP in mammalian cell lines. Our results highlight the altered densities and molecular packing within these phase-separated condensates formed under divergent cellular conditions and localization.

Taken together, our data showcases the sensitive technique of anisotropy imaging as a versatile tool to probe the fundamental property of molecular packaging and the internal architecture of biomolecular condensates formed via phase separation. Cellular studies that regularly employ tagging of molecules with fluorescent proteins can be readily extended to gain deeper insights into the organization and supramolecular packing within the dynamic membraneless cellular compartments. A wide range of fluorophores, including the extensively used fluorescent proteins (RFP, YFP, CFP, mCherry, etc.) can be utilized for homoFRET imaging within condensates both *in vitro* and *in situ*. In addition to phase separation,

homoFRET via anisotropy imaging can also report on the higher-order species or nanoclusters formed as the precursors of these supramolecular assemblies[59,60]. Previous studies have highlighted the use of fluorescent protein lifetimes as a measure of droplet densities and crowding[61]. In addition to the droplet interior, steady-state anisotropy can distinctly report on the alterations in polypeptide chain clustering and condensate architecture resulting from the intermolecular associations characteristic of the given condensates. The requirement of a single fluorescent probe for homoFRET broadens the scope substantially and, thus, the availability of fluorescent reporters for simultaneously tagging multiple proteins of interest. HomoFRET studies with two or more homoFRET reporters in conjunction with intra or intermolecular heteroFRET studies can further shed light on the critical molecular events associated with multicomponent heterotypic phase separation[62-64]. Previous studies have utilized homoFRET to identify and characterize membrane-induced clustering and oligomerization *in vitro* as well as in membrane-anchored proteins *in situ*[65]. HomoFRET imaging can be employed to investigate membrane-associated phase separation of membrane-bound proteins[66,67]. Recent studies have shown the tuning of FUS condensates and their material properties by the protein quality control (PQC) machinery, including small heat shock proteins and chaperones[68,69]. HomoFRET imaging can be successfully employed to uncover the molecular details and reorganization associated with this chaperoning effect of the PQC machinery on the preformed condensates of FUS and other pathological proteins. In contrast to the original hypothesis, several reports now suggest the presence of a heterogeneous organization or a distinct small-world architecture within biomolecular condensates[41-43,59,70]. Recent studies have suggested the presence of distinct conformations (spatial heterogeneity) at the center and periphery of these condensates. Anisotropy imaging can illuminate this spatial heterogeneity, presumably arising due to the non-uniform, selective distribution and interactions of constituent proteins and nucleic acids within the phase-separated droplets. These localized density variations will be efficiently recorded in the homoFRET efficiency fluctuations in the form of distinct steady-state anisotropy values throughout the condensates. Thus, we believe this methodology can provide a unique approach to discern the condensate packaging and differential intermolecular interactions within a wide range of biological condensates and facilitate a comprehensive understanding of *in vitro* and cellular phase-separated assemblies.

4.5 References

1. Kilgore, H. R., & Young, R. A. Learning the chemical grammar of biomolecular condensates. *Nat. Chem. Biol*. **18,** 1298–1306 (2022).

2. Alberti, S., & Hyman, A. A. Biomolecular condensates at the nexus of cellular stress, protein aggregation disease and ageing. *Nat. Rev. Mol. Cell Biol.* **22,** 196–213 (2021).

3. Lyon, A. S., Peeples, W. B., & Rosen, M. K. A framework for understanding the functions of biomolecular condensates across scales. *Nat. Rev. Mol. Cell Biol.* **22,** 215–235 (2021).

4. Mittag, T., & Pappu, R. V. A conceptual framework for understanding phase separation and addressing open questions and challenges. *Mol. Cell* **82,** 2201–2214 (2022).

5. Boeynaems, S., Alberti, S., Fawzi, N. L., Mittag, T., Polymenidou, M., Rousseau, F., Schymkowitz, J., Shorter, J., Wolozin, B., Van Den Bosch, L., Tompa, P., & Fuxreiter, M. Protein Phase Separation: A New Phase in Cell Biology. *Trends Cell Biol*. **28,** 420-435 (2018).

6. Roden, C., & Gladfelter, A. S. RNA contributions to the form and function of biomolecular condensates. *Nat. Rev. Mol. Cell Biol.* **22**, 183–195 (2021).

7. Choi, J. M., Holehouse, A. S., & Pappu, R. V. Physical principles underlying the complex biology of intracellular phase transitions. *Annu. Rev. Biophys.* **49**, 107–133 (2020).

8. Ruff, K. M., Choi, Y. H., Cox, D., Ormsby, A. R., Myung, Y., Ascher, D. B., Radford, S. E., Pappu, R. V., & Hatters, D. M. Sequence grammar underlying the unfolding and phase separation of globular proteins. *Mol. Cell.* **82**, 3193-3208 (2022).

9. Yu, M., Heidari, M., Mikhaleva, S., Tan, P. S., Mingu, S., Ruan, H., Reinkemeier, C. D., Obarska-Kosinska, A, Siggel, M., Beck, M., Hummer, G., & Lemke, E. A. Visualizing the disordered nuclear transport machinery in situ. *Nature* **617,** 162-169 (2023).

10. Shapiro, D. M., Ney, M., Eghtesadi, S. A., & Chilkoti, A. Protein phase separation arising from intrinsic disorder: First-principles to bespoke applications. *J. Phys. Chem. B* **125,** 6740–6759 (2021).

11. Mitrea, D. M., Cika, J. A., Guy, C. S., Ban, D., Banerjee, P. R., Stanley, C. B., Nourse, A., Deniz, A. A., & Kriwacki, R. W. Nucleophosmin integrates within the nucleolus via multi-

modal interactions with proteins displaying R-rich linear motifs and rRNA. *eLife* **5**, e13571 (2016).

12. Brangwynne, C. P., Tompa, P., & Pappu, R. V. Polymer physics of intracellular phase transitions. *Nat. Phys.* **11**, 899–904 (2015).

13. Uversky, V. N. Intrinsically disordered proteins in overcrowded milieu: Membrane-less organelles, phase separation, and intrinsic disorder. *Curr. Opin. Struct. Biol.* **44,** 18–30 (2017).

14. Shin, Y., & Brangwynne, C. P. Liquid phase condensation in cell physiology and disease. *Science* **357**, eaaf4382 (2017).

15. Mitrea, D. M., & Kriwacki, R. W. Phase separation in biology; functional organization of a higher order. *Cell Commun. Signal.* **14,** 1 (2016).

16. Martin, E. W., Holehouse, A. S., Peran, I., Farag, M., Incicco, J. J., Bremer, A., Grace, C. R., Soranno, A., Pappu, R. V., & Mittag, T. Valence and patterning of aromatic residues determine the phase behavior of prion-like domains. *Science* **367**, 694-699 (2020).

17. Mukhopadhyay, S. The dynamism of intrinsically disordered proteins: Binding induced folding, amyloid formation, and phase separation. *J. Phys. Chem. B* **124**, 11541–11560 (2020).

18. Martin, E. W., & Mittag, T. Relationship of sequence and phase separation in protein low-complexity regions. *Biochemistry* **57,** 2478–2487 (2018).

19. Bhopatkar, A. A., Dhakal, S., Abernathy, H. G., Morgan, S. E., & Rangachari, V. Charge and redox states modulate granulin-TDP-43 coacervation toward phase separation or aggregation. *Biophys. J.* **121,** 2107-2126 (2022).

20. Vendruscolo, M., & Fuxreiter, M. Protein condensation diseases: therapeutic opportunities. *Nat. Commun.* **13,** 5550 (2022).

21. Alberti, S., Gladfelter, A., & Mittag, T. Considerations and challenges in studying liquid-liquid phase separation and biomolecular condensates. *Cell*, **176**, 419e434 (2019).

22. Pattanashetty, S. G., Joshi, A., Walimbe, A., & Mukhopadhyay, S. Guidelines for in vitro Characterization of Liquid-liquid Phase Separation. In: Uversky, U. (ed.) Droplets of life:

Membrane-less Organelles, Biomolecular Condensates, and Biological Liquid-liquid Phase Separation. *Elsevier* **1**, 233-249 (2022).

23. Agam, G., Gebhardt, C., Popara, M., Mächtel, R., Folz, J., Ambrose, B., Chamachi, N., Chung, S. Y., Craggs, T. D., de Boer, M., Grohmann, D., Ha, T., Hartmann, A., Hendrix, J., Hirschfeld, V., Hübner, C. G., Hugel, T., Kammerer, D., Kang, H. S., Kapanidis, A. N., Krainer, G., Kramm, K., Lemke, E. A., Lerner, E., Margeat, E., Martens, K., Michaelis, J., Mitra, J., Moya Muñoz, G. G., Quast, R. B., Robb, N. C., Sattler, M., Schlierf, M., Schneider, J., Schröder, T., Sefer, A., Tan, P. S., Thurn, J., Tinnefeld, P., van Noort, J., Weiss, S., Wendler, N., Zijlstra, N., Barth, A., Seidel, C. A. M., Lamb, D. C., & Cordes, T. Reliability and accuracy of single-molecule FRET studies for characterization of structural dynamics and distances in proteins. *Nat. Methods.* **20,** 523-535 (2023).

24. Brucale, M., Schuler, B., & Samorì, B. Single-molecule studies of intrinsically disordered proteins. *Chem. Rev.* **26,** 3281-317 (2014).

25. Metskas, L. A., & Rhoades, E. Single-Molecule FRET of Intrinsically Disordered Proteins. *Annu. Rev. Phys. Chem.* **71**, 391-414 (2020).

26. Ghosh, S., Saha, S., Goswami, D., Bilgrami, S., & Mayor, S. Dynamic imaging of homo-FRET in live cells by fluorescence anisotropy microscopy. *Meth. Enzymol.* ***505*****,** 291–327 (2012).

27. Teijeiro-Gonzalez, Y., Crnjar, A., Beavil, A. J., Beavil, R. L., Nedbal, J., Le Marois, A., Molteni, C., & Suhling, K. Time-Resolved Fluorescence Anisotropy and Molecular Dynamics Analysis of a Novel GFP Homo-FRET Dimer. *Biophys. J.* ***120*****,** 254–269 (2021).

28. Majumdar, A., Das, D., Madhu, P., Avni, A., & Mukhopadhyay, S. Excitation Energy Migration Unveils Fuzzy Interfaces within the Amyloid Architecture. *Biophys. J.* ***118*****,** 2621–2626 (2020).

29. Driouchi, A., Gray-Owen, S. D., & Yip, C. M. Correlated STORM-homoFRET imaging reveals highly heterogeneous membrane receptor structures. *J. Biol. Chem.* ***298*****,** 102448 (2022).

30. Butcher, R.J., & Tabor, J. J. Real-time detection of response regulator phosphorylation dynamics in live bacteria. *Proc. Natl. Acad. Sci. U.S.A*. **119,** e2201204119 (2022).

31. Murthy, A. C., Dignon, G. L., Kan, Y., Zerze, G. H., Parekh, S. H., Mittal, J., & Fawzi, N. L. Molecular interactions underlying liquid-liquid phase separation of the FUS low-complexity domain. *Nat. Struct. Mol. Biol.* **26,** 637–648 (2019).

32. Portz, B., Lee, B. L., & Shorter, J. FUS and TDP-43 Phases in Health and Disease. *Trends Biochem. Sci.* **46**, 550-563 (2021).

33. Wang, J., Choi, J. M., Holehouse, A. S., Lee, H. O., Zhang, X., Jahnel, M., Maharana, S., Lemaitre, R., Pozniakovsky, A., Drechsel, D., Poser, I., Pappu, R. V., Alberti, S., & Hyman, A. A. A Molecular Grammar Governing the Driving Forces for Phase Separation of Prion-like RNA Binding Proteins. *Cell* **174** (3), 688–699 (2018).

34. Sanders, D. W., Kedersha, N., Lee, D. S. W., Strom, A. R., Drake, V., Riback, J. A., Bracha, D., Eeftens, J. M., Iwanicki, A., Wang, A., Wei, M. T., Whitney, G., Lyons, S. M., Anderson, P., Jacobs, W. M., Ivanov, P., & Brangwynne, C. P. Competing protein- RNA interaction networks control multiphase intracellular organization. *Cell* **181**, 306–324 (2020).

35. Silva, J. L., & Cordeiro, Y. The "Jekyll and Hyde" actions of nucleic acids on the prion-like aggregation of proteins. *J. Biol. Chem.* **291**, 15482–15490 (2016).

36. Loughlin, F. E., Lukavsky, P. J., Kazeeva, T., Reber, S., Hock, E. M., Colombo, M., Von Schroetter, C., Pauli, P., Cléry, A., Mühlemann, O., Polymenidou, M., Ruepp, M. D., & Allain., F. H. The Solution Structure of FUS Bound to RNA Reveals a Bipartite Mode of RNA Recognition with Both Sequence and Shape Specificity. *Mol. Cell* **73,** 490–504 (2019).

37. Avni, A., Joshi, A., Walimbe, A., Pattanashetty, S. G., & Mukhopadhyay, S. Single-droplet surface-enhanced Raman scattering decodes the molecular determinants of liquid-liquid phase separation. *Nat. Commun.* **13,** 4328 (2022).

38. Monahan, Z., Ryan, V. H., Janke, A. M., Burke, K. A., Rhoads, S. N., Zerze, G. H., O'Meally, R., Dignon, G. L., Conicella, A. E., Zheng, W., Best, R. B., Cole, R. N., Mittal, J., Shewmaker, F., & Fawzi, N. L. Phosphorylation of the FUS low-complexity domain disrupts phase separation, aggregation, and toxicity. *EMBO J.* **36,** 2951-2967 (2017).

39. Agarwal, A., Rai, S. K., Avni, A., & Mukhopadhyay, S. An intrinsically disordered pathological prion variant Y145Stop converts into self-seeding amyloids via liquid-liquid phase separation. *Proc. Natl. Acad. Sci. U.S.A.* **118,** e2100968118 (2021).

40. Cochard, A., Garcia-Jove Navarro, M., Piroska, L., Kashida, S., Kress, M., Weil, D., & Gueroui, Z. RNA at the surface of phase-separated condensates impacts their size and number. Biophys. J. **121,** 1675–1690 (2022).

41. Kar, M., Dar, F., Welsh, T. J., Vogel, L. T., Kühnemuth, R., Majumdar, A., Krainer, G., Franzmann, T. M., Alberti, S., Seidel, C. A. M., Knowles, T. P. J., Hyman, A. A., & Pappu, R. V. Phase-separating RNA-binding proteins form heterogeneous distributions of clusters in subsaturated solutions. *Proc. Natl. Acad. Sci. U.S.A.* ***119*****,** e2202222119 (2022).

42. Rai, S. K., Khanna, R., Avni, A., & Mukhopadhyay, S. Heterotypic electrostatic interactions control complex phase separation of tau and prion into multiphasic condensates and co-aggregates. *Proc. Natl Acad. Sci. U.S.A.* **120**, e2216338120 (2023).

43. Kaur, T., Raju, M., Alshareedah, I., Davis, R.B., Potoyan, D.A., & Banerjee, P. R. Sequence-encoded and composition-dependent protein-RNA interactions control multiphasic condensate morphologies. *Nat. Commun.* **12,** 872 (2021).

44. Ganser, L. R., Niaki, A. G., Yuan, X., Huang, E., Deng, D., Djaja, N. A., Ge, Y., Craig, A., Langlois, O., & Myong, S. The roles of FUS-RNA binding domain and low complexity domain in RNA-dependent phase separation. *Structure* (2024).

45. Hofweber, M., Hutten, S., Bourgeois, B., Spreitzer, E., Niedner-Boblenz, A., Schifferer, M., Ruepp, M. D., Simons, M., Niessing, D., Madl, T., & Dormann, D. Phase Separation of FUS Is Suppressed by Its Nuclear Import Receptor and Arginine Methylation. *Cell* **173,** 706-719 (2018).

46. Qamar, S., Wang, G., Randle, S. J., Ruggeri, F. S., Varela, J. A., Lin, J. Q., Phillips, E. C., Miyashita, A., Williams, D., Ströhl, F., Meadows, W., Ferry, R., Dardov, V. J., Tartaglia, G. G., Farrer, L. A., Kaminski Schierle, G. S., Kaminski, C. F., Holt, C. E., Fraser, P. E., Schmitt-Ulms, G., Klenerman, D., Knowles, T., Vendruscolo, M., & St George-Hyslop, P. FUS Phase Separation Is Modulated by a Molecular Chaperone and Methylation of Arginine Cation-π Interactions. *Cell* **173,** 720–734 (2018).

47. Babinchak, W. M., Dumm, B. K., Venus, S., Boyko, S., Putnam, A. A., Jankowsky, E., & Surewicz, W. K. Small molecules as potent biphasic modulators of protein liquid-liquid phase separation. *Nat. commun.* ***11*****,** 5574 (2020).

48. Fang, M. Y., Markmiller, S., Vu, A. Q., Javaherian, A., Dowdle, W. E., Jolivet, P., Bushway, P. J., Castello, N. A., Baral, A., Chan, M. Y., Linsley, J. W., Linsley, D., Mercola, M., Finkbeiner, S., Lecuyer, E., Lewcock, J. W., & Yeo, G. W. Small-Molecule Modulation of TDP-43 Recruitment to Stress Granules Prevents Persistent TDP-43 Accumulation in ALS/FTD. *Neuron* ***103*****,** 802–819.e11 (2019).

49. Patel, A., Malinovska, L., Saha, S., Wang, J., Alberti, S., Krishnan, Y., & Hyman, A. A. ATP as a biological hydrotrope. *Science* ***356*****,** 753–756 (2017).

50. Ren, C. L., Shan, Y., Zhang, P., Ding, H. M., & Ma, Y. Q. Uncovering the molecular mechanism for dual effect of ATP on phase separation in FUS solution. *Sci. Adv.* ***8*****,** eabo7885 (2022).

51. Mahapatra, S., Sarbahi, A., Punia, N., Joshi, A., Avni, A., Walimbe, A., & Mukhopadhyay, S. ATP modulates self-perpetuating conformational conversion generating structurally distinct yeast prion amyloids that limit autocatalytic amplification. *J. Biol. Chem.* ***299*****,** 104654 (2023).

52. Yewdall, N. A., André, A. A. M., van Haren, M. H. I., Nelissen, F. H. T., Jonker, A., & Spruijt, E. ATP:Mg^{2+} shapes material properties of protein-RNA condensates and their partitioning of clients. *Biophys. J.* ***121*****,** 3962–3974 (2022).

53. Sun, S., Ling, S. C., Qiu, J., Albuquerque, C. P., Zhou, Y., Tokunaga, S., Li, H., Qiu, H., Bui, A., Yeo, G. W., Huang, E. J., Eggan, K., Zhou, H., Fu, X. D., Lagier-Tourenne, C., & Cleveland, D. W. ALS-causative mutations in FUS/TLS confer gain and loss of function by altered association with SMN and U1-snRNP. *Nat. commun.* ***6*****,** 6171 (2015).

54. Zhou, B., Wang, H., Cai, Y., Wen, H., Wang, L., Zhu, M., Chen, Y., Yu, Y., Lu, X., Zhou, M., Fang, P., Li, X., & Hong, D. FUS P525L mutation causing amyotrophic lateral sclerosis and movement disorders. *Brain Behav.* ***10*****,** e01625 (2020).

55. Szewczyk, B., Günther, R., Japtok, J., Frech, M. J., Naumann, M., Lee, H. O., & Hermann, A. FUS ALS neurons activate major stress pathways and reduce translation as an early protective mechanism against neurodegeneration. *Cell Rep.* ***42*****,** 112025 (2023).

56. Bosco, D. A., Lemay, N., Ko, H. K., Zhou, H., Burke, C., Kwiatkowski, T. J., Jr, Sapp, P., McKenna-Yasek, D., Brown, R. H., Jr, & Hayward, L. J. Mutant FUS proteins that cause

amyotrophic lateral sclerosis incorporate into stress granules. *Hum. Mol. Genet.* ***19*****,** 4160–4175 (2010).

57. Baron, D. M., Kaushansky, L. J., Ward, C. L., Sama, R. R. K., Chian, R. J., Boggio, K. J., Quaresma, A. J. C., Nickerson, J. A., & Bosco, D. A. Amyotrophic lateral sclerosis-linked FUS/TLS alters stress granule assembly and dynamics. *Mol. Neurodegener.* **8,** 30 (2013).

58. Bentmann, E., Neumann, M., Tahirovic, S., Rodde, R., Dormann, D., & Haass, C. Requirements for stress granule recruitment of fused in sarcoma (FUS) and TAR DNA-binding protein of 43 kDa (TDP-43). *J. Biol. Chem*. **287,** 23079-23094 (2012).

59. Farag, M., Cohen, S. R., Borcherds, W. M., Bremer, A., Mittag, T., & Pappu, R. V. Condensates formed by prion-like low-complexity domains have small-world network structures and interfaces defined by expanded conformations. *Nat. Commun.* **13,** 7722 (2022).

60. Agarwal, A., Arora, L., Rai, S. K., Avni, A., & Mukhopadhyay, S. Spatiotemporal modulations in heterotypic condensates of prion and α-synuclein control phase transitions and amyloid conversion. *Nat. Commun.* **13,** 1154 (2022).

61. Joron, K., Viegas, J. O., Haas-Neill, L., Bier, S., Drori, P., Dvir, S., Lim, P. S. L., Rauscher, S., Meshorer, E., & Lerner, E. Fluorescent protein lifetimes report densities and phases of nuclear condensates during embryonic stem-cell differentiation. *Nat. commun.* ***14*****,** 4885 (2023).

62. Galvanetto, N., Ivanović, M. T., Chowdhury, A., Sottini, A., Nüesch, M. F., Nettels, D., Best, R. B., & Schuler, B. Extreme dynamics in a biomolecular condensate. *Nature*, **619,** 876–883 (2023).

63. Joshi, A., Walimbe, A., Avni, A., Rai, S. K., Arora, L., Sarkar, S., & Mukhopadhyay, S. Single-molecule FRET unmasks structural subpopulations and crucial molecular events during FUS low-complexity domain phase separation. *Nat. Commun.* **14**, 7331 (2023).

64. Melo, A. M., Coraor, J., Alpha-Cobb, G., Elbaum-Garfinkle, S., Nath, A., & Rhoades, E. A. Functional role for intrinsic disorder in the tau-tubulin complex. *Proc. Natl. Acad. Sci. USA* **13,** 14336-14341 (2016).

65. Raghupathy, R., Anilkumar, A. A., Polley, A., Singh, P. P., Yadav, M., Johnson, C., Suryawanshi, S., Saikam, V., Sawant, S. D., Panda, A., Guo, Z., Vishwakarma, R. A., Rao, M., & Mayor, S. Transbilayer lipid interactions mediate nanoclustering of lipid-anchored proteins. *Cell,* **161**, 581–594 (2015).

66. Böddeker, T. J., Rosowski, K. A., Berchtold, D., Emmanouilidis, L., Han, Y., Allain, F. H. T., Style, R. W., Pelkmans, L., & Dufresne, E. R. Non-specific adhesive forces between filaments and membraneless organelles. *Nat. Phys.* **18**, 571–578 (2022).

67. do Amaral, M. J., Mohapatra, S., Passos, A. R., Lopes da Silva, T. S., Carvalho, R. S., da Silva Almeida, M., Pinheiro, A. S., Wegmann, S., & Cordeiro, Y. Copper drives prion protein phase separation and modulates aggregation. *Sci. Adv.* **9**, eadi7347 (2023).

68. Gu, J., Liu, Z., Zhang, S., Li, Y., Xia, W., Wang, C., Xiang, H., Liu, Z., Tan, L., Fang, Y., Liu, C., & Li, D. Hsp40 proteins phase separate to chaperone the assembly and maintenance of membraneless organelles. *Proc. Natl. Acad. Sci. U.S.A*. **117,** 31123–31133 (2020).

69. Liu, Z., Zhang, S., Gu, J., Tong, Y., Li, Y., Gui, X., Long, H., Wang, C., Zhao, C., Lu, J., He, L., Li, Y., Liu, Z., Li, D., & Liu, C. Hsp27 chaperones FUS phase separation under the modulation of stress-induced phosphorylation. *Nat. Struct. Mol. Biol*. **27,** 363–372 (2020).

70. Farag, M., Borcherds, W. M., Bremer, A., Mittag, T., & Pappu, R. V. Phase separation of protein mixtures is driven by the interplay of homotypic and heterotypic interactions. *Nat. commun.* ***14*****,** 5527 (2023).

******

Conclusions and Future Directions

5.1 Conclusions

The human body consists of billions of biomolecules, which are essential to perform key cellular functions. Phase separation of biomolecules into liquid-like supramolecular assemblies has emerged as a critical organizing principle within living cells. Intrinsically disordered proteins/regions (IDPs/IDRs) comprising low-complexity (LC) and prion-like domains have been identified as the key candidates driving intracellular phase separation leading to the formation of noncanonical membrane-less organelles (MLOs), also known as biomolecular condensates. IDPs/IDRs are a special class of proteins that do not follow one structure-one function paradigm and provide multivalent interactions to facilitate protein-protein and protein-nucleic acid interactions. These condensates are thought to spatiotemporally regulate critical cellular functions and are also known to undergo aberrant phase transitions associated with a range of neurodegenerative diseases such as Amyotrophic lateral sclerosis (ALS), Frontotemporal dementia (FTDs) and Alzheimer's disease.

This thesis describes novel tools and concepts that are developed to understand key molecular events during the biological phase transition of an archetypical prion-like RNA binding protein Fused in Sarcoma (FUS). Below, I summarize the key questions and findings discussed in various chapters of this thesis.

I. Single-molecule FRET illuminates structural subpopulations and dissects crucial molecular events during phase separation of a prion-like low-complexity domain of Fused in Sarcoma (FUS) protein (Chapter 2).
II. Utilizing single-droplet vibrational Raman spectroscopy to illuminate the structural changes in the biological water/ hydration layer upon phase separation (Chapter 3).
III. Energy migration via homoFRET captures the dynamic architecture of *in vitro* and *in situ* formed phase-separated biomolecular compartments of Fused in Sarcoma (FUS) (Chapter 4).

Phase separation of biomolecules is a general phenomenon adopted by cells to organize their intricate biochemical processes. A current flurry of reports suggests the involvement of biological phase separation in an array of cellular processes like replication, transcription, translation, DNA damage repair, immune system, host-pathogen interaction, and so on. However, these on-demand functional condensates, if unregulated, lead to a large number of neuropathological disorders, including Parkinson's, Alzheimer's, Amyotrophic lateral

sclerosis, etc. Therefore, dissecting the key molecular factors involved in phase separation has now become the need of the hour. Although a large number of microscopy and spectroscopy tools exist to study phase transitions, the majority of these provide average information from both condensed and dispersed phases of protein. Most of them fail to provide a droplet-by-droplet interrogation with ultrasensitive length and time resolution. In this direction, we utilized a combination of molecular, biophysical, biochemical, fluorescence, vibrational Raman spectroscopy, and cell biology to decipher the role of chain dynamics, hydration layer structures, and molecular packaging within an archetypical prion-like RNA binding protein FUS. Our goal is to explore the significance of heterogeneity, the processes involved in the formation and dissolution of these on-demand organelles, and oligomerization in the context of FUS phase separation linked to cellular functions and diseases. To conduct these studies, we utilize state-of-the-art techniques such as single-molecule Förster resonance energy transfer (smFRET), super-resolution imaging, picosecond time-resolved spectroscopy, fluorescence correlation spectroscopy (FCS), dynamic light scattering (DLS), vibrational Raman spectroscopy, and ensemble fluorescence lifetime/anisotropy.

In order to observe the chain fluctuations upon phase separation directly, we performed residue-specific single-droplet single-molecule FRET experiments within the dispersed and condensed phases. Our data show the presence of distinct conformational subpopulations in the dispersed phase and droplet phase, which undergo interconversion at the millisecond timescale (Chapter 2). Based on our smFRET data, we propose that the FUS-LC polypeptide chain exists in a collapsed paperclip conformation within the dispersed phase. This kind of paperclip conformation has also been observed for other collapsed IDPs, such as the microtubule-binding protein tau. The paperclip structure undergoes a conformational expansion within the condensates as observed through single-droplet single-molecule FRET measurements. This chain opening indicates a release of long-range contacts to facilitate a shift from intramolecular to intermolecular interactions, leading to a dense network of chain-chain interactions favoring phase separation. Our FCS experiments, in agreement with the steady-state and time-resolved anisotropy data, reveal a loss of conformational flexibility and a highly viscous environment in the droplet interior. The interior of the droplets of FUS-LC shows a remarkably slower diffusion of molecules compared to the dispersed phase, as evident from a ~ 500 times slower diffusion time. The introduction of a single point mutation at the 156th position (G156E) corresponding to the clinically-relevant ALS associated mutant G156E FUS-LC showed changes that could be captured by our smFRET and FCS measurements. Single-

droplet, single-molecule FRET measurements showed a further opening of the polypeptide chain inside G156E FUS-LC droplets, hinting towards the formation of a larger number of intermolecular interactions required for an accelerated liquid-to-solid transition of G156E FUS-LC condensates as compared to the wild-type droplets. Taken together, our data indicate an expansion in the polypeptide chain, which enhances the multivalency, resulting in a large-scale network of interchain interactions known to drive phase separation. This opening of the polypeptide chain for collapsed IDPs/IDRs causes an increase in valency, resulting in the predominance of intermolecular interactions over intramolecular interactions, favoring phase separation. These interactions, if unchecked, lead to aberrant phase transitions to pathological aggregates. We hypothesize that this might be a general phenomenon accompanying the phase separation of IDPs/IDRs containing low-complexity sequences.

Water, a major constituent of biomolecular condensates, is one of the most overlooked aspects of the complex process of phase separation. These water molecules are known to largely modulate the structural and functional properties of biomolecules, including protein and RNA, via altering the solute-solute, solute-solvent, and solvent-solvent interactions. However, these changes in the solvent properties and structural reorganization associated with the formation of biomolecular condensates are yet to be understood. In this direction, we utilize single-droplet vibrational Raman spectroscopy to investigate the hydration water network and observe changes in the internal hydrogen-bonding network, including the release of strongly coordinated hydration water and accompanying condensate formation (Chapter 3). Our research focuses on three well-studied phase separation systems, namely Fused in Sarcoma (FUS), FUS low-complexity domain (FUS-LC), and tau, illuminating correlations between water release and predominant interactions (electrostatic/hydrophobic) driving phase separation. Additionally, we show the effect of small molecule modulators, such as salt and RNA, on hydration water structure within condensates. This work provides insights into the internal restructuring of solvent hydrogen bonding networks during phase separation, indicating its significance in the condensate formation process.

The phase transition of biomolecules resulting in the formation of liquid condensates and solid aggregates holds significant relevance from the physiological and pathological points of view. Thus, the development of tools for probing the distinct assemblies and assessing their internal organization, molecular association, and resulting material properties has become the need of the hour. We demonstrate the utilization of a fundamental principle of homoFRET to investigate phase-separated biomolecular condensates by performing anisotropy imaging.

Steady-state values report on the extent of energy migration, which is determined by the local density or molecular proximities of the fluorophore molecules constituting the liquid droplets. Using eGFP tagged Fused in Sarcoma (FUS), we study the dispersed and condensed phases of FUS-eGFP *in vitro* and *in situ*. Anisotropy imaging readily captures the dense packaging and enhanced protein-protein association upon phase separation. Further, the picosecond time-resolved fluorescence anisotropy measurements provide us with the diverse underlying components contributing to the overall depolarization of anisotropy. The depolarization kinetics yield multiple energy migration time constants, presumably originating from the distinct modes of excitation energy migration. Using these sensitive steady-state measurements, we also detect alteration in the droplet architecture and compactness in response to phase separation modulators such as RNA, ATP, and post-translational methylation on FUS-eGFP condensates. Lastly, we advance our studies to explore the utility of this tool within cells and capture the formation and dynamic organization of assemblies formed *in situ* via phase separation of FUS-eGFP in response to cellular cues. In summary, our data showcase the efficacy of anisotropy as a powerful tool for a deeper understanding of the droplet interior and intermolecular clustering within *in vitro* and cellular assemblies.

5.2 Limitations and future improvements of the study

- Our single-molecule FRET data within droplets exhibited large fluorescence background noise due to the densely concentrated condensates focused near the coverslip surface. Further modifications of the glass surface are required to ensure the complete absence of non-specific protein-glass interactions.
- The accurate estimation of inter-residue distances requires further incorporation of multiple corrections arising from the broadening of the FRET efficiency histogram due to photon shot noise, altered refractive index, and orientation factor (κ^2) within the densely packed condensates.
- The time-dependent dynamics of hydration water could not be captured due to the lack of time-resolved Raman measurements.
- Picosecond time-resolved anisotropy measurements were unsuccessful *in situ* due to incomplete depolarization of anisotropy decay even at longer time scales and the unavailability of advanced analysis software for these data.

5.3 Future directions

- Recent reports have indicated the presence of a non-uniform radial distribution of conformationally distinct populations within the heterogeneous droplet interior. Single-molecule FRET studies coupled with time-resolve anisotropy measurements at different droplet locations can shed light on the conformational distribution and spatial heterogeneity within these condensates.
- Confocal-based Z-stack scanning through vibrational Raman spectroscopy coupled with terahertz spectroscopy can be performed to get radial distribution and dynamics of water from the core to the periphery of droplets.
- The role of the RNA-binding domain of FUS in driving and modulating the phase separation of FUS and its interaction with the LC domain and RNA can be studied using three-color and four-color FRET measurements, respectively.
- HomoFRET, in conjunction with heteroFRET, can reveal the molecular packaging and inner workings of the intricate, multicomponent phase separating systems and provide deeper insights into the complex interplay of scaffold-scaffold and scaffold-client interactions, modulating phase separation.

******